Unveiling the Star-Disk Interaction in Young Stars with High-Resolution Spectrophotometric Observations

Dissertation

der Mathematisch-Naturwissenschaftlichen Fakultät

der Eberhard Karls Universität Tübingen

zur Erlangung des Grades eines

Doktors der Naturwissenschaften

(Dr. rer. nat.)

vorgelegt von

Antonio Armeni

aus Massa Marittima (Italien)

Tübingen

2025

Gedruckt mit Genehmigung der Mathematisch-Naturwissenschaftlichen Fakultät der Eberhard Karls Universität Tübingen.

Tag der mündlichen Qualifikation:	09.05.2025
Dekan:	Prof. Dr. Thilo Stehle
1. Berichterstatter/-in:	Prof. Dr. Beate Stelzer
2. Berichterstatter/-in:	Prof. Dr. Klaus Werner

To my family and my friends,
the brightest stars in my everyday sky

PUBLICATIONS

1. Armeni, A., Stelzer, B., Claes, R. A. B., Manara, C. F., Frasca, A., Alcalá, J. M., Walter, F. M., Kóspál, Á., Campbell-White, J., Gangi, M., Mauco, K., and Tychoniec, L. (2023).
   PENELLOPE. V. The magnetospheric structure and the accretion variability of the classical T Tauri star HM Lup.
   Astronomy & Astrophysics, 679:A14.

2. Armeni, A., Stelzer, B., Frasca, A., Manara, C. F., Walter, F. M., Alcalá, J. M., Schneider, P. C., Sicilia-Aguilar, A., Campbell-White, J., Fiorellino, E., Gameiro, J. F., and Gangi, M. (2024).
   Evidence for magnetic boundary layer accretion in RU Lup: A spectrophotometric analysis.
   Astronomy & Astrophysics, 690:A225.

3. Armeni, A., Stelzer, B., Frasca, A., Manara, C. F., Campbell-White, J., Gameiro, J. F., and Gangi, M. (2025).
   Spinning-down RU Lup: Constraints on the physics of the outflow from high-resolution spectroscopy.
   submitted to Astronomy & Astrophysics.

Nr.	Status	Scientific ideas	Data generation[†]	Analysis and interpretation	Writing
1	accepted	70%	15%	85%	90%
2	accepted	90%	15%	95%	90%
3	submitted	90%	15%	95%	90%

Table 1: My contribution to the publications.

[†]: Light curves for the *Transiting Exoplanet Survey Satellite* (TESS) are publicly available on the MAST archive (`https://archive.stsci.edu/`). Basic data reduction for the *Echelle SPectrograph for Rocky Exoplanets and Stable Spectroscopic Observations* (ESPRESSO) and X-Shooter spectroscopic observations has been performed by members of the PENELLOPE team for general use within the collaboration. Basic data reduction for the CHIRON spectroscopic observations has been performed by Frederick M. Walter.

ABBREVIATIONS

ALMA Atacama Large Millimeter/submillimeter Array

BC broad component

CTTS Classical T Tauri Star

CWT Continuous Wavelet Transform

DACs discrete absorption components

ESO European Southern Observatory

ESPRESSO *Echelle SPectrograph for Rocky Exoplanets and Stable Spectroscopic Observations*

FELs Forbidden emission lines

FIR far infrared

FWHM full width at half maximum

HST *Hubble Space Telescope*

HVA high velocity absorption

HVC high velocity component

LVA low velocity absorption

LVC low velocity component

MBL magnetic boundary layer

MHD magnetohydrodynamic

MRI magnetorotational instability

MUSE *Multi Unit Spectroscopic Explorer*

MVA medium velocity absorption

NC narrow component

PMS Pre-Main-Sequence

QPOs quasi-periodic oscillations

RT Rayleigh-Taylor

SED spectral energy distribution

SpT spectral type

TESS *Transiting Exoplanet Survey Satellite*

ULLYSES *UV Legacy Library of Young Stars as Essential Standards*

UVES *Ultraviolet and Visual Echelle Spectrograph*

VLT *Very Large Telescope*

WTTS Weak-lined T Tauri Star

YSO young stellar object

ZUSAMMENFASSUNG

Neu entstehende Sterne akkretieren Material aus ihrer Mutterwolke, das aufgrund der Drehimpulserhaltung zu einer scheibenförmigen Struktur um den jungen Stern kollabiert. Nach etwa einer Million Jahren hat sich die Hülle um den Stern vollständig aufgelöst und das System wird bei optischen Wellenlängen beobachtbar, so dass die Wechselwirkung zwischen dem Stern und der Scheibe untersucht werden kann. Sterne mit geringer Masse, so genannte klassische T-Tauri-Sterne (CTTS), haben in diesem Stadium starke Magnetfelder, die den inneren Rand der Akkretionsscheibe auf einige Sternradien begrenzen. Das Gas strömt entlang der Magnetfeldlinien von der Scheibe auf den Stern in einem Prozess, der magnetosphärische Akkretion genannt wird. Der Akkretionsstrom endet in einem Schock an der Sternoberfläche, der die Photosphäre aufheizt und einen heißen Fleck erzeugt.

Die magnetosphärische Akkretion ist ein komplexer Prozess, der den Austausch von Materie, Drehimpuls und Energie zwischen Scheibe und Stern beinhaltet. Dieser Prozess wird von Massenverlust durch Stern- und Scheibenwinde begleitet, die durch offene Magnetfeldlinien angetrieben werden. Diese Materieausströmungen spielen eine entscheidende Rolle bein Drehimpulstransport und verhindern eine übermäßige Zunahme der Rotationsgeschwindigkeit des Sterns.

In meiner Dissertation untersuche ich die Wechselwirkung zwischen jungen Sternen und ihren Scheiben mit Hilfe von hochaufgelösten spektroskopischen Daten des *Echelle SPectrograph for Rocky Exoplanet and Stable Spectroscopic Observations* (ESPRESSO), dem Echelle-Spektrographen der neuesten Generation am Very Large Telescope (VLT) der Europäischen Südsternwarte, und photometrischen Daten des *Transiting Exoplanet Survey Satellite* (TESS). Meine Studie konzentriert sich auf drei klassische T-Tauri-Sterne: HM Lup, RU Lup und TW Hya.

Durch die Analyse der zahlreichen “erlaubten” Emissionslinien in den optischen Spektren von HM Lup und RU Lup habe ich die Struktur der Magnetosphäre und ihre Temperaturschichtung untersucht. Diese Analyse ermöglichte es mir, den Breitengrad des heißen Flecks auf der Sternoberfläche zu bestimmen und seine interne Temperaturstruktur zu erforschen. Die Untersuchung von “verbotenen” Emissionslinien und von blauverschobenen Absorptionskomponenten in den Spektren von RU Lup offenbarte zudem die Kinematik magnetischer Ausströmungen und deren komplexe, geschichteten Struktur.

Lichtkurven mit hoher Zeitauflösung von TW Hya und RU Lup ermöglichten es mir, magnetohydrodynamische Simulationen zu testen, indem ich die Rotationsmodulation des heißen Flecks analysierte. Diese Analyse führte zur Bestimmung des Radius, bei dem die Scheibe durch das stellare Magnetfeld abgeschnitten wird, und zur Berechnung des pro Zeiteinheit vom Stern auf die Scheibe übertragenen Drehimpulses.

Durch das Kombinieren spektroskopischer und photometrischer Techniken habe ich

untersucht, wie die Magnetosphäre auf Variationen der Akkretionsrate reagiert und wie Ausströmungen dem System Drehimpuls entziehen.

Zusammenfassend lässt sich sagen, dass meine Arbeit zu einem tieferen Verständnis der komplexen Prozesse beiträgt, die die Stern-Scheiben-Wechselwirkungen in jungen stellaren Objekten bestimmen.

Abstract (English)

Newly formed stars accrete material from their parent cloud, which, due to conservation of angular momentum, collapses into a disk-like structure around the young star. After approximately one million years, the envelope around the star has completely dissipated and the system becomes observable at optical wavelengths, making it possible to study the interaction between the star and the disk. Low-mass stars at this stage, known as Classical T Tauri Stars (CTTSs), have strong magnetic fields that disrupt the accretion disk at a distance of a few stellar radii from the star. Gas flows from the disk to the star along the magnetic field lines in a process called magnetospheric accretion, ending in a shock at the stellar surface, which heats the photosphere and creates a hot spot.

Magnetospheric accretion is a complex process involving the exchange of matter, angular momentum, and energy between the disk and the star. This process is accompanied by mass loss via stellar and disk winds, which are driven by open magnetic field lines. These outflows play a critical role in angular momentum extraction, preventing the star from spinning up.

In my thesis, I explore the interaction between young stars and their disks using high-resolution spectroscopic data from the *Echelle SPectrograph for Rocky Exoplanet and Stable Spectroscopic Observations* (ESPRESSO), the latest-generation echelle spectrograph at the European Southern Observatory's Very Large Telescope (VLT), and photometric data from the *Transiting Exoplanet Survey Satellite* (TESS). My study focuses on three Classical T Tauri Stars: HM Lup, RU Lup, and TW Hya.

Through the analysis of the numerous permitted emission lines in the optical spectra of HM Lup and RU Lup, I investigated the structure of the magnetosphere and its temperature stratification. This analysis enabled me to determine the latitude of the hot spot on the stellar surface and explore its internal temperature structure. Furthermore, the examination of forbidden emission lines and blueshifted absorption components in the spectra of RU Lup revealed the kinematics of magnetic outflows and their complex, layered structure.

High-cadence light curves of TW Hya and RU Lup allowed me to test magnetohydrodynamic simulations by analyzing the rotational modulation of the hot spot. This analysis led to the determination of the radius at which the disk is truncated by the stellar magnetic field and the determination of the amount of angular momentum transferred from the star to the disk per unit time.

By combining spectroscopic and photometric techniques, I studied how the magnetosphere responds to variations in the accretion rate and I constrained how outflows extract angular momentum from the system in RU Lup.

In summary, my work contributes to a deeper understanding of the complex processes governing star-disk interactions in young stellar objects.

CHAPTER 1

SETTING THE STAGE: STAR FORMATION AND ACCRETION DISKS

"One must have chaos in oneself to give birth to a dancing star"[1]. There is perhaps no better way to picture how a star is formed. From the onset of the gravitational collapse to the moment the star reaches the main sequence, the birth of a star is fundamentally a story of *chaos* - a dynamic interplay of turbulence, accretion, ejection, and radiative processes that ultimately gives rise to order.

The process begins in a cold, dense region of a molecular cloud, where turbulence, fragmentation, and gravitational instabilities act to seed the formation of protostellar cores. After ~ 1 million years from its birth, the so-called Classical T Tauri phase represents a crucial period in the star formation process, where the young star is no longer embedded in its parental cloud but it is still actively accreting material from its circumstellar disk. During this stage, the interplay between the star and the disk defines many of the observable properties of the system. Magnetically channeled accretion funnels gas onto the stellar surface, producing variability across multiple timescales. Simultaneously, outflows and winds regulate angular momentum loss, influencing both the evolution of the star and the dispersal of the disk. These processes leave distinct signatures on photometric and spectroscopic observations, providing important insight into the mechanisms that govern this chaotic interplay.

When nuclear fusion ignites, equilibrium is established between the outward radiation pressure and the inward pull of gravity, and the young star begins its life on the main sequence, where it will shine steadily for millions to billions of years. Thus, Nietzsche's quote

[1] Friedrich Nietzsche, Thus Spoke Zarathustra (1883 - 1885).

finds a counterpart in astrophysics: chaos is *necessary* for the birth of a star.

The aim of this thesis is to shed light on the interaction between a low-mass young star and its disk by means of high-cadence photometry and high-resolution spectroscopy. Through these observations, I seek to disentangle the complex variability of Classical T Tauri Stars, probing the mechanisms that drive the accretion and ejection processes at this crucial stage.

1.1 Star formation

Star formation begins with the gravitational collapse of a dense core of matter within a molecular cloud. The dense core is initially in hydrostatic equilibrium, a balance between its self-gravity, which tends to compress the object, and a pressure gradient, which acts in the opposite direction. In this pre-stellar phase (André, 2002), the young stellar object (YSO) gains mass from the surrounding parent cloud until the internal gas pressure of the core is no longer strong enough to counteract the gravitational pull, and the collapse begins. Jeans (1902) showed that this instability occurs when the mass of the core is greater than a critical value, the Jeans mass[2]

$$M_{\mathrm{J}} = \left(\frac{\pi k_{\mathrm{B}} T}{G \mu m_{\mathrm{p}}}\right)^{3/2} \rho^{-1/2}. \tag{1.1}$$

Here k_{B} is the Boltzmann constant, G is the gravitational constant, m_{p} is the proton mass, μ is the mean molecular weight, and T and ρ are the temperature and density of the cloud, respectively. Star formation is likely to take place in cold ($T \sim 10$ K) regions. Typical densities of molecular clouds are $n = \rho/\mu m_{\mathrm{p}} \sim 10^4$ cm^{-3}.

The collapse increases the density of the pre-stellar object up to the point where the core becomes opaque to radiation. Since the optically thick cloud can radiate efficiently, the matter heats up until the gravitational collapse is stopped by the pressure gradient and hydrostatic equilibrium is reached again. A protostar, also called a Class 0 object (first row of Fig. 1.1), is formed. In this phase the protostar is deeply embedded in the parental cloud and the system emits as a black body in the far infrared (FIR).

The newly formed (proto)star still accretes material from the cloud, but the conservation of angular momentum makes the accreting material collapse to a disk-like structure around the YSO. The envelope becomes progressively more optically thin by infalling onto the protostar and the disk. During this stage (Class I stage, second row of Fig. 1.1) the protostar emits as a black body at $T \lesssim 650$ K. The dusty envelope produces an excess in the FIR,

[2] See, e.g., `https://web.iucaa.in/~dipankar/ph217/jeans.pdf` for a derivation.

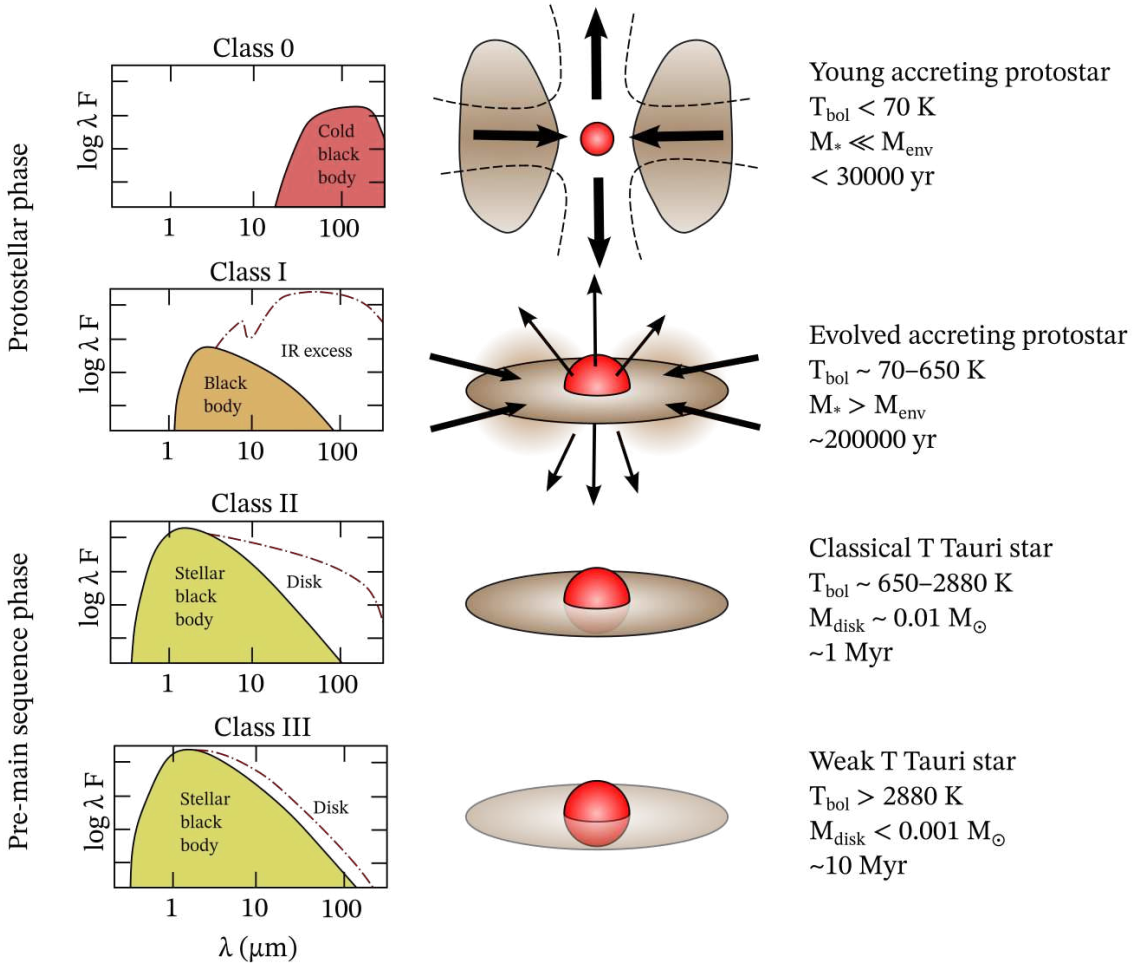

Figure 1.1: Stages of the star formation process (central column). The left column shows the spectrum emitted from the YSO during each stage. The right column reports the typical parameters of the YSO during each stage. Adapted from André (2002).

with a characteristic positive slope of the spectral energy distribution (SED) in the wavelength interval between 2.2 μm and 20 μm (Lada 1987, and second row of Fig. 1.1).

After ~ 1 Myr from the initial collapse, the envelope has completely dissipated and the YSO becomes observable at visible wavelengths. This is the end of the protostellar phase and the beginning of the Pre-Main-Sequence (PMS) phase. During this stage the young star is referred to as a Class II object (third row of Fig. 1.1). The system still shows a moderate infrared excess produced by the dusty disk, but the SED has now a negative slope (Lada, 1987). A star having a stellar mass ($M_\star$) lower than 2 $M_\odot$ (i.e., spectral types F-M) in the Class II stage is usually defined as a Classical T Tauri Star (CTTS) (Joy, 1945; Herbig, 1962). Stars with higher masses, up to 8 $M_\odot$, are instead called Herbig Ae/Be stars (Herbig, 1960).

The importance of the PMS stage lies in the fact the central object is not obscured by the envelope. For this reason, the Class II stage is the best evolutionary phase in which to study the accretion process and the interaction between the star and the disk. Moreover, the stellar properties such as the effective temperature, the stellar luminosity, and the stellar gravity, can be determined by studying the absorption spectrum of the young star (e.g., Frasca et al. 2017).

When the disk becomes optically thin, that is, the mass reservoir in the disk has completely dissipated and accretion has ceased, the YSO is in the Class III stage (fourth row of Fig. 1.1) and it is also defined as a Weak-lined T Tauri Star (WTTS). This is because the emission lines that typically trace the accretion flow in the Class II stage are instead produced in the stellar chromosphere for a Class III object, resulting in a weaker and narrower emission. WTTSs have an SED of a Main Sequence star.

This thesis focuses on the interaction between the star and its disk during the Class II stage of low mass stars (CTTSs).

1.2 Observational properties of Classical T Tauri Stars

Before dealing with the development of the theory that led to the current explanation of accretion in CTTSs, it is useful to list the main observational properties which are of interest for this thesis.

The discovery of this class of variable stars is attributed to Joy (1945), who observed "*eleven irregular variable stars*" in the Taurus-Auriga cloud and named them after its brightest member, T Tauri. He found that these stars were faint, with late spectral types (F5-G5) and "*emission lines resembling the solar chromosphere*". They displayed irregular and large light variations, and they were apparently associated with dark or bright nebulae. The hypothesis that T Tauri stars are young stars of low mass still in the process of gravitational contraction was first pointed out by Ambartsumian (1947), who found that they occur in groups which he named T-associations, and that these groups are often found in connection with groups of OB stars. Therefore, he postulated that T Tauri stars were the low-mass counterparts of the more recently formed OB stars. Herbig (1962) pointed out that two features of the T Tauri stars, namely, their elevation above the main sequence in the HR diagram and their abnormally wide absorption lines, have a natural explanation if the stars are contracting toward the main sequence. He also refined the defining criteria of Joy (1945) by basing the classification only on the following spectroscopic properties:

1. Hydrogen lines and Ca II H & K lines in emission.

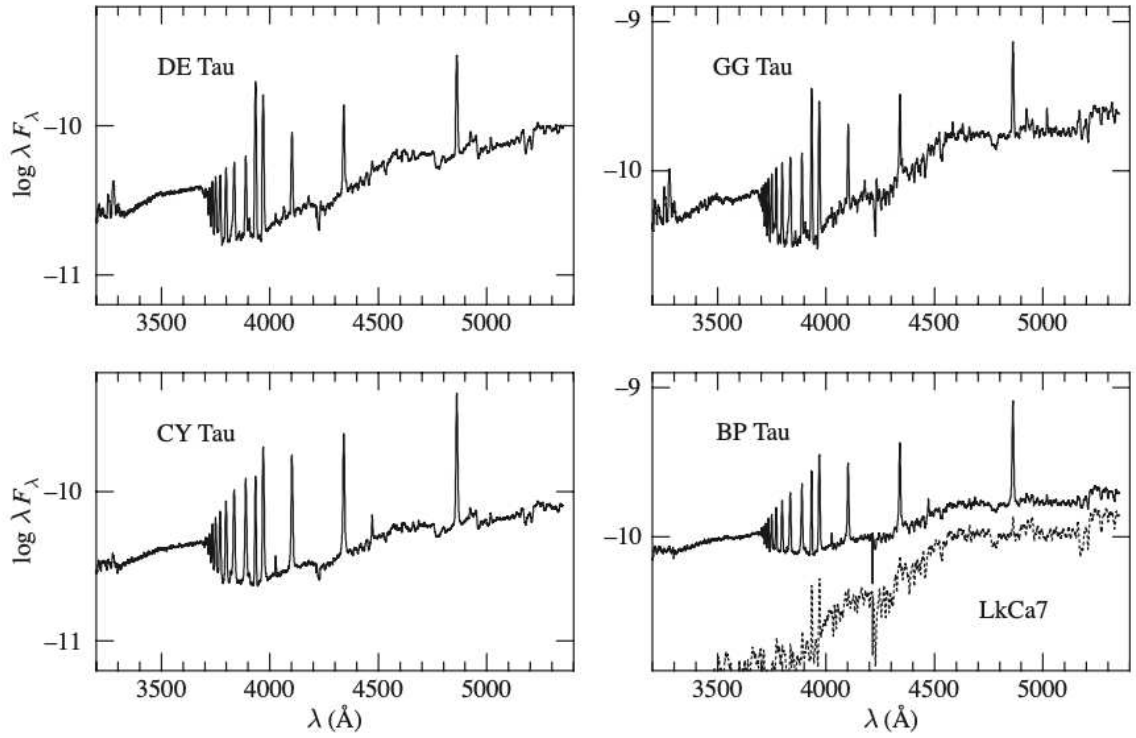

Figure 1.2: Optical spectra of selected CTTSs in the Taurus star-forming region, showing the emission lines and continuum emission. In the bottom right panel, the spectrum of BP Tau is compared with the spectrum of the WTTS LkCa7. From Gullbring et al. (1998).

2. Fluorescent emission in the Fe I doublet at 4063 and 4132 Å.
3. Emission in forbidden lines such as [S II] 6717, 6731 and [O I] 6300, 6363.
4. Presence of strong Li I 6707 absorption.

Herbig (1962) further noted that the stars with the above properties are irregular variables and are all associated with nebulosity, connecting his spectroscopic definition with the work of Joy (1945).

In the optical spectrum ($\sim 3600-7500$ Å) of a CTTS, the strongest emission lines are the Balmer lines of hydrogen, that result from electron transitions from higher energy levels ($n \gtrsim 3$) to the second energy level ($n = 2$), associated with the emission of a photon at the wavelength corresponding to the energy difference between the two levels. A similar process gives rise to continuum emission. When the gas is ionized, electrons recombine with protons and can settle into the second energy level from a free state. This leads to emission in a continuous range of wavelengths, the so-called Balmer continuum, starting from the Balmer jump at 3646 Å and extending toward shorter wavelengths in the ultraviolet (UV).

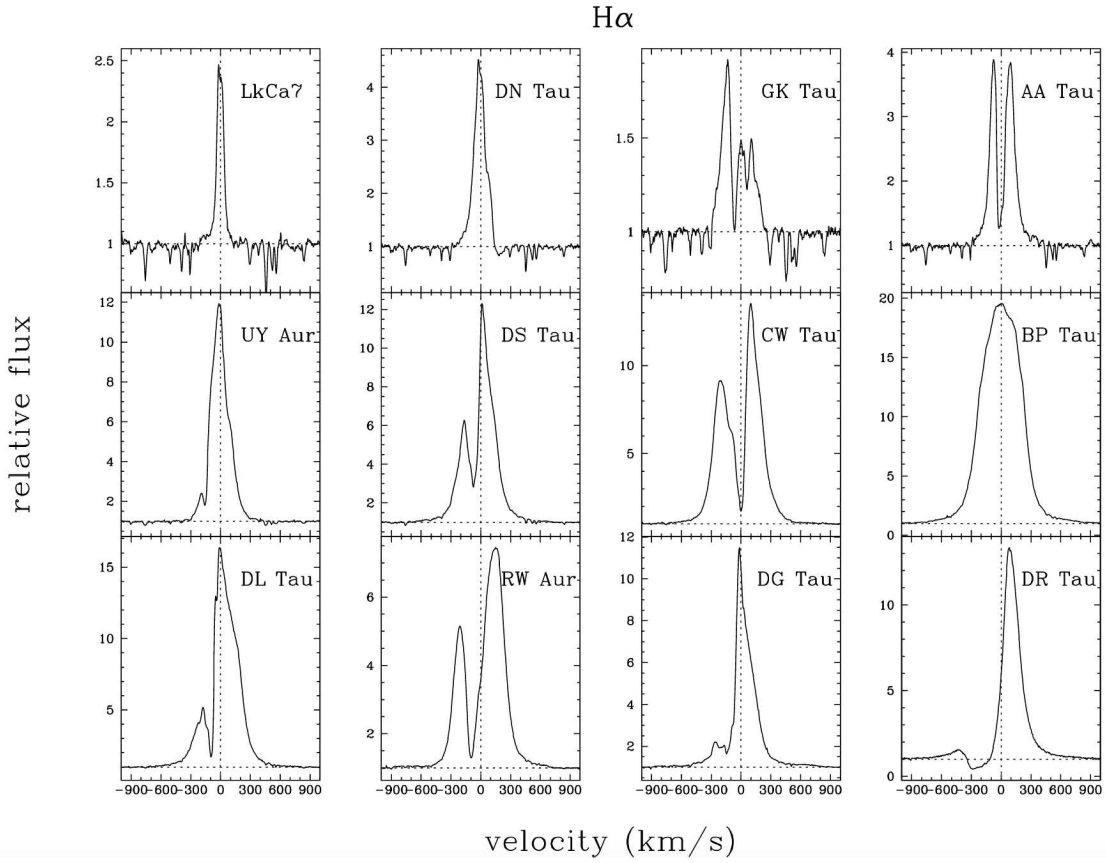

Figure 1.3: Hα profiles of selected CTTSs. From Muzerolle et al. (1998).

Figure 1.2 displays spectra of four CTTSs in the Taurus star-forming region in the spectral range between 3200 and 5300 Å. The emission-line spectrum is superposed on a continuous spectrum which has a very pronounced Balmer jump. The bottom right panel of Fig. 1.2 shows that the Balmer continuum is stronger in the CTTS BP Tau than in the WTTS LkCa7. This suggests a link between this observational feature and the interaction between the star and the disk.

Once high-dispersion spectra of the brightest CTTSs were obtained, it became clear that the emission lines were broad and highly variable. For example, Fig. 1.3 shows that blueshifted absorption components are commonly observed in the Hα emission line of CTTSs. This has been for a long time an indication that the material in CTTS envelopes is predominantly outflowing. However, inverse P Cygni profiles (i.e., profiles with a red-displaced absorption component) with radial velocities up to $\sim +400$ km s^{-1} were observed in the higher members of the Balmer series of a subclass of T Tauri stars, named YY Ori stars by Walker (1972). These stars also display inverse P Cygni profiles in lines from metals (e.g.,

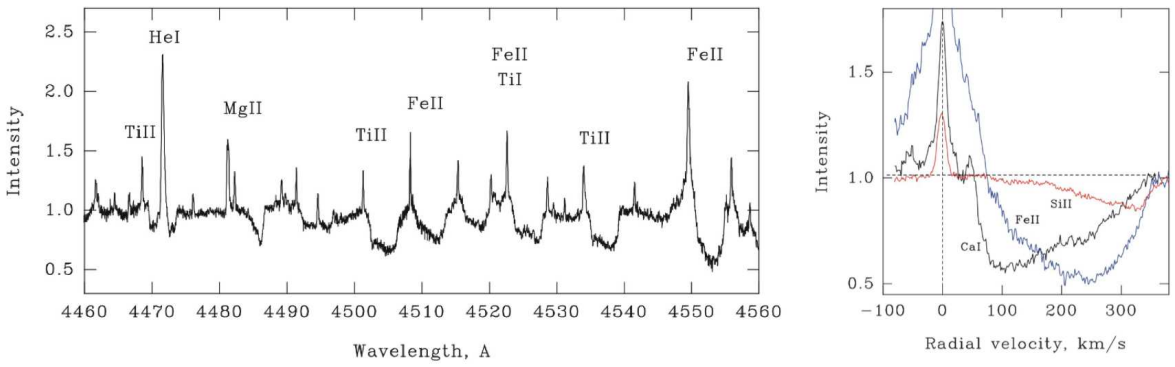

Figure 1.4: Inverse P Cygni profiles in the YY Ori star S CrA. Left: high resolution spectrum of S CrA between 4460 and 4560 Å. Right: Ca I 4226, Fe II 5018, and Si II 6347 emission lines plotted in radial velocity. From Petrov et al. (2014a).

in S CrA, Fig. 1.4). Inverse P Cygni profiles are line profiles in which the emission is on the blue side of the absorption. The presence of redshifted absorption below the continuum served as strong evidence of material infalling toward the star: as the continuum emission originates from the stellar surface, gas moving toward the star absorbs against this background. This observational feature led to the first development of gravitational accretion models, initially described through spherical infall scenarios (Appenzeller and Wolf, 1977).

In summary, the main observational properties of CTTSs are:

- late (from F to M) spectral type;
- presence of an excess continuum relative to the standard photospheric spectrum of a late-type star;
- the photospheric absorption lines are *veiled*, i.e., they appear shallower than in standard late-type stars;
- strong and broad emission lines in hydrogen and Ca II lines; the Balmer lines can have both P Cygni and inverse P Cygni profiles;
- irregular photometric variability.

In the remainder of this chapter, I will review the stages which led to the development of the current theory of accretion in CTTSs.

1.3 The "angular momentum problem" and the accretion disk as a solution

When the collapse of an over-dense region of a molecular cloud begins, the embryonic core has a net angular momentum. Suppose that a molecular cloud of hydrogen ($\mu = 2$) with $T = 10$ K and $n = 10^4$ cm^{-3} contains a mass of 1 $M_\odot$. The radius for which such a cloud becomes Jeans-unstable is the Jeans length, $\lambda_J = (3M_J/4\pi\rho)^{1/3} = 0.1$ pc. If the cloud has a small velocity difference Δv of 1 km s^{-1} from side to side, then its angular momentum is $L = \lambda_J M_J \Delta v = 0.1\ M_\odot$ km s^{-1} pc or $6.1 \cdot 10^{55}$ g cm^2 s^{-1} (Ray, 2012). The collapse will eventually produce a CTTS, which has typically a mass of $M_\star = 0.5\ M_\odot$, a radius of $R_\star = 2\ R_\odot$ (Hartmann et al., 2016), and rotates with a period $P_\star$ of 1 – 10 days (Bouvier et al., 2014). The angular momentum of such an object, assuming that it rotates as a rigid body, is $L = (2/5) M_\star R_\star^2 (2\pi/P_\star) \approx 10^{50}$ g cm^2 s^{-1}, that is, $\sim 10^5$ times smaller than that of its parent cloud. It is evident that during its formation, that is, in the first few million years of its life, the YSO must efficiently get rid of angular momentum. This is the so-called "angular momentum problem of star formation".

Angular momentum transport is also a key ingredient in order for the matter to accrete onto the star. To understand this, consider a particle revolving around a star of mass $M_\star$. The energy per unit mass e at a distance r from the center of the star is $e(r) = -GM_\star/2r$, and the particle rotates with an angular velocity Ω given by Kepler's third law, that is, $\Omega_K(r) = (GM_\star/r^3)^{1/2}$. In a polar coordinate system (r, ϕ) the velocity of the particle has only an azimuthal component

$$v_\phi(r) = r\Omega_K(r) = \sqrt{\frac{GM_\star}{r}}. \tag{1.2}$$

The angular momentum per unit mass $l = L/m$ is also a function of the distance from the center, r, and its expression is $l(r) = r\,v_\phi(r) = (GM_\star r)^{1/2}$. Therefore, for the particle to fall onto the star, it must lose angular momentum. In other words, a net transport of matter inward requires angular momentum to be either lost or transported outward in the disk.

Part of the angular momentum is lost from the system in the form of jets and/or disk winds (e.g., Bacciotti et al. 2002; Ray 2012; Lesur 2021; Pascucci et al. 2023), while the outward transport of angular momentum is driven by viscous processes in the accretion disk (e.g., Hartmann 2008). In this Section I discuss how mass and angular momentum can be transported in the disk.

In the solar system, although just 1% of the mass is contained in the planets, they contain roughly 99% of the angular momentum. Therefore, disks and the subsequent planet

formation appear to be one of the ways to remove angular momentum while the YSO is still building up mass. Recently, interferometric observations with the Atacama Large Millimeter/submillimeter Array (ALMA) were able to spatially resolve a CTTS disk for the first time, that of the ~ 1 Myr old star HL Tau (ALMA Partnership et al., 2015). The observations showed that the disk extends to 10^3 AU from the star and demonstrated that the gas is in Keplerian rotation around a ~ 1.3 $M_\odot$ star (ALMA Partnership et al., 2015). Meanwhile, disks around CTTSs are routinely imaged with ALMA (e.g., Ansdell et al. 2016, 2018).

Shear viscosity is one of the mechanisms that allows the gas to lose angular momentum and accrete (Pringle, 1981; Frank et al., 2002; Pringle and King, 2007). The key point is that a Keplerian velocity field such as the one of Eq. (1.2) implies a differential rotation: the inner parts of the disk rotate faster than the outer ones. This means that nearby orbits of matter move relative to each other, in other words, there is a shear ($\partial v_i/\partial x_j \neq 0$) in the fluid. If the disk presents a form of viscosity, that is, the fluid is non-ideal, the shear generates a stress in the fluid which transfers momentum in an irreversible way.

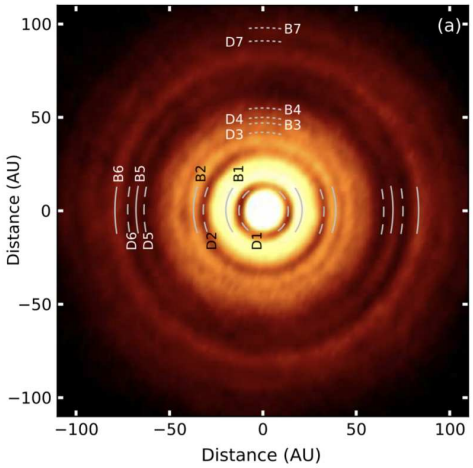

Figure 1.5: Deprojected 1.0 mm image of the disk in HL Tau, showing the substructures in the disk, such as gaps and rings. From ALMA Partnership et al. (2015).

The equation of transport for the angular momentum per unit area, $\ell = \Sigma r^2 \Omega$, where Σ is the surface density, in cylindrical symmetry is

$$\frac{\partial \ell}{\partial t} + \frac{1}{r}\frac{\partial}{\partial r}(r v_r \ell) = \frac{1}{r}\frac{\partial}{\partial r}\left(\nu \Sigma r^3 \frac{\partial \Omega}{\partial r}\right) \tag{1.3}$$

(Frank et al., 2002), where I introduced the kinematic viscosity ν, which has dimensions $[\nu] = L^2 T^{-1}$, that is, the square of a length divided by a time. The right-hand side of this equation is the net torque per unit area between two adjacent disk annuli. This equation shows that since the torque is nonzero and the angular momentum gradient is in the radial direction, under steady state conditions ($\partial_t \ell = 0$) there must be a radial component of the velocity, v_r, that transports angular momentum and, by definition, mass.

As angular momentum is transported outward, mass is transported inward. Equation (1.3) for the angular momentum transport can be used together with the continuity equation in

polar coordinates, that is,

$$\frac{\partial \Sigma}{\partial t} + \frac{1}{r}\frac{\partial}{\partial r}(r v_r \Sigma) = 0, \tag{1.4}$$

to derive the radial structure of a Keplerian accretion disk. Under steady state conditions ($\partial_t \to 0$), Eqs. (1.3) and (1.4) can be written as

$$\begin{cases} -r v_r \Sigma = \text{const.} \equiv \dot{\mathrm{M}} \\ \Sigma v_r \Omega - \nu \Sigma \frac{\partial \Omega}{\partial r} = \text{const.} \equiv -\frac{\mathrm{C}}{\mathrm{r}^3} \end{cases} \tag{1.5}$$

where I introduced the accretion rate $\dot{M} = dM/dt$ and another constant of integration C. The constant C can be determined at a point in the flow where $\partial\Omega/\partial r = 0$. Defining this radius as the inner boundary of the Keplerian disk, $R_{\rm in}$, we can write

$$C = -R_{\rm in}^3 \Sigma v_r(R_{\rm in})\Omega(R_{\rm in}) = \dot{M}\Omega(R_{\rm in})R_{\rm in}^2. \tag{1.6}$$

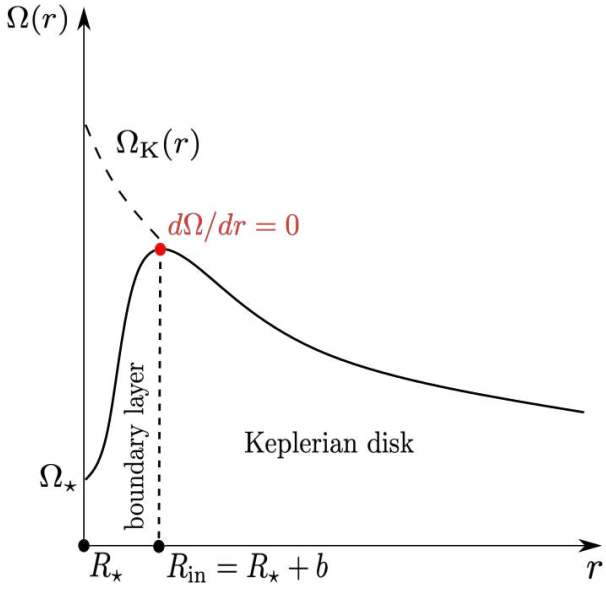

Figure 1.6: Angular velocity profile of an accretion disk around a star with angular velocity $\Omega_\star$. Adapted from Frank et al. (2002).

The rotational angular velocity of the star, $\Omega_\star$, must be lower than its break-up velocity, i.e., $\Omega_\star < (GM_\star/R_\star^3)^{1/2}$. This means that the velocity profile of the disk cannot be Keplerian all the way down to the stellar surface, but it must have a maximum somewhere ($\partial\Omega/\partial r = 0$) and then decrease to co-rotate with the star at its surface, as shown in Fig. 1.6. The region in which the angular velocity decreases is called "boundary layer", and it can be shown (Pringle, 1981) that its extent $b \equiv R_{\rm in} - R_\star$ is $\ll R_\star$. The problem of the inner edge of the Keplerian disk is of crucial importance in young stars, because of their magnetic nature. I will return to this point in Sect. 2.1. For the moment, we approximate $\Omega(R_{\rm in}) \approx \Omega_K(R_\star) = (GM_\star/R_\star^3)^{1/2}$ and $R_{\rm in} \approx R_\star$, and Eq. (1.6) becomes $C = -\dot{M}(GM_\star R_\star)^{1/2}$. Setting $\Omega(r) = \Omega_K(r)$ in the angular momentum equation, we find

$$\nu\Sigma = \frac{\dot{M}}{3\pi}\left[1 - \sqrt{\frac{R_\star}{r}}\right] \quad \text{and} \quad \mathrm{v_r} = -\frac{3\nu}{2\mathrm{r}}\left[1 - \sqrt{\frac{\mathrm{R_\star}}{\mathrm{r}}}\right]^{-1}. \tag{1.7}$$

To summarize, in a Keplerian disk in steady-state conditions material and angular momentum can be transported due to viscosity.

1.3.1 Sources of viscosity in the disk

The result of the previous section highlights the importance of the kinematic viscosity parameter to set the rate at which mass is transported inward in the disk. Therefore, it is important to quantify the magnitude of ν.

A simple dimensional estimate shows that the standard "molecular" viscosity, that is, the viscosity produced by shearing motion at a molecular level, is not able to transport enough angular momentum in the disk. Since the kinematic viscosity has dimensions of a velocity times a length, $U \cdot L$, we might estimate the typical length-scale of molecular viscosity to be the mean free path $\lambda_{\rm D}$ of the particles, and the average velocity to be their thermal speed $v_{\rm th}$. Therefore, we can write $\nu = v_{\rm th}\lambda_{\rm D}$. From Eq. (1.7) we see that $v_r \sim \nu/r$, hence the typical velocity to travel a radial distance R in the accretion disk in presence of molecular viscosity is

$$v_r \sim v_{\rm th}\frac{\lambda_{\rm D}}{R}. \tag{1.8}$$

Since the radial extent of an accretion disk is clearly larger than the mean free path of the particles ($R \gg \lambda_{\rm D}$), we find $v_r \ll v_{\rm th}$. Such a weak source of viscosity would lead to a slow disk evolution, which is not what is observed.

The fact that molecular viscosity is inefficient in transporting angular momentum has led to the idea that accretion disks are generally highly turbulent. The Reynolds number of the flow, which quantifies the importance of the inertial forces relative to the viscous ones (e.g, Landau and Lifshitz 1959), is usually of the order of 10^{14} under typical conditions for accretion disks (Frank et al., 2002). If the disk is turbulent, the flow will be characterized by the size $L_{\rm turb}$ and velocity $U_{\rm turb}$ of the largest turbulent eddies. Thus, a new source of viscosity, the turbulent viscosity, is present in the disk: $\nu \sim U_{\rm turb}L_{\rm turb}$.

The typical size of the largest turbulent eddies cannot exceed the disk thickness H. The velocity must be subsonic, otherwise the turbulent motions would be thermalized by shocks (Frank et al., 2002). Therefore, a convenient parametrization for the kinematic viscosity is

$$\nu = \alpha c_{\rm s} H, \tag{1.9}$$

where c_s is the sound speed. For the reasoning above, the free parameter α is expected to be ≤ 1. This is the famous α-prescription by Shakura and Sunyaev (1973), an elegant way

of condensing our ignorance about the viscosity mechanism into a single parameter. This parametrization has encouraged a semi-empirical approach to the viscosity problem, in which the magnitude of α is estimated by comparing theory with observations.

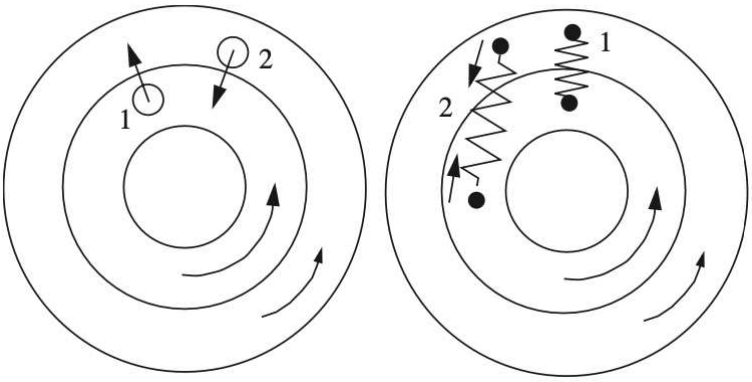

Figure 1.7: Schematic explanation of two ways of transferring angular momentum through turbulent processes in a Keplerian disk. Left: hydrodynamic viscosity. Right: viscosity from magnetorotational instability. From Hartmann (2008).

However, pure hydrodynamic turbulence does not seem to be effective in transporting angular momentum outward. The reason is that the flow is stable to axisymmetric disturbances because the specific angular momentum Ωr^2 increases outwards (the so-called Rayleigh stability criterion, e.g., Pringle and King 2007). This is shown schematically in Fig. 1.7 (left). The idea is that since the angular momentum scales as $\Omega r^2 \propto r^{1/2}$ in a Keplerian disk, an hydrodynamic vortex in the disk would transport material with lower angular momentum outward (blob 1 in Fig. 1.7, left) and material with higher angular momentum inward (blob 2), which is the opposite of what is required for accretion.

This is where magnetic fields come into play. Currently, the mechanism that looks most promising to produce viscosity of the right magnitude and sign is the development of magnetohydrodynamic (MHD) turbulence, the so-called magnetorotational instability (MRI). The stability of a rotating viscous fluid affected by a vertical magnetic field was originally discussed by Velikhov (1959) and Chandrasekhar (1960, 1961), but it was specifically applied to accretion disks by Balbus and Hawley (1991).

The idea behind this instability is sketched in Fig. 1.7 (right). The fundamental point is that magnetic fields in a conducting plasma behave as springs, that is, when the fluid is displaced they produce a restoring force proportional to the displacement itself (e.g., Balbus 2003). Suppose to have a magnetic field line which connects two parcels of gas at different radii in a Keplerian disk (situation 1 in Fig. 1.7, right). Since the inner blob rotates

faster than the outer one, the magnetic field line stretches (situation 2) and produces a magnetic tension that tries to restore the initial situation. This requires slowing down the inner blob relative to the outer blob, that is, transferring angular momentum outward. As the inner blob loses angular momentum, it will move inwards, while the opposite happens for the outer blob. The result is that the distance between the fluid elements increases and so does the magnetic tension, leading to the development of an instability.

Three-dimensional numerical results (e.g., Brandenburg et al. 1996; Heyvaerts et al. 1996) suggest that the MRI can produce a turbulence that behaves as an α-viscosity, with typical values of α between 0.01 and 0.1. A crucial problem for the application of the MRI to the disks of CTTSs is the fact that the gas must be coupled to the magnetic field. This means that the gas must be sufficiently ionized. At temperatures $T \gtrsim 1000$ K, atoms with low ionization potential such as K and Na can provide enough electrons for the MRI to operate. These conditions are met in the inner 0.1 AU of the disk, but most of the mass of YSO disks is likely to reside in much colder regions. A detailed discussion of the so-called "ionization problem" in the disk of YSOs is beyond the scope of this thesis, but can be found in Hartmann (2008).

1.3.2 Disk luminosity

The friction generated due to viscosity dissipates the energy of the gas as heat, and this heat is ultimately radiated away. In other words, viscosity makes the disk self-luminous. The rate of energy generation per unit area $D(r)$ can be found by computing the rate of energy dissipated per unit volume due to viscosity (ϵ) in cylindrical coordinates, that is, $\partial_t \epsilon = \nu\rho(\partial_r v_\phi)^2$ (Landau and Lifshitz, 1959). Integrating,

$$D(r) = \int (\partial_t \epsilon)\, dz = \int \nu\rho \left(r\frac{\partial\Omega}{\partial r} \right)^2 dz = \nu\Sigma r^2 \left(\frac{\partial\Omega}{\partial r} \right)^2 . \tag{1.10}$$

Since $\Omega = \Omega_K$, then $\partial_r\Omega = -(3/2)(\Omega/r)$, and we find

$$D(r) = \frac{9}{4}\nu\Sigma\frac{GM_\star}{r^3}. \tag{1.11}$$

Using the steady-state solution for the Keplerian disk, Eq. (1.7), we obtain

$$D(r) = \frac{3GM_\star\dot{M}}{4\pi r^3}\left[1 - \sqrt{\frac{R_\star}{r}} \right]. \tag{1.12}$$

The very important result is that $D(r)$ does not depend on the kinematic viscosity ν. $D(r)$ is of primary importance, because it is related to the spectrum emitted by the disk, and to

its total luminosity, i.e., the emitted energy per unit time. The luminosity produced by the disk can be found by integrating $D(r)$ over the disk surface, that is,

$$L_{\rm D} = 2\int_{R_\star}^{+\infty} \frac{3GM_\star \dot{M}}{4\pi r^3}\left[1-\sqrt{\frac{R_\star}{r}}\right] 2\pi r dr = \frac{GM_\star \dot{M}}{2R_\star}. \tag{1.13}$$

Under the approximation that the disk is optically thick in the vertical direction and that all the energy produced by viscosity is ultimately radiated away, each annulus emits roughly as a blackbody with a temperature given by

$$T(r) = \left(\frac{D(r)}{\sigma}\right)^{1/4} = T_{\rm D}\left(\frac{r}{R_\star}\right)^{-3/4}\left[1-\sqrt{\frac{R_\star}{r}}\right]^{1/4}, \tag{1.14}$$

where $T_{\rm D} = [(3GM_\star \dot{M})/(4\pi\sigma R_\star^3)]^{1/4}$ is a characteristic temperature in the disk.

The result of Eq. (1.13) implies that the total disk luminosity is half of the accretion luminosity, $L_{\rm acc} = GM_\star \dot{M}/R_\star$, that is, the luminosity produced if all the energy of the infalling matter were converted into radiation. The other half of the energy is retained by the gas as kinetic energy, and it is still available to be radiated from the boundary layer (Sect. 2.1) or in an accretion shock (Sect. 2.2). How this additional energy is dissipated and what are the consequences for the star are the main topics of the next chapter.

CHAPTER 2

STAR-DISK INTERACTION IN CLASSICAL T TAURI STARS

In the previous chapter, the standard theory of accretion disks has been introduced as a way of solving the angular momentum problem. The main idea is that some mechanism, most probably the MRI, gives rise to turbulence in the disk. This turbulence is a source of viscosity, and it is capable of transporting angular momentum outward while mass is accreted.

So far, the way angular momentum is exchanged between the disk and the young star has not been examined. In this chapter I will discuss how historically the boundary layer theory has been applied to fit the spectrum of CTTSs, and how further discoveries, the most important of which is the existence of strong magnetic fields in CTTSs, have led to the replacement of this theory with the now commonly accepted scenario of magnetospheric accretion. I will describe the physics of this process, the main observable quantities that it produces, and the way the disk and the star exchange mass and angular momentum. I will conclude by discussing the mechanism of angular momentum loss within the framework of the magnetospheric accretion scenario, specifically focusing on magnetic winds from both the star and the disk.

The magnetospheric accretion paradigm fundamentally relies on magnetic fields to mediate mass and angular momentum exchange between the star and disk. In my PhD research, I directly addressed this mechanism by analyzing high-resolution spectrophotometric observations of CTTSs (Chap. 4). These observations allowed me to constrain the structure of the accretion flow and the wind in CTTSs, ultimately providing insights into how the disk and the star exchange angular momentum and how part of this angular momentum is extracted from the system.

2.1 Boundary layers

Figure 2.1 shows a schematic view of a boundary layer. Under the assumption of a Keplerian disk, the boundary layer must be radially narrow (e.g., Pringle 1977; Frank et al. 2002). It is clear that the radiation emitted by the layer passes through a region of the disk that has a radial extent $\sim H$. If the density of this region is high enough, it will be optically thick. As a first approximation, this region radiates as a blackbody of area $\sim 2 \cdot 2\pi R_\star H$, where the factor 2 considers the two faces of the disk.

As discussed in Sect. 1.3.2, the boundary layer of a disk accreting onto a slowly rotating star emits a luminosity comparable to that released in the rest of the accretion disk. The reasoning above shows that this luminosity is released over a very small area. Therefore, the boundary layer must be much hotter than the Keplerian disk, and so it will radiate at shorter wavelengths. The blackbody temperature of an optically thick boundary layer, $T_{\rm BL}$, can be obtained from

$$4\pi R_\star H \sigma T_{\rm BL}^4 = \frac{GM_\star \dot{M}}{2R_\star}. \tag{2.1}$$

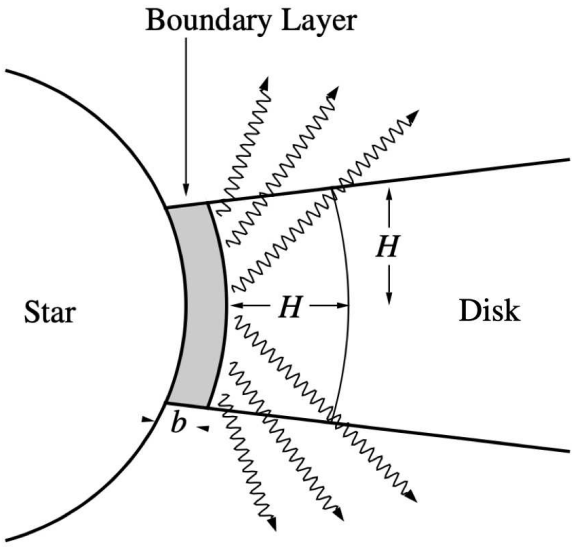

Figure 2.1: Schematic view of an optically thick boundary layer. From Frank et al. (2002).

For a young star with $M_\star = 0.5\ M_\odot$ and $R_\star = 2\ R_\odot$, accreting at $\dot{M} = 10^{-8}\ M_\odot\ {\rm yr}^{-1}$, the temperature at the inner edge of the disk is ~ 2850 K (Eq. 1.14). From the disk aspect ratio $H/R = c_s/(\Omega_K R)$ (Frank et al., 2002) with $c_s = (k_{\rm B}T/m_{\rm p})^{1/2}$, the disk thickness at $\sim R_\star$ is $H \approx 0.02\ R_\star$. The temperature of the boundary layer is $T_{\rm BL} \sim 5000$ K. According to Wien's displacement law, radiation from such a boundary layer peaks at ~ 6000 Å and has a tail in the ultraviolet. For this reason Lynden-Bell and Pringle (1974) suggested that the hot optical and ultraviolet excess emission observed in CTTSs is emitted in the disk boundary layer. The first models used to reproduce the accretion spectrum of CTTSs were the so-called slab models, in which the UV excess is fitted with a slab of emitting hydrogen. For instance, Valenti et al. (1993) reproduced the observed UV-excess in the spectra of various accreting young stars with this model, finding typical $\dot{M}$ values of $10^{-8}\ M_\odot\ {\rm yr}^{-1}$.

In the boundary layer the shear, which is proportional to $\partial\Omega/\partial r$, changes sign. This is clear from Fig. 1.6: between $R_\star$ and $R_{\rm in}$ we have $\partial\Omega/\partial r < 0$. This means that angular

momentum is transported inward, i.e., the boundary layer exerts a torque on the star and spins it up, so that after few Myrs the star should rotate at its break-up velocity (Hartmann and Stauffer, 1989). However, CTTSs and WTTSs rotate at velocities an order of magnitude lower, with typical projected rotational velocities of $\sim 10-30$ km s^{-1} (e.g., Bertout 1989). This poses a problem to the boundary layer interpretation.

2.2 Magnetospheric accretion

As explained in Sect. 2.1, the slow rotation of CTTSs is not compatible with the boundary layer model. There must be some mechanism that prevents the star from reaching the break-up velocity. Another argument against the boundary layer hypothesis is the evidence for non-axisymmetric accretion. For instance, Bertout et al. (1988) observed a periodic light variation in the CTTS DF Tau (Fig. 2.2), compatible with the rotational modulation of a spot on the stellar surface. The variations of the light curve amplitude with wavelength observed in DF Tau could only be reproduced assuming that the spot was brighter than the photosphere.

In analogy with the magnetically controlled accretion model proposed by Ghosh and Lamb (1978) for neutron stars, it was suggested that if the magnetic field is large enough, the inner parts of the accretion disk can be disrupted, causing accretion to occur along magnetic field lines. This way, the accretion energy would be released in a shock near the stellar photosphere and a hot spot would be formed. If the magnetic field axis and the stellar rotation axis are not aligned, the rotation of the spot would induce periodic variations in the overall luminosity, similar to those shown in Fig. 2.2.

Indirect evidence for the existence of strong magnetic fields in CTTSs was the powerful X-ray emission (e.g., Feigelson et al. 2007) as well as the presence of starspots (e.g., Herbst et al. 1994). Using the technique of Zeeman broadening of photospheric lines, magnetic fields of the order of $1-3$ kG were measured for CTTSs (Guenther et al., 1999; Johns-Krull et al., 1999, 2001).

These discoveries confirmed the applicability of the theory of magnetospheric accretion for CTTSs, sketched in Fig. 2.3. Such strong magnetic fields are indeed able to disrupt the disk at a distance of a few stellar radii from the star. The idea is that for a sufficiently strong magnetic field, the magnetic pressure ($P_{\rm B} = B^2/8\pi$) can exceed the ram pressure of the accreting material in the disk ($P_{\rm D} = \rho v^2/2$). The point at which $P_{\rm D} = P_{\rm B}$ is usually referred to as the truncation (or magnetospheric) radius, $R_{\rm T}$. A simple scaling relation for $R_{\rm T}$ can be obtained assuming spherical accretion. In this case, the velocity is close to the free

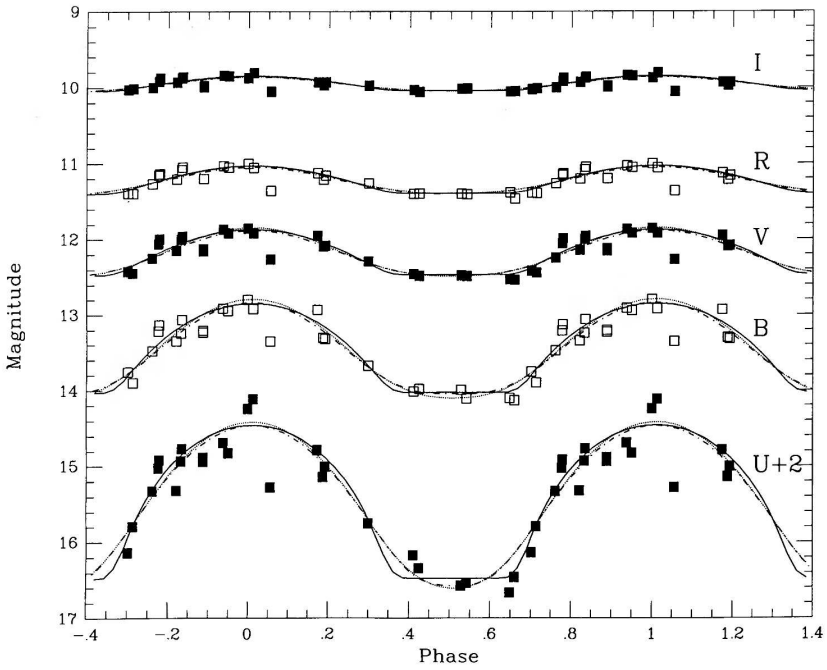

Figure 2.2: Phase-folded light curve of DF Tau with models of variability from a rotating hot spot superposed to it. From Bertout et al. (1988).

fall value $v = (2GM_\star/r)^{1/2}$, and the continuity equation gives $\rho v = \dot{M}/(4\pi r^2)$. Then, the ram pressure in the disk is

$$P_{\rm D} = \frac{1}{2}\rho v^2 = \frac{1}{2}\frac{\dot{M}}{4\pi r^2}\left(\frac{2GM_\star}{r}\right)^{1/2} = \frac{\dot{M}\,(2GM_\star)^{1/2}}{8\pi r^{5/2}}. \tag{2.2}$$

Assuming a dipolar magnetic field for the star, $B(r) = B_\star(R_\star/r)^3$, the magnetic pressure is

$$P_{\rm B} = \frac{B_\star^6 R_\star^6}{8\pi r^6}. \tag{2.3}$$

Equating $P_{\rm D} = P_{\rm B}$ yields the truncation radius as a function of $B_\star$ and $\dot{M}$. The result is

$$\frac{R_{\rm T}}{R_\star} = \left(\frac{B_\star^2}{\dot{M}}\right)^{2/7}\left(\frac{R_\star^5}{2GM_\star}\right)^{1/7} \tag{2.4}$$

(Bouvier et al., 2007). For $M_\star = 0.5\ M_\odot$, $R_\star = 2\ R_\odot$, and $\dot{M} = 10^{-8}\ M_\odot\ {\rm yr}^{-1}$, a stellar magnetic field $B_\star$ of 1 kG is able to disrupt the disk at a distance of 7.1 $R_\star$.

In the case of disk accretion, the condition of the disruption of the disk at $R_{\rm T}$ is that the torque exerted by the magnetic field on the disk is equal to the viscous torque. The main difficulty in this calculation is in trying to find an expression for the magnetic torque at $R_{\rm T}$, because this involves the azimuthal component of the magnetic field, B_ϕ, which in turn depends on how much the magnetic field lines are distorted from a dipole-like configuration

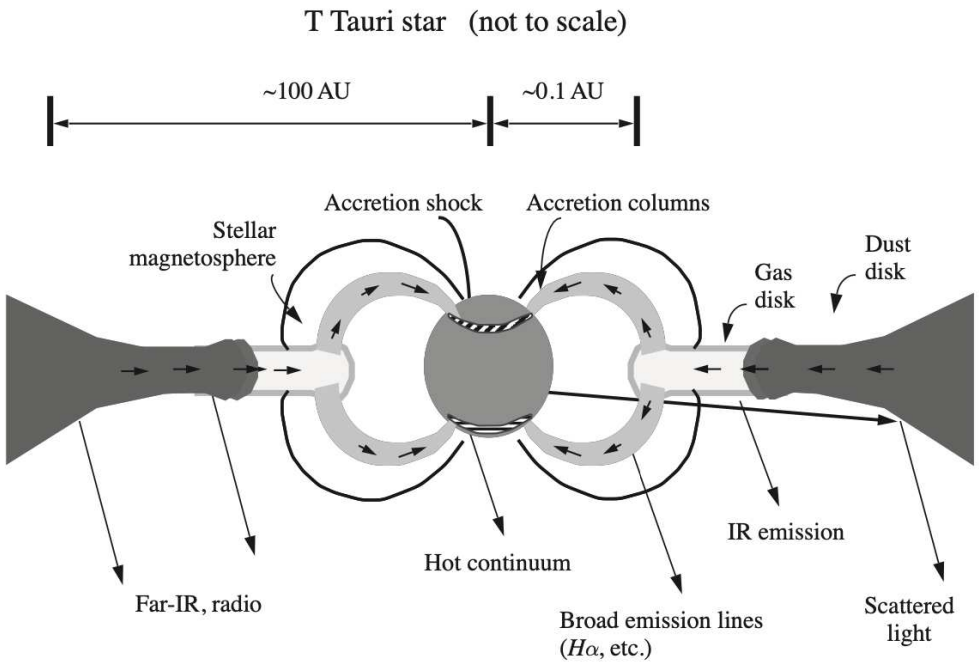

Figure 2.3: Schematic view of a young star accreting from a disk through the stellar magnetosphere. From Hartmann (2008).

by the interaction with the disk (Frank et al., 2002). Therefore, Eq. (2.4) must be regarded as a rough estimate of the value of R_T.

The stellar magnetic field allows the star and the disk to interact and exchange angular momentum. Clearly, the disk material must lose angular momentum to accrete onto the star. As the field lines rotate with the stellar angular velocity $\Omega_\star$, this means that the magnetospheric radius must satisfy the condition

$$\Omega_K(R_\mathrm{T}) > \Omega_\star. \tag{2.5}$$

Alternatively, we can define the disk radius at which the Keplerian angular velocity is equal to $\Omega_\star$, the so-called corotation radius,

$$R_\mathrm{co} = \left(\frac{GM_\star}{\Omega_\star^2}\right)^{1/3} = (GM_\star)^{1/3}\left(\frac{P_\star}{2\pi}\right)^{2/3}. \tag{2.6}$$

Combining these two conditions, the criterion for accretion becomes $R_\mathrm{T} < R_\mathrm{co}$. Just like the boundary layer accretion, this process transfers angular momentum to the star. Therefore, it was surprising to find that CTTSs rotate more slowly than WTTSs (Bouvier et al., 1993, 1995, 1997), which have already dispersed their disk (Sect. 1.1) and are thus not accreting. Together with the fact that young stars do not rotate at break-up velocities, it appears that

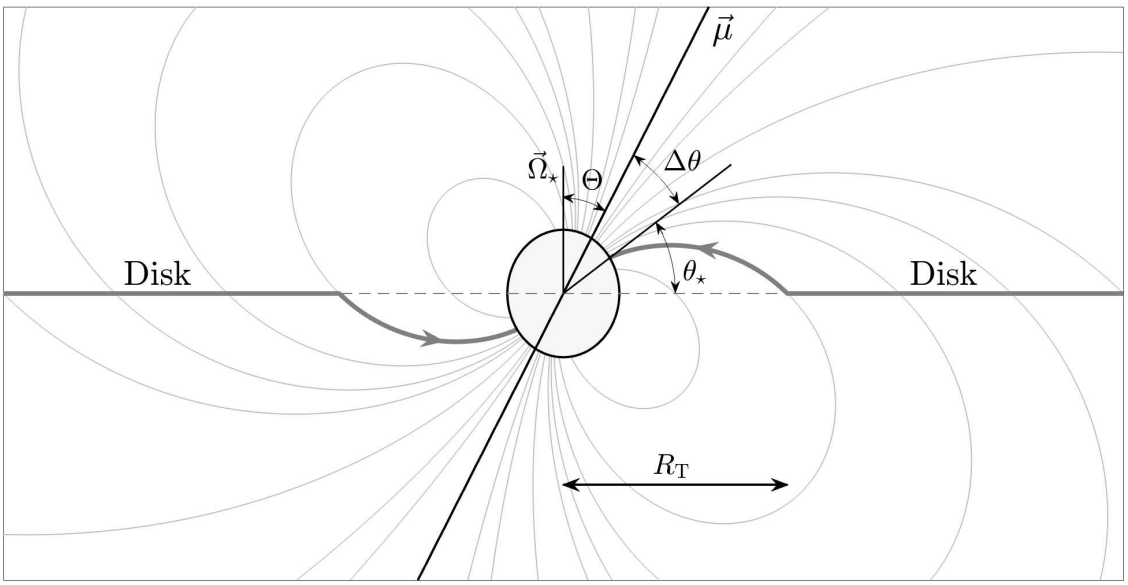

Figure 2.4: Accretion from a disk through a dipolar magnetic field. Adapted from Frank et al. (2002).

CTTSs actually spin down while accreting material. This suggested that some stellar magnetic field lines couple to the disk outside of R_co to prevent stellar spin-up, the so-called disk-locking scenario (Königl, 1991).

Magnetically controlled accretion leads to an immediately recognizable observational signature, that is, the presence of a "hot spot". This happens because the accretion flow is channelled onto a small fraction of the stellar surface. Consider the situation depicted in Fig. 2.4, where a dipolar magnetic field disrupts the disk at a distance R_T. In general, the magnetic field axis, $\vec{\mu}$, can be misaligned with respect to the stellar rotation axis, $\vec{\Omega}_\star$. The angle between the two axes is called the magnetic obliquity Θ. We define a system of spherical coordinates (r,θ,ϕ), where θ is the angle measured relative to the plane perpendicular to $\vec{\Omega}_\star$ (the latitude) and ϕ is the azimuth in the plane. In this system, the magnetic field lines have the form $r = C\sin^2(\theta+\Theta)$. The magnetic field line that crosses the disk plane at $r = R_\mathrm{T}$ has $\theta = \pi/2$, therefore it is defined by $C = R_\mathrm{T}/\sin^2(\pi/2+\Theta) = R_\mathrm{T}/\cos^2\Theta$. This means that it intercepts the stellar surface ($r = R_\star$) at a latitude $\theta_\star$ given by the equation

$$R_\star = \frac{R_\mathrm{T}}{\cos^2\Theta}\sin^2(\theta_\star+\Theta), \tag{2.7}$$

that is,

$$\theta_\star = \sin^{-1}\left[\sqrt{\frac{R_\star}{R_\mathrm{T}}}\cos\Theta\right] - \Theta. \tag{2.8}$$

Since the disk is disrupted at R_T, the matter in the upper hemisphere is channeled onto the star at latitudes between $\theta_\star$ and $\pi/2-\Theta$, that is, the hot spot has a latitudinal extension

$$\Delta\theta = \left(\frac{\pi}{2}-\Theta\right)-\theta_\star = \frac{\pi}{2}-\sin^{-1}\left[\sqrt{\frac{R_\star}{R_\mathrm{T}}}\cos\Theta\right]. \tag{2.9}$$

Approximating the spot as a spherical cap[1] with half-aperture $\Delta\theta/2$, its area is

$$S_\mathrm{spot} = 2\pi R_\star^2\left(1-\cos\frac{\Delta\theta}{2}\right). \tag{2.10}$$

Therefore, the spot occupies a fraction

$$f_\mathrm{S} = \frac{S_\mathrm{spot}}{4\pi R_\star^2} = \frac{1}{2}\left(1-\cos\frac{\Delta\theta}{2}\right) \tag{2.11}$$

of the stellar surface. For instance, if $R_\mathrm{T}=5\ R_\star$ and $\Theta=5^\mathrm{o}$ we get $\Delta\theta\approx 64^\mathrm{o}$ and $f_\mathrm{S}=0.075$.

The energy emitted in the shock at the stellar surface can be estimated with a simple energetic argument, that is, by assuming that the gas is radially at rest at R_T and has the free-fall velocity v_FF at $R_\star$. The conservation of energy yields

$$\frac{1}{2}v_\mathrm{FF}^2-\frac{GM_\star}{R_\star} = -\frac{GM_\star}{R_\mathrm{T}}, \tag{2.12}$$

i.e.,

$$v_\mathrm{FF} = \sqrt{\frac{GM_\star}{R_\star}}\cdot\sqrt{1-\frac{R_\star}{R_\mathrm{T}}}. \tag{2.13}$$

For $M_\star=0.5\ M_\odot$, $R_\star=2\ R_\odot$, and $R_\mathrm{T}=5\ R_\star$, we get $v_\mathrm{FF}=195\ \mathrm{km\ s^{-1}}$. The accretion luminosity, that is, the energy per unit time emitted by the shock, is

$$L_\mathrm{acc} = \frac{1}{2}\dot{M}v_\mathrm{FF}^2 = \frac{GM_\star\dot{M}}{R_\star}\left(1-\frac{R_\star}{R_\mathrm{T}}\right). \tag{2.14}$$

This means that a measure of the accretion luminosity, together with the knowledge of the stellar parameters, provides an estimate of the accretion rate.

Since the sound speed of the flow is typically less than $\sim 10\ \mathrm{km\ s^{-1}}$, the freely falling material is highly supersonic. This justifies the strong shock approximation (e.g., Landau and Lifshitz 1959), in which the temperature of the shocked gas is

$$T_\mathrm{S} = \frac{3}{16}\frac{m_\mathrm{p}}{k_\mathrm{B}}v_\mathrm{FF}^2, \tag{2.15}$$

[1] A spherical cap is portion of a sphere cut by a plane. See `https://en.wikipedia.org/wiki/Spherical_cap` for a definition.

i.e., $9 \cdot 10^5$ K for the parameters above. Therefore, the shock emits soft X-rays that irradiate the surrounding medium (Hartmann et al., 2016).

The accretion column is usually divided into three sub-regions, as shown in Fig. 2.5. These are the pre-shock region, the post-shock region, and the heated photosphere below the shock (Calvet and Gullbring, 1998; Gullbring et al., 2000). Calvet and Gullbring (1998) calculated the emission from this type of shock structure, modelling the shock as a plane-parallel, uniform column that depends on two main parameters: the accretion rate ($\dot{M}_{\rm acc}$), which sets the density and the energy flux of the accreting matter, and the filling factor (f), defined as the ratio between the area covered by the hot spot (A) and the stellar surface, $f = A/4\pi R_\star^2$.

The pre-shock region absorbs 1/2 of the X-rays emitted by the shock and re-processes them to longer wavelengths, mostly contributing as emission in the Balmer continuum, as shown in Fig. 2.6. In the strong shock approximation, the shocked gas decelerates to 1/4 of the pre-shock velocity and gets 4 times denser in the post-shock region. This region does not contribute to the optical continuum, but cools in X-rays (Sacco et al., 2008) and in high energy lines. Most of these lines are in the far-ultraviolet (Ardila et al., 2013) but some of them, such as the He II 4686 and the He I lines, are in the optical spectrum. The photosphere below the shock is altered by the radiation of the shock, and it is heated up to a temperature of $\sim 7000-8000$ K (Hartmann et al., 2016). Therefore, it contributes to the spectrum at shorter wavelengths than the unperturbed stellar photosphere (Fig. 2.6). This model has been employed to fit the excess continuum emission observed in CTTSs (e.g., Fig. 1.2), yielding estimates of accretion rates and filling factors (Calvet and Gullbring, 1998; Calvet et al., 2004; Ingleby et al., 2013).

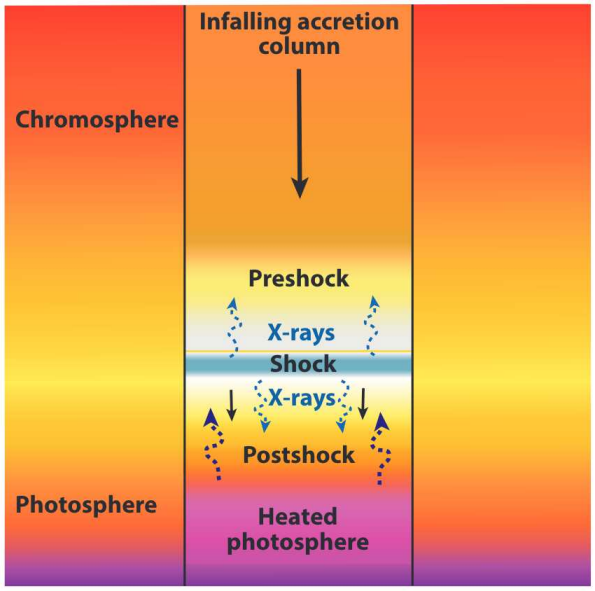

Figure 2.5: Vertical structure of the accretion shock in CTTSs. From Hartmann et al. (2016).

The broad emission lines observed in the spectrum of CTTSs can also be reproduced in the framework of magnetospheric accretion. The Hα profiles of CTTSs have high velocities, up to +400 km s^{-1} (e.g., Fig.1.3), and a complex behaviour. On the one hand, blueshifted

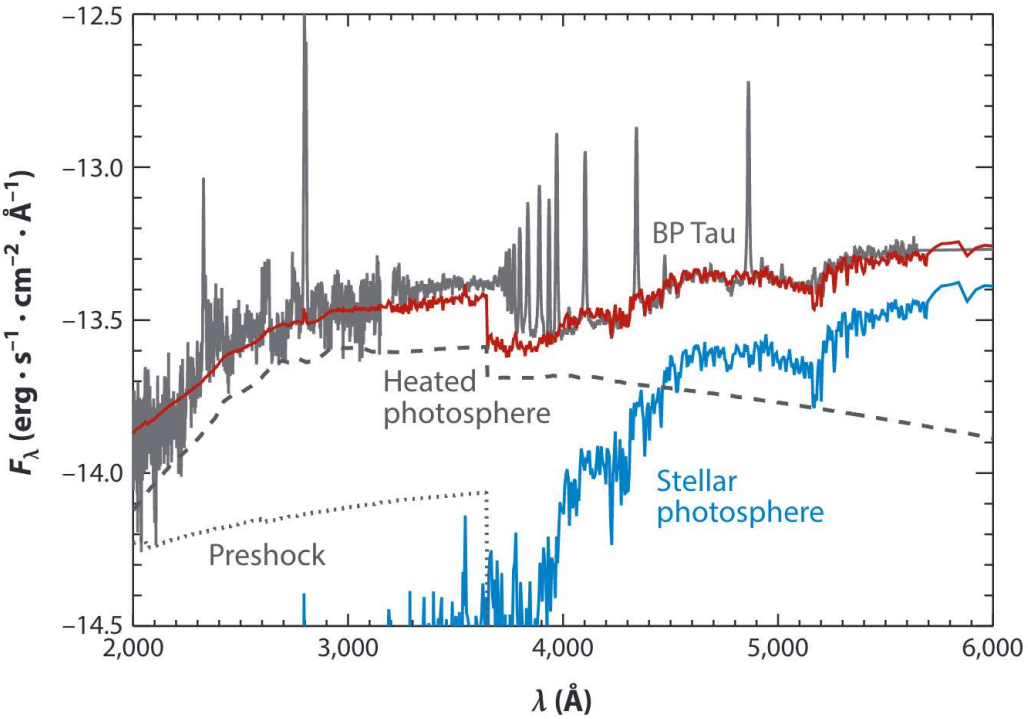

Figure 2.6: The observed spectrum of the CTTS BP Tau (gray line), and a model (red line) composed of the undisturbed stellar photosphere (blue line) and an accretion shock model, made up of the contribution from the pre-shock region (dotted line) and the heated photosphere (dashed line). From Hartmann et al. (2016).

absorption is ofted observed (e.g., UY Aur, DL Tau, and RW Aur in Fig. 1.3), which is evidence for mass loss. On the other hand, the YY Ori stars (e.g., S CrA, Fig. 1.4) show inverse P-Cygni profiles, which imply the presence of infalling material.

Boundary layer models fail to replicate both the extreme velocities and the observed redshifted absorption components. Calvet and Hartmann (1992) explored the possibility that the Balmer emission lines in CTTSs originate from infalling envelopes rather than winds, challenging the original hypothesis (Sect. 1.2). Assuming a simple conical geometry with the velocity law of Eq. (2.13), they were able to reproduce the main features of the Balmer lines. Hartmann et al. (1994) and Muzerolle et al. (1998, 2001) refined this model, studying the radiative transfer of light emitted from material that free falls along the field lines of a dipolar magnetic field. Once the broadening mechanisms, the most important of which is the Stark broadening, were taken into account, the models were able to reproduce the observed velocity widths and the line profiles.

In summary, the presence of strong stellar magnetic fields, the excess continuum that is compatible with a formation in an accretion shock, the existence of hot spots, and the

observed broad line profiles all confirm the general picture of magnetospheric accretion.

2.3 Angular momentum loss through winds

Although the paradigm of the interaction between the stellar magnetosphere and the disk is well established, there are still open issues. The most uncertain aspect of the star-disk interaction in CTTSs is the way angular momentum is transferred. Both the disk and the star must lose angular momentum during the accretion phase.

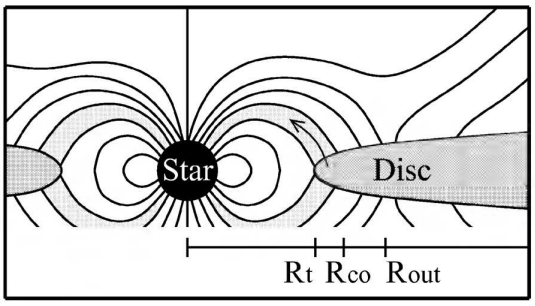

Figure 2.7: Sketch of the disk-locking mechanism, in which the stellar magnetic field connects to the disk from inside (R_T) to outside (R_{out}) of the corotation radius R_{co}. From Matt and Pudritz (2005b).

For a disk to accrete, it must transport angular momentum outward. As discussed in Sect. 1.3, one possible mechanism for this is turbulent viscosity in a disk that is unstable to the magnetorotational instability (MRI). Another mechanism involves magneto-centrifugal winds, which can form over a wide range of disk radii, removing both mass and angular momentum from the disk (Pudritz et al., 2007).

Regarding the star, magnetospheric accretion occurs from within the corotation radius. This process causes the star to spin up. Therefore, to explain the observed slow rotation of CTTSs we must invoke a mechanism of angular momentum loss. In the original scenario depicted by Ghosh and Lamb (1978), this was accomplished by postulating that the magnetic field lines are linked to the disk in a region which extends from inside to outside the corotation radius, the so-called disk-locking mechanism (e.g., Agapitou and Papaloizou 2000; Matt and Pudritz 2005b; Zanni and Ferreira 2009, and Fig. 2.7).

However, Matt and Pudritz (2005b) discussed several problems of the disk-locking scenario. They demonstrated that in this configuration, due to the disk's differential rotation, most of the magnetic field lines should be open rather than connected to the disk. As a result, the spin down mechanism is less effective and stellar rotational velocity is one order of magnitude higher than what was predicted by previous models. This challenges the idea that the disk-locking mechanism is effective in CTTSs.

The presence of open stellar field lines allows the material to leave the system via stellar winds, possibly carrying away angular momentum to counteract the accretion torque. In

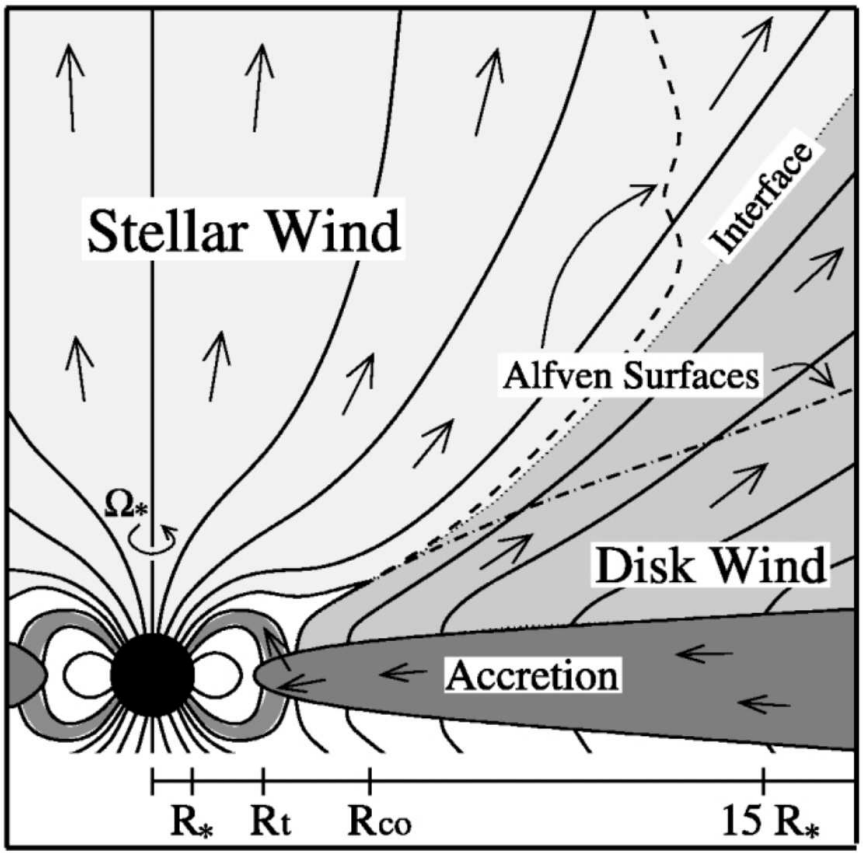

Figure 2.8: Illustration of the magnetic winds originating from a YSO and its disk. From Matt and Pudritz (2005a).

a subsequent paper, Matt and Pudritz (2005a) considered this hypothesis, and found that the wind can lead to enough angular momentum loss to counteract the accretion torque, provided that the mass outflow rate in the stellar winds is ~ 10% of the accretion rate.

Both disk winds and stellar winds are observed to be at play in CTTSs (Edwards et al., 1993; Fang et al., 2018; Banzatti et al., 2019), contributing to mass and angular momentum extraction from the system (Fig. 2.8). Spectrophotometric observations of CTTSs enable to study the star-disk interaction region, allowing us to estimate the amount of angular momentum that is transferred from the disk to the star. Additionally, spectroscopic diagnostics of mass loss help us understand the structure of CTTSs outflows, giving us insights into how young stars slow down their rotation rate.

CHAPTER 3

MAGNETOHYDRODYNAMIC SIMULATIONS: UNSTABLE REGIME OF ACCRETION AND STRUCTURE OF THE OUTFLOW

The interaction between the star and the disk through the stellar magnetic field involves a complex interplay of accretion and outflow processes. To unravel these dynamics, three-dimensional MHD simulations are essential, as they capture the relationships between the stellar magnetic field, accretion, and outflows. Such simulations, governed by highly non-linear, time-dependent equations, provide insights into how the star-disk interaction depends on system parameters such as the stellar rotation period, the structure of the stellar magnetic field, and the accretion rate. They are crucial for predicting observational signatures and, conversely, for understanding how to use observations to infer the behavior of magnetospheric accretion in YSOs.

In this chapter, I will introduce the key findings from MHD simulations of accretion and outflow processes in CTTSs. The results of these simulations are relevant to my PhD research, where I used high-resolution spectrophotometric observations to provide evidence for the magnetic boundary layer regime of accretion, a mechanism predicted by MHD models (Sect. 3.3). Furthermore, by comparing high-resolution spectroscopic data with MHD simulations of outflows from CTTSs, my work constrained the mechanisms driving mass and angular momentum loss in the benchmark CTTS RU Lup.

The disk-magnetosphere interaction has been studied in a number of analytical works (e.g., Ghosh and Lamb 1978, Königl 1991, Koldoba et al. 2002). The general prediction was that the disk should be truncated by the magnetic field of the star, and matter should flow along the magnetic field lines, forming a *funnel* flow. However, to investigate the disk-

magnetosphere interaction and its variability, time-dependent two or three-dimensional simulations are required. Early axisymmetric simulations, such as those by Miller and Stone (1997) and Hirose et al. (1997), were limited by their short time duration, typically spanning only a few Keplerian rotations at the inner disk. This constraint allowed only to study rapid free-fall accretion, as the simulations were unable to capture the more complex and non-stationary processes involved in magnetospheric accretion (Romanova and Owocki, 2015). The development of "quiescent" initial conditions (Romanova et al., 2002) allowed to avoid the fast initial evolution seen in earlier studies, and to investigate accretion through the funnel flows. These axisymmetric simulations helped to understand many elements of the disk-magnetosphere interaction, such as the truncation of the accretion disk by the stellar magnetosphere, the formation of funnel flows, and the angular momentum exchange between the disk and the star.

To model a more realistic situation, the interaction between the disk and the stellar magnetosphere must be considered in three dimensions. The main reasons are the following. First, the stellar magnetic dipole may be tilted with respect to the stellar rotational axis of the star. This breaks the axial symmetry of the problem. Second, the inner disk matter is expected to penetrate through the magnetosphere in non-axisymmetric instabilities, such as the Rayleigh-Taylor (RT) (Rayleigh, 1882; Taylor, 1950) and Kelvin-Helmholtz (Helmholtz, 1868; Kelvin, 1871) instabilities, as it was already suggested by Arons and Lea (1976).

3.1 Onset of the unstable regime

As already discussed in Sect. 2.2, magnetospheric accretion can take place only when the disk extends inward of the corotation radius (Fig. 3.1, left). In this way, the accreting matter interacts with the magnetosphere, loses angular momentum, and accretes onto the star. In the opposite case, where the disk is truncated outside $R_{\rm co}$ (Fig. 3.1, right), the inner disk gains angular momentum at the expense of the star, and matter can be pushed outwards by the rapidly-rotating magnetosphere. This is the so-called "propeller" regime (e.g., Ustyugova et al. 2006).

The scaling relation for $R_{\rm T}$ (Eq. 2.4) has been obtained under the assumption of spherical accretion and a dipolar magnetic field. However, by fitting the results of a series of 3D MHD simulations, Kulkarni and Romanova (2013) showed that

$$\frac{R_{\rm T}}{R_\star} = 1.06 \left(\frac{B_\star^4 R_\star^5}{\dot{M}^2 G M_\star} \right)^{1/10}, \tag{3.1}$$

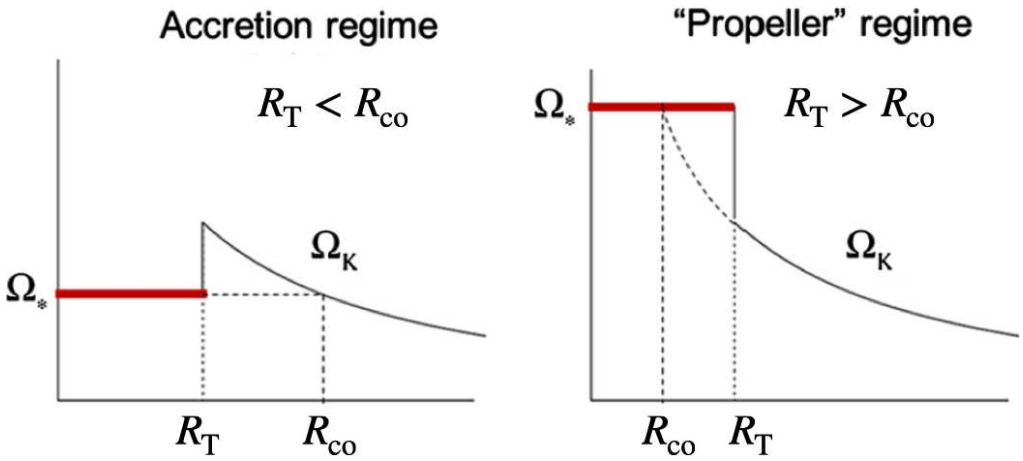

Figure 3.1: Illustration of how the star and the disk interact in a different way according to the position of R_T relative to R_{co}. Left: accretion regime. Right: propeller regime. Adapted from Romanova and Owocki (2015).

where all parameters are in cgs units. The truncation radius, thus, scales as $(B_\star^2/\dot{M})^{1/5}$, and not as $(B_\star^2/\dot{M})^{1/7}$ as in the case of spherical accretion. This is mainly because of the non-dipolar form of the magnetic field, which results from the compression of the magnetosphere by the matter in the accretion disk.

Since the accretion regime is characterized by the ratio between R_T and R_{co}, it is convenient to use the dimensionless parameter ω_s, the so-called fastness parameter. It is defined as the ratio between the rotational angular velocity of the star and the Keplerian velocity at R_T, that is,

$$\omega_s = \frac{\Omega_\star}{\Omega_K(R_T)} = \left(\frac{R_T}{R_{co}}\right)^{3/2}. \tag{3.2}$$

With this parameter, the requirement for accretion becomes $\omega_s < 1$.

As already analytically predicted by Arons and Lea (1976), simulations have shown that the disk-magnetosphere boundary is prone to the RT instability (e.g., Kulkarni and Romanova 2008). In the original derivation, Rayleigh (1882) showed that an instability arises at the interface between a heavier fluid and a lighter fluid when the heavier fluid is "on top" of the lighter one, where "on top" is defined by the direction of gravity. In such a situation, an infinitesimal displacement of the heavier fluid across the interface produces a state in which the potential energy is lower than in the previous configuration. This leads to the formation of an instability in which the heavier fluid continues to penetrate into the lighter one.

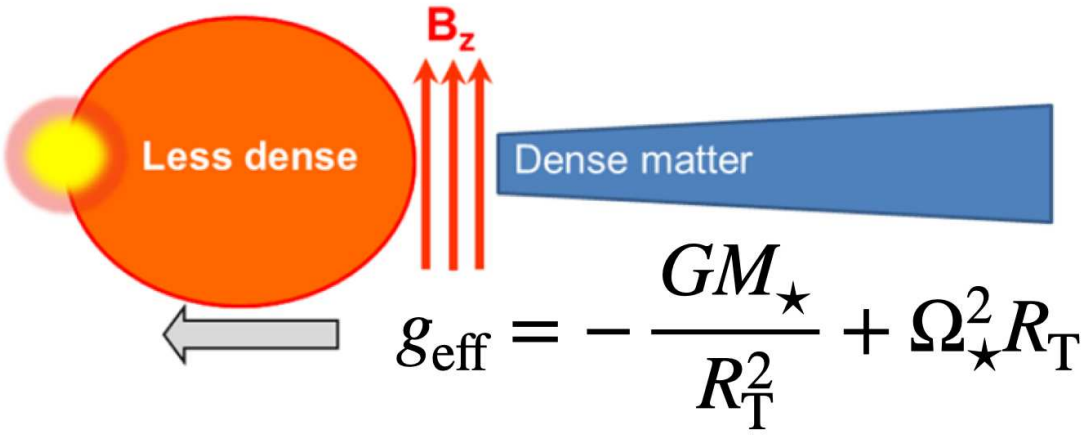

Figure 3.2: Schematics of the development of RT instability in CTTSs. Adapted from Romanova and Owocki (2015).

At the disk-magnetosphere boundary in CTTSs, the situation is similar. The gas in the magnetosphere is less dense than the gas in the disk. If the effective gravity at R_T, i.e., $g_{eff} = -GM_\star/R_T^2 + \Omega_\star^2 R_T$, is negative as in Fig. 3.2, the interface is RT-unstable, meaning that the disk material penetrates into the magnetosphere in several *tongues* of matter. Given that $GM_\star/R_T^2 = \Omega_K^2(R_T)R_T$, then

$$g_{eff} = -\Omega_K^2(R_T)R_T + \Omega_\star^2 R_T = -\Omega_K^2(R_T)R_T(1-\omega_s^2). \tag{3.3}$$

Therefore, in this simple case the disk-magnetosphere boundary is RT-unstable if $\omega_s < 1$. However, there are some factors that can suppress the instability, such as the angular velocity gradient, viscosity in the disk, or the azimuthal component of the magnetic field (Blinova et al. 2016 and references therein), so that in numerical simulations the instability arises at lower values of ω_s. Since ω_s is proportional to R_T/R_{co}, this means that unstable accretion is more likely to occur for systems with either a weak magnetic field or a high accretion rate (where R_T is smaller, Eq. 3.1).

Figure 3.3 shows the result of 3D MHD simulations by Blinova et al. (2016) in the $R_{co} - R_T$ plane. A clear boundary between stable and unstable accretion can be seen at $R_T/R_{co} = 0.71$, or $\omega_s = 0.6$. The existence of a third regime of accretion, the so-called magnetic boundary layer (MBL) regime, was found in MHD simulations of accretion through small magnetospheres (Romanova and Kulkarni, 2009). In this type of unstable regime, the chaotic tongues merge into one or two tongues and unstable accretion becomes ordered. In contrast with the standard unstable regime, in which accretion is "chaotic", Blinova et al. (2016) called this regime "unstable ordered". Figure 3.3 shows that the transition to the MBL (or

unstable ordered) regime occurs for $R_T/R_{co} = 0.59$, or $\omega_s = 0.45$. The phenomenology of these two different regimes of unstable accretion are discussed in Sects. 3.2 and 3.3.

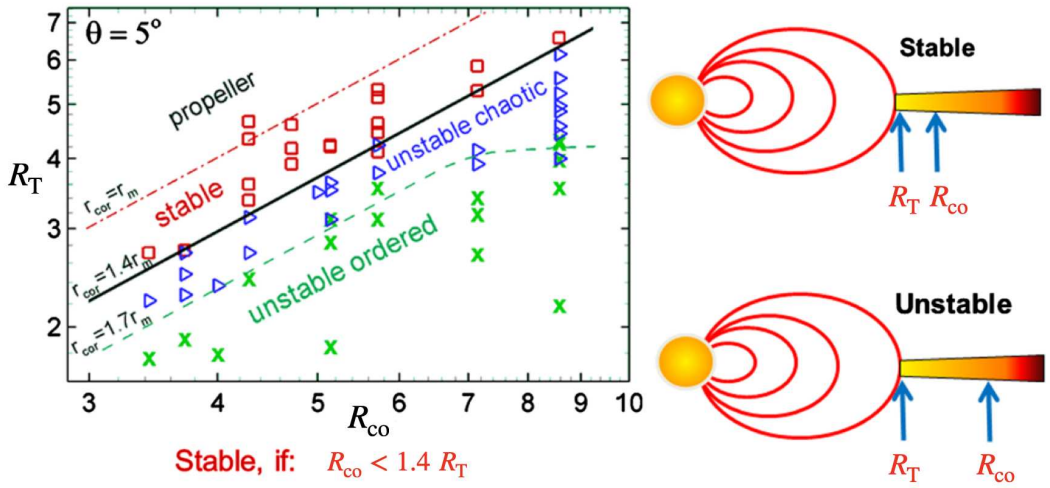

Figure 3.3: Boundary between stable and unstable accretion regimes in the $R_{co} - R_T$ plane. Stable, unstable chaotic, and MBL (or unstable ordered) accretion cases are represented by red squares, blue triangles, and green crosses, respectively. Adapted from Romanova and Owocki (2015).

3.2 Unstable hot spots and quasi-periodic oscillations

The RT instability is expected to develop at the boundary between the disk and the magnetosphere because the dense disk matter is pulled downward by gravity while resting on the low-density gas in the magnetosphere (Fig. 3.2). Although analytical analysis is useful to understand the basic features of the instabilities, it is limited to the linear regime. To study the actual evolution of the instability one must solve the MHD equations in the non-linear regime, and to do this numerical simulations are needed.

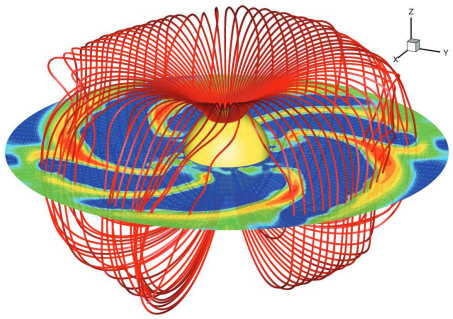

Figure 3.4: MHD simulation showing the penetration of the accretion tongues through the magnetosphere. The colors show the density of the gas flow, with the lowest (highest) density in blue (red). From Romanova et al. (2008).

Such simulations have shown that when conditions are met for the development of the RT instability, the disk gas penetrates the magnetosphere in the equatorial plane in tongues of material (Kulkarni and Romanova,

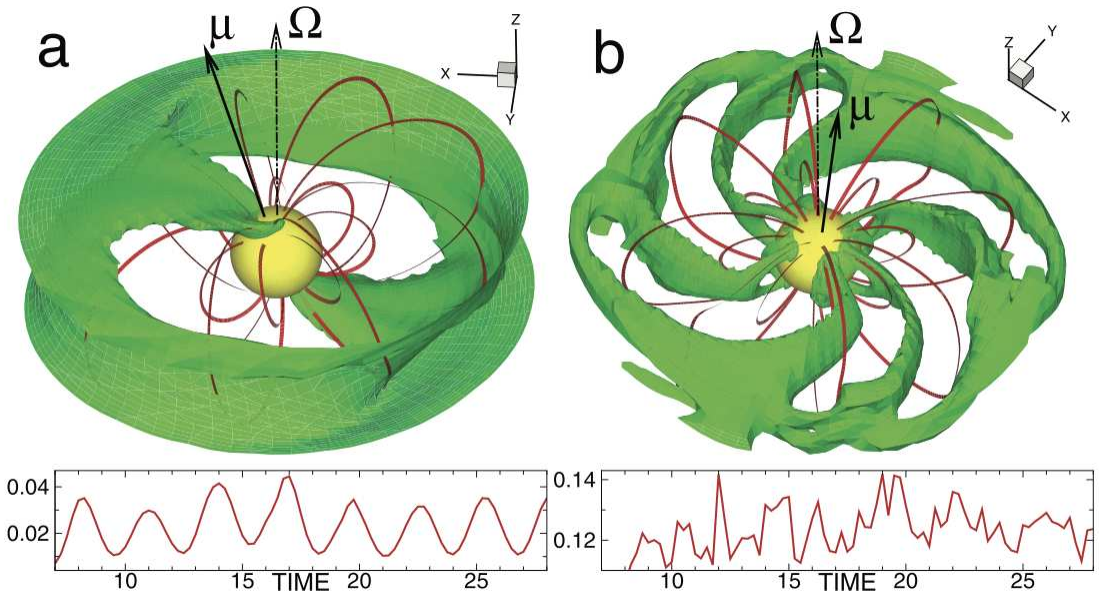

Figure 3.5: Light curves produced from the hot spots during (a) stable and (b) unstable accretion according to MHD simulations. From Romanova et al. (2008).

2008; Romanova et al., 2008), as shown in Fig. 3.4. When the tongues get closer to the star, the stronger magnetic field stops their equatorial motion and the tongues turn into short funnel flows. The resulting hot spots on the stellar surface are much closer to the stellar equator than in the case of stable accretion (Kulkarni and Romanova, 2008).

Figure 3.5 compares the light curves obtained from simulations of stable and unstable of accretion. Due to the stability of the spot structure, the light curves of CTTSs accreting in the stable regime are periodic with the stellar rotation period $P_\star$. In the unstable regime, each tongue creates its own hot spot when it reaches the stellar surface. Therefore the shape, intensity, number, and position of the spots change on the inner disk dynamical timescale. As a result, the light curve is usually chaotic and shows no definite periodicity.

However, Kulkarni and Romanova (2009) discussed how even in the case of unstable accretion it might be possible to observe some quasi-periodic behaviour in the light curves. This is because sometimes a certain number of tongues dominate the accretion flow, and their related hot spots dominate the variability in the light curve. The most interesting result is that the tongues and the hot spots rotate with the Keplerian period at the truncation radius, $P_{\rm K}(R_{\rm T})$. Since in the case of unstable accretion $\omega_{\rm s} = P_{\rm K}(R_{\rm T})/P_\star \leq 0.6$, this means that the unstable hot spots rotate faster than the star itself, that is, they are *non-stationary* on the stellar surface.

Although the unstable hot spots do not last more than 2-3 rotational cycles, Kulkarni and Romanova (2009) suggested that information about unstable accretion can be extracted by studying the Fourier spectrum of the light curves. Figure 3.6 displays the power spectrum of a simulated light curve from a system accreting in the unstable regime, together with its wavelet spectrum. Unlike Fourier analysis, which decomposes a signal into sinusoidal components, wavelet analysis uses functions that are localized in both time and frequency to decompose a signal. Thus, the wavelet spectrum is a way of studying the frequency content of the light curve as a function of time. The power spectrum of Fig. 3.6 has a peak at the stellar rotation period, but also power at shorter periods which are attributed to the rotation of the unstable spots. The wavelet analysis shows indeed that there are epochs in which the rotation of the unstable hot spots dominates the variability of the light curve.

3.3 Magnetic boundary layer regime

Another important regime of unstable accretion was found in MHD simulations of accretion in systems with a small magnetosphere. In analogy with the standard "hydrodynamic" boundary layer, this regime was called magnetic boundary layer (MBL) regime due to the compactness of the magnetosphere. Romanova and Kulkarni (2009) showed that at very high accretion rates, the multiple tongues typical of the unstable regime merge into one or

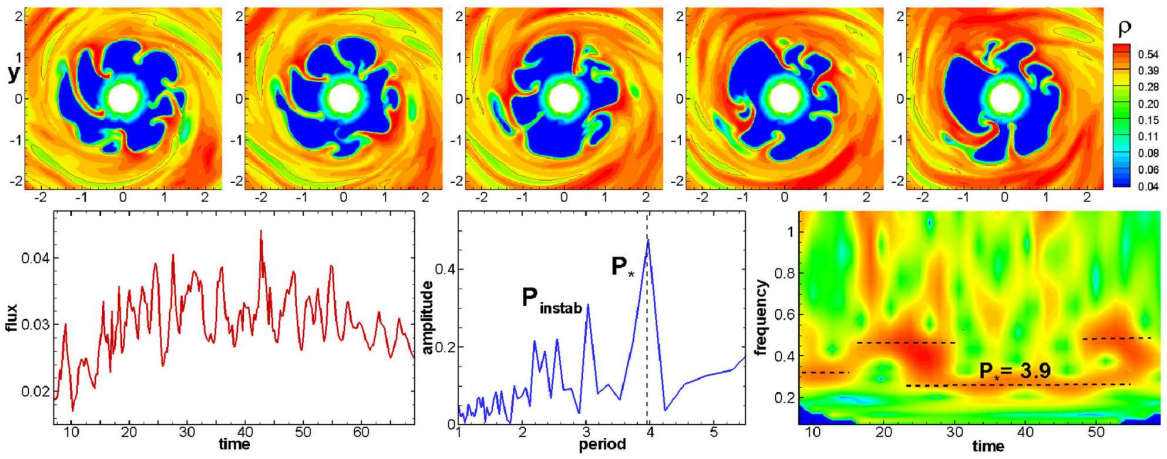

Figure 3.6: Analysis of periodic modulations and their temporal variability in a system accreting in the unstable regime, as predicted by MHD simulations. The top panels show the evolution of the unstable accretion tongues. The bottom panels show the light curve of the system (left), the power spectrum of the light curve (center), and the wavelet spectrum of the light curve (right). Adapted from Blinova et al. (2016).

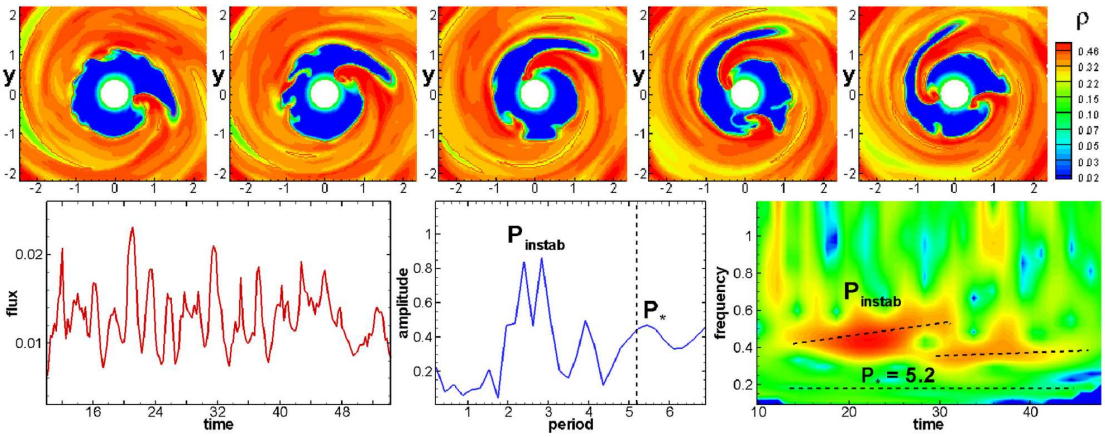

Figure 3.7: Same as Fig. 3.6 but for the MBL regime. Adapted from Blinova et al. (2016).

two ordered tongues which rotate with the Keplerian angular velocity of the disk at R_T. Blinova et al. (2016) investigated the conditions for the development of this regime, which they called unstable "ordered" regime in contrast with the unstable regime discussed above, in which accretion is "chaotic". They showed that it occurs for systems with $R_T \leq 4.2\ R_\star$ when $R_T/R_{co} < 0.57$, or $\omega_s \leq 0.45$. Unlike the chaotic regime, in the MBL regime the period associated with the instability dominates in both the Fourier and wavelet spectra (Fig. 3.7).

In their simulations, Romanova and Kulkarni (2009) observed a clear correlation between the size of the magnetosphere (parameterized by R_T) and the period of the quasi-periodic oscillations (QPOs). When the magnetosphere is smaller, the period decreases. Therefore, the period of the oscillations depends on the accretion rate. When the accretion rate increases, the truncation radius moves closer to the star (cf. Eq. 3.1), and the period of the oscillations decreases (and vice versa). Blinova et al. (2016) showed that when a star is observed for a few stellar rotations, the period of the oscillations associated with the MBL regime can be mistaken for the stellar rotation period.

Accretion in the MBL regime can be important during accretion outbursts, when the inner disk moves inward and compresses the magnetosphere, such that the R_T/R_{co} ratio is small.

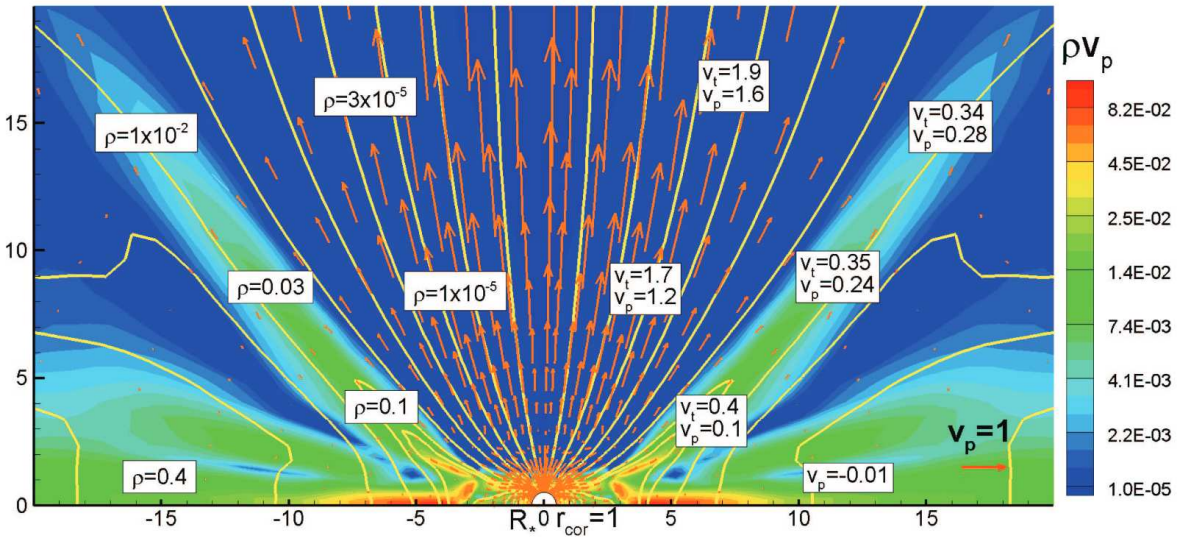

Figure 3.8: Snapshot of an MHD simulation of the outflow from a CTTS showing the conical wind and the jet. The labels mark the density ρ, and the poloidal ($v_{\rm p}$) and toroidal ($v_{\rm t}$) velocity components in dimensionless units. From Romanova et al. (2009).

3.4 Disk winds and jets

Romanova et al. (2009) used axisymmetric 3D MHD simulations to investigate magnetically driven outflows from CTTSs with dipolar magnetic fields interacting with an accretion disks. They showed that the outflow consists of two distinct components, as illustrated in Fig. 3.8. The first component is a fast low-density jet which originates from the stellar surface and is collimated by the magnetic field. The second component is a less collimated wind formed in the inner disk between $R_{\rm co}$ and $R_{\rm T}$. This "conical" wind has the shape of a cone that encloses the jet, and it has lower velocities and higher densities than the jet itself.

The velocity vector in the outflow can be decomposed into two components: the poloidal velocity ($v_{\rm p}$), which is directed along the open magnetic field lines, and the toroidal velocity (v_ϕ), which represents the rotational velocity in the plane perpendicular to the rotation axis of the star-disk system. Simulations by Romanova et al. (2009) showed that at the base of the conical wind, the gas rotates with the Keplerian velocity in the disk and has a negligible poloidal velocity component. Far from the launching region, $v_{\rm p}$ reaches terminal values on the order of ~ 50 km s^{-1} (Fig. 3.9). The jet, instead, has an "onion-like" velocity structure in which the region close to the axis has higher poloidal velocities with respect to the outer regions (Fig. 3.10). Terminal velocities for the jet are on the order of ~ 400 km s^{-1} (Fig. 3.9). The gas densities are on the order of $\sim 10^{10}$ cm^{-3} in the conical wind and ~ 2 orders of magnitude lower in the jet (Fig. 3.9).

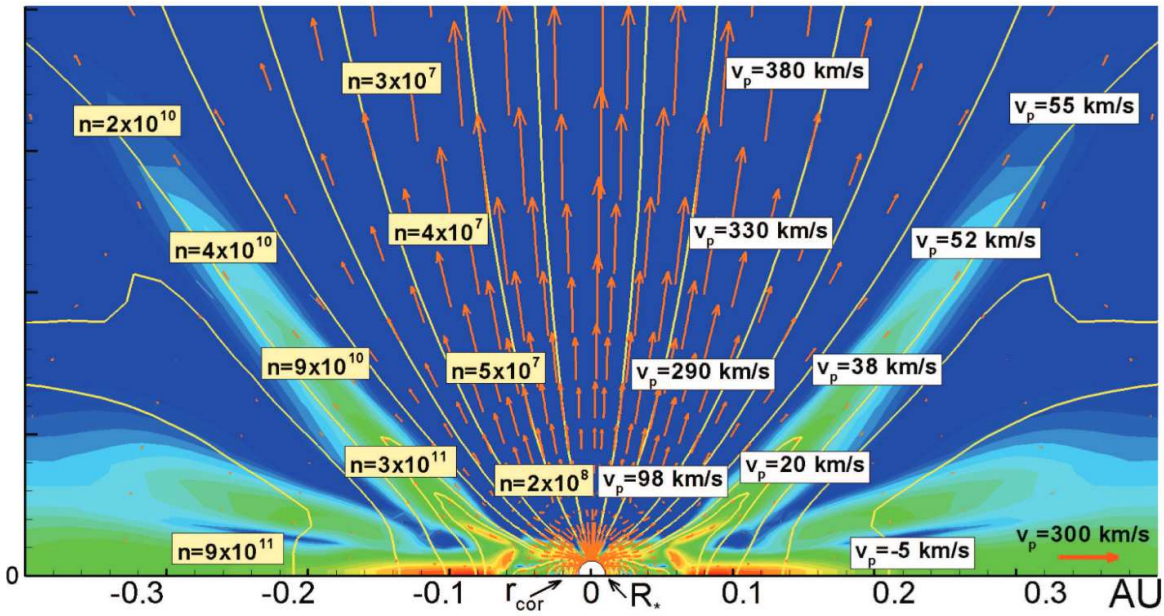

Figure 3.9: Same as Fig. 3.8 but with dimensional values. The particle density, n, is in units of cm^{-3} and the poloidal velocity, $v_{\rm p}$, is in units of km s^{-1}. From Romanova et al. (2009).

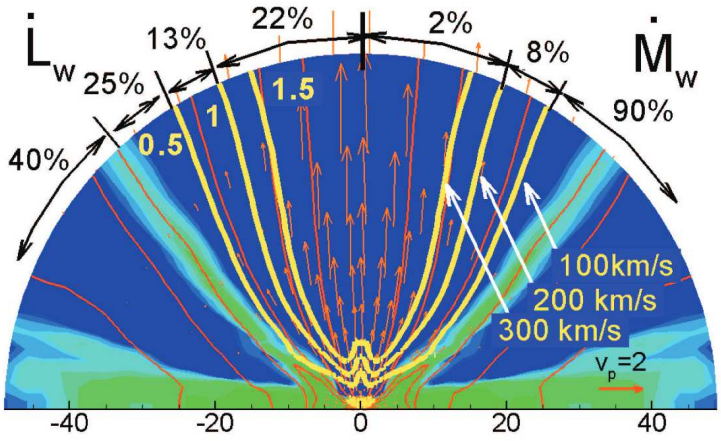

Figure 3.10: Matter and angular momentum distribution in the outflow of a CTTS. The parabolas represent contours of constant poloidal velocity. The numbers on top of the plot show the amount of mass and angular momentum per unit time ($\dot{M}_{\rm w}$ and $\dot{L}_{\rm w}$, respectively) carried by each region of the outflow. From Romanova et al. (2009).

Different regions of the outflow transport different amounts of mass and angular momentum. Figure 3.10 shows that although most ($\sim 90\%$) of the mass is carried by the conical wind, the jet is responsible for removing a large part of the angular momentum ($\sim 60\%$).

CHAPTER 4

RESULTS: SPECTROPHOTOMETRIC OBSERVATIONS OF CLASSICAL T TAURI STARS

Although the paradigm of the interaction between the star and the disk is well established, the detailed physics of this process is still not very well understood. As discussed at the end of Chapter 2, the most important issue that has not been resolved yet is the way young stars lose angular momentum to counteract the natural spin-up caused by accretion. Studying the immediate vicinity of the star is important to constrain the way mass and angular momentum are exchanged between the star and its disk. In this framework, high-resolution spectroscopy enables the analysis of the accretion flow and the winds, constraining the accretion rate, the mass loss rate, and the variability of these structures. Photometry allows the investigation of the stellar hot spots, whose rotational period is linked to the position of the disk truncation radius (see Chap. 3).

In this chapter I will discuss the main results of my PhD, by summarizing the spectrophotometric analysis of two accreting CTTSs, HM Lup and RU Lup, published by Armeni et al. (2023), and Armeni et al. (2024) and Armeni et al. (2025), respectively. In addition, I will discuss some unpublished results on the photometric variability of TW Hya.

4.1 Motivation

The interaction between the star and the disk takes place in the inner ~ 0.1 AU of the accretion disk. The distance to the closest CTTSs to us, TW Hya, is 60 pc (Gaia Collaboration

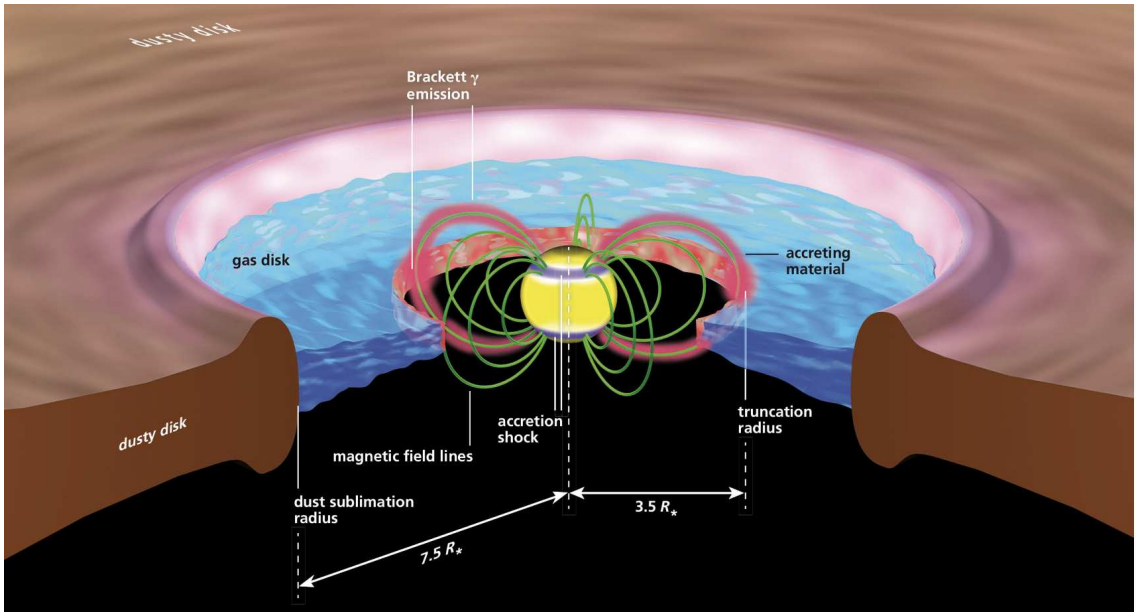

Figure 4.1: Illustration of the inner disk region of TW Hya as derived from interferometric observations with GRAVITY. From Gravity Collaboration et al. (2020).

et al., 2021). This means that the inner disk of TW Hya subtends an angle smaller than $\sim$ 2 mas. The new-generation instrument GRAVITY, an interferometer that uses the four 8-m telescopes of the European Southern Observatory (ESO) *Very Large Telescope* (VLT) (GRAVITY Collaboration et al., 2017), is able to resolve the inner disk of CTTSs in the K band ($2-2.4$ μm). In this spectral region, the size of the magnetosphere can be investigated with the Brγ line of Hydrogen ($\lambda = 21.66$ μm). Brγ emission is a tracer of the accretion process in young stars, since the luminosity of this line correlates with the accretion rate (Alcalá et al., 2014, 2017). The size of the Brγ emitting region in TW Hya has been measured to be $R_{\mathrm{Br}\gamma} = (3.49 \pm 0.20)\ R_\star$ with GRAVITY, indicating that the hydrogen emission originates in the accretion columns (Gravity Collaboration et al., 2020), as shown in Fig. 4.1. Although interferometry has opened up the possibility of resolving the magnetosphere, this technique is limited to the derivation of the size of the emitting region. If we want to study the unsteady interaction between the star and the disk and its variability, we must resort to integrated measures, that is, spectroscopic and photometric observations.

4.2 Targets

By combining spectroscopic and photometric data of a CTTS, we can obtain a complete and time-resolved picture of how mass and angular momentum are exchanged between the star and the disk. In my PhD, I mainly focused on two CTTSs: HM Lup and RU Lup. These two systems were chosen for their rich emission line spectrum and for the amount of simultaneous data provided by different instruments.

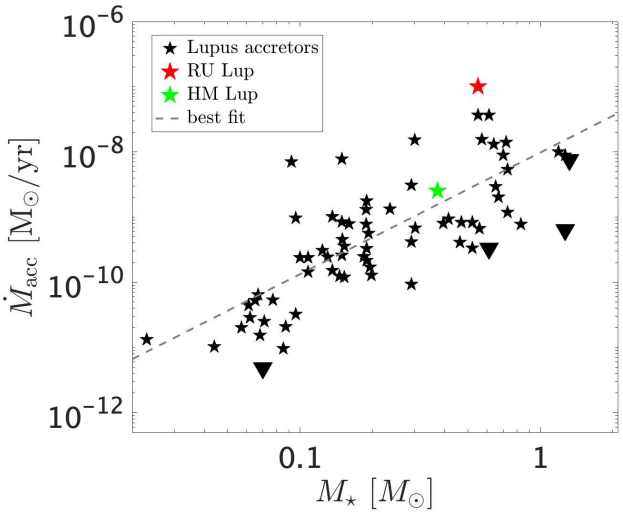

Figure 4.2: $\dot{M}_{\rm acc} - M_\star$ diagram for accreting CTTSs in the Lupus star forming region, marking the position of HM Lup and RU Lup. The values are from Manara et al. (2023). The triangles indicate upper limits on $\dot{M}_{\rm acc}$. The dashed line is a linear best fit to the data.

Figure 4.2 shows the relation between mass accretion rate and stellar mass, the so called $\dot{M}_{\rm acc} - M_\star$ diagram, for the accreting stars in the Lupus star forming region. My targets, HM Lup and RU Lup, have different spectral type (SpT), hence different masses. HM Lup has SpT M2 and $M_\star = 0.37 \pm 0.12\ M_\odot$, while RU Lup has SpT K7 and $M_\star = 0.55 \pm 0.13\ M_\odot$ (Manara et al., 2023). The stellar radii are $R_\star = 1.39 \pm 0.34\ R_\odot$ and $R_\star = 2.27 \pm 0.52\ R_\odot$ for HM Lup and RU Lup, respectively. The two stars accrete at a different rate. According to the values from Manara et al. (2023), $\dot{M}_{\rm acc}$ is almost two orders of magnitude lower for HM Lup ($\dot{M}_{\rm acc} = 2.5 \cdot 10^{-9}\ M_\odot\ {\rm yr}^{-1}$) than for RU Lup ($\dot{M}_{\rm acc} = 10^{-7}\ M_\odot\ {\rm yr}^{-1}$).

The other CTTS that I will discuss is TW Hya. Being the closest CTTSs to us (Sect. 4.1), it is one of the best studied YSOs. The star belongs to a ~ 8 Myr old association (Donaldson et al., 2016) and it has SpT K7 (Herczeg et al., 2023), $M_\star = 0.80 \pm 0.05\ M_\odot$, and $R_\star = 1.16 \pm 0.13\ R_\odot$ (Donati et al., 2024). Consistent with its evolutionary age at the end of the Class II stage (cf. Sect. 1.1), it has a low accretion rate of $\sim 2.5 \cdot 10^{-9}\ M_\odot\ {\rm yr}^{-1}$ (Herczeg et al., 2023).

4.3 Spectroscopy: accretion and ejection

High-resolution spectroscopy provides a powerful tool for studying the dynamic processes of accretion and ejection in CTTSs, allowing for a detailed analysis of the physical condi-

tions and the kinematics of the accreting material and the ejected plasma. This section explains how the most recent spectroscopic observations of HM Lup and RU Lup contribute to our understanding of the star-disk interaction in CTTSs.

4.3.1 Observational database

A large part of the spectroscopic data of HM Lup and RU Lup used in my work were obtained in the framework of the ESO large program PENELLOPE (Manara et al., 2021), a public survey of 250 hours with the VLT (ESO Program ID 106.20Z8) which aims at supplementing the spectroscopic data from the *Hubble Space Telescope* (HST) *UV Legacy Library of Young Stars as Essential Standards* (ULLYSES) program (Roman-Duval et al., 2020; Espaillat et al., 2022) with contemporaneous optical spectroscopy.

In my thesis I used spectra obtained with two of the three spectrographs involved in the PENELLOPE program. The first one is X-Shooter (Vernet et al., 2011), a medium-resolution spectrograph which consists of three spectroscopic arms, that is, the UVB (3000 – 5600 Å, $R \sim 5400$), VIS (5600 – 10200 Å, $R \sim 18400$), and NIR (10200 – 24800 Å, $R \sim 11600$). X-Shooter records spectra from the near ultraviolet to the near infrared. This allows the study of the stellar photospheric spectrum and the excess continuum, as I will discuss in Sect. 4.3.2.1. The second one is the *Echelle SPectrograph for Rocky Exoplanets and Stable Spectroscopic Observations* (ESPRESSO), a fibre-fed échelle high-resolution spectrograph designed for detecting and characterising Earth-like planets in the habitable zone of solar-like stars (Pepe et al., 2021). The ESPRESSO spectra cover the wavelength range between 3800 Å and 7880 Å with a resolution $R \sim 140000$. The very high resolution allows to perform a detailed study of emission lines and their variability. The X-Shooter and ESPRESSO spectra were reduced by the PENELLOPE team, as is described in Manara et al. (2021).

For the study of RU Lup, we supplemented the PENELLOPE data set with spectroscopic data obtained with CHIRON (Tokovinin et al., 2013), a medium-resolution ($R \sim 27800$) spectrograph mounted on a 1.5 m telescope that is part of the *Small and Moderate Aperture Research Telescope System* (SMARTS) at Cerro Tololo Inter-American Observatory. These spectra were reduced and made available to us by Frederick M. Walter.

The spectroscopic database for HM Lup consists of one X-Shooter observation and four ESPRESSO observations, all obtained in 2021. In this thesis, the four ESPRESSO spectra of HM Lup are labeled as "ES j", where j ranges from 1 to 4, corresponding to the sequence of observations. The dataset for RU Lup is significantly more extensive, comprising seven ESPRESSO spectra from the PENELLOPE program and 58 spectra from CHIRON. The ESPRESSO spectra for RU Lup were collected over two years: two in 2021 and five in 2022.

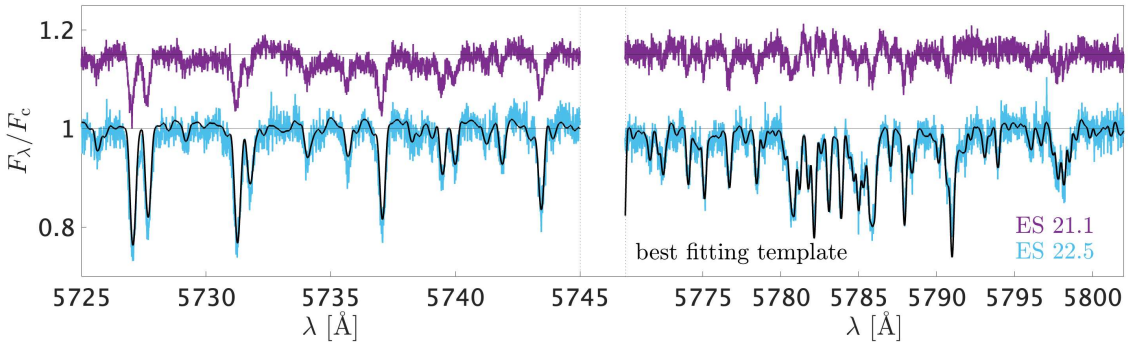

Figure 4.3: Two high-resolution ESPRESSO spectra of RU Lup (violet and light blue) and the best fitting template (black) in two spectral regions where the photospheric absorption lines are seen. The spectra are normalized to the continuum. Adapted from Armeni et al. (2024).

The CHIRON spectra were acquired in three distinct epochs, with 19 spectra obtained in 2021, 27 in 2022, and 12 in 2023. Given the high number of spectra for RU Lup, each spectrum is labeled as "ID yy.j" where ID is either CH (CHIRON) or ES (ESPRESSO), yy represents the last two digits of the year, and j is the j^{th} observation from that spectrograph in that year. The log of the high-resolution spectroscopic observations used in this thesis is reported in Table 4.1.

4.3.2 Basic observational diagnostics

From the spectrum of an accreting young star, we can extract different pieces of information. The continuous spectrum allows us to derive the stellar parameters and the accretion rate by fitting the photospheric spectrum and the accretion-related excess continuum, as discussed in Sect. 2.2. The permitted emission lines superposed to the continuum enable the investigation of the structure of the accretion flow, its temperature stratification, and changes in the accretion rate. Additionally, the analysis of forbidden emission lines and blueshifted absorption components in permitted lines can reveal the structure and variability of the outflow, allowing constraints on the mechanisms responsible for mass and angular momentum loss in CTTSs.

4.3.2.1 Stellar photosphere and excess continuum

Figure 4.3 shows a portion of two ESPRESSO spectra of RU Lup. The spectrum of RU Lup is so rich in emission lines that most of the photospheric absorption lines cannot be observed because they are overwhelmed by line emission. However, there are some regions which

ID	MJD (days)	S/N	V_{mag} (mag)	VF	ID	MJD (days)	S/N	V_{mag} (mag)	VF
HM Lup									
ES 1	71.91	21	14.59	2.2 ± 0.8	ES 3	74.77	18	14.67	0.9 ± 0.4
ES 2	72.85	17	14.43	1.4 ± 0.7	ES 4	81.88	16	14.66	0.6 ± 0.3
RU Lup									
CH 21.1	0.04	65	-	5.4 ± 0.9	CH 22.12	537.64	50	10.79	2.9 ± 0.4
CH 21.2	53.92	66	-	11.7 ± 1.6	ES 22.2	537.73	44	11.14	3.2 ± 0.4
CH 21.3	130.72	58	10.78	-	CH 22.13	538.63	44	11.22	3.5 ± 0.5
CH 21.4	170.66	29	10.73	-	CH 22.14	539.66	45	11.29	2.8 ± 0.6
CH 21.5	171.64	51	10.89	4.1 ± 0.5	ES 22.3	539.76	42	11.29	2.9 ± 0.4
CH 21.6	172.66	70	-	8.7 ± 1.3	CH 22.15	540.72	65	11.07	4 ± 0.5
CH 21.7	173.64	63	-	11.1 ± 1.6	CH 22.16	541.66	44	11.39	2.4 ± 0.4
CH 21.8	174.68	65	10.39	6.5 ± 0.7	CH 22.17	542.66	48	11.74	1.4 ± 0.3
CH 21.9	175.65	52	10.78	5.3 ± 0.6	ES 22.4	542.76	24	11.74	1.8 ± 0.2
CH 21.10	177.7	44	10.68	-	CH 22.18	543.71	42	11.81	1.8 ± 0.4
CH 21.11	178.68	52	10.63	8.3 ± 1.2	CH 22.19	544.73	50	11.59	1.9 ± 0.4
CH 21.12	178.8	62	10.63	-	CH 22.20	545.7	40	11.63	1.9 ± 0.4
CH 21.13	179.68	57	10.56	9.5 ± 1	CH 22.21	546.71	50	11.17	3.9 ± 0.5
CH 21.14	179.69	33	10.56	-	CH 22.22	547.68	64	11.05	6.3 ± 0.7
CH 21.15	182.69	40	10.21	7.1 ± 1	CH 22.23	548.72	64	11.17	3.5 ± 0.5
CH 21.16	183.66	47	10.83	5.2 ± 0.6	CH 22.24	549.67	40	11.53	1.8 ± 0.4
ES 21.1	184.66	57	10.79	5.6 ± 0.9	ES 22.5	549.7	38	11.53	1.6 ± 0.3
CH 21.17	184.7	62	10.79	7.1 ± 0.8	CH 22.25	550.71	71	10.76	6.5 ± 0.7
CH 21.18	185.64	55	10.67	10 ± 1.4	CH 22.26	551.69	61	11.17	3.8 ± 0.5
CH 21.19	188.67	58	10.35	-	CH 22.27	552.7	65	11.19	3.4 ± 0.5
ES 21.2	193.73	43	10.63	7.7 ± 1.1	CH 23.1	804.86	38	-	4.3 ± 0.5
CH 22.1	411.86	59	-	5.1 ± 0.6	CH 23.2	805.88	57	-	3.9 ± 0.5
CH 22.2	418.83	52	-	4.6 ± 0.5	CH 23.3	806.96	56	-	4.6 ± 0.8
CH 22.3	425.92	30	-	3.4 ± 0.4	CH 23.4	812.89	41	11.54	1.8 ± 0.3
CH 22.4	434.86	51	-	4.5 ± 0.5	CH 23.5	813.84	56	-	2.8 ± 0.4
CH 22.5	450.83	64	-	4.7 ± 0.6	CH 23.6	814.93	28	-	-
CH 22.6	458.8	49	-	4.7 ± 0.6	CH 23.7	815.86	48	-	2.4 ± 0.5
CH 22.7	471.77	62	-	6.6 ± 0.7	CH 23.8	820.83	53	-	2.8 ± 0.4
CH 22.8	525.77	56	-	5.5 ± 0.6	CH 23.9	821.94	44	-	2.5 ± 0.4
CH 22.9	534.69	48	11.16	3.6 ± 0.5	CH 23.10	831.8	49	-	2.5 ± 0.6
CH 22.10	535.69	68	11.15	3.5 ± 0.7	CH 23.11	832.82	46	-	2.3 ± 0.6
CH 22.11	536.67	67	10.96	7.4 ± 0.8	CH 23.12	833.82	47	-	2.9 ± 0.4
ES 22.1	536.7	47	10.96	6.7 ± 0.7					

Table 4.1: Log of the spectroscopic observations used in this thesis. The MJDs were computed relative to $MJD_0 \equiv 59264.336$. The S/N was computed at 5830 Å. The typical uncertainty on V_{mag} is 0.01. The VF was computed at 6300 Å for HM Lup (Armeni et al., 2023) and at 5735 Å or 5800 Å for RU Lup (see Armeni et al. 2024 for details on the procedure).

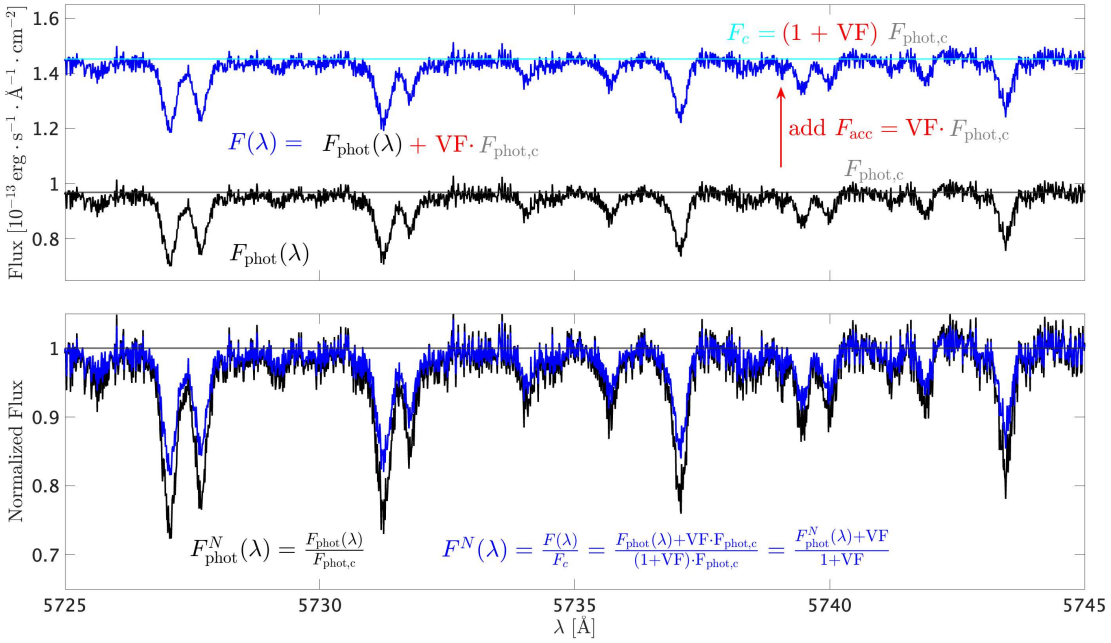

Figure 4.4: Illustration of the veiling phenomenon. In the upper panel, the spectra are plotted in absolute flux. The blue spectrum, $F(\lambda)$, is obtained from the black one, $F_{\mathrm{phot}}(\lambda)$, by adding F_{acc}, parameterized as a fraction VF of the continuum ($F_{\mathrm{phot,c}}$). This results in a spectrum with a higher continuum, $F_{\mathrm{c}} = (1+\mathrm{VF})F_{\mathrm{phot,c}}$. Normalizing the spectra, that is, dividing the spectra by their continuum level, produces the result shown in the lower panel, where $F^N_{\mathrm{phot}}(\lambda)$ and $F^N(\lambda)$ are the normalized spectra, and the absorption lines are weaker by a factor $(1+\mathrm{VF})$ in the blue spectrum than in the black one.

have weak line emission that can be used to extract the properties of the stellar photosphere. The comparison between the two spectra of Fig. 4.3 shows that the absorption lines are weaker in the violet spectrum (ES 21.1) than in the light blue one (ES 22.5). This is due to the excess accretion continuum, an effect called "veiling" (Hartigan et al., 1989). The veiling fraction (VF) is defined as the ratio of the excess flux, $F_{\mathrm{acc}}(\lambda)$, produced in the hot spot (cf. Sect. 2.2) relative to the photospheric flux, $F_{\mathrm{phot}}(\lambda)$; that is, $\mathrm{VF}(\lambda) = \mathrm{F_{acc}}(\lambda)/\mathrm{F_{phot}}(\lambda)$. An illustration of this phenomenon is shown in Fig. 4.4.

The veiling fraction can be used to qualitatively estimate the accretion rate through the strength of the excess continuum. For example, the weaker absorption lines in the ES 21.1 spectrum compared to the ES 22.5 spectrum (Fig. 4.3), corresponding to a higher veiling fraction, indicate that the accretion rate of RU Lup is higher in ES 21.1 than in ES 22.5.

The spectrum of a CTTS can be fitted with dedicated routines to estimate the photospheric parameters and the magnitude of the excess continuum. The spectra of HM Lup

and RU Lup were fitted with ROTFIT (Frasca et al., 2015) by Antonio Frasca. This routine uses a collection of spectra of main-sequence stars, characterized by the effective temperature $T_{\rm eff}$ and the gravity $\log g$, to fit the photospheric spectrum. These spectra are rotationally broadened according to the stellar projected rotational velocity $v \sin i$ and veiled according to VF. The best fit solution is found by minimizing the chi-square as a function of these parameters. As an example, Fig. 4.3 shows the template spectrum that best fits the ES 22.5 spectrum of RU Lup, superposed on the observed spectra. The best-fitting template has $T_{\rm eff} = 4250 \pm 60$ K, $v \sin i = 8.6 \pm 1.4$ km s^{-1}, and VF $= 1.57 \pm 0.31$. The value of $\log g$ is not constrained because the template spectra are from main-sequence stars, that is, the determined $\log g$ value is usually overestimated.

The X-Shooter spectra have the advantage of being absolutely flux-calibrated. In the PENELLOPE survey, the "science exposure" was carried out at medium-resolution (for the resolving power of X-Shooter, see Sect. 4.3.1) with slit widths of 1.0″, 0.4″, 0.4″ in the UVB, VIS and NIR arms, respectively. The flux calibration was performed by correcting for slit losses, that is, by scaling the medium-resolution spectrum to a low-resolution spectrum of the target star obtained in the same night with a 5″ slit (Manara et al., 2021).

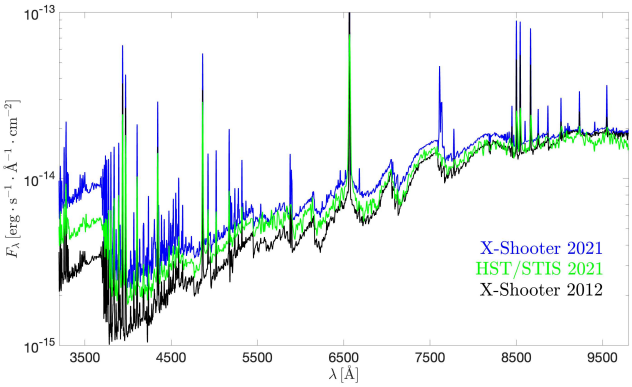

Figure 4.5: Two X-Shooter and one HST/STIS spectra of HM Lup. From Armeni et al. (2023).

The absolutely flux-calibrated spectra can be fitted to simultaneously obtain the stellar parameters and the accretion rate. There are mainly two methods to do this. The first method is the one developed by Calvet and Gullbring (1998), which takes into account the structure of the accretion shock (Fig. 2.5) to reproduce the excess continuum (Fig. 2.6). The second method is the so-called "slab model" fitting. In this case, a multi-component fit is used to reproduce the observed spectrum (Manara et al., 2013). The components are: (1) a set of photospheric templates used to determine the SpT, hence $T_{\rm eff}$; (2) the Cardelli et al. (1989) extinction law, parameterized by the extinction coefficient A_V; (3) a model for the continuum emission from a slab of hydrogen, which represents the accretion shock. The spectrum of the slab can be integrated to find the accretion luminosity, $L_{\rm acc}$, which can be converted to the accretion rate, $\dot{M}_{\rm acc}$, if the stellar mass and radius are known (Eq. 2.14).

As an example, Fig. 4.5 shows three spectra of HM Lup which have been fitted with a

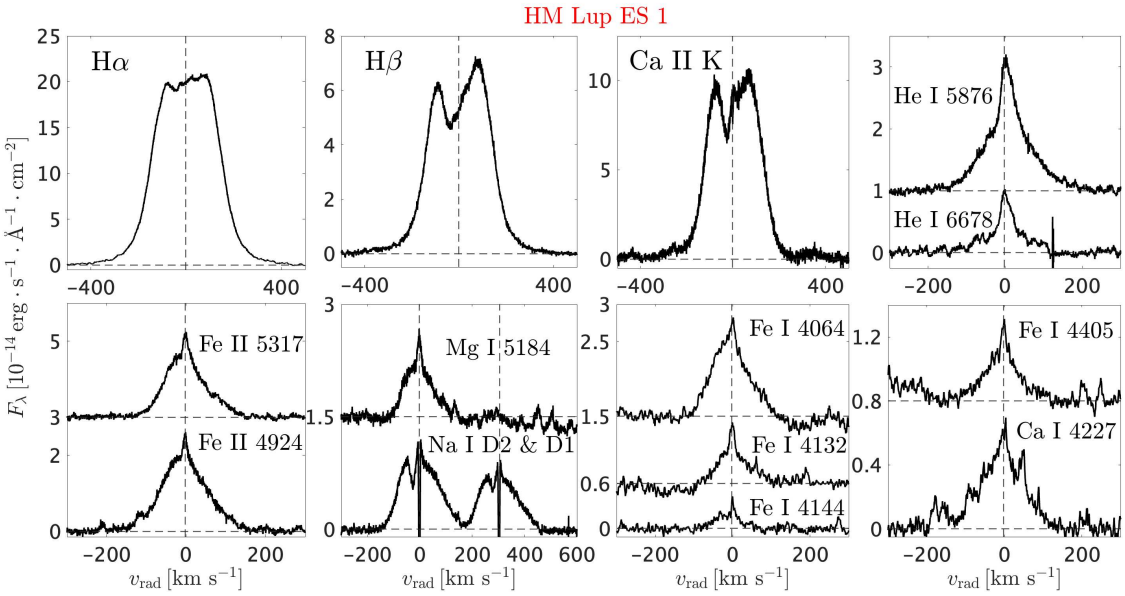

Figure 4.6: Selection of continuum-subtracted emission lines in the first ESPRESSO spectrum of HM Lup. Adapted from Armeni et al. (2023).

slab model by Rik Claes and Carlo Manara. These spectra are: one X-Shooter spectrum from 2021 obtained in the framework of the PENELLOPE program; a spectrum obtained with the *Space Telescope Imaging Spectrograph* (STIS) mounted on HST, taken ∼ 1.5 days after the 2021 X-Shooter spectrum in the framework of the ULLYSES program; an archival X-Shooter spectrum from 2012 (Alcalá et al., 2014). The best fit of the 2021 X-Shooter spectrum yielded a SpT M2, $A_V = 1$ mag, and $\dot{M}_{\rm acc} = 9.5 \cdot 10^{-9}\ M_\odot\ {\rm yr}^{-1}$ (Armeni et al., 2023). Keeping the SpT and A_V values fixed, the procedure was repeated on the HST/STIS spectrum, obtaining $\dot{M}_{\rm acc} = 6.4 \cdot 10^{-9}\ M_\odot\ {\rm yr}^{-1}$. The comparison with $\dot{M}_{\rm acc}$ obtained from the 2012 X-Shooter spectrum, that is, $\dot{M}_{\rm acc} = 2.5 \cdot 10^{-9}\ M_\odot\ {\rm yr}^{-1}$ (Alcalá et al., 2014; Manara et al., 2023) indicates that the system was observed in a state of enhanced accretion in 2021, as is also clear from the stronger Balmer continuum excess in Fig. 4.5.

4.3.2.2 Permitted emission lines

The accretion flow and the shock are hotter than the stellar photosphere. Therefore, spectral lines that originate in these regions are seen in emission above the continuum. The Balmer series of H I, the Ca II H & K lines, and the He I lines are in emission in all CTTSs. However, both HM Lup and RU Lup display an unusually rich emission line spectrum, in which permitted lines from neutral and singly ionized metals can be seen in emission. For example, Fig. 4.6 displays, besides the ubiquitous Balmer, Ca II K and He I lines, emission

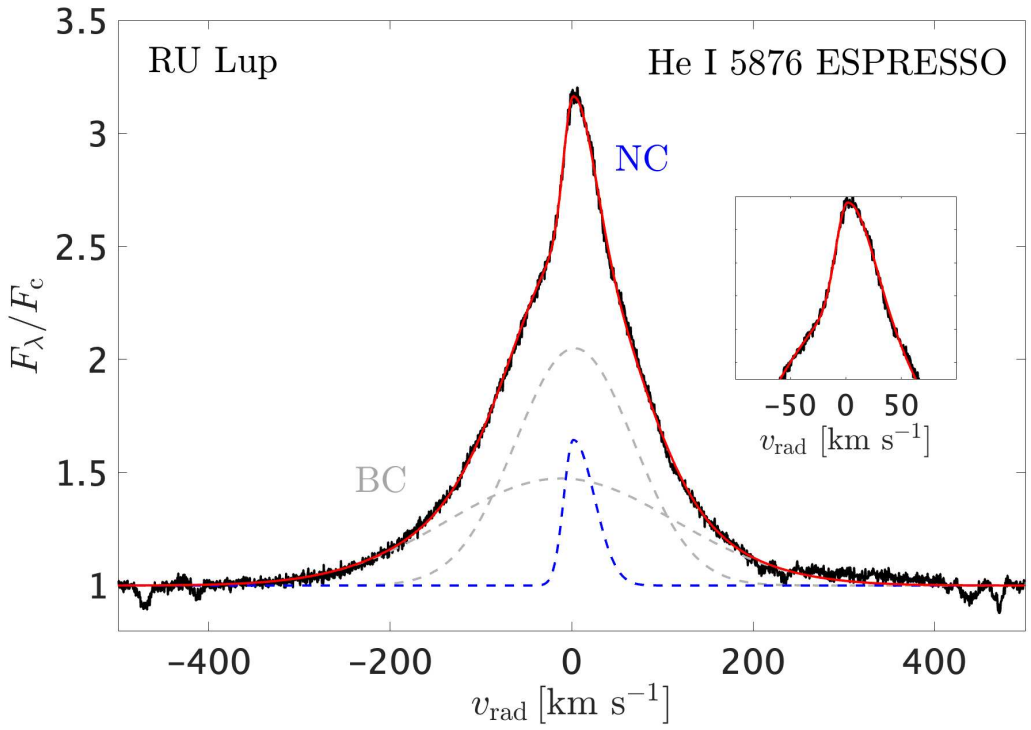

Figure 4.7: He I 5876 line in an ESPRESSO spectrum of RU Lup, showing the decomposition into narrow and broad components (NC and BC), and a best fit with a triple Gaussian (red line). The inset shows a zoom on the NC. Adapted from Armeni et al. (2024).

lines from Na I, Ca I, Mg I, Fe I, and Fe II in the spectrum of HM Lup.

These emission lines originate in different regions of the star-disk system and can be used to infer the structure of the accretion flow and the outflow. Assuming a typical value of the disk truncation radius, $R_{\rm T}$, of 5 $R_\star$ (Calvet and Gullbring, 1998), the free-fall velocity of Eq. (2.13) is $\sim$ 200 km s^{-1} for HM Lup. Figure 4.6 shows that the typical widths of the He I and metallic lines are in agreement with this velocity. Conversely, the wings of the Balmer and Ca II K lines of HM Lup reach $\sim$ 500 km s^{-1}, exceeding the free-fall velocity. This indicates that either the lines have contributions from other regions than the accretion flow, or they are substantially broadened by some other mechanism. Thermal broadening cannot account for the line widths, since the thermal velocity for a hydrogen atom, $v_{\rm th} = (2k_{\rm B}T/m_{\rm H})^{1/2}$, is $\sim$ 10 km s^{-1} at T = 10000 K, and the accretion flow is expected to be cooler than that (e.g., Hartmann et al. 1994). Radiative transfer models of accretion through an axisymmetric magnetosphere have shown that these velocities can be reproduced assuming that the lines are pressure-broadened (Muzerolle et al., 2001; Wilson et al., 2022).

In Armeni et al. (2023) and Armeni et al. (2024) I focused on the emission lines from helium and metals to study the structure of the accretion flow in HM Lup and RU Lup, respectively. Figure 4.7 shows the profile of the He I 5876 line in RU Lup, which also represents the typical emission line profile of the metallic lines. The line profile can be decomposed into two different components, a broad component (BC) which has a typical half-width at zero intensity of ~ 200 km s^{-1}, and a narrow component (NC) which is only ~ 50 km s^{-1} broad. Several works have shown that these two components originate in two different regions of the accretion flow (Beristain et al., 1998, 2001; Petrov et al., 2011; Sicilia-Aguilar et al., 2023). The typical width of the BC, which is compatible with $v_{\rm ff}$, indicates that it is formed in the circumstellar material and along the magnetic field lines (Beristain et al., 1998, 2001). On the other hand, the properties of the NC are compatible with an origin in the post-shock region (see Fig. 2.5), where the gas decelerates and gets denser. The formation of these features close to the stellar surface is supported by the fact that in CTTSs the NCs are rotationally modulated with the stellar rotation period (Sicilia-Aguilar et al., 2015; Campbell-White et al., 2021). This is further demonstrated by my analysis of the He I 5876 line NC in RU Lup, as presented in Armeni et al. (2024) and Sect. 4.3.3.3. Additionally, in my work I investigated the vertical stratification of the hot spot by analyzing NCs from various species.

4.3.2.3 Line strength: accretion rate and its variability

Expanding on previous works (e.g., Muzerolle et al. 1998; Herczeg and Hillenbrand 2008; Rigliaco et al. 2012), Alcalá et al. (2014, 2017) showed that the luminosity of the emission lines in the optical spectrum of CTTSs, $L_{\rm line}$, is correlated with the accretion luminosity, $L_{\rm acc}$. This correlation was determined from the analysis of a sample of X-Shooter spectra of stars in the Lupus star forming region. The accretion luminosity was derived from a slab model fit to the UV excess, while the line luminosity was obtained by integrating the lines in the flux-calibrated spectra and converting the integrated flux to the line luminosity using the distance to the source. An example of this result is shown in Fig. 4.8 for

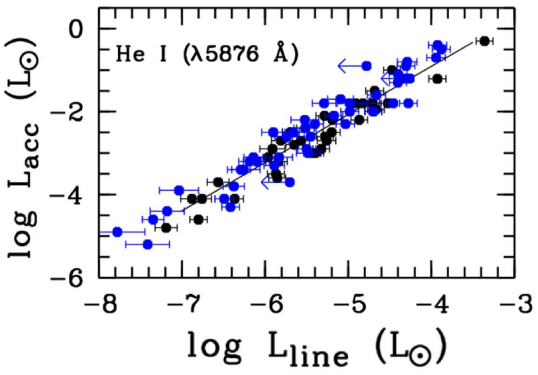

Figure 4.8: Empirical relation between the line luminosity ($L_{\rm line}$) and the accretion luminosity ($L_{\rm acc}$) for the He I 5876 line. From Alcalá et al. (2017).

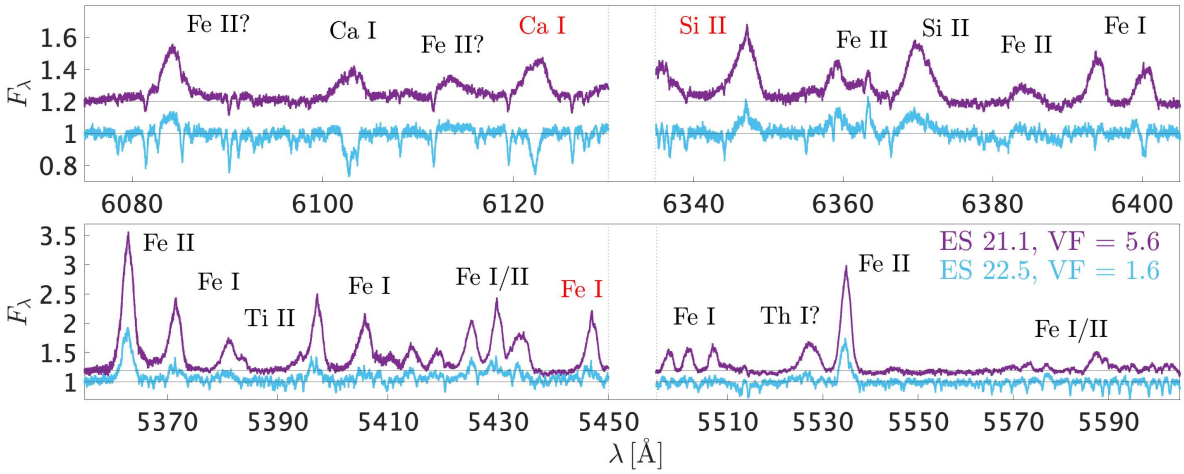

Figure 4.9: Emission lines in four spectral regions for two ESPRESSO spectra of RU Lup. Adapted from Armeni et al. (2024).

the He I 5876 line. The significance of this correlation is that, even in spectra lacking Balmer continuum coverage, such as those from ESPRESSO, we can estimate $\dot{M}_{\rm acc}$ from the line luminosities, provided the spectra are flux-calibrated. If the spectra are not flux-calibrated, we can still compare different spectra in normalized flux units to understand if the accretion rate varies.

One measure related to $\dot{M}_{\rm acc}$ that can be extracted from normalized spectra is the veiling fraction, as already discussed in Sect. 4.3.2.1. The ES 21.1 and ES 22.5 spectra of Fig. 4.3 have VF = 5.6±0.9 and 1.6±0.3, respectively, and Fig. 4.9 shows that the emission line spectrum is very different between these two observations. Some transitions, e.g., the Fe II lines, are always in emission but they get stronger in the ES 21.1 spectrum. Others, such as the Fe I and Ti I lines, are absent in ES 22.5 and appear in emission in ES 21.1. Therefore, the strength of the lines relative to the continuum is a good proxy of the accretion rate, although it does not allow to quantify it.

4.3.2.4 Forbidden emission lines and blueshifted absorption

Forbidden emission lines (FELs) are well-known tracers of outflowing gas in CTTSs (e.g., Edwards et al., 1993; Ray et al., 2007; Banzatti et al., 2019). These lines are formed in low-density environments. This is because they arise from transitions that violate electric dipole selection rules but can occur through higher-order interactions like magnetic dipole or electric quadrupole, albeit with much lower probabilities. In a low-density medium, once an atom is collisionally excited to the upper level of such a transition, it can remain in this

metastable state long enough to decay radiatively via the forbidden transition. The key condition for the formation of these lines is that radiative decay must dominate over collisional de-excitation, which typically occurs when the electron density (n_e) is below a critical density (n_c) specific to the transition in question (Osterbrock and Ferland, 2006).

Among the FELs in the optical spectrum of CTTSs, the [O I] 6300 line is the most prominent. Due to its strength, it has been widely used as a tracer to study the kinematics of outflows in CTTSs (Banzatti et al., 2019). This line is part of a doublet with the [O I] 6364 line, and together they have a critical density of $n_c = 1.8 \cdot 10^6$ cm^{-3}. Other notable FELs in the optical spectrum of CTTSs include the [O I] 5577 line ($n_c = 10^8$ cm^{-3}), two [S II] doublets at 4068-4076 Å ($n_c = 2.6 \cdot 10^6$ cm^{-3} and $1.9 \cdot 10^6$ cm^{-3}, respectively) and 6716-6730 Å ($n_c = 1.7 \cdot 10^6$ cm^{-3} and $1.6 \cdot 10^6$ cm^{-3}, respectively), and the [N II] doublet at 6548-6583 Å ($n_c = 8.5 \times 10^4$ cm^{-3}). These lines are particularly useful when analyzed together, as their distinct critical densities, ionization potentials, and temperature sensitivities allow to disentangle density, temperature, and excitation mechanisms in outflows (e.g., Simon et al. 2016, Fang et al. 2018).

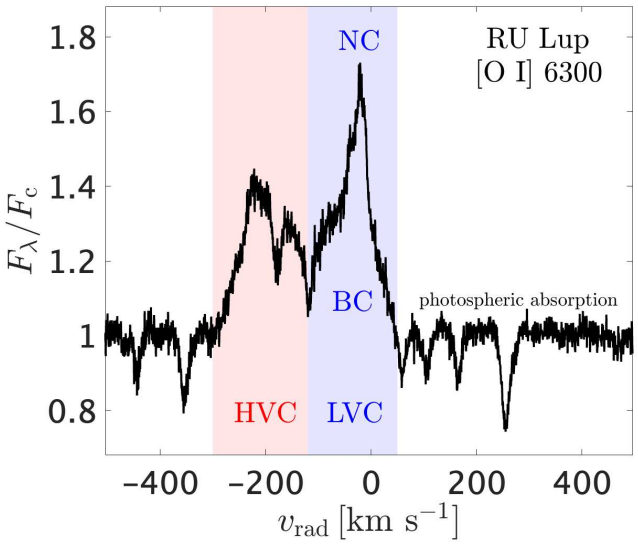

Figure 4.10: [O I] 6300 line in the normalized ES 22.5 spectrum of RU Lup. The shaded regions highlight the HVC and the LVC, with the latter further divided into a BC and a NC. The absorption lines on top of the emission profile are of photospheric origin.

In CTTSs, the FELs typically show two distinct velocity components: a HVC with blueshifted emission that can reach hundreds of km s^{-1}, and a LVC with blueshifted velocities $\lesssim$ 50 km s^{-1} (Hartigan et al., 1995). Figure 4.10 shows the typical line profile of a FEL on the example of the [O I] 6300 line of RU Lup. The HVC originates in a jet that is collimated by magnetic fields (Kwan and Tademaru, 1988) and extends to hundreds AU from the star (Hirth et al., 1997). The collimated jet can originate from either a disk wind or a stellar wind (Ferreira et al., 2006). On the other hand, the LVC originates in a more compact region than the HVC. This feature is in turn distinguished into a broad component (LVC-BC) and a narrow component (LVC-NC) (Rigliaco et al., 2013; Simon et al., 2016; Fang et al., 2018). The

different width of these two components indicates a different origin. The LVC-BC is likely formed in a magnetocentrifugal disk wind that is launched from a radial distance $\lesssim 0.5$ AU (Simon et al., 2016). The LVC-BC originates at larger disk radii, either in a photoevaporative thermal wind (Weber et al., 2020) or in an MHD wind (e.g., Whelan et al. 2021).

Information provided by the FELs can be complemented by another spectroscopic diagnostic to investigate the physics of outflowing gas in CTTSs. This additional diagnostic involves blueshifted absorption components in spectral lines, which indicate gas moving towards the observer. A well-known example of such a diagnostic in CTTSs is the He I line at 10830 Å (Edwards et al., 2003; Erkal et al., 2022). The lower level of this line is metastable, i.e., it has a relatively long lifetime, making the line sensitive to absorption by intervening gas. The typical signature of the outflow in this line is a P Cygni profile, that is, a profile with redshifted emission and blueshifted absorption below the continuum (Fig. 4.11). These absorption components originate in inner wind regions close to the star, augmenting the FEL diagnostics of larger-scale jets.

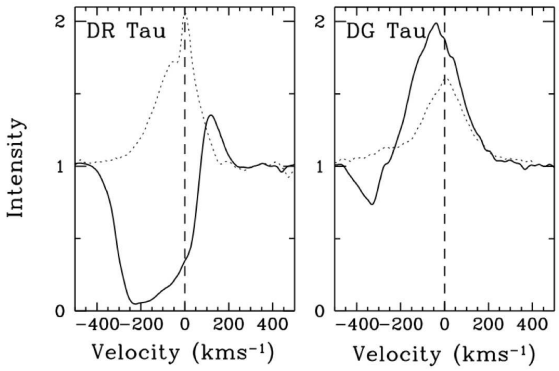

Figure 4.11: P Cygni profiles in the He I 10830 line of the two CTTSs DR Tau and DG Tau. Adapted from Edwards et al. (2003).

Other tracers of absorption in CTTS outflows are resonance lines, that is, transitions that originate from the ground state of an ion (Mundt, 1984; Najita et al., 2000). The strongest resonance lines in the optical spectrum of CTTSs are from the Na I D and the Ca II H & K doublets. High-resolution spectra show that unlike the smooth and broad absorption profile observed in the He I 10830 line, these lines exhibit narrower absorption features in their blue wings, as shown in Fig. 4.12 for the Na I D2 and the Ca II K lines in a series of observations of RU Lup, taken with the *Ultraviolet and Visual Echelle Spectrograph* (UVES, Dekker et al. 2000) at a resolving power of ~ 60000. The narrowness of these discrete absorption components (DACs) compared to the broad absorption observed in the He I 10830 line suggests that they originate in substructures of the outflow close to the launching region, likely in gas "shells" with different temperature and density conditions relative to the rest of the wind (Gahm et al., 2013; Petrov et al., 2014b).

MHD simulations have demonstrated that CTTSs outflows, due to their magnetic nature, have both a poloidal and a toroidal velocity component (Sect. 3.4). In Armeni et al.

(2025), I proposed that the width of the DACs is indicative of the toroidal velocity component in the absorbing region.

To understand this, assume that the DACs are formed in a spatially compact region along the line of sight, as suggested from constraints on the column density (Armeni et al., 2025). In a cylindrical coordinate system (r, ϕ, z), where r represents the distance from the rotation axis in the x-y plane, ϕ is the azimuthal angle measured relative to the x-axis, and z corresponds to the rotation axis (Fig. 4.13), the radial velocity field is the projection of the velocity vector $\vec{v} = v_r\hat{r} + v_\phi\hat{\phi} + v_z\hat{z}$ along the line of sight $\hat{s}$. In cartesian coordinates, the unit vectors have the following expressions: $\hat{r} = (\cos\phi, \sin\phi, 0)$, $\hat{\phi} = (-\sin\phi, \cos\phi, 0)$, $\hat{z} = (0,0,1)$, and $\hat{s} = (\sin i_\star, 0, \cos i_\star)$. The resulting radial velocity is

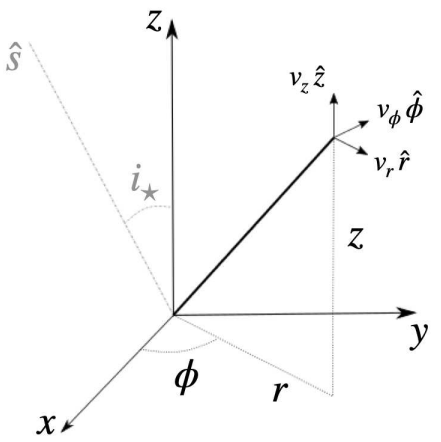

Figure 4.13: Sketch of the cyclindrical coordinate system adopted for the analysis of the DACs. From Armeni et al. (2025).

$$v_{\rm rad} = -v_r \cos\phi \sin i_\star + v_\phi \sin\phi \sin i_\star - v_z \cos i_\star \tag{4.1}$$

(Armeni et al., 2025). Although the region is narrow along the line of sight, it can still have a significant extension in the azimuthal direction. In such a region, under the assumption

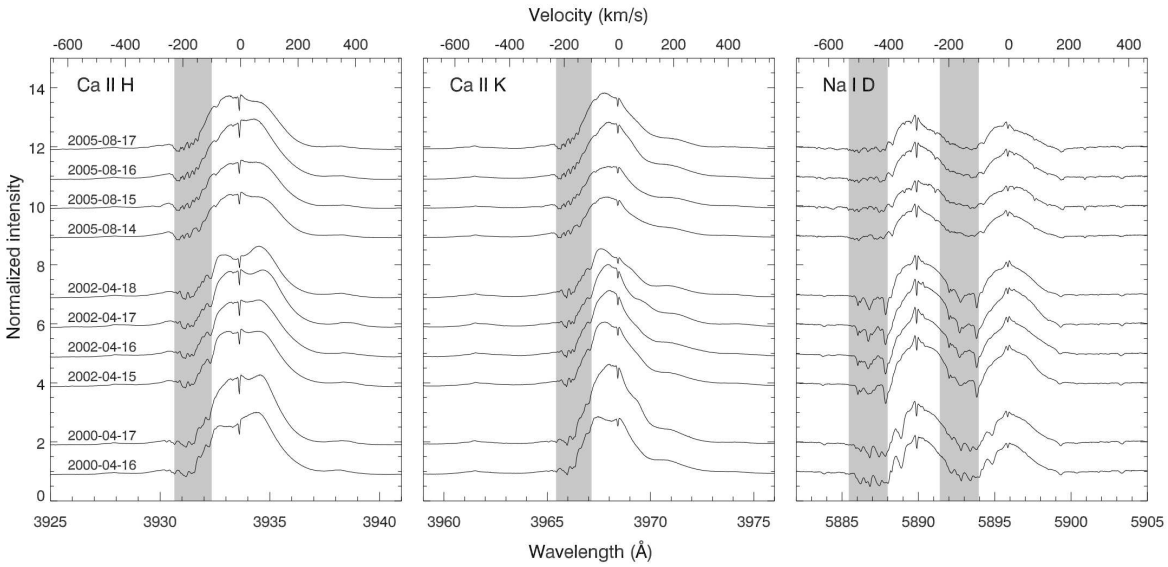

Figure 4.12: Discrete absorption components (DACs) observed for the Ca II H & K and the Na I D lines in a series of UVES spectra of RU Lup. From Gahm et al. (2013).

that the poloidal flow is predominantly parallel to the z-axis, so we can neglect v_r with respect to v_z, $v_{\rm rad}$ covers a range of values due to the term $v_\phi \sin\phi \sin i_\star$. This highlights the influence of the toroidal component on the observed velocity distribution.

Provided that the absorbing region is limited between ϕ_1 and ϕ_2 in azimuth, I calculated synthetic absorption line profiles from the wind. The details of the procedure are outlined in Armeni et al. (2025). The model depends on seven parameters: the vertical and toroidal velocities, v_z and v_ϕ; the angles ϕ_1 and ϕ_2; the width σ and the maximum value τ_0 of a Gaussian that represents the local optical depth; the covering fraction CF of the emitting region. Figure 4.14 shows a gallery of absorption profiles for fixed velocity values, that is, $v_z = 70$ km s^{-1} and $v_\phi = 50$ km s^{-1}. The main characteristic of the profiles is the double-dipped nature, with the position of the dips depending on the azimuth angles ϕ_1 and ϕ_2.

The separation between poloidal and toroidal components allows the derivation of many properties of the outflow. In a steady, axisymmetric MHD wind, three main quantities are

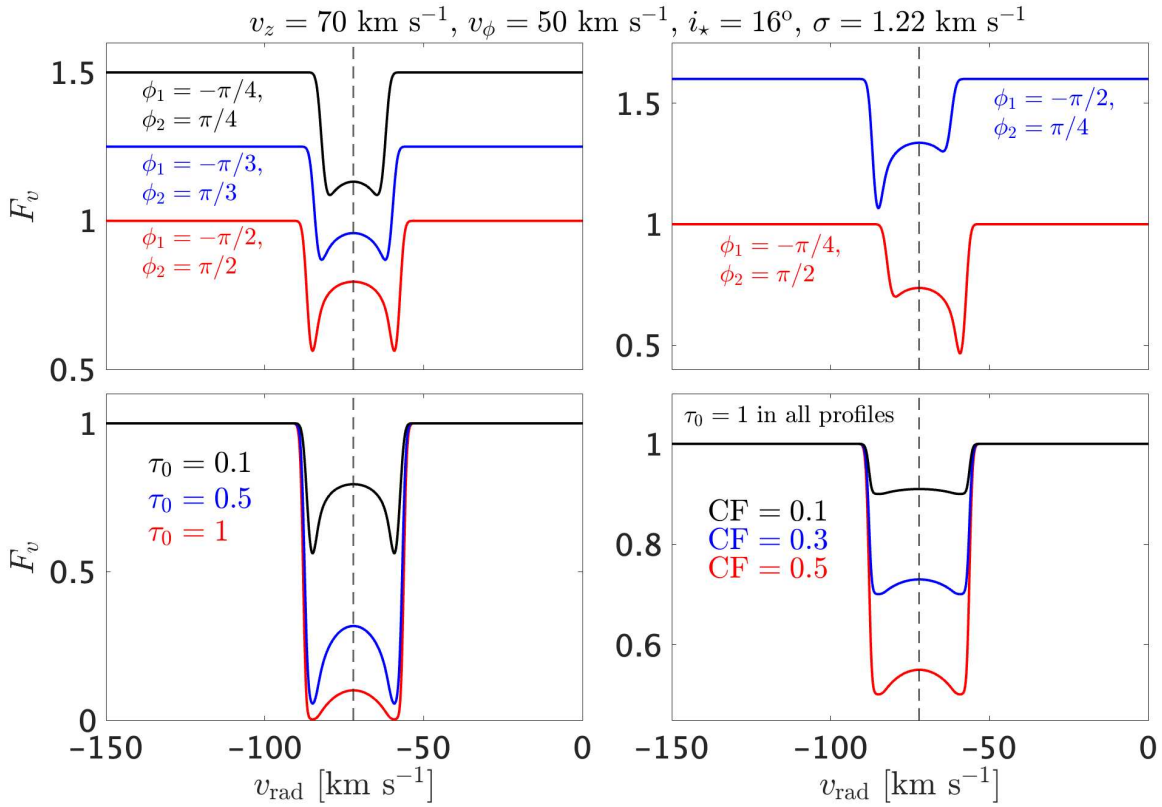

Figure 4.14: Absorption profiles from a region of a wind which is narrow along the line of sight but extended in azimuth. In all panels, $v_z = 70$ km s^{-1}, $v_\phi = 50$ km s^{-1}, $i_\star = 16^o$, and $\sigma = 1.22$ km s^{-1}. Where they are not explicitly reported, the parameters are $\phi_1 = -\pi/2$, $\phi_2 = \pi/2$, $\tau_0 = 0.1$, and CF = 1. The vertical dashed lines are at $-v_z \cos i_\star$.

conserved along a magnetic field line (Mestel, 1968). These are the angular velocity Ω, the energy E, and the angular momentum L. They can be combined to construct another conserved quantity, $J = E - \Omega L$, which does not depend on the magnetic field components (Lovelace et al., 1986). In a cylindrical system of coordinates, the expression for J is

$$J = \frac{1}{2}(v_{\rm p}^2 + v_\phi^2) - \frac{GM_\star}{\sqrt{r^2+z^2}} - \Omega r\, v_\phi. \tag{4.2}$$

Here, the first term is the kinetic energy of the gas, the second term is the gravitational potential $\phi_{\rm g}$, and the third term represents the work done by the magnetic field on the matter (Ghosh et al., 1977). The constant J can be evaluated at the base of the wind, where the flow has $v_{\rm p} \approx 0$ and corotates with the underlying structure, which is either the star or the disk. If the magnetic field line is anchored to a Keplerian disk at r_0, the angular velocity is $\Omega_0 = (GM_\star/r_0^3)^{1/2}$. Then, $\phi_{\rm g}$ is $GM_\star/r_0 = \Omega_0^2 r_0^2$ and $v_\phi = \Omega_0 r_0$. Therefore, the constant is equal to

$$J = -\frac{3}{2}\Omega_0^2 r_0^2 = -\frac{3}{2}(GM_\star)^{2/3}\Omega_0^{2/3}. \tag{4.3}$$

Equating this value to the value at large distance from the launching site, where $\phi_{\rm g}$ is negligible, we get

$$\Omega_0 r\, v_\phi - \frac{3}{2}(GM_\star)^{2/3}\Omega_0^{2/3} - \frac{1}{2}(v_{\rm p}^2 + v_\phi^2) = 0. \tag{4.4}$$

This is a relation between the angular velocity at the launching radius (Ω_0), and the quantities r, $v_{\rm p}$, and v_ϕ along a given magnetic field line. If the three latter quantities are measured, the launching radius of the disk wind can be retrieved by solving this third order equation in $\Omega_0^{1/3}$ (Anderson et al., 2003).

In a wind originating from the stellar surface, Ω_0 is equal to the stellar angular velocity $\Omega_\star$. At the launching point, $\phi_{\rm g} = GM_\star/R_\star$ and $v_\phi \approx \Omega_\star R_\star$. The difference with the previous case is that $\phi_{\rm g}$ is equal to $\Omega_{\rm K}^2(R_\star)R_\star^2$, where $\Omega_{\rm K}(R_\star)$ is the Keplerian angular velocity at the stellar surface, and not to $\Omega_\star^2 R_\star^2$. Therefore, the constant is equal to

$$J \approx -\left[\Omega_{\rm K}^2(R_\star) + \frac{1}{2}\Omega_\star^2\right] R_\star^2 \tag{4.5}$$

Since CTTSs are slow rotators, i.e., $\Omega_\star \ll \Omega_{\rm K}(R_\star)$ (Chap. 1), the second term of Eq. (4.5) can be neglected, and the conservation equation becomes

$$\Omega_\star r\, v_\phi - \frac{GM_\star}{R_\star} - \frac{1}{2}(v_{\rm p}^2 + v_\phi^2) = 0. \tag{4.6}$$

If $\Omega_\star$ is known, this equation provides a relation between r, $v_{\rm p}$, and v_ϕ.

The analysis of the DACs in the Na I and Ca II lines of RU Lup allowed me to calculate the angular momentum per unit mass carried by the wind, given by $l = r v_\phi$ (Anderson et al., 2003), as I will show in Sect. 4.3.3.4. This quantity is useful for determining the Alfvén radius, R_A, of the wind, which is the point where the wind velocity equals the local Alfvén speed, $v_A = B/(4\pi\rho)^{1/2}$. In a magnetic wind, the constant angular momentum per unit mass corresponds to the value it would have if it were a solid body rotating out to R_A, that is, $l = \Omega_0 R_A^2$ (e.g., Mestel, 1984; Lamers and Cassinelli, 1999).

4.3.3 Results

In the following, I summarize the results from my work in which I used high-resolution spectroscopic observations of HM Lup and RU Lup to describe the fundamental properties of the star-disk interaction in CTTSs. By combining insights from both systems, I present a detailed picture of accretion and ejection processes in CTTSs. This analysis takes advantage of the rich emission line spectra of HM Lup and RU Lup to reveal detailed structures of accretion flows and outflows, providing new insights into the complex dynamics governing these processes. My work advances our understanding of CTTSs by revealing the temperature stratification of the accretion flow and the structure and kinematics of the outflow, providing new insights into the complex dynamics of these systems.

In the analysis of RU Lup, when highlighting a particular spectral feature, I will use the ES 22.5 spectrum, as it is the ESPRESSO spectrum with the highest signal-to-noise ratio. For discussions on the spectroscopic variability of RU Lup, I will also utilize other spectra, using the notation provided in Table 4.1.

4.3.3.1 Broad component: non-axisymmetric, temperature-stratified accretion flow

The BCs of different emission lines in the spectrum of CTTSs can be used to probe the temperature stratification of the accretion flow and to study its geometry. If compared to the typical energies required for the excitation of the He I lines, that is, $E_j \gtrsim 20$ eV, the metallic lines have much lower excitation conditions. This suggests that although they are all formed in the accretion flow, different lines trace different regions of it. In other words, these lines trace the temperature gradient in the accretion flow. As an example, the energy of the upper level of the He I 5876 line is $E_j = 23.07$ eV, while the ionization energy of the Na I is $\chi_I = 5.14$ eV. This tells us that a region where conditions are met for the formation of He I cannot emit in Na I, because the latter is completely ionized (e.g., Muzerolle et al. 2001). The conditions for the formation of the Mg I, Fe I, and Fe II lines of Fig. 4.6 are intermediate

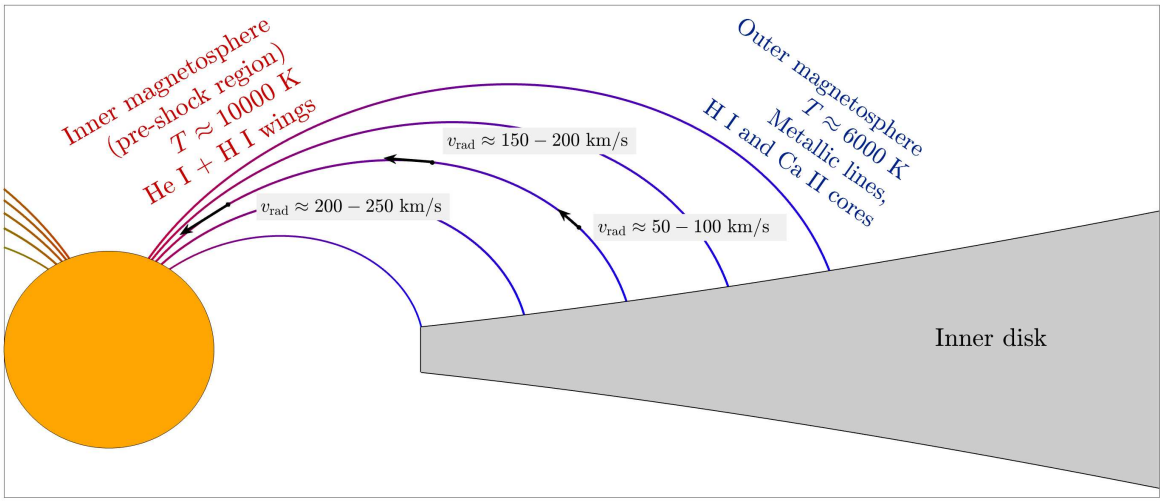

Figure 4.15: Illustration of the temperature stratification of the accretion flow that emerges from the comparison of the properties of the He I and metallic lines. From Armeni et al. (2023).

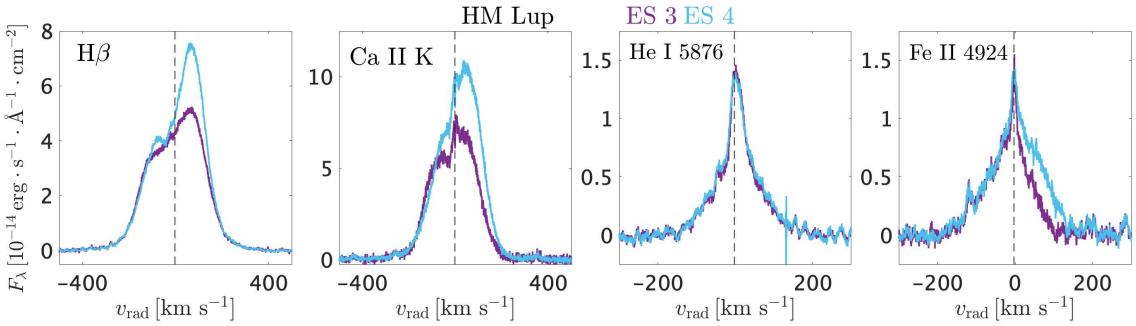

Figure 4.16: Variability of the Hβ, Ca II K, He I 5876, and Fe II 4924 lines between two consecutive ESPRESSO spectra of HM Lup. Adapted from Armeni et al. (2023).

between these two extremes. Therefore, the picture that emerges from this simple reasoning is the one illustrated in Fig. 4.15. The high-energy conditions required for He I emission is, in the magnetospheric accretion model, achieved in the pre-shock region. This region is directly exposed to the X-rays from the shock (Fig. 2.5) and heats up to temperatures of $\sim$ 10000 K (Hartmann et al., 2016). Conversely, since the metallic lines must be produced in lower ionization conditions, they originate further out in the accretion flow, closer to the disk truncation radius where the mass is loaded onto the magnetic field lines.

The multi-epoch ESPRESSO data enabled me to provide additional evidence that these lines originate from distinct regions, as revealed by their variability patterns. As an example, Fig. 4.16 shows that in HM Lup the He I BC does not vary between the third and fourth

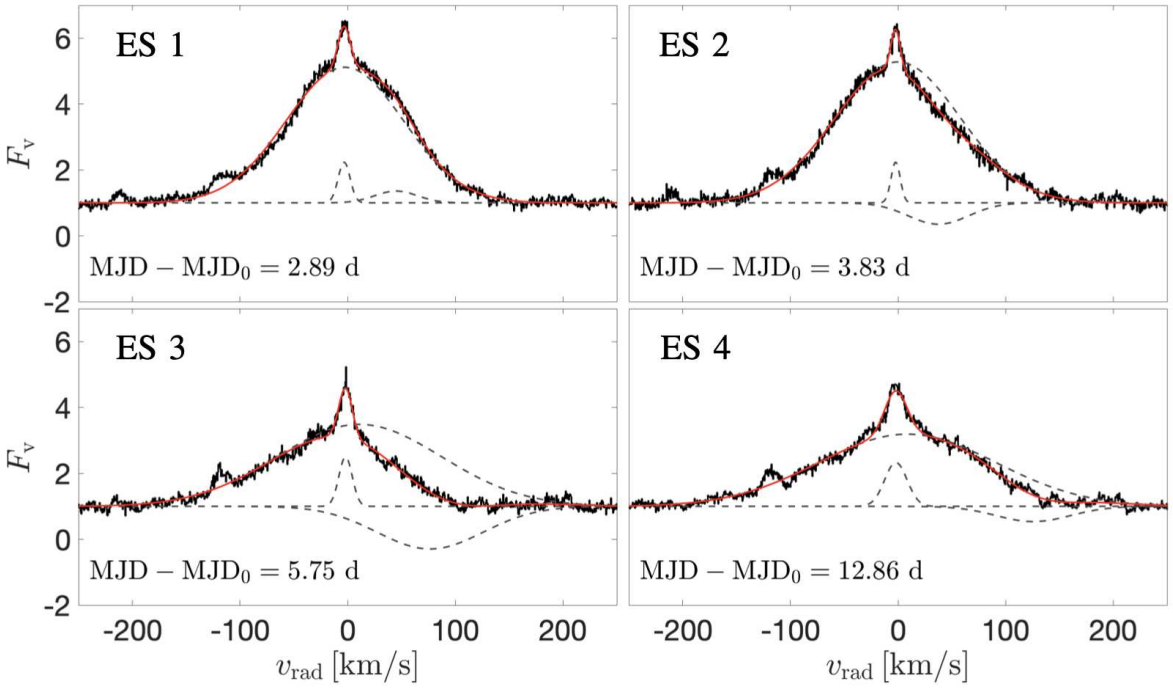

Figure 4.17: Triple gaussian fit to the Fe II 4924 line in the ESPRESSO spectra of HM Lup. Adapted from Armeni et al. (2023).

ESPRESSO spectra (in violet and light blue, respectively), while the red wing of the Fe II 4924 line becomes more extended. I observed the same variability of the red wing in the Hβ and Ca II K lines, suggesting that the low velocity portion of the red wing of these lines is formed in the same region as the red wing of the metallic lines.

The time variability of the BC can also be used to study the geometry of the accretion flow. Figure 4.17 presents the best fit of the Fe II 4924 line for all four ESPRESSO spectra of HM Lup with a triple Gaussian model. While in the first spectrum the line is overall symmetric, in the second and third spectra its red wing is suppressed, requiring a negative Gaussian to replicate the reduced emission. However, it remains unclear whether this suppression is caused by decreased emission or absorption within that velocity range. From this observation I concluded that the accretion flow is non-axisymmetric. This is because the BCs trace a flow that rotates, being tied to both the disk and the star. Consequently, rotation of any asymmetry in the flow results in time variability in the emission lines.

Using the higher number of spectra available for RU Lup, I was able to refine the picture of the accretion flow by studying the time variability of different emission lines. I selected three emission lines that probe different conditions. These lines are the Fe I 5447, Si II 6347 and He I 6678 lines. I fitted the BC of these lines with an asymmetric Gaussian, that is, a

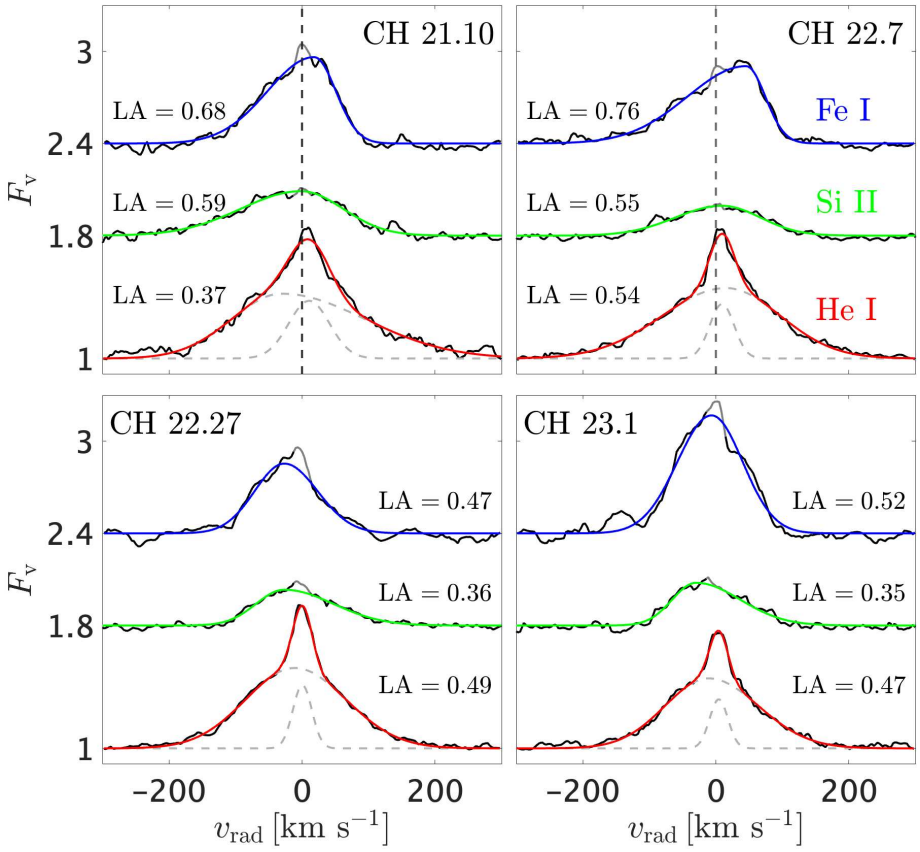

Figure 4.18: Selection of four CHIRON spectra of RU Lup which highlight the variability in the line asymmetry of the BC of the Fe I 5447, Si II 6347, and He I 6678 lines. The blue, green and red lines are the best fits to the three emission lines. From Armeni et al. (2024).

Gaussian that has two different standard deviations σ, one for the red wing (σ_r) and the other for the blue wing (σ_b). From this fit I extracted (1) the line asymmetry to the blue (LA), defined as LA $= \sigma_b/(\sigma_b+\sigma_r)$ and (2) the full width at half maximum (FWHM), defined as FWHM $= \sqrt{2\ln 2}\cdot(\sigma_b+\sigma_r)$.

A selection of CHIRON (CH) spectra which illustrate the variability of the line asymmetry in the Fe I, Si II and He I lines of RU Lup is displayed in Fig. 4.18. In the same spectrum, different lines have different asymmetries. For example, in CH 21.10 the Fe I line is asymmetric to the blue (LA > 0.5), the He I line is asymmetric to the red (LA < 0.5) and the Si II line has LA between these two. For a given line, e.g., Si II 6347, Fig. 4.18 shows that the asymmetry varies in time. In the two top panels the line has an extended blue wing (LA > 0.5), while the situation is opposite (LA < 0.5) in the two bottom panels. These findings confirm the temperature stratification hypothesis and the fact that the accretion flow is non-axisymmetric. In addition, the lines have different FWHM. This parameter is on average ~ 250, 190, and 173 km s^{-1}, for the He I, Si II, and Fe I lines, respectively. As explained

above, in a temperatured-stratified flow, the He I line is formed closer to the star, namely, at higher velocities. Therefore, the values of the FWHM of the three lines are in agreement with the picture of Fig. 4.15.

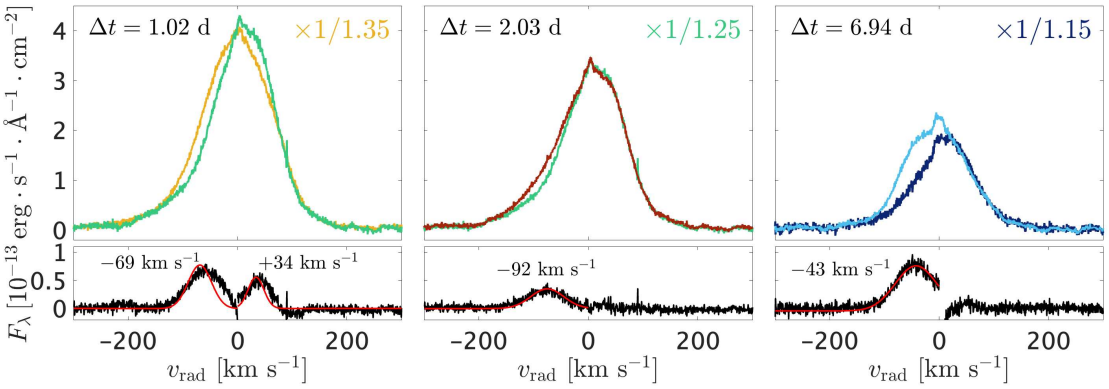

Figure 4.19: Subtraction between line profiles of the Fe II 5317 line from consecutive ESPRESSO spectra. The profiles were rescaled by a constant reported in the upper right corner. The bottom panels show the subtracted profiles, with Gaussian fits superposed. From Armeni et al. (2024).

The non-axisymmetric nature of the accretion flow has already been observed in other CTTSs, such as RW Aur (Petrov et al., 2001), DR Tau (Petrov et al., 2011), and EX Lup (Sicilia-Aguilar et al., 2023). In particular, to explain the variability of the BC of Ca II infrared lines, Sicilia-Aguilar et al. (2023) proposed that the lines are formed in a portion of a Keplerian disk that revolves around the star. However, my analysis of the Fe II 5317 line in the ESPRESSO spectra of RU Lup showed that its radial velocity variations are not compatible with the velocities in a Keplerian disk. This is illustrated in Fig. 4.19, which shows the results of subtracting three pairs of consecutive ESPRESSO spectra from each other in the Fe II 5317 line. The subtraction highlights the presence of a component which contributes to the observed changes in the line profile. The component has velocities ranging between ~ -90 km s^{-1} and $\sim +35$ km s^{-1}, higher than the maximum radial velocity that can be observed in a Keplerian disk around RU Lup, that is, $(GM_\star/R_\star)^{1/2}\sin i_\star \approx 60$ km s^{-1}, where $i_\star = 16^o$ is the inclination of the stellar rotation axis (Armeni et al., 2024). Velocities of this order are instead compatible with free fall along dipolar magnetic field lines (Armeni et al., 2024). For this reason, I rejected the scenario proposed by Sicilia-Aguilar et al. (2023) and favored the line formation in tongues of matter that leave the disk at the truncation radius R_T and accrete onto the star. Considering the similar excitation conditions of the Fe II 5317 and Si II 6347 lines, I proposed that these lines, along with other singly ionized metals, form primarily along the magnetic field lines.

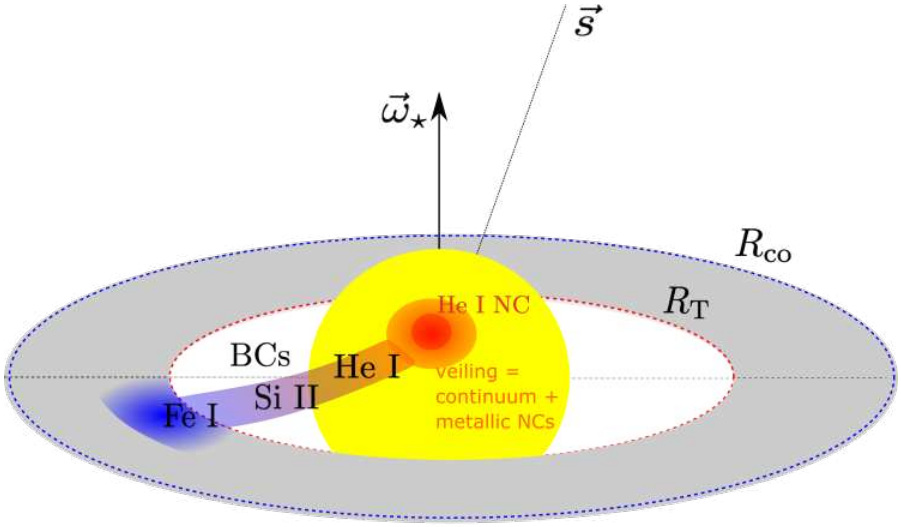

Figure 4.20: Structure that emerges from the analysis of the BCs. From Armeni et al. (2024).

In summary, my analysis of the BCs of the emission lines in the spectrum of RU Lup refined our understanding of line formation in the accretion flow of CTTSs. I confirmed the stratification I previously inferred for HM Lup (Fig. 4.15). Additionally, my findings revealed that the accretion flow has the properties of a non-axisymmetric rotating flow tied to the disk at the truncation radius, R_T, similar to the scenario described by Sicilia-Aguilar et al. (2023), but it is likely more complex, consisting of tongues of matter that connect the disk to the star. The resulting picture is illustrated in Fig. 4.20.

4.3.3.2 Herbig fluorescence

Another hint at the stratification of the flow comes from a very peculiar effect that is rarely observed in CTTSs. The third panel in the second row of Fig. 4.6 shows three Fe I lines (4064 Å, 4132 Å, and 4144 Å) from the same multiplet, sharing nearly identical upper-level energies and Einstein A coefficients. The Grotrian diagram in Fig. 4.21 specifically highlights the energy levels and transitions responsible for these lines, illustrating their similarity.

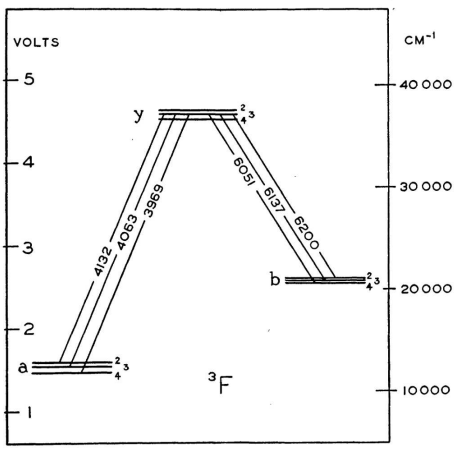

Figure 4.21: Grotrian diagram of Fe I, showing the lines involved in the fluorescence phenomenon (on the left). From Herbig (1945).

Despite having similar properties, the Fe I 4064 and 4132 lines are much stronger than the Fe I 4144 line. These lines form a doublet, that is, they have the same upper level.

The unusual strength of these two lines was first noticed by Herbig (1945) in the spectrum of the CTTS RW Aur A. In his note, he proposed that their anomalous intensity is due to a fluorescence mechanism. There is indeed a third transition which shares the upper level with the Fe I 4064 and 4132 lines, that is, the Fe I line at 3969.26 Å. This line is nearly coincident in wavelength with the Ca II H (3968.47 Å) and Hϵ (3970.08 Å) lines. Herbig suggested that the prominent Ca II H and Hϵ emission often observed in CTTSs could be absorbed in the Fe I 3969 line, producing an overpopulation of the level from which the Fe I 4064 and Fe I 4132 emission originates.

In my analysis of HM Lup (Armeni et al., 2023), I have revisited this phenomenon and provided new insights into its nature. Figure 4.22 compares the Ca II H and K lines of HM Lup. The H line is partially blended with Hϵ. The Ca II lines are a doublet, hence they should have a similar profile. However, the red wing of the Ca II H line is strongly absorbed in the spectral region of the Fe I 3969 line. The observation of Fe I absorption indicates that a region that is optically thick in Fe I must be between us and the region that emits in Ca II and/or H I. On top of that, the Fe I region must see either the Ca II emission as redshifted or the H I emission as blueshifted. In Armeni et al. (2023) I interpreted this absorption and the "Herbig" fluorescence in the framework of the current picture of the star-disk interaction. Recalling the hypothesis proposed by Gahm (2001) (Fig 4.23), if our line of sight to the Ca II emitting region crosses the region where iron is mostly neutral, this would lead to absorption in Fe I 3969 against the Ca II H emission.

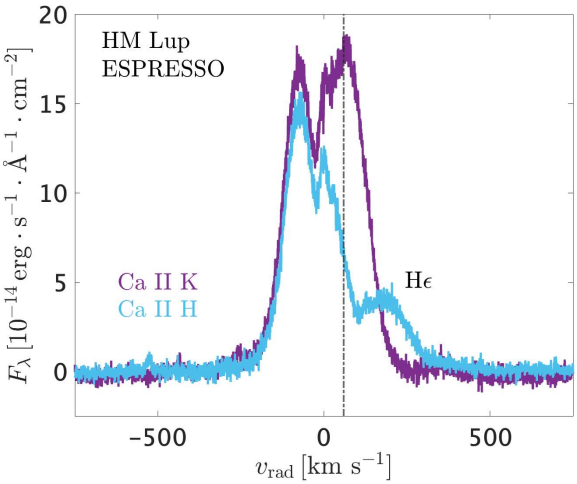

Figure 4.22: Comparison between the Ca II H and K lines in the spectrum of HM Lup. The emission line at ~ 150 km s^{-1} from the rest wavelength of Ca II H is the Hϵ line. The dashed line marks the position of the Fe I 3969 line.

This scenario is consistent with the picture of a temperature-stratified accretion flow that I derived from the analysis of the spectra of HM Lup and RU Lup (Figs. 4.15 and 4.20). In such a situation, Ca II is formed closer to the star than Fe I, i.e., at higher velocities. If the star-disk system is seen at intermediate-to-high inclinations, the region in which iron is neutral would be between us and the Ca II emission, and it would see the Ca II emission as

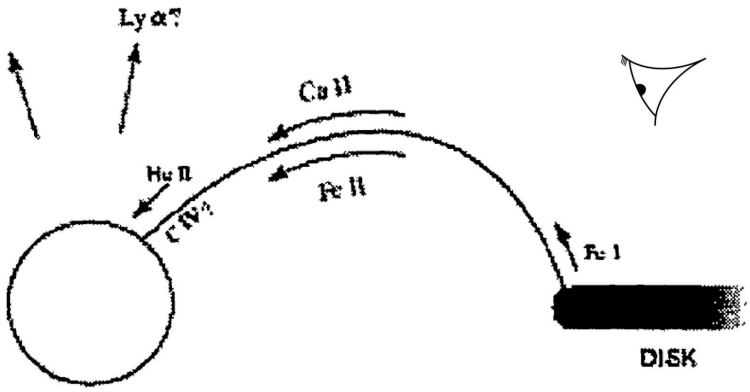

Figure 4.23: Illustration of a possible scenario that would lead to the observation of the "Herbig" fluorescence. Adapted from Gahm (2001).

redshifted. Bertout (2024) studied the radiative transfer problem associated to the "Herbig" fluorescence for different velocity fields. He showed that Doppler shifts in the flow make the Ca II H, Fe I 3969, and Hϵ lines interact with each other in a very complex way, leading to amplified emission in all three lines. However, the profiles he calculated are somewhat different from the observed ones.

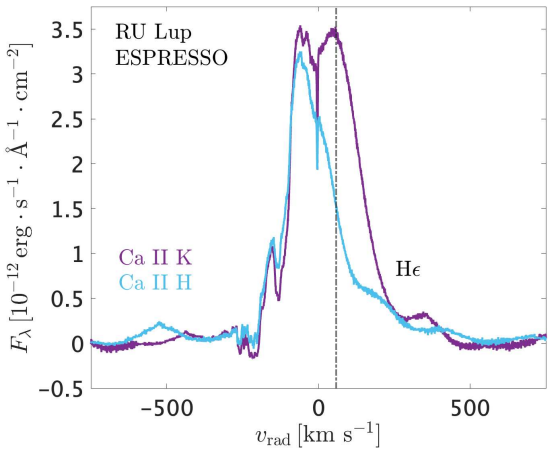

Figure 4.24: Same as Fig. 4.22 but for RU Lup.

Although the explanation in terms of a temperature gradient along the magnetic field lines seems plausible for the fluorescence observed in HM Lup, a detailed study of this phenomenon from an observational point of view is required to constrain the geometry of the flow that leads to the fluorescence. For example, the same behaviour of the Ca II H line is observed in RU Lup (Fig. 4.24), in which the star-disk system is known to be seen at low-inclination (stellar inclination $i_\star = 16^o$, Armeni et al. 2024) such that our line of sight does not cut successively the Fe I and Ca II emitting region (Fig. 4.23). This seems to argue against the stratification hypothesis.

My work highlights the importance of this fluorescence mechanism in understanding the geometry of the star-disk interaction, demonstrating its potential as a diagnostic tool for probing the complex structures involved in the accretion process.

4.3.3.3 Narrow component: latitude and vertical structure of the hot spot

The NC of the emission lines is formed in the post-shock region, where the gas decelerates from the free-fall velocity to ~ 1/4 of it (Sect. 2.2). From the conservation of mass, this corresponds to a 4× density increase from the pre-shock region to the post-shock region.

The post-shock region is a sub-structure of the hot spot (see Fig. 2.5). Therefore, we expect to see radial velocity variations in the NC of the emission lines as the star rotates. Specifically, since it is formed close to the stellar surface, the NC is expected to be rotationally modulated with the stellar rotation period, $P_\star$. Under the assumption that the spot is not very extended, so that it can be treated as a point source, the radial velocity of the NC describes a sinusoidal curve, i.e.,

$$v_{\rm NC}(\phi) = v_0 + v \sin i \cdot \cos\theta_{\rm S} \sin[2\pi \cdot (\phi - \phi_{\rm S})] \tag{4.7}$$

(e.g, McGinnis et al. 2020). In this formula, v_0 is an arbitrary offset that includes the stellar velocity and other velocities due to gas motions; $v \sin i$ is the projected rotational velocity of the star; $\theta_{\rm S}$ is the latitude of the spot, i.e., the angle between the stellar equator and the position of the spot; ϕ is the phase angle ($0 < \phi < 1$) that represents the fraction of a full rotational cycle that has been completed at a given time; $\phi_{\rm S}$ is an arbitrary offset in phase. As can ben seen from Eq. (4.7), the amplitude of the radial velocity modulation is a fraction of $v \sin i$ and depends on the latitude of the spot on the stellar surface. The closer the spot is to the pole, the smaller the modulation.

In Armeni et al. (2024) I focused on the He I 5876 line to study the modulation of the radial velocity of the NC with the collection of 65 CHIRON + ESPRESSO spectra of RU Lup. I fitted the profile of the He I 5876 line with a combination of three Gaussian functions. Two Gaussians were needed to reproduce the BC, while I used an asymmetric Gaussian to fit the NC. This fit is displayed in Fig. 4.7 for the He I 5876 line in the ES 21.1 spectrum. In this spectrum, the red wing of the NC is ~ 2 times more extended than the blue wing,

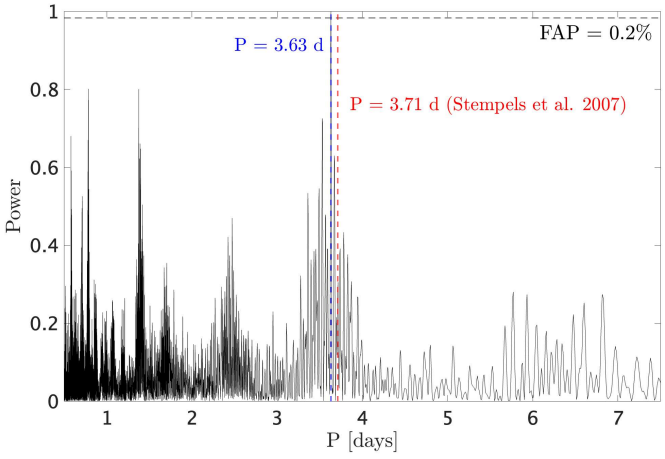

Figure 4.25: Lomb-Scargle Periodogram of the radial velocity of the He I 5876 NC in RU Lup. The blue line marks the highest peak, detected with a false alarm probability of 0.2%. The red line marks the stellar rotation period given by Stempels et al. (2007). From Armeni et al. (2024).

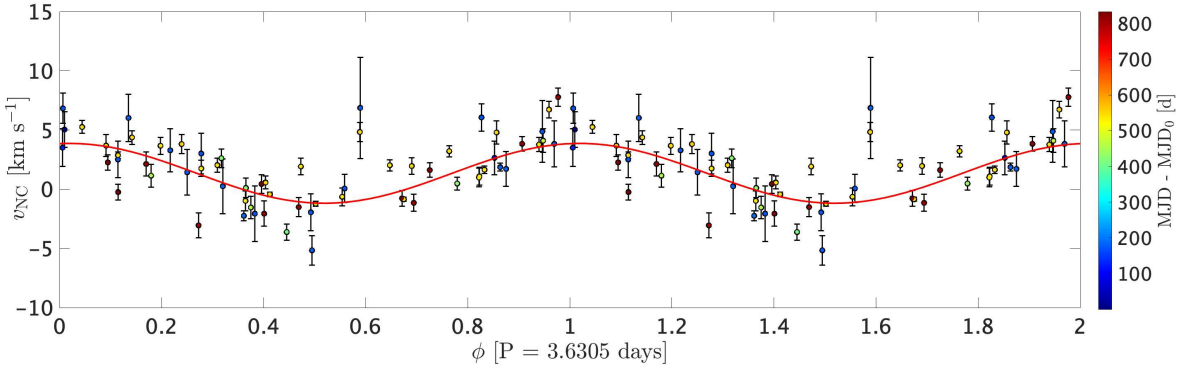

Figure 4.26: Phase-folded radial velocity curve of the He I 5876 NC, and the best-fitting sinusoidal function of Eq. (4.7). From Armeni et al. (2024).

with $\sigma_r = 32.9 \pm 0.5$ km s^{-1} and $\sigma_b = 14.9 \pm 0.4$ km s^{-1}. I applied this procedure to each spectrum and obtained v_{NC} as a function of time. The Lomb-Scargle periodogram (Lomb, 1976; Scargle, 1982) of this time series is shown in Fig. 4.25. I detected a signal with a false alarm probability (FAP) of 0.2% at a period $P = 3.63$ days. This period differs only by ~ 2 h from the stellar rotation period given by Stempels et al. (2007) ($P_\star = 3.71$ days). The discrepancy between the two periods can be attributed to the intrinsic variability of the region traced by the He I 5876 NC. This result marks the first detection of a periodic modulation in the NC of the emission lines of RU Lup, confirming the stellar rotation period previously determined by Stempels et al. (2007) from the analysis of the absorption lines.

The hot spot phase angle ϕ of Eq. (4.7) can be derived by phase-folding the time series, i.e., from $\phi = \lfloor (t - t_0)/P \rfloor$ where $\lfloor \cdot \rfloor$ is the floor function, P is the detected period and t_0 is a reference date. Figure 4.26 displays the phase-folded radial velocity curve of the NC of the He I 5876 line of RU Lup, with the best-fit of Eq. (4.7) superposed to the observations. The relevant parameters of the best fit are the amplitude of the modulation, $A = v \sin i \cos \theta_S = 2.53 \pm 0.13$ km s^{-1} and the phase offset $\phi_S = 0.75 \pm 0.01$. The latter represents the moment in the cycle when the hot spot is most directly facing the observer, corresponding to the transition of v_{NC} from redshifted to blueshifted relative to the rest velocity v_0. Using $v \sin i = 8.6 \pm 1.4$ km s^{-1}, I derived the latitude of the spot to be $\theta_s = 73 \pm 3$ °. This result indicates that the magnetic field is misaligned with respect to the stellar rotation axis, as illustrated in Fig. 4.27.

The NC of different emission lines have different properties. This is clear from the comparison between the NC of the He I lines and the NC of the Fe II lines in Fig. 4.6. The He I NCs are generally broader and more asymmetric than the NCs of the metallic lines. To compare the NCs of different species with each other, I selected six emission lines and fitted their NC. These lines are: Fe I 5447, Fe II 5347, Mg I 5184, Si II 6347, He I 5876, and He II

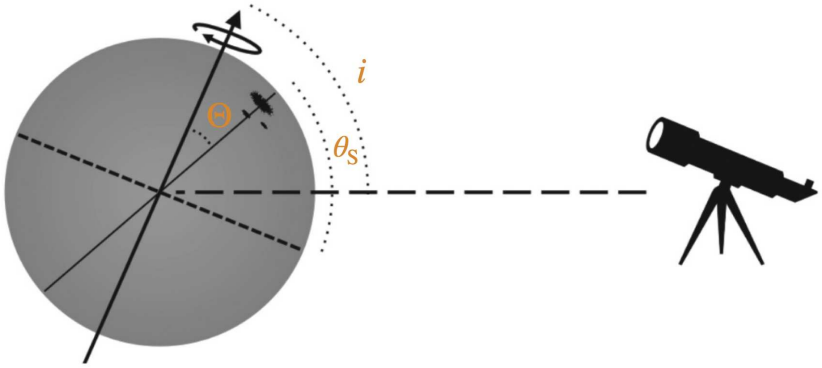

Figure 4.27: Illustration of a hot spot at latitude θ_S on the surface of a star viewed at inclination i. Θ is the magnetic obliquity, i.e., the angle between the stellar rotation axis and the position of the hot spot. Adapted from McGinnis et al. (2020).

4686. Most of them have already been discussed in Sect. 4.3.3.1 for the analysis of the BCs. The only new transition is the He II line, which probes very high energy conditions because it has an upper state with energy $E_j = 51.01$ eV. The procedure for deriving the parameters of the NCs is illustrated in Fig 4.28. I used the ES 22.5 spectrum because of its high S/N and the fact that the NCs are visible in all selected lines. Since some line profiles are contaminated by the photospheric absorption, I removed the stellar spectrum by using the best-fitting photospheric template (Fig. 4.3). Then, I fitted the photospheric subtracted spectra with multiple Gaussians to separate the BC and the NC. For all lines, the NC was fitted with an asymmetric Gaussian, which I already introduced in Sect. 4.3.3.1 for the analysis of the BC. The best fit values for the red and blue standard deviations (σ_r and σ_b, respectively) of the NC are provided in the inset of each panel in Fig. 4.28.

The most interesting result is the gradient in the width of the red wing σ_r of the NC from the most energetic transitions (He I and He II) to the least energetic ones (Fe I). The He I NC is broad and asymmetric to the red, with $\sigma_r = 33$ km s^{-1}. Conversely, the Fe I line is narrower and almost symmetric, with $\sigma_r = 9$ km s^{-1}. The Mg I, Fe II, and Si II lines, which have intermediate excitation conditions, have σ_r between these two extreme values.

The fact that the helium NCs are substantially broader than the metallic NCs is indicative of the broadening mechanism, which can be either turbulent or thermal, or both. In both cases, the broader NCs of the helium lines are compatible with a formation in the post-shock region, which is directly exposed to the X-ray radiation from the shock and it is expected to be hot and possibly turbulent. The red asymmetry observed in the He I 5876 line is also compatible with this hypothesis, given that the gas slows down to velocities of $\sim (1/4)\, v_{ff} = 60$ km s^{-1} in the post-shock region.

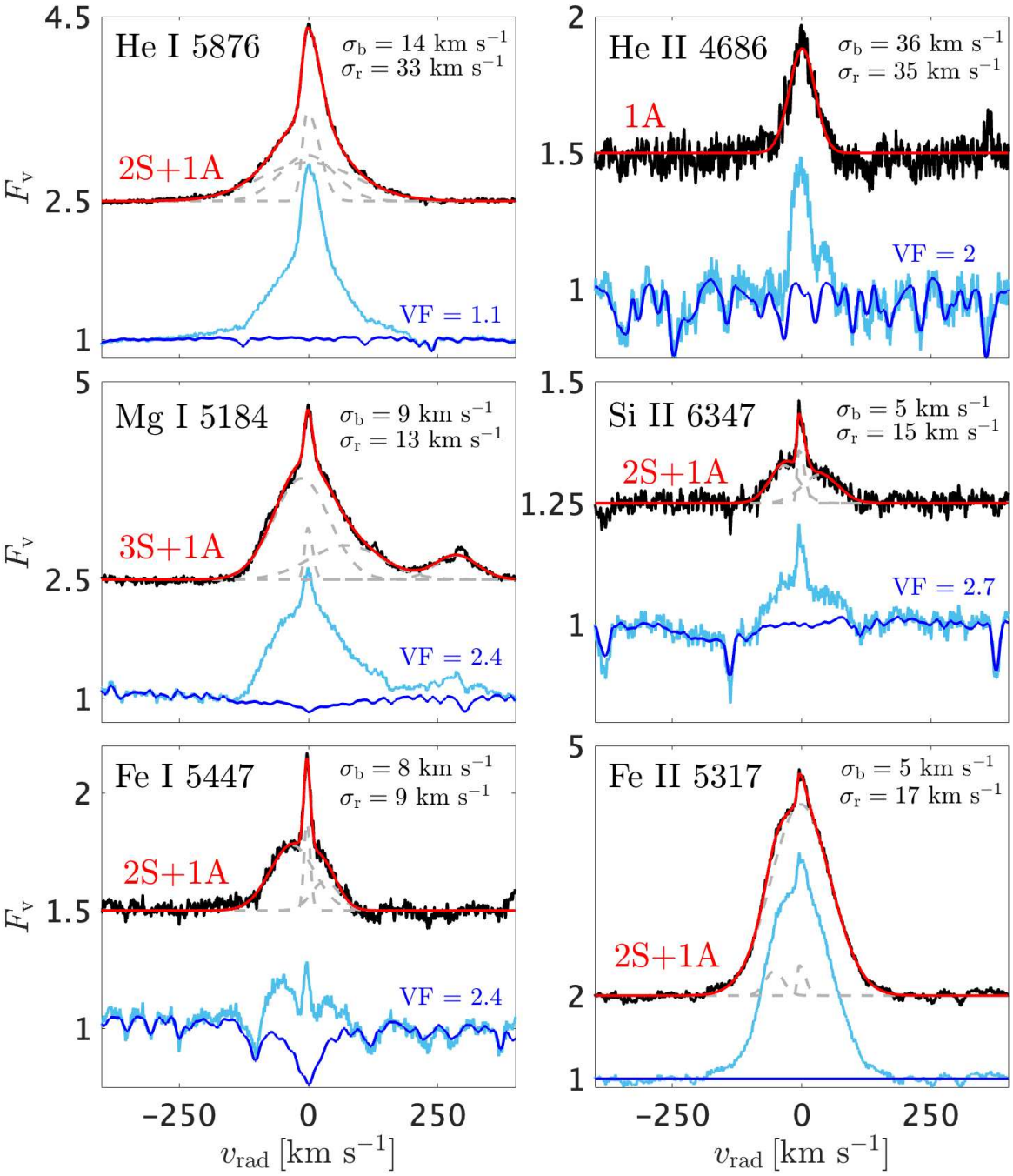

Figure 4.28: Illustration of the procedure to extract the asymmetry of the NC of a selection of lines in the ES 22.5 spectrum of RU Lup. For each line, the light blue spectrum is the observed profile, the dark blue spectrum is the photospheric template, the black spectrum is the photospheric subtracted profile, and the red line is the best fit with multiple Gaussians. The used model is reported in red as nS+mA, where n and m are the number of symmetric and asymmetric Gaussians, respectively. In each panel σ_r and σ_b are the best-fitting standard deviations obtained from the asymmetric Gaussian model described in Sect. 4.3.3.1. From Armeni et al. (2024).

The narrower NCs of the metallic lines are clearly formed in a different region. Dodin and Lamzin (2012) showed that the heated photosphere below the shock (Fig. 2.5) which is responsible for the continuum emission in the optical (Fig. 2.6), also emits in NCs of metallic species. The narrow emission is formed in a structure which resembles a stellar chromosphere, i.e., it has a temperature that increases with the height in the atmosphere due to the radiation from the overlying shock. The more energetic metallic transitions (i.e., Fe II and Si II) have a greater line asymmetry to the red than the less energetic ones (Fe I and Mg I). This suggests that the Fe II and Si II lines could originate in the upper part of this structure, at higher temperature, and still have a residual infall velocity.

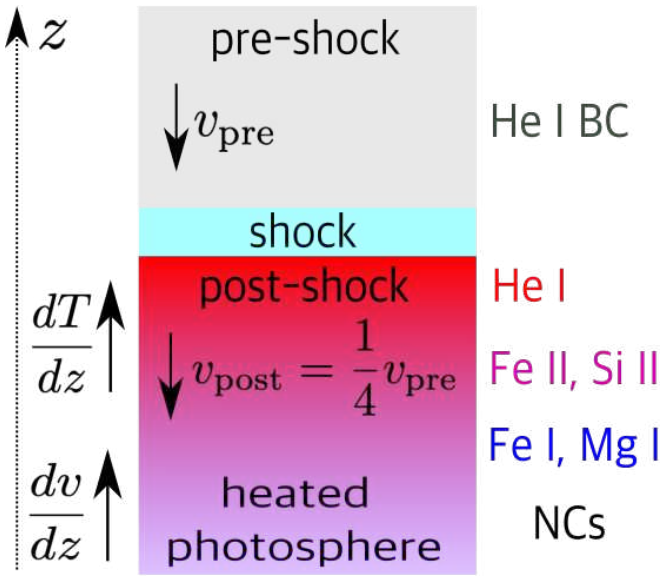

Figure 4.29: Sketch of the vertical stratification of the hot spot that emerges from the analysis of the NCs (Fig 4.28). v_{pre} and v_{pre} are the pre- and post-shock velocities, respectively. From Armeni et al. (2024).

In summary, my time-resolved analysis of the NC of the emission lines of RU Lup allowed the derivation of the latitude of the accretion hot spot and confirmed the stellar rotation period obtained by Stempels et al. (2007) with a different technique. By introducing an asymmetric Gaussian model to fit the NC, I was able to study the vertical stratification of the spot. With my observations I confirmed the prediction of the magnetospheric accretion scenario that, from the post-shock region down to the photosphere, the gas slows down and cools, as illustrated in Fig. 4.29.

4.3.3.4 Forbidden emission lines and discrete absorption components: structure of the outflow

For the analysis of the outflowing gas in CTTSs, I concentrated on RU Lup. The complex profiles of its forbidden emission lines (Natta et al., 2014) indicate a non-trivial outflow geometry and kinematics, which I investigated using high-resolution spectroscopy.

These lines are heavily blended with absorption lines from the stellar photosphere, as evident in Fig. 4.10. To study the structure of the outflow, the stellar contribution must be removed. This can be achieved by using the template spectrum that best fits the photo-

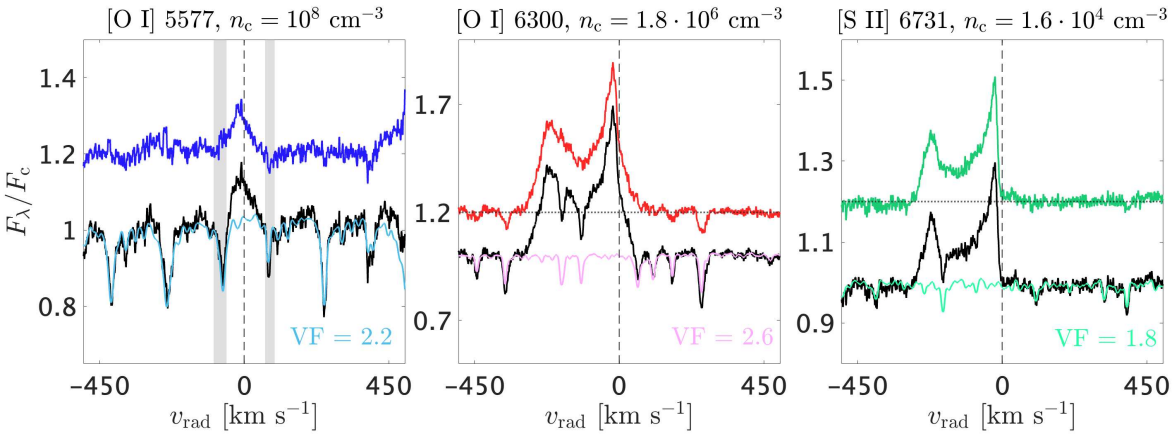

Figure 4.30: Photospheric subtraction procedure for the [O I] 5577, [O I] 6300, and [S II] 6731 lines in the ES 22.5 spectrum of RU Lup. The black lines are the observed spectra. The colored lines superposed on the observed spectra are from the template for the photospheric spectrum of RU Lup (Fig. 4.3). The resulting photospheric-subtracted spectra are shifted vertically by 0.2. In the left panel the shaded areas flag the region where there might be a residual contamination from the photospheric spectrum. From Armeni et al. (2025).

spheric spectrum of RU Lup (Sect. 4.3.2.1 and Fig. 4.3), adjusting the veiling fraction (VF) in the vicinity of each FEL to match the depth of the photospheric lines. The procedure is shown in Fig. 4.30 for three prominent FELs in the ES 22.5 spectrum of RU Lup: the [O I] 5577, [O I] 6300, and [S II] 6731 lines.

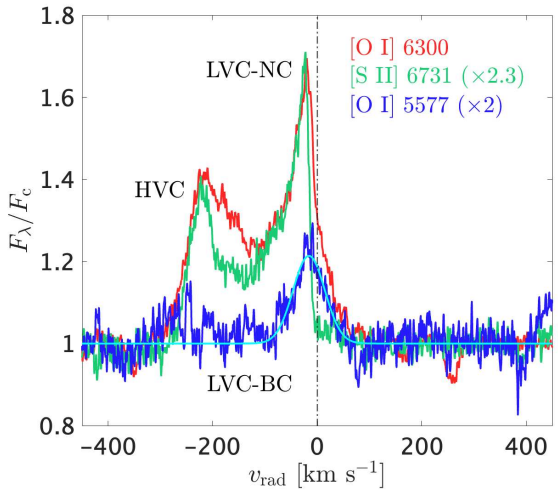

Figure 4.31: Photospheric subtracted profiles of the [O I] 5577, [O I] 6300, and [S II] 6731 lines in the ES 22.5 spectrum of RU Lup. The cyan line is the best fit to the [O I] 5577 line with a Gaussian model. From Armeni et al. (2025).

The resulting line profiles exhibit the typical velocity structure observed in CTTSs (Sect. 4.3.2.4), as shown in Fig. 4.31. The HVC and LVC-NC are visible in the [O I] 6300 and [S II] 6731 lines and trace a jet that extends out to $\sim$ 100 AU from the star and an MHD wind launched from the outer disk, respectively (Whelan et al., 2021; Birney et al., 2024). The LVC-BC is most evident in the [O I] 5577 line, and can be fitted with a Gaussian. The best fit (in cyan in Fig. 4.31) reveals a blueshifted centroid velocity $v_0 = -15.7 \pm 1.5$ km s^{-1} and symmetric line wings with $\sigma = 30.5 \pm 1.5$ km s^{-1}. The blueshifted centroid is

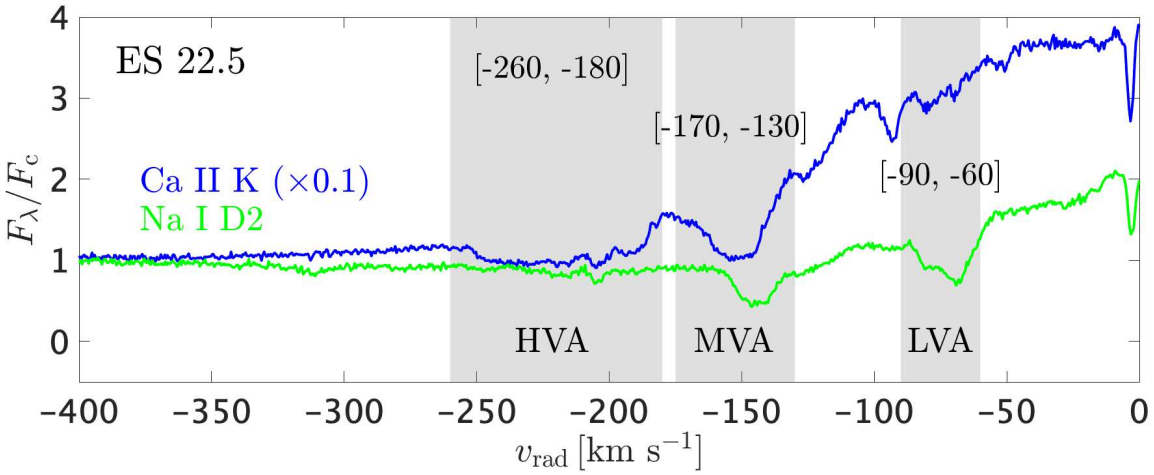

Figure 4.32: Discrete absorption components (DACs) observed for the Na I D2 and the Ca II K lines in the ES 22.5 spectrum of RU Lup. The shaded areas mark the approximate velocity ranges where absorption is observed. The narrow absorption at ~ 0 km s^{-1} is interstellar. From Armeni et al. (2025).

compatible with formation in a wind, but the presence of a redshifted wing indicates that some of the emitting material also moves away from us. The overall line symmetry and the observed velocities suggest formation in a region that is in Keplerian rotation. Assuming the stellar parameters of Sect. 4.2 and a stellar inclination of 16^o (Armeni et al., 2024) for RU Lup, the projected Keplerian velocity $(GM_\star/r)^{1/2}\ \sin i_\star$ is ~ 40 km s^{-1} at $r = 2\ R_\star$, compatible with the observed velocities. The LVC-BC is observed also in the [O I] 6300 line but not in the [S II] 6731 line, which shows no emission at positive velocities. Since the [O I] lines have higher critical densities than the [S II] 6731 line, this implies the LVC-BC traces denser material compared to the jet (HVC) and outer disk wind (LVC-NC). Although the formation of the LVC-BC in an MHD wind launched for small disk radii had been already suggested by, e.g., Simon et al. (2016) and Banzatti et al. (2019), my results provide stronger constraints by demonstrating that the wind is launched within the corotation radius. This finding aligns with the conical wind model proposed by Romanova et al. (2009) (Sect. 3.4).

The DACs provide complementary information to the FELs. Although the DACs have been noted in a few studies (e.g., Gahm et al. 2013; Petrov et al. 2014b), they remain a relatively under-explored aspect of CTTS outflows. My analysis of the DACs in RU Lup makes a substantial contribution to understanding their formation and the valuable information that can be derived from their profiles. Figure 4.32 shows the blue wings of the Na I D2 and the Ca II K lines in the ES 22.5 spectrum of RU Lup. The unprecedented resolution of ESPRESSO (compared to, e.g., UVES, Fig. 4.12) allows for a detailed study of the components and their variability. Three different DACs can be distinguished in the ES 22.5 spec-

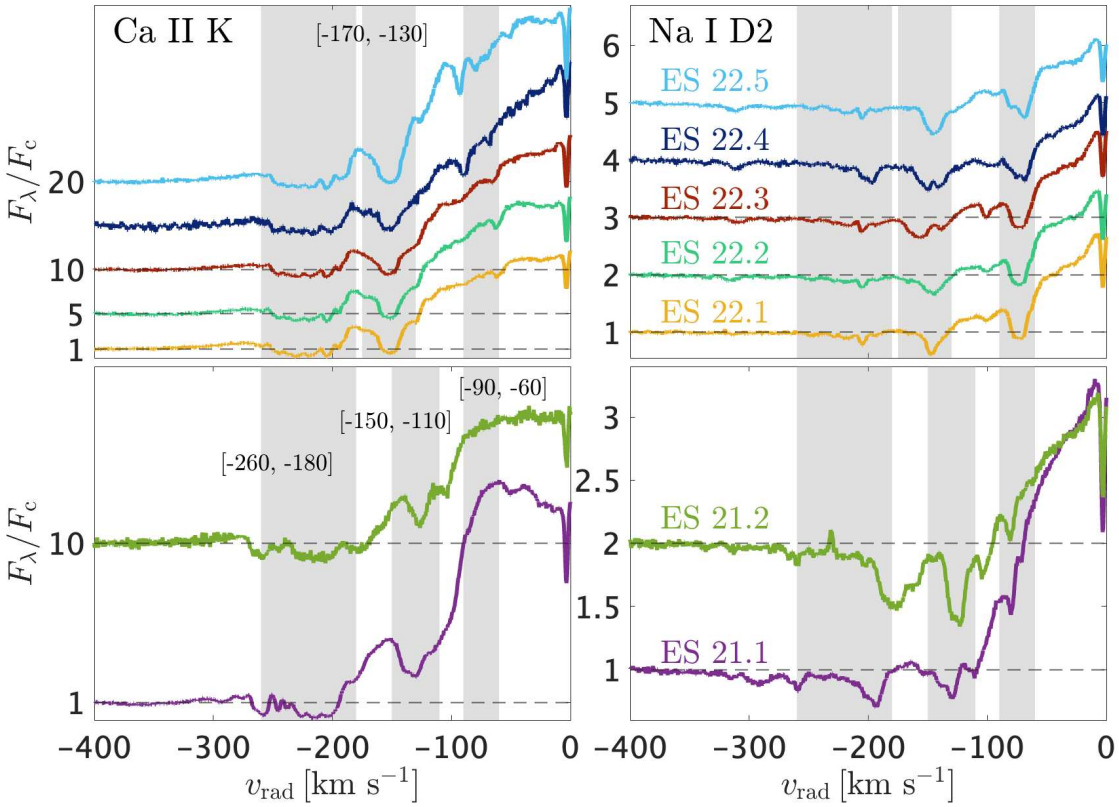

Figure 4.33: Variability of the blue wings of the Ca II K and Na I D2 lines in the ESPRESSO spectra of RU Lup. The shaded areas mark the velocity ranges where absorption is observed.

trum of RU Lup: a high velocity absorption (HVA) that extends between -260 km s^{-1} and -180 km s^{-1}, a medium velocity absorption (MVA) that extends between -170 km s^{-1} and -130 km s^{-1}, and a low velocity absorption (LVA) that extends between -90 km s^{-1} and -60 km s^{-1}.

The variability of the DACs in the seven ESPRESSO spectra of RU Lup is shown in Fig. 4.33. The key points that can be extracted from these observations are:

- the HVA is weak in Na I and strong in Ca II; it is stable in velocity, although its velocity sub-components change in 2021 and stabilize in 2022;
- the MVA is observed in both Na I and Ca II; from ES 21.1 to ES 21.2, the MVA strengthens in Na I but weakens in Ca II K; between 2021 and 2022, the entire MVA shifts by ~ 20 km s^{-1} to the blue in both species;
- the LVA is weak in Ca II and strong in Na I; it is prominent in 2022, but its presence in 2021 is unclear.

The varying optical depths of the DACs, the differing strengths of these components between Na I and Ca II, and their variability, all indicate that these absorption features trace distinct regions within the layered, "onion-like" structure of the outflow of RU Lup.

The low velocities observed in the LVA suggest an origin in the conical wind predicted by Romanova et al. (2009). The terminal velocity in the conical wind is of the order of ~ 55 km s^{-1} (Fig. 3.9), similar to what is observed for the LVA of RU Lup. The Na I LVA in ES 22.5 appears to have a double-dipped structure. The similarity with the absorption line profiles produced in a narrow region of a wind (the model I developed in Sect. 4.3.2.4) might suggest that the outflowing gas has a toroidal component of velocity. Using this model, the vertical and toroidal components of the velocity vector can be separated. To this end, the LVA profile must be normalized relative to the background emission. In Armeni et al. (2025), I used the red wing of the Na I D2 line as a template for the blue wing emission, by folding the D2 line profile around the line center. The ratio between the blue wing and the folded red wing is the normalized profile of the LVA. The best fit was done assuming CF = 1, i.e., a complete coverage of the emitting region, in order to remove the degeneracy between τ_0 and CF (Fig. 4.14). The result of the fit of the Na I LVA in the ES 22.5 spectrum with the wind absorption model is shown in Fig. 4.34 (left panel). The best fit parameters are v_z = 77.03±0.62 km s^{-1}, v_ϕ = 29.2±1.2 km s^{-1}, $\phi_1 = -100\pm21$ °, $\phi_2 = 163\pm43$ °, $\tau_0 = 0.126\pm0.001$, and $\sigma = 4.39 \pm 0.03$ km s^{-1}.

Birney et al. (2024) resolved the large-scale outflow of RU Lup with the *Multi Unit Spectroscopic Explorer* (MUSE) (Bacon et al., 2010) showing that the jet has a full opening angle

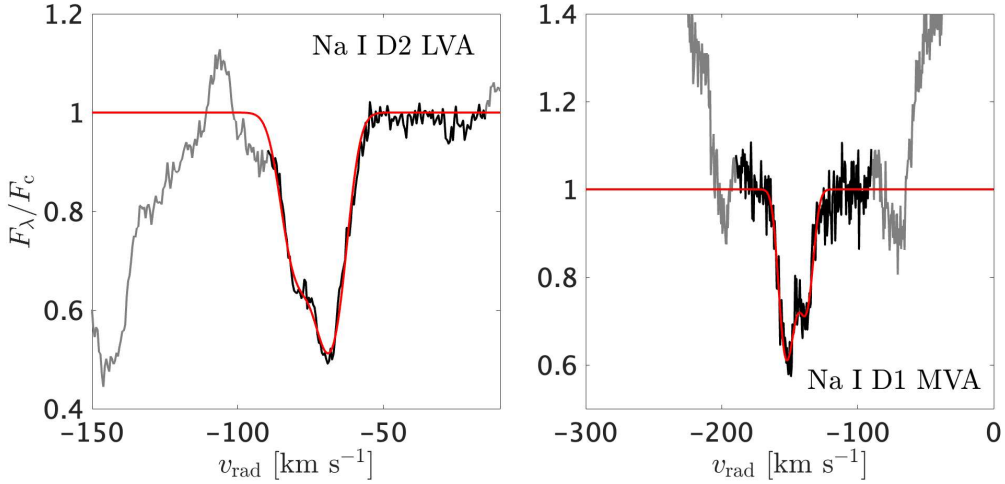

Figure 4.34: Best fits (red lines) of the normalized absorption profiles of the LVA and MVA components. In the left panel, the LVA is from the Na I D2 line in the ES 22.5 spectrum. In the right panel, the MVA is from the Na I D1 line in the ES 22.4 spectrum. The regions excluded from the fit are plotted in gray. Adapted from Armeni et al. (2025).

θ of 25°. Adopting this geometry also for the inner regions of the outflow of RU Lup, we can find the radial distance r from the star where the absorption originates. Under the assumptions that (1) the Na I emission comes from the magnetosphere and (2) absorption occurs at the limb of a conical outflow that originates from the corotation radius ($R_{\rm co}$), the LVA is produced at the intersection of the line of sight to the magnetosphere and the boundary of the conical wind that is closer to us, as sketched in Fig. 4.35. The position (r, z) at which the absorption occurs is the solution of the system

$$z = \frac{r + r_1}{\tan i_\star}; \quad z = \frac{r - R_{\rm co}}{\tan \theta/2}. \tag{4.8}$$

Here $i_\star$ is the stellar inclination and $r_1 = [0, R_{\rm T}]$ is the radial range of the region from which the magnetospheric emission originates. For r_1 between 0 and $R_{\rm T}$, and the values of $i_\star$, $R_{\rm T}$, and $R_{\rm co}$ from Armeni et al. (2024), the solution of the system is $r = 19.5 \pm 3.4\ R_\star$, where the central value and the uncertainty are obtained from varying r_1 in its range of definition.

Using this value, and $v_z = 77.0$ km s^{-1} and $v_\phi = 29.2$ km s^{-1} from the best fit, the launching radius of the wind can be derived from Eq. (4.4), assuming that the poloidal velocity has only a vertical component. The equation can be solved for the Keplerian velocity $\Omega_{\rm d}$ at the disk launching radius, $r_{\rm d}$. The result is $\Omega_{\rm d} = 3.5 \times 10^{-5}$ s^{-1}, and $r_{\rm d} = 0.026$ AU $= 2.47$ R$_\star$. These values confirm that the LVA originates in a wind launched from close to the disk truncation radius.

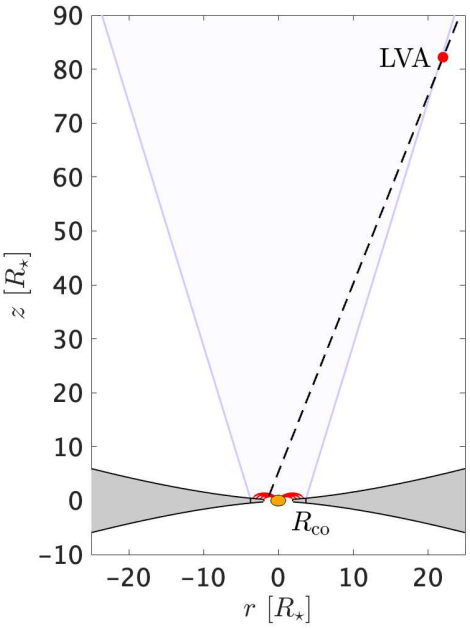

Figure 4.35: Illustration of the origin of the LVA in the wind of RU Lup. The outflow is represented as a truncated cone with a full opening angle of 25° (Birney et al., 2024) that departs from the corotation radius $R_{\rm co}$. The dashed line is the line of sight to the magnetosphere. Adapted from Armeni et al. (2025).

From the separation between the toroidal and vertical components of velocity, I was able to derive the angular momentum per unit mass carried by the wind, $l = r v_\phi$, and the Alfvén radius, related to l as $\Omega_{\rm d} R_{\rm A}^2 = l$ (Sect. 4.3.2.4). For the wind traced by the LVA, the values are $l \approx 6$ AU km s^{-1} and $R_{\rm A} \approx 7.3\ R_\star$.

I repeated the same procedure for the Na I MVA in the ES 22.4 spectrum, which also

shows a double-dipped profile (Fig. 4.33). In this case, I used the Na I D1 line instead of the D2 line because the MVA of the D1 line falls between the redshifted wing of the Na I D2 line and the blueshifted wing of the Na I D1 line, allowing for easy extraction of the local continuum needed for the normalization of the profile. The result of the fit is shown in Fig. 4.34 (right panel). The parameters are $v_z = 151.49 \pm 0.44$ km s^{-1}, $v_\phi = 34.8 \pm 1.8$ km s^{-1}, $\phi_1 = -165 \pm 33$ ^{o}, $\phi_2 = 113 \pm 15$ ^{o}, $\tau_0 = 0.106 \pm 0.002$, and $\sigma = 4.45 \pm 0.04$ km s^{-1}.

Comparing the results obtained for the LVA and the MVA, it emerges that the region in which the MVA originates has higher poloidal and toroidal velocities compared to the LVA gas. Moreover, while the LVA is observed only in Na I, the MVA is strongly optically thick in Ca II. This indicates that the LVA gas is predominantly neutral while the MVA gas is ionized. Therefore, these two DACs likely originate in two different regions of the outflow. According to MHD simulations (Romanova et al., 2009), the gas has higher v_p and v_ϕ closer to the rotation axis. Thus, the MVA component is likely produced in the jet.

Under this assumption, I derived the radial distance at which this DAC is formed by using Eq. (4.6), assuming again that $v_\mathrm{p} \approx v_z$. Using the known value of the stellar angular velocity, $\Omega_\star = 2\pi/P_\star = 1.95 \times 10^{-6}$ s^{-1} (Armeni et al., 2024), the derived velocities v_z and v_ϕ, and the stellar parameters $M_\star$ and $R_\star$ of RU Lup (Sect. 4.2), the result is $r = 0.57$ AU $= 54.1$ R$_\star$. From these values, the angular momentum per unit mass carried by the MVA gas is $l = r v_\phi = 19.8$ AU km s^{-1}. The Alfvén radius can be found from $\Omega_\star R_\mathrm{A}^2 = l$, and it is $R_\mathrm{A} = 7.8\ R_\star$.

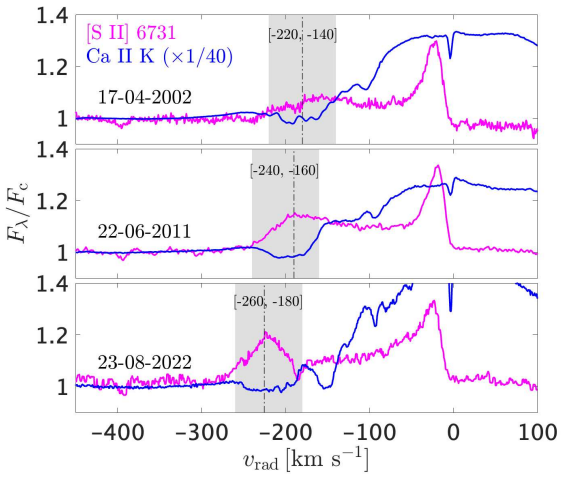

Figure 4.36: Comparison between the Ca II K (blue) and [S II] 6731 (magenta) lines for a selection of spectra of RU Lup, showing the similar evolution of the two components. From the top panel to the bottom panel, the spectra are from UVES (Gahm et al., 2008), ESPaDOnS (Stock et al., 2022), and ESPRESSO (Armeni et al., 2024). From Armeni et al. (2025).

Figure 4.36 presents a comparison between the Ca II K line and the [S II] 6731 line in a selection of spectra for RU Lup, including the ES 22.5 observation supplemented with archival data. The profiles of these two lines exhibit a similar evolutionary behavior, most notably drifting towards higher blueshifted velocities with time. This result indicates a common origin for these two features. Whelan et al. (2021) showed that in RU Lup the HVC component of the FELs is formed in a "knot" of the outflow at a distance of ~ 55 AU from the star. Thus, its counter-

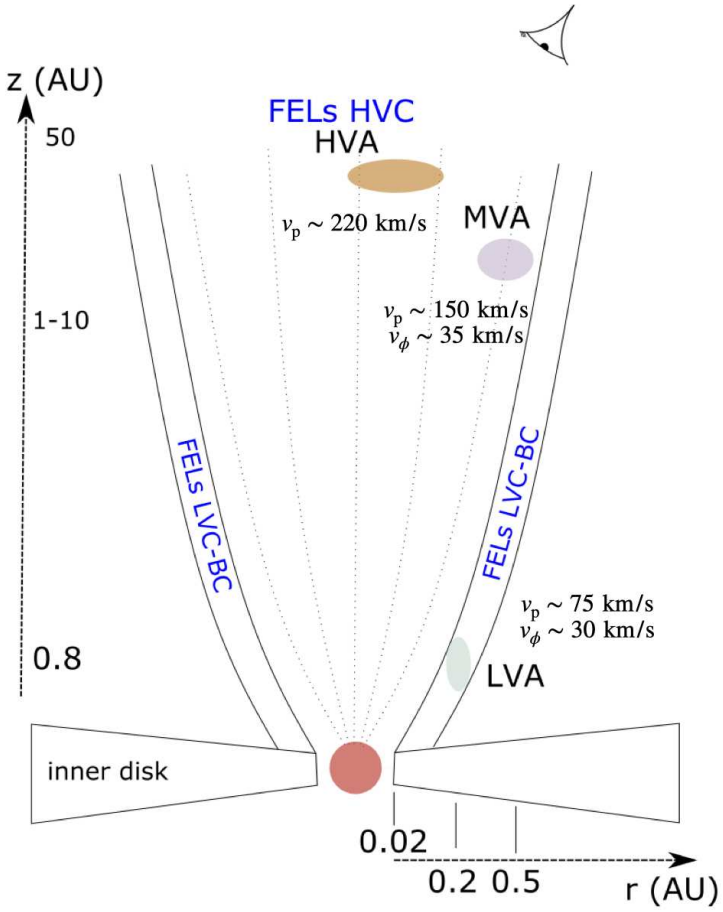

Figure 4.37: Sketch of the "onion-like" structure of the outflow of RU Lup inferred from the analysis of the FELs and the DACs. The figure is not to scale. From Armeni et al. (2025).

part in the profile of Ca II K, i.e., the HVA, likely forms because the knot absorbs against a background region that emits in Ca II. My analysis suggests distinct origins for the HVA component compared to the LVA and MVA components. Specifically, the HVA appears linked to the large-scale, low-density jet structure, whereas the LVA and MVA components likely form within the outflow closer to the launching region.

The structure of the outflow of RU Lup inferred from my analysis of the FELs and the DACs is illustrated in Fig. 4.37. In summary, the high resolution ESPRESSO spectra of RU Lup allowed me to reveal the "onion-like" structure of the outflow proposed in MHD simulations. My analysis of the DACs introduces an innovative methodology that allows the determination of physical properties associated with stellar outflows in the immediate vicinity of the central star, such as the specific angular momentum and the Alfvén radius. These parameters are crucial for constraining the spin-down mechanism in RU Lup, as I will discuss in Sect. 4.5.

4.4 Photometry: timescales and accretion regime

As discussed in Chap. 2, the photometric variability of CTTSs is caused by the stellar hot spots, which are the result of the accretion process. There are two main sources of photometric variability related to a stellar hot spot. The first one is the periodic variability produced by the rotation of a spot on the stellar surface, the so-called rotational modulation. The rotational period of the spot is the main feature that we can derive from the light curves of a CTTS. MHD simulations have shown that this period is either the stellar rotation period (in the stable regime) or related to the Keplerian period at the truncation radius (in the unstable regime, Sect. 3.2). The amplitude of the modulation depends on the flux emitted from the hot spot, that is, on its temperature, size, and latitude on the stellar surface. The second source of photometric variability is the intrinsic variability in the accretion rate, which produces temperature variations in the hot spot, that is, a higher $\dot{M}_{\rm acc}$ produces an overall brighter system.

4.4.1 Observational database

Understanding the photometric variability of CTTSs is crucial for deciphering their accretion dynamics. The analysis of high-cadence light curves has been a key tool in this regard, providing insights into the complex variability patterns exhibited by these stars. For example, Cody et al. (2014, 2022) analyzed light curves of young disk-bearing stars in the NGC 2264 and Taurus star forming region, respectively. Their work revealed a range of variability types that reflect different underlying physical processes and geometric effects. These include “dippers”, which show episodic decreases in brightness likely caused by occultations from circumstellar material passing along our line of sight; “bursters”, which exhibit sudden increases in brightness due to episodic accretion events; and other types of variability related to the interplay of starspots, rotation, and more gradual changes in accretion rate. In addition to these classifications, they also investigated the periodic and quasi-periodic signals present in the light curves, finding a range of characteristic timescales from hours to several days, often associated with stellar rotation or Keplerian orbital periods in the inner disk. The relative importance of these different variability types and timescales provides insights into the structure and dynamics of the inner circumstellar disk and the accretion process.

Analyzing the variability in the frequency spectrum of high-cadence light curves, when compared to 3D MHD simulations of accreting CTTSs, provides a detailed view of the accretion dynamics. The systems discussed in my analysis, TW Hya and RU Lup, have pre-

viously been observed with the *Microvariability and Oscillations of STars* (MOST) satellite. The photometric variability of TW Hya has been discussed in a series of works by Rucinski et al. (2008) and Siwak et al. (2011, 2014). Their analyses revealed a quasi-periodic signal around 3.6 days, attributed to the continuum emission of an accretion hot spot modulated by the stellar rotation. Furthermore, they found evidence for aperiodic variations and flaring events, indicating that the accretion regime of TW Hya transitions between stable and unstable states, influencing the observed light curve morphology.

Siwak et al. (2016) present a detailed photometric analysis of RU Lup using MOST data. Their analysis revealed a complex variability pattern, with the star exhibiting a combination of rotational modulation, likely caused by starspots or accretion hotspots, and irregular variations arising from accretion fluctuations. They identified several periodicities shorter than the stellar rotation period of RU Lup, and suggested that these shorter periodicities could be related to the Keplerian orbital periods of material at specific inner disk radii (approximately 0.02 – 0.03 AU), in accordance with the results of MHD simulations (Sect. 3.2).

Building upon these results, in my work I used the high-cadence data from the *Transiting Exoplanet Survey Satellite* (TESS) to further explore the photometric variability of TW Hya and RU Lup. TESS is a NASA space telescope designed to search for exoplanets using the transit method (Ricker et al., 2014). The mission was originally planned as a two-year all-sky survey, covering approximately 85% of the sky to identify transiting exoplanets around nearby stars.

Figure 4.38: The Transiting Exoplanet Survey Satellite (TESS). From `http://tess.gsfc.nasa.gov/documents/TESS-Litho.pdf`.

The telescope has four identical charged couple device (CCD) cameras and each camera has a $24^o \times 24^o$ field of view. Therefore, the four cameras together can monitor a $24^o \times 96^o$ strip of the sky, called a "Sector". By monitoring each Sector for 27 days, TESS has monitored the southern hemisphere in the first year (or Cycle) and the northern hemisphere in the second year with a total of 26 Sectors, as shown in Fig. 4.39.

TESS was launched on 18 April 18 2018 and the science phase officially started on 25 July 2018. On 5 July 2020, the two-year Primary Mission ended, and the Extended Mission began. During the Extended Mission TESS re-observed both the southern and northern

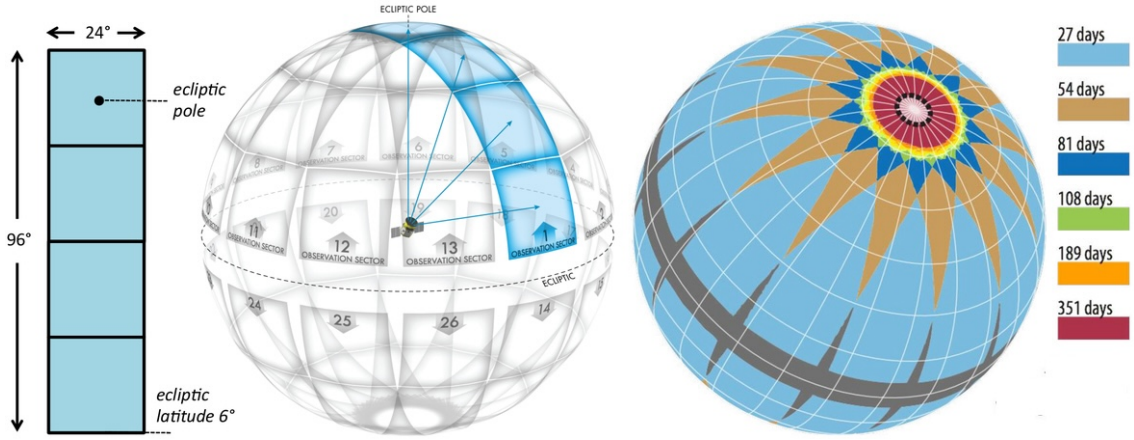

Figure 4.39: TESS observing strategy. Left: the field of view of the four TESS cameras. Center: division of the northern and southern sky hemisphere into Sectors. Right: duration of the observation for different zones of one hemisphere, taking into account the overlap between Sectors. From Ricker et al. (2014).

hemispheres, and for the first time, it covered approximately 60% of the ecliptic plane. Currently, TESS is in the seventh year of its mission and observations are scheduled for the eighth year.

The spectral response of TESS spans a wavelength range from approximately ~ 6000 Å to ~ 10000 Å, centered on the Cousins I_c band with a central wavelength of 7865 Å (Fig. 4.40). This setup is optimized for detecting exoplanetary transits, as the contrast between the planet and its host star is reduced in the red portion of the spectrum. However, the TESS red bandpass limits its ability to capture the full extent of accretion variability, which is often more pronounced at blue wavelengths.

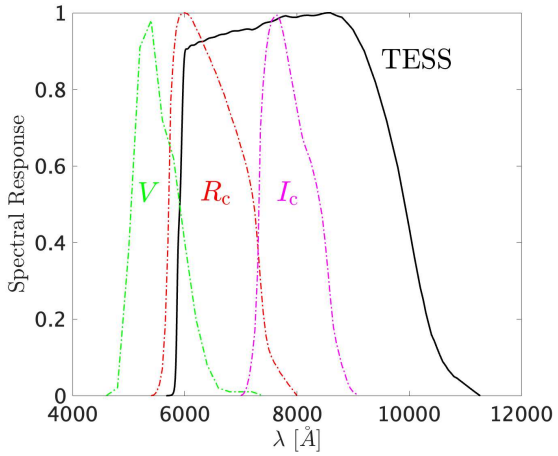

Figure 4.40: TESS spectral response compared to the Johnson V and Cousins R_c and I_c filters.

TESS offers the possibility of recording light curves at high-cadence. The four cameras of TESS take consecutive images every 2 seconds. The two-second data are used for spacecraft guiding but they are not downloaded to the ground. A collection of every single pixel's data that TESS records, i.e., a Full Frame Image (FFI), is obtained by co-adding the individual 2-second exposures. The FFIs have an observational cadence of 30 minutes (Cycles 1 and 2), 10 minutes (Cycles 3 and 4), and 200 seconds

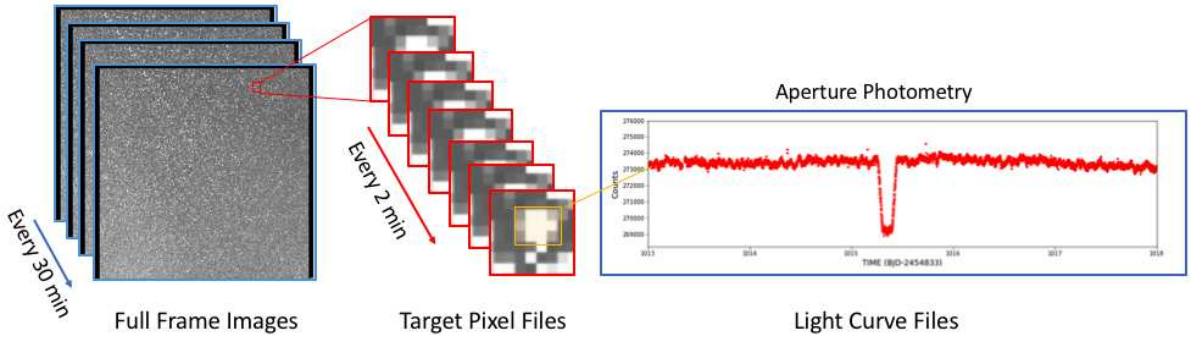

Figure 4.41: Illustration of the different data produced with TESS. From `https://heasarc.gsfc.nasa.gov/docs/tess/data-products.html`.

(from Cycle 5 on). For selected targets, light curves are produced at higher cadences based on a predefined target list. The spacecraft identifies these targets, locates them on the CCDs, and selects small pixel cut-outs around them. During the Primary Mission, these cut-outs were stored with a cadence of 2 minutes. With the first Extended Mission, an additional option for 20-second data products was introduced. Both the FFIs and the cut outs are down-linked. The FFIs are uploaded on the *Mikulski Archive for Space Telescopes* (MAST) archive[1], while the cut-outs are processed by the TESS Science Processing Operations Center (SPOC) into the so-called Target Pixel files (TPF), which can then be transformed into a light curve (LC) by performing aperture photometry. A summary of the TESS data products is shown in Fig. 4.41.

4.4.2 Results

In this section, I analyze the TESS light curves of TW Hya and RU Lup to explore their photometric variability and its implications for the accretion process. The timescales detected in these light curves allowed me to infer the position of the disk truncation radius, providing valuable insights into the dynamics of the star-disk interaction.

4.4.2.1 Unstable accretion in TW Hya

Due to its privileged distance ($d \sim 60$ pc, Gaia Collaboration et al. 2021), TW Hya is one of the best-studied CTTSs. Setiawan et al. (2008) discovered a ~ 0.2 km s^{-1} radial velocity modulation in the photospheric lines of TW Hya with a period of 3.56 days. They also claimed a lack of correlation between the radial velocity variation and the bisector of the

[1] `https://mast.stsci.edu/`

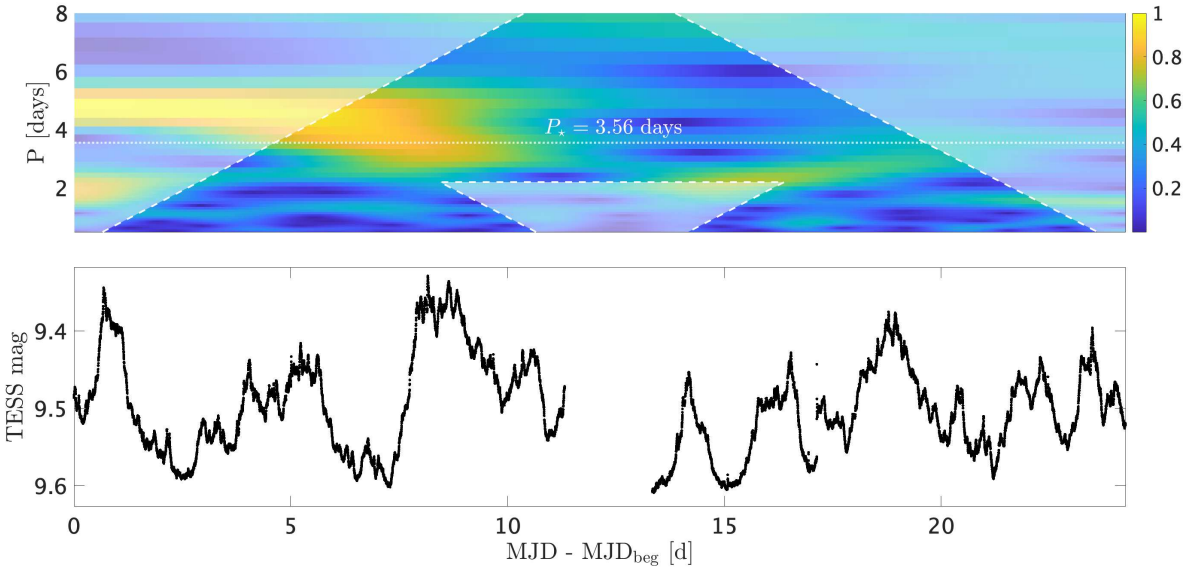

Figure 4.42: TESS Sector 9 light curve of TW Hya (bottom panel) and its CWT (top panel). Here MJD$_{beg}$ = 58543.73.

cross-correlation function. These findings were interpreted as due to the presence of a Hot Jupiter in orbit at a distance of 0.04 AU from the star.

However, Huélamo et al. (2008) showed that a cold spot covering 7% of the stellar surface and located at a latitude of 54^o could also reproduce the reported radial velocity variations, and that the variability of the bisector induced from such a spot would be less than 10 m s^{-1}, below the uncertainty of the radial velocity measurements of Setiawan et al. (2008). Therefore, the authors concluded that the best explanation for the radial velocity signal observed in TW Hya is the presence of a cool stellar spot, that is, the detected period is the stellar rotation period, $P_\star$, of TW Hya. This hypothesis was confirmed by the discovery of a modulation of the radial velocity of the NC of the emission lines, which are produced in a hot spot on the stellar surface (as described in Sect. 2.2), with periods compatible to this value (Sicilia-Aguilar et al., 2023).

Figure 4.42 shows the TESS Sector 9 light curve of TW Hya, together with its wavelet analysis, which I introduced in Sect. 3.2. The contours in the top panel of Fig. 4.42 represent the power spectrum of the light curve as a function of time, the so-called continuous wavelet transform (CWT). The TESS Sector 9 light curve of TW Hya shows two different behaviours. The first one is an oscillation at a period close to, but longer than $P_\star$ which lasts from the beginning of the observation to the gap in the light curve. The second behaviour is a quasi-periodic oscillation at a period shorter than $P_\star$ which seems to begin after the

gap.

The Lomb-Scargle periodogram of this light curve (Fig. 4.43) resembles the predictions of MHD simulations for accretion in the unstable chaotic regime (Fig. 3.6). The peak of the Lomb-Scargle periodogram is at $P_\star$, but there is also power at periods shorter than $P_\star$. These peaks are in agreement with the timescales detected in the CWT after the observational gap. They are typical of RT-unstable accretion and, therefore, indicate accretion from inward of R_{co}.

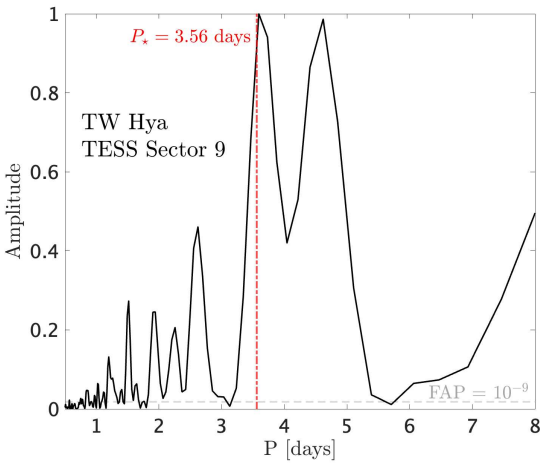

Figure 4.43: Lomb-Scargle periodogram of the TESS Sector 9 light curve of TW Hya of Fig. 4.42. FAP is the False Alarm Probability.

From the known value of $P_\star$, the position of the disk truncation radius can be obtained by inverting Eq. (3.2), i.e.,

$$\frac{R_T}{R_{co}} = \left(\frac{P_T}{P_\star}\right)^{2/3}. \tag{4.9}$$

From the CWT, I estimated $P_T = 1.5-2$ days. This results in $R_T/R_{co} = 0.57-0.68$. Therefore, according to the limits provided by Blinova et al. (2016) (Fig. 3.3), TW Hya was accreting in the unstable regime in the second portion of the TESS Sector 9 light curve.

Donati et al. (2024) performed four epochs of spectro-polarimetric observations of TW Hya in 2019, 2020, 2021, and 2022. Using these data, they reconstructed the magnetic field topology, showing that the stellar magnetic field is predominantly dipolar and its strength varies between 1.0 kG and 1.2 kG. Together with an estimate on the accretion rate, this allows the direct computation of the disk truncation radius (Eq. 2.4). Assuming an average value of $2.5\cdot10^{-9} M_\odot$ yr^{-1} for $\dot{M}_{acc}$ (Herczeg et al., 2023), they derived $R_T = 0.57^{+0.25}_{-0.15}\, R_{co}$, in agreement with the value I obtained from the TESS light curve. This result highlights the importance of high-cadence light curves for determining the position of the disk truncation radius and examining its variability.

4.4.2.2 Evidence for magnetic boundary layer accretion in RU Lup

RU Lup is the strongest accretor in the Lupus star forming region (Fig. 4.2). With a reported accretion rate of 10^{-7} $M_\odot$ yr^{-1} (Manara et al., 2023), the star is likely accreting in the unstable regime (Stock et al., 2022) and we expect to observe quasi-periodic oscillations in high-cadence light curves of this system.

Figure 4.44 shows a TESS 200-s-cadence light curve of RU Lup from Sector 65, together with the epochs of simultaneous spectroscopic observations with CHIRON (introduced in Sect. 4.3.1). The radial velocity modulation of the He I 5876 NC revealed the presence of a hot spot at a latitude of $\sim 70^{o}$ that rotates with the stellar rotation period (Sect. 4.3.3.3). If the TESS light curve traced the variability of the hot spot observed in the He I 5876 NC, one would expect to see a periodic oscillation at $P_{\star}$ with a maximum at phase $\phi_{S} = 0.75$ (Eq. 4.7). This is because ϕ_{S} is a quarter of a period before/after the maximum redshift/blueshift of the hot spot, that is, it is the position where the spot area projected along the line of sight is maximum. However, the variability of the TESS light curve is much more complicated. First, for most cycles the phase ϕ_{S} does not coincide with a maximum in the light curve. Second, the photometric oscillations appear to be at timescales shorter than $P_{\star}$. This is clear, for instance, between the first two blue lines of Fig. 4.44, in which the light curve has three maxima instead of one. Therefore, it can be concluded that the hot spot that traces the He I 5876 NC does not significantly contribute to the continuum emission seen with TESS.

The light curve has two different levels of maximum brightness, with a clear transition at $t \approx 9.15$ days. In the first portion of the light curve, $t \lesssim 9.15$ days, the system reaches 9.5 mag as maximum brightness. In the second portion, $t \gtrsim 9.15$ days, this value is reduced to 9.8 mag. My continuous wavelet analysis of the light curve (Fig. 4.45) confirms that the oscillations are at timescales shorter than $P_{\star}$, and shows that the two portions of the light curve have a different frequency spectrum. The CWT displays QPOs at different periods in the two portions.

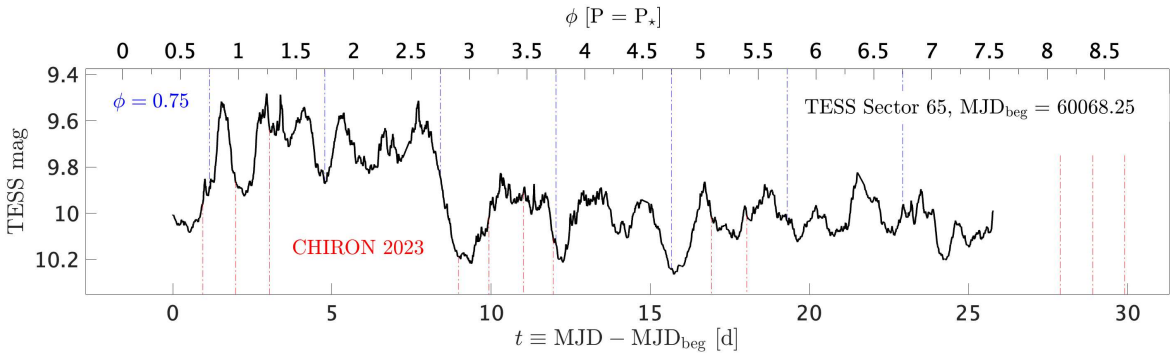

Figure 4.44: TESS light curve of RU Lup from Sector 65 (2023). The top axis shows the phase ϕ computed as explained in Sect. 4.3.3.3. The blue lines mark the phase $\phi_{S} = 0.75$ of Eq. (4.7), obtained from the best fit of the radial velocity modulation of the He I 5876 NC (Fig. 4.26). The red lines mark the epochs of the CHIRON spectroscopic observations. From Armeni et al. (2024).

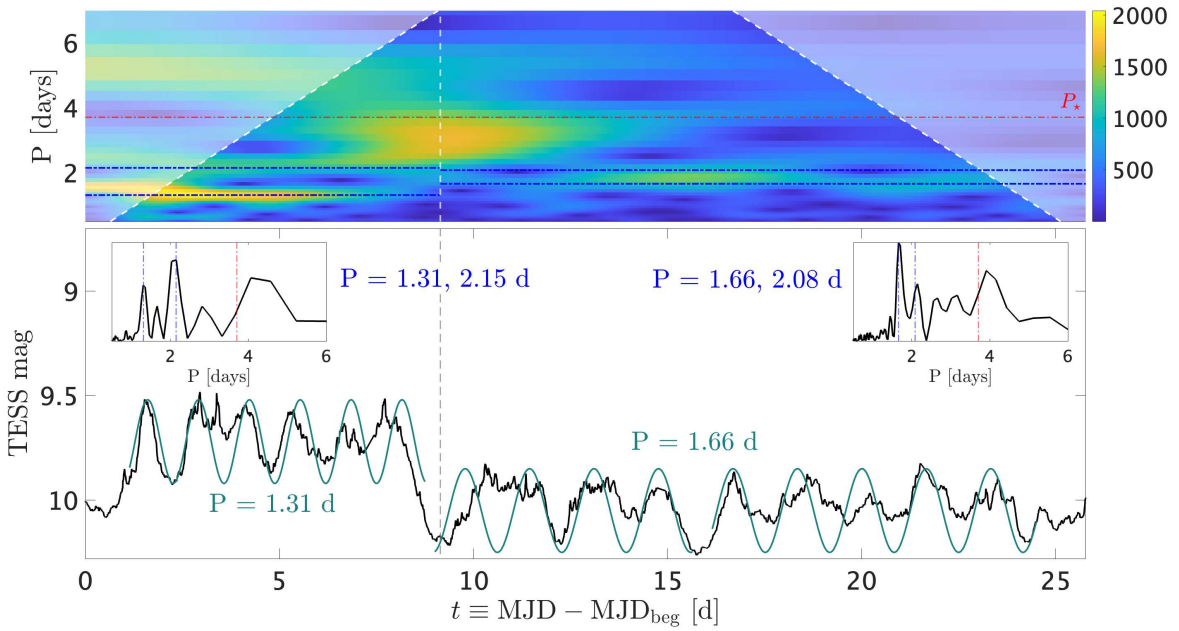

Figure 4.45: Continuous wavelet analysis of the TESS Sector 65 light curve of RU Lup. The insets in the bottom panel show the Lomb-Scargle periodograms for the two portions of the light curve separated by the vertical dashed line. The blue and red lines mark the periods detected in each portion and $P_\star$, respectively. Sinusoidal oscillations at $P = 1.31$ days and 1.61 days are superposed on the light curve in turquoise. From Armeni et al. (2024).

To refine the estimate of the timescales, I computed the Lomb-Scargle periodograms for the two portions of the light curve separately. The periodograms are shown as insets in the bottom panel of Fig. 4.45, and are very similar to what is expected from MHD simulations of accretion in the MBL regime (Fig. 3.7). Unlike the case of TW Hya (Fig. 4.43), most of the power is concentrated at periods shorter than $P_\star$.

In the periodograms, only the two highest peaks at periods shorter than $P_\star$ were considered as relevant. In the first portion of the light curve, these peaks are at $P = 1.31 \pm 0.06$ days and $P = 2.15 \pm 0.14$ days. In the second portion, the peaks are instead at $P = 1.66 \pm 0.07$ days and $P = 2.08 \pm 0.10$ days. For each portion, the timescale detected in the CWT is compatible with the shorter of the two considered periods. Indeed, superposing a sinusoidal function with that period on the relative portion of the light curve (see Fig. 4.45), most of the maxima in the sinusoids match a peak in the TESS light curve. The conclusion is that the typical timescales of the variability are $P_1 = 1.31$ days and $P_2 = 1.66$ days for the first and second portion of the light curve, respectively.

According to MHD simulations, oscillations at timescales shorter than $P_\star$ in the light curve are interpreted as the Keplerian period at R_T. Since the value of $P_\star$ is known for

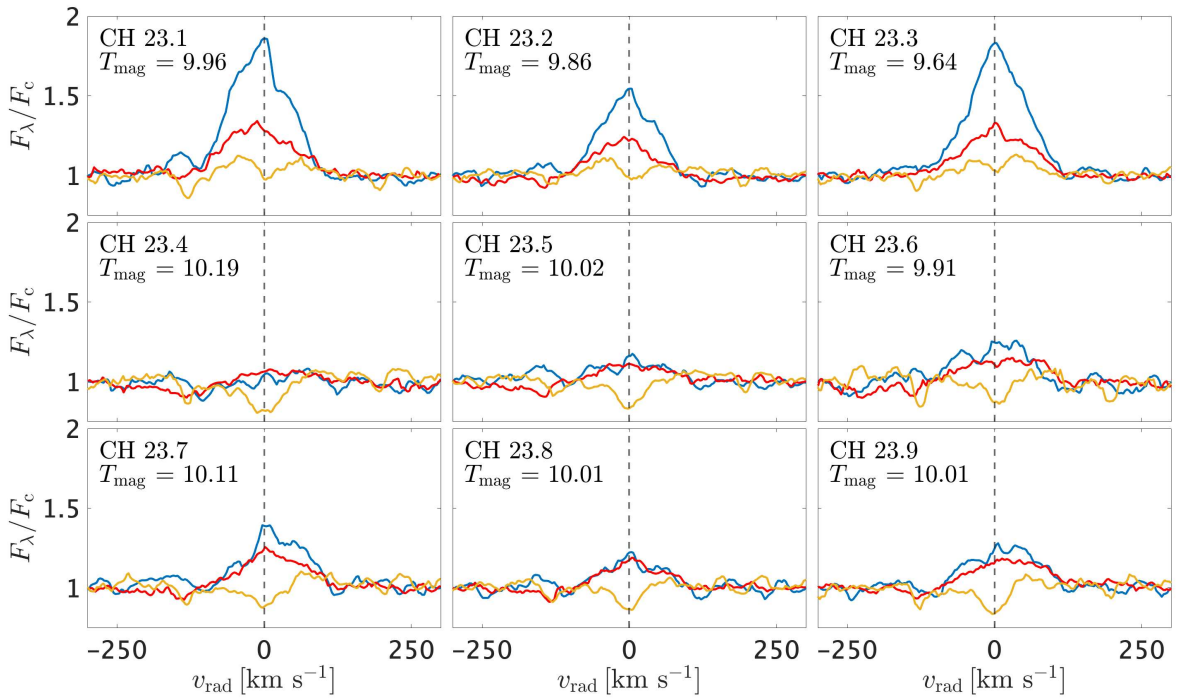

Figure 4.46: Fe I 5447, Si II 6347, and Ca I 6122 normalized line profiles in the 9 CHIRON spectra of RU Lup that are contemporaneous to the TESS light curve of Fig. 4.44. $T_{\rm mag}$ is the TESS magnitude. From Armeni et al. (2024).

RU Lup, P_1 and P_2 can be converted to a ratio between $R_{\rm T}$ and $R_{\rm co}$ (Eq. 4.9). We obtain $R_{\rm T}/R_{\rm co} = 0.50$ and $R_{\rm T}/R_{\rm co} = 0.59$ for the first and second portion of the TESS light curve, respectively. The derived $R_{\rm T}/R_{\rm co}$ ratios indicate that RU Lup accretes in the MBL regime (for which $R_{\rm T}/R_{\rm co} \lesssim 0.59$, Blinova et al. 2016 and Sect. 3.3). Using the stellar parameters of RU Lup (Sect. 4.2) and $P_\star$, the corotation radius is $R_{\rm co} = 3.64\ R_\star$. Therefore, the disk truncation radius is at 1.82 $R_\star$ and 2.15 $R_\star$ in the first and second portion of the light curve, respectively.

The fact that the system is ~ 30% brighter in flux in the first segment, where the detected period is lower, suggests that the variability in the observed periods might be driven by a variation in $\dot{M}_{\rm acc}$. The simultaneous spectroscopic monitoring with CHIRON can be used to check this hypothesis. Figure 4.46 shows the Fe I 5447, Si II 6347, and Ca I 6122 lines in the 9 CHIRON observations that are simultaneous to the TESS light curve (see Fig. 4.44 for the timing of the spectroscopic observations). The first three spectra, which are taken in the portion of the light curve with higher continuum flux, are the ones with stronger line emission. According to the relation between emission line luminosity and accretion luminosity (Sect. 4.3.2.3), this indicates that $\dot{M}_{\rm acc}$ is higher in the first portion of the light

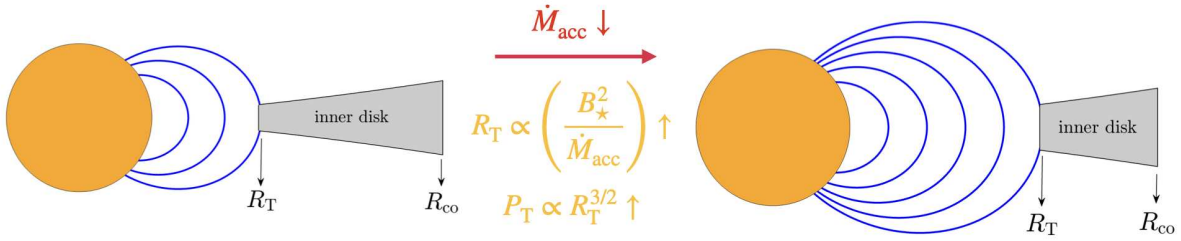

Figure 4.47: Schematic picture of the variability in the truncation radius that leads to the variability in the detected period observed in the TESS light curve of RU Lup.

curve.

Therefore, the variability from the first to the second portion of the TESS light curve is likely caused by a decrease in $\dot{M}_{\rm acc}$. According to Eq. (2.4), this moves $R_{\rm T}$ outward and makes the detected period increase, as sketched in Fig. 4.47. The correlation between the size of the magnetosphere and the detected period in the light curves is also observed in MHD simulations of MBL accretion (Romanova and Kulkarni 2009, and Sect. 3.3), providing further evidence that this accretion regime is operative in RU Lup.

4.5 Spectrophotometric constraints on stellar spin-down

The analysis of the frequency spectrum of high-cadence light curves of CTTSs opens up the possibility of studying the theory of stellar spin-down from observations. In the accretion regime, that is, when $R_{\rm T} < R_{\rm co}$ (Fig. 3.1), the material at $R_{\rm T}$ rotates faster than the star, and the disk transfers angular momentum to the star. Within 1 Myr, the star should be spun up to velocities of ~ 150 km s^{-1} (Hartmann and Stauffer, 1989). The fact that CTTSs rotate at velocities which are one order of magnitude smaller (Chap. 1) indicates that the star must have an efficient way to lose angular momentum. As already discussed at the end of Sect. 2.2, the most promising mechanism is the one in which angular momentum is carried away by magnetic winds, as depicted in Fig. 2.8. The idea is that the higher the accretion rate, the more the shear at the disk-magnetosphere boundary is able to twist the stellar magnetic field lines. These field lines eventually open up and can drive mass and angular momentum loss.

In this framework, light curves help to understand the amount of angular momentum per unit time that is transferred from the disk to the star (or equivalently, the accretion torque), and how this process occurs. The accretion torque, $\tau_{\rm acc}$, is

$$\tau_{\rm acc} = \dot{M}_{\rm acc} \sqrt{G M_\star R_{\rm T}} \tag{4.10}$$

i.e., the accretion rate times the angular momentum per unit mass at R_T (e.g., Matt and Pudritz 2005a; Pantolmos et al. 2020). In systems with known $P_\star$, the detection of a timescale shorter than $P_\star$ allows the computation of R_T. For RU Lup, the value of $\dot{M}_{acc}$ during the TESS Sector 65 observation can be estimated using the He I 5876 line, the luminosity of which is correlated with the accretion luminosity (Sect. 4.3.2.3), in the CH 23.4 spectrum. This spectrum is the only flux-calibrated spectrum among the CHIRON spectra obtained simultaneously with the TESS Sector 65 light curve. To calculate $\dot{M}_{acc}$, I computed the integrated flux of the line and converted it to the line luminosity, L_{line}, using the distance to RU Lup of 158.9 pc (Gaia Collaboration et al., 2021). Using the $L_{line} - L_{acc}$ relation by Alcalá et al. (2017), this value is converted to the accretion luminosity, L_{acc}. From Eq. (2.14) with the parameters of RU Lup, I derived $\dot{M}_{acc} = 1.47 \cdot 10^{-7}\ M_\odot\ \mathrm{yr}^{-1}$. Combining this value with $R_T = 2\ R_\star = 4.54\ R_\odot$ (Sect. 4.4.2.2) and the obtained value of $\dot{M}_{acc}$, the accretion torque is

$$\tau_{acc} = 3.2 \cdot 10^{-7}\ M_\odot\ \mathrm{yr}^{-1}\ \mathrm{AU\ km\ s}^{-1}, \tag{4.11}$$

where $1\ M_\odot\ \mathrm{yr}^{-1}\ \mathrm{AU\ km\ s}^{-1} = 9.46 \cdot 10^{43}\ \mathrm{g\ cm}^2\ \mathrm{s}^{-2}$. This represents the first computation of the accretion torque from the light curve of a CTTS, introducing a novel method to investigate the interaction between the star and its disk. This torque spins up the star on a characteristic timescale $t_{acc} = I_\star \Omega_\star / \tau_{acc}$, where $I_\star = (2/5) M_\star R_\star^2$ is the stellar moment of inertia and $\Omega_\star = 2\pi / P_\star$ is the stellar angular velocity. For RU Lup, this timescale is $t_{acc} \approx 3.57 \cdot 10^4$ yr, much lower than the age of the star ($\sim 2-3$ Myr, Herczeg et al. 2005). This means that in absence of a spin-down mechanism, RU Lup should already rotate at the break-up velocity. Since this is not observed, most of the accretion torque must be balanced by a braking torque provided by the wind.

In the theory of magnetic stellar winds (e.g., Mestel, 1984; Pantolmos et al., 2020), this torque is parameterized as

$$\tau_{wind} = -k \dot{M}_{wind} \Omega_0 R_\star^2 \lambda_M. \tag{4.12}$$

Here, k is a dimensionless parameter of order unity which depends on the geometry of the outflow and is equal to 2/3 in a spherically symmetric wind (Matt and Pudritz, 2005a), $\dot{M}_{wind}$ is the rate of mass loss, Ω_0 is the angular velocity at the base of the flow, and λ_M is the magnetic lever arm. This parameter is defined as $\lambda_M = R_A^2 / R_\star^2$, that is, as the square of the ratio between the Alfvén radius and the stellar radius.

Birney et al. (2024) derived $\dot{M}_{wind} = 4.7 \times 10^{-9}\ M_\odot\ \mathrm{yr}^{-1}$ for the jet traced by the HVC of the FELs of RU Lup. This value was obtained from the luminosity of the [O I] 6300 HVC using the method described in Fang et al. (2018). Assuming that the large-scale jet originates at

the stellar surface, the wind torque can be estimated from Eq. (4.12) using $\Omega_0 = \Omega_\star$, $\lambda_M = 7.8^2 = 60.84$ from the analysis of the MVA (Sect. 4.3.3.4), and $k = 2/3$. The resulting value is $\tau_{wind} = 6.2 \times 10^{-8}\ M_\odot\ \mathrm{yr}^{-1}\ \mathrm{AU\ km\ s}^{-1}$.

Since this value is smaller than τ_{acc} by a factor of ~ 5, it suggests that the portion of the jet traced by the MVA is not effective in spinning down the star. However, the MHD simulations of Romanova et al. (2009) indicate that different regions of the jet carry different amounts of angular momentum away from the star, with the majority being removed by the jet's "backbone", that is, the portion close to the rotation axis (Fig. 3.10). Indeed, the velocities of the MVA ($130-150\ \mathrm{km\ s}^{-1}$, Fig. 4.33) are characteristic of the jet's outer regions rather than its backbone (Figs. 3.9 and 3.10). This suggests that the outflow's launching region includes a high-velocity component (the backbone) that is not detected in absorption in the Na I and Ca II lines. This region differs from the one traced by the HVA, which is unrelated to the jet dynamics close to the launching region, but forms at larger distances from the star. Since it is not possible to determine the mass-loss rate of each outflow component separately, the value of $\dot{M}_{wind}$ from Birney et al. (2024) provides an upper limit on the angular momentum carried away by the backbone of the jet. Assuming this component alone is capable of maintaining the spin equilibrium, and taking again $k = 2/3$ in Eq. (4.12), the magnetic lever arm of the jet's backbone is $\lambda_M \lesssim 313$, meaning its Alfvén radius is $R_A \lesssim 17.7\ R_\star$. Interestingly, the ratio $R_A/R_\star$ is comparable to the solar value, $R_A/R_\odot = 12-16$ (Li, 1999).

Photometric light curves can also reveal how the angular momentum transfer between the star and the disk occurs. In this regard, RU Lup and TW Hya show two different kinds of behaviour. For RU Lup, the TESS light curve suggests that the system is always accreting from much inward of the corotation radius, that is, the disk always spins up the star. On the contrary, the QPOs at $P < P_\star$ are not steady in the TESS light curve of TW Hya, but they alternate with oscillations at $P \approx P_\star$ (as in the first portion of the light curve of Fig. 4.42). This suggests that mass and angular momentum are transferred in "bursts" from the disk to the star in TW Hya.

In summary, combining the spectroscopic analysis of the outflow from the DACs with constraints on the accretion torque derived from the high-cadence TESS light curve of RU Lup has provided valuable insights into the spin-down mechanisms of this strongly accreting young star and, by extension, of CTTSs in general.

CHAPTER 5

CONCLUSIONS AND OUTLOOK

This thesis is focused on spectro-photometric observations of three CTTSs, namely HM Lup, RU Lup, and TW Hya, with the aim of characterizing the environment in the immediate vicinity of the young star. The importance of these systems lies in their unique properties: HM Lup and RU Lup offer a rich emission line spectrum, ideal for studying the accretion flow stratification and the physics of the outflow, while RU Lup and TW Hya are among the most extensively studied CTTSs, providing a solid basis for further research. Additionally, RU Lup benefits from simultaneous spectroscopic and photometric coverage, enabling a comprehensive analysis of its accretion dynamics. The investigation of star-disk interaction in these CTTSs using high-cadence photometry and high-resolution spectroscopy has provided insights into the processes of accretion and ejection mediated by magnetic fields.

The combination of high-resolution spectroscopy and space-based photometry has proven to be a valuable approach for studying the inner disk dynamics and accretion processes. The spectroscopic analysis of the rich emission line spectrum of HM Lup and RU Lup has revealed distinct temperature and density structures within the accretion columns, shedding light on the distribution of material in the magnetospheric flow. The variability observed in the high-cadence TESS light curves of TW Hya and RU Lup made it possible to derive the disk truncation radii in these two systems and to study how its variability is linked to the accretion rate. The study of the outflow of RU Lup through the FELs and the DACs provided constraints on the angular momentum removal mechanisms operating in the system. Combining these data with the insights on accretion torque derived from the TESS light curve provided a direct link to the regulation of the stellar rotation rate, con-

straining the mechanism of angular momentum loss through winds.

Despite these advancements, several open questions remain. The key challenge is certainly to understand the connection between the mechanisms of accretion and ejection. While accretion and mass loss are known to be intrinsically linked, the exact processes regulating this interaction remain uncertain. Investigating how outflows contribute to angular momentum removal and how they influence the evolution of the star-disk system is crucial for a complete understanding of CTTSs.

As a future perspective, spectroscopy and photometry remain essential tools for probing the structure and variability of the immediate surroundings of young stars. Simultaneous monitoring of young stars using these two techniques will enable the study of how changes in the accretion rate are linked to the variability of the truncation radius, as well as the mechanisms by which angular momentum is accreted and/or dispersed from the system. To gain a comprehensive understanding, it is crucial to conduct simultaneous monitoring of young stars across a diverse range of parameters, including different evolutionary stages, magnetic field strengths, stellar inclinations, and system geometries.

These techniques must be used together with high angular resolution imaging to bridge the gap between small-scale accretion dynamics and the larger-scale outflow structures. For example, combining time-resolved spectroscopy with spatially resolved imaging of outflows would allow for a direct correlation between accretion-driven variability and the kinematics and geometry of ejected material. Such a synergy could reveal how episodic accretion events, detected via photometric bursts or spectroscopic line variability, trigger or modulate outflow activity, providing direct observational links between angular momentum transport in the disk and large-scale mass-loss processes.

BIBLIOGRAPHY

Agapitou, V. and Papaloizou, J. C. B. (2000).
Accretion disc-stellar magnetosphere interaction: field line inflation and the effect on the spin-down torque.
Monthly Notices of the Royal Astronomical Society, 317(2):273–288.

Alcalá, J. M., Manara, C. F., Natta, A., et al. (2017).
X-shooter spectroscopy of young stellar objects in Lupus. Accretion properties of class II and transitional objects.
Astronomy & Astrophysics, 600:A20.

Alcalá, J. M., Natta, A., Manara, C. F., et al. (2014).
X-shooter spectroscopy of young stellar objects. IV. Accretion in low-mass stars and substellar objects in Lupus.
Astronomy & Astrophysics, 561:A2.

ALMA Partnership et al. (2015).
The 2014 ALMA Long Baseline Campaign: First Results from High Angular Resolution Observations toward the HL Tau Region.
Astrophysical Journal Letters, 808(1):L3.

Ambartsumian, V. A. (1947).
The evolution of stars and astrophysics.

Anderson, J. M., Li, Z.-Y., Krasnopolsky, R., and Blandford, R. D. (2003).
Locating the Launching Region of T Tauri Winds: The Case of DG Tauri.
Astrophysical Journal Letters, 590(2):L107–L110.

André, P. (2002).
The Initial Conditions for Protostellar Collapse: Observational Constraints.
In *Star Formation and the Physics of Young Stars*, volume 3 of *EAS Publications Series*, pages 1–38.

Ansdell, M., Williams, J. P., Trapman, L., et al. (2018).
ALMA Survey of Lupus Protoplanetary Disks. II. Gas Disk Radii.
Astrophysical Journal, 859(1):21.

Ansdell, M., Williams, J. P., van der Marel, N., et al. (2016).
ALMA Survey of Lupus Protoplanetary Disks. I. Dust and Gas Masses.
Astrophysical Journal, 828(1):46.

Appenzeller, I. and Wolf, B. (1977).
S CrA: a bright southern YY Orionis star.
Astronomy & Astrophysics, 54:713–722.

Ardila, D. R., Herczeg, G. J., Gregory, S. G., et al. (2013).
Hot Gas Lines in T Tauri Stars.
Astrophysical Journal, 207:1.

Armeni, A., Stelzer, B., Claes, R. A. B., et al. (2023).
PENELLOPE. V. The magnetospheric structure and the accretion variability of the classical T Tauri star HM Lup.
Astronomy & Astrophysics, 679:A14.

Armeni, A., Stelzer, B., Frasca, A., et al. (2024).
Evidence for magnetic boundary layer accretion in RU Lup: A spectrophotometric analysis.
Astronomy & Astrophysics, 690:A225.

Armeni, A., Stelzer, B., Frasca, A., et al. (2025).
Spinning-down RU Lup: Constraints on the physics of the outflow from high-resolution spectroscopy.
Submitted to Astronomy & Astrophysics.

Arons, J. and Lea, S. M. (1976).
Accretion onto magnetized neutron stars: structure and interchange instability of a model magnetosphere.
Astrophysical Journal, 207:914–936.

Bacciotti, F., Ray, T. P., Mundt, R., et al. (2002).
Hubble Space Telescope/STIS Spectroscopy of the Optical Outflow from DG Tauri: Indications for Rotation in the Initial Jet Channel.
Astrophysical Journal, 576(1):222–231.

Bacon, R., Accardo, M., Adjali, L., et al. (2010).
The MUSE second-generation VLT instrument.
In McLean, I. S., Ramsay, S. K., and Takami, H., editors, *Ground-based and Airborne Instrumentation for Astronomy III*, volume 7735 of *Society of Photo-Optical Instrumentation Engineers (SPIE) Conference Series*, page 773508.

Balbus, S. A. (2003).
Enhanced Angular Momentum Transport in Accretion Disks.
Annual Review of Astronomy & Astrophysics, 41:555–597.

Balbus, S. A. and Hawley, J. F. (1991).
A Powerful Local Shear Instability in Weakly Magnetized Disks. I. Linear Analysis.
Astrophysical Journal, 376:214.

Banzatti, A., Pascucci, I., Edwards, S., et al. (2019).
Kinematic Links and the Coevolution of MHD Winds, Jets, and Inner Disks from a High-resolution Optical [O I] Survey.
Astrophysical Journal, 870:76.

Beristain, G., Edwards, S., and Kwan, J. (1998).
Permitted Iron Emission Lines in the Classical T Tauri Star DR Tauri.
Astrophysical Journal, 499(2):828–852.

Beristain, G., Edwards, S., and Kwan, J. (2001).
Helium Emission from Classical T Tauri Stars: Dual Origin in Magnetospheric Infall and Hot Wind.
Astrophysical Journal, 551(2):1037–1064.

Bertout, C. (1989).
T Tauri stars: wild as dust.
Annual Review of Astronomy & Astrophysics, 27:351–395.

Bertout, C. (2024).
Spectral line fluorescence in moving envelopes of stars: I. Theoretical background, numerical code, and proof of concept.
Astronomy & Astrophysics, 689:A71.

Bertout, C., Basri, G., and Bouvier, J. (1988).
Accretion Disks around T Tauri Stars.
Astrophysical Journal, 330:350.

Birney, M., Whelan, E. T., Dougados, C., et al. (2024).
Forbidden emission line spectro-imaging of the RU Lupi jet and low-velocity component.
Astronomy & Astrophysics, 692:L5.

Blinova, A. A., Romanova, M. M., and Lovelace, R. V. E. (2016).
Boundary between stable and unstable regimes of accretion. Ordered and chaotic unstable regimes.
Monthly Notices of the Royal Astronomical Society, 459:2354–2369.

Bouvier, J., Alencar, S. H. P., Harries, T. J., et al. (2007).
Magnetospheric Accretion in Classical T Tauri Stars.
In Reipurth, B., Jewitt, D., and Keil, K., editors, *Protostars and Planets V*, page 479.

Bouvier, J., Cabrit, S., Fernandez, M., et al. (1993).
COYOTES I: the photometric variability and rotational evolution of T Tauri stars.
Astronomy & Astrophysics, 272:176–206.

Bouvier, J., Covino, E., Kovo, O., et al. (1995).
COYOTES II: SPOT properties and the origin of photometric period variations in T Tauri stars.
Astronomy & Astrophysics, 299:89.

Bouvier, J., Matt, S. P., Mohanty, S., et al. (2014).
Angular Momentum Evolution of Young Low-Mass Stars and Brown Dwarfs: Observations and Theory.
In *Protostars and Planets VI*, page 433.

Bouvier, J., Wichmann, R., Grankin, K., et al. (1997).
COYOTES IV: the rotational periods of low-mass Post-T Tauri stars in Taurus.
Astronomy & Astrophysics, 318:495–505.

Brandenburg, A., Nordlund, A., Stein, R. F., and Torkelsson, U. (1996).
The Disk Accretion Rate for Dynamo-generated Turbulence.
Astrophysical Journal Letters, 458:L45.

Calvet, N. and Gullbring, E. (1998).
The Structure and Emission of the Accretion Shock in T Tauri Stars.
Astrophysical Journal, 509(2):802–818.

Calvet, N. and Hartmann, L. (1992).
Balmer Line Profiles for Infalling T Tauri Envelopes.
Astrophysical Journal, 386:239.

Calvet, N., Muzerolle, J., Briceño, C., et al. (2004).
The Mass Accretion Rates of Intermediate-Mass T Tauri Stars.
Astronomical Journal, 128(3):1294–1318.

Campbell-White, J., Sicilia-Aguilar, A., Manara, C. F., et al. (2021).
The STAR-MELT PYTHON package for emission-line analysis of YSOs.
Monthly Notices of the Royal Astronomical Society, 507(3):3331–3350.

Cardelli, J. A., Clayton, G. C., and Mathis, J. S. (1989).
The Relationship between Infrared, Optical, and Ultraviolet Extinction.
Astrophysical Journal, 345:245.

Chandrasekhar, S. (1960).
The Stability of Non-Dissipative Couette Flow in Hydromagnetics.
Proceedings of the National Academy of Science, 46(2):253–257.

Chandrasekhar, S. (1961).
Hydrodynamic and hydromagnetic stability.
International Series of Monographs on Physics.

Cody, A. M., Hillenbrand, L. A., and Rebull, L. M. (2022).
The Many-faceted Light Curves of Young Disk-bearing Stars in Taurus as Seen by K2.
Astronomical Journal, 163(5):212.

Cody, A. M., Stauffer, J., Baglin, A., et al. (2014).
CSI 2264: Simultaneous Optical and Infrared Light Curves of Young Disk-bearing Stars in NGC 2264 with CoRoT and Spitzer—Evidence for Multiple Origins of Variability.
Astronomical Journal, 147(4):82.

Dekker, H., D'Odorico, S., Kaufer, A., et al. (2000).
Design, construction, and performance of UVES, the echelle spectrograph for the UT2 Kueyen Telescope at the ESO Paranal Observatory.
In Iye, M. and Moorwood, A. F., editors, *Optical and IR Telescope Instrumentation and Detectors*, volume 4008 of *Society of Photo-Optical Instrumentation Engineers (SPIE) Conference Series*, pages 534–545.

Dodin, A. V. and Lamzin, S. A. (2012).
Interpretation of the veiling of the photospheric spectrum for T Tauri stars in terms of an accretion model.
Astronomy Letters, 38(10):649–666.

Donaldson, J. K., Weinberger, A. J., Gagné, J., et al. (2016).
New Parallaxes and a Convergence Analysis for the TW Hya Association.
Astrophysical Journal, 833(1):95.

Donati, J. F., Cristofari, P. I., Lehmann, L. T., et al. (2024).
SPIRou spectropolarimetry of the T Tauri star TW Hydrae: magnetic fields, accretion, and planets.
Monthly Notices of the Royal Astronomical Society, 531:3256–3278.

Edwards, S., Fischer, W., Kwan, J., et al. (2003).
He I λ10830 as a Probe of Winds in Accreting Young Stars.
Astrophysical Journal Letters, 599(1):L41–L44.

Edwards, S., Ray, T., and Mundt, R. (1993).
Energetic Mass Outflows from Young Stars.
In Levy, E. H. and Lunine, J. I., editors, *Protostars and Planets III*, page 567.

Erkal, J., Manara, C. F., Schneider, P. C., et al. (2022).
The He I λ10830 Å line as a probe of winds and accretion in young stars in Lupus and Upper Scorpius.
Astronomy & Astrophysics, 666:A188.

Espaillat, C. C., Herczeg, G. J., Thanathibodee, T., et al. (2022).
The ODYSSEUS Survey. Motivation and First Results: Accretion, Ejection, and Disk Irradiation of CVSO 109.
Astronomical Journal, 163(3):114.

Fang, M., Pascucci, I., Edwards, S., et al. (2018).
A New Look at T Tauri Star Forbidden Lines: MHD-driven Winds from the Inner Disk.
Astrophysical Journal, 868(1):28.

Feigelson, E., Townsley, L., Güdel, M., and Stassun, K. (2007).
X-Ray Properties of Young Stars and Stellar Clusters.
In Reipurth, B., Jewitt, D., and Keil, K., editors, *Protostars and Planets V*, page 313.

Ferreira, J., Dougados, C., and Cabrit, S. (2006).
Which jet launching mechanism(s) in T Tauri stars?
Astronomy & Astrophysics, 453(3):785–796.

Frank, J., King, A., and Raine, D. (2002).
Accretion Power in Astrophysics.
Cambridge University Press, 3 edition.

Frasca, A., Biazzo, K., Alcalá, J. M., Manara, C. F., et al. (2017).
X-shooter spectroscopy of young stellar objects in Lupus. Atmospheric parameters, membership, and activity diagnostics.
Astronomy & Astrophysics, 602:A33.

Frasca, A., Biazzo, K., Lanzafame, A. C., et al. (2015).
The Gaia-ESO Survey: Chromospheric emission, accretion properties, and rotation in γ Velorum and Chamaeleon I.
Astronomy & Astrophysics, 575:A4.

Gahm, G. F. (2001).
Probing Unusual Processes from Spectra of Young Stars.
In Gull, T. R., Johannson, S., and Davidson, K., editors, *Eta Carinae and Other Mysterious Stars: The Hidden Opportunities of Emission Spectroscopy*, volume 242 of *Astronomical Society of the Pacific Conference Series*, page 263.

Gahm, G. F., Stempels, H. C., Walter, F. M., et al. (2013).
Face to phase with RU Lupi.
Astronomy & Astrophysics, 560:A57.

Gahm, G. F., Walter, F. M., Stempels, H. C., et al. (2008).
Unveiling extremely veiled T Tauri stars.
Astronomy & Astrophysics, 482(3):L35–L38.

Gaia Collaboration et al. (2021).
Gaia Early Data Release 3. Summary of the contents and survey properties.
Astronomy & Astrophysics, 649:A1.

Ghosh, P. and Lamb, F. K. (1978).
Disk accretion by magnetic neutron stars.
Astrophysical Journal, 223:L83–L87.

Ghosh, P., Lamb, F. K., and Pethick, C. J. (1977).
Accretion by rotating magnetic neutron stars. I. Flow of matter inside the magnetosphere and its implications for spin-up and spin-down of the star.
Astrophysical Journal, 217:578–596.

GRAVITY Collaboration et al. (2017).
First light for GRAVITY: Phase referencing optical interferometry for the Very Large Telescope Interferometer.
Astronomy & Astrophysics, 602:A94.

Gravity Collaboration et al. (2020).
A measure of the size of the magnetospheric accretion region in TW Hydrae.
Nature, 584(7822):547–550.

Guenther, E. W., Lehmann, H., Emerson, J. P., and Staude, J. (1999).
Measurements of magnetic field strength on T Tauri stars.
Astronomy & Astrophysics, 341:768–783.

Gullbring, E., Calvet, N., Muzerolle, J., and Hartmann, L. (2000).
The Structure and Emission of the Accretion Shock in T Tauri Stars. II. The Ultraviolet-Continuum Emission.
Astrophysical Journal, 544:927–932.

Gullbring, E., Hartmann, L., Briceño, C., and Calvet, N. (1998).
Disk Accretion Rates for T Tauri Stars.
Astrophysical Journal, 492(1):323–341.

Hartigan, P., Edwards, S., and Ghandour, L. (1995).
Disk Accretion and Mass Loss from Young Stars.
Astrophysical Journal, 452:736.

Hartigan, P., Hartmann, L., Kenyon, S., et al. (1989).
How to Unveil a T Tauri Star.
Astrophysical Journal, 70:899.

Hartmann, L. (2008).
Accretion Processes in Star Formation.
Cambridge Astrophysics. Cambridge University Press, 2nd edition.

Hartmann, L., Herczeg, G., and Calvet, N. (2016).
Accretion onto pre-main-sequence stars.
Annual Review of Astronomy & Astrophysics, 54:135–180.

Hartmann, L., Hewett, R., and Calvet, N. (1994).
Magnetospheric Accretion Models for T Tauri Stars. I. Balmer Line Profiles without Rotation.
Astrophysical Journal, 426:669.

Hartmann, L. and Stauffer, J. R. (1989).
Additional Measurements of Pre-Main-Sequence Stellar Rotation.
Astronomical Journal, 97:873.

Helmholtz, H. (1868).
Xliii. on discontinuous movements of fluids.
The London, Edinburgh, and Dublin Philosophical Magazine and Journal of Science, 36(244):337–346.

Herbig, G. H. (1945).
Emission Lines of Fe I in RW Aurigae.
Publications of the Astronomical Society of the Pacific, 57:166.

Herbig, G. H. (1960).
The Spectra of Be- and Ae-Type Stars Associated with Nebulosity.
Astrophysical Journal Supplement, 4:337.

Herbig, G. H. (1962).
The Properties and Problems of T Tauri Stars and Related Objects.
Advances in Astronomy & Astrophysics, 1:47–103.

Herbst, W., Herbst, D. K., Grossman, E. J., and Weinstein, D. (1994).
Catalogue of UBVRI Photometry of T Tauri Stars and Analysis of the Causes of Their Variability.
Astronomical Journal, 108:1906.

Herczeg, G. J., Chen, Y., Donati, J.-F., et al. (2023).
Twenty-five Years of Accretion onto the Classical T Tauri Star TW Hya.
Astrophysical Journal, 956(2):102.

Herczeg, G. J. and Hillenbrand, L. A. (2008).
UV Excess Measures of Accretion onto Young Very Low Mass Stars and Brown Dwarfs.
Astrophysical Journal, 681:594–625.

Herczeg, G. J., Walter, F. M., Linsky, J. L., et al. (2005).
The Loopy Ultraviolet Line Profiles of RU Lupi: Accretion, Outflows, and Fluorescence.
Astronomical Journal, 129(6):2777–2791.

Heyvaerts, J., Priest, E. R., and Bardou, A. (1996).
Magnetic Field Diffusion in Self-consistently Turbulent Accretion Disks.
Astrophysical Journal, 473:403.

Hirose, S., Uchida, Y., Shibata, K., and Matsumoto, R. (1997).
Disk Accretion onto a Magnetized Young Star and Associated Jet Formation.
Publications of the Astronomical Society of Japan, 49:193–205.

Hirth, G. A., Mundt, R., and Solf, J. (1997).
Spatial and kinematic properties of the forbidden emission line region of T Tauri stars.
Astronomy & Astrophysics Supplement Series, 126:437–469.

Huélamo, N., Figueira, P., Bonfils, X., et al. (2008).
TW Hydrae: evidence of stellar spots instead of a Hot Jupiter.
Astronomy & Astrophysics, 489:L9–L13.

Ingleby, L., Calvet, N., Herczeg, G., et al. (2013).
Accretion Rates for T Tauri Stars Using Nearly Simultaneous Ultraviolet and Optical Spectra.
Astrophysical Journal, 767(2):112.

Jeans, J. H. (1902).
The Stability of a Spherical Nebula.
Philosophical Transactions of the Royal Society of London Series A, 199:1–53.

Johns-Krull, C. M., Valenti, J. A., Hatzes, A. P., and Kanaan, A. (1999).
Spectropolarimetry of Magnetospheric Accretion on the Classical T Tauri Star BP Tauri.
Astrophysical Journal, 510(1):L41–L44.

Johns-Krull, C. M., Valenti, J. A., Piskunov, N. E., et al. (2001).
New Measurements of T Tauri Magnetic Fields: Testing Magnetospheric Accretion.

In *Magnetic Fields Across the Hertzsprung-Russell Diagram*, volume 248 of *Astronomical Society of the Pacific Conference Series*, page 527.

Joy, A. H. (1945).
T Tauri Variable Stars.
Astrophysical Journal, 102:168.

Kelvin, L. (1871).
Hydrokinetic solutions and observations.
Philosophical Magazine, 42:362–377.

Koldoba, A. V., Lovelace, R. V. E., Ustyugova, G. V., and Romanova, M. M. (2002).
Funnel Flows from Disks to Magnetized Stars.
Astronomical Journal, 123(4):2019–2026.

Königl, A. (1991).
Disk Accretion onto Magnetic T Tauri Stars.
Astrophysical Journal Letters, 370:L39.

Kulkarni, A. K. and Romanova, M. M. (2008).
Accretion to magnetized stars through the Rayleigh-Taylor instability: global 3D simulations.
Monthly Notices of the Royal Astronomical Society, 386:673–687.

Kulkarni, A. K. and Romanova, M. M. (2009).
Possible quasi-periodic oscillations from unstable accretion: 3D magnetohydrodynamic simulations.
Monthly Notices of the Royal Astronomical Society, 398(2):701–714.

Kulkarni, A. K. and Romanova, M. M. (2013).
Analytical hotspot shapes and magnetospheric radius from 3D simulations of magnetospheric accretion.
Monthly Notices of the Royal Astronomical Society, 433(4):3048–3061.

Kwan, J. and Tademaru, E. (1988).
Jets from T Tauri Stars: Spectroscopic Evidence and Collimation Mechanism.
Astrophysical Journal Letters, 332:L41.

Lada, C. J. (1987).
Star formation: from OB associations to protostars.

In *Star Forming Regions*, volume 115 of *IAU Symposium*, page 1.

Lamers, H. J. and Cassinelli, J. P. (1999).
Introduction to Stellar Winds.
Cambridge University Press.

Landau, L. D. and Lifshitz, E. M. (1959).
Fluid mechanics.

Lesur, G. R. J. (2021).
Systematic description of wind-driven protoplanetary discs.
Astronomy & Astrophysics, 650:A35.

Li, J. (1999).
Magnetic braking of the present Sun.
Monthly Notices of the Royal Astronomical Society, 302(1):203–208.

Lomb, N. R. (1976).
Least-Squares Frequency Analysis of Unequally Spaced Data.
Astrophysics and Space Science, 39(2):447–462.

Lovelace, R. V. E., Mehanian, C., Mobarry, C. M., and Sulkanen, M. E. (1986).
Theory of Axisymmetric Magnetohydrodynamic Flows: Disks.
Astrophysical Journal Supplement, 62:1.

Lynden-Bell, D. and Pringle, J. E. (1974).
The evolution of viscous discs and the origin of the nebular variables.
Monthly Notices of the Royal Astronomical Society, 168:603–637.

Manara, C. F., Ansdell, M., Rosotti, G. P., et al. (2023).
Demographics of Young Stars and their Protoplanetary Disks: Lessons Learned on Disk Evolution and its Connection to Planet Formation.
In Inutsuka, S., Aikawa, Y., Muto, T., Tomida, K., and Tamura, M., editors, *Protostars and Planets VII*, volume 534, page 539.

Manara, C. F., Beccari, G., Da Rio, N., et al. (2013).
Accurate determination of accretion and photospheric parameters in young stellar objects: The case of two candidate old disks in the Orion Nebula Cluster.
Astronomy & Astrophysics, 558:A114.

Manara, C. F., Frasca, A., Venuti, L., et al. (2021).
PENELLOPE: The ESO data legacy program to complement the Hubble UV Legacy Library of Young Stars (ULLYSES). I. Survey presentation and accretion properties of Orion OB1 and σ-Orionis.
Astronomy & Astrophysics, 650:A196.

Matt, S. and Pudritz, R. E. (2005a).
Accretion-powered Stellar Winds as a Solution to the Stellar Angular Momentum Problem.
Astrophysical Journal, 632(2):L135–L138.

Matt, S. and Pudritz, R. E. (2005b).
The spin of accreting stars: dependence on magnetic coupling to the disc.
Monthly Notices of the Royal Astronomical Society, 356(1):167–182.

McGinnis, P., Bouvier, J., and Gallet, F. (2020).
The magnetic obliquity of accreting T Tauri stars.
Monthly Notices of the Royal Astronomical Society, 497(2):2142–2162.

Mestel, L. (1968).
Magnetic braking by a stellar wind-I.
Monthly Notices of the Royal Astronomical Society, 138:359.

Mestel, L. (1984).
Angular Momentum Loss During Pre-Main Sequence Contraction.
In Baliunas, S. L. and Hartmann, L., editors, *Cool Stars, Stellar Systems, and the Sun*, volume 193, page 49.

Miller, K. A. and Stone, J. M. (1997).
MHD Simulations of Stellar Magnetosphere - Accretion Disk Interaction.
In *American Astronomical Society, 191st AAS Meeting*, volume 29 of *Bulletin of the American Astronomical Society*, page 1214.

Mundt, R. (1984).
Mass loss in T Tauri stars : observational studies of the cool parts of their stellar winds and expanding shells.
Astrophysical Journal, 280:749–770.

Muzerolle, J., Calvet, N., and Hartmann, L. (2001).

Emission-Line Diagnostics of T Tauri Magnetospheric Accretion. II. Improved Model Tests and Insights into Accretion Physics.
Astrophysical Journal, 550:944–961.

Muzerolle, J., Hartmann, L., and Calvet, N. (1998).
Emission-Line Diagnostics of T Tauri Magnetospheric Accretion. I. Line Profile Observations.
Astronomical Journal, 116:455–468.

Najita, J. R., Edwards, S., Basri, G., and Carr, J. (2000).
Spectroscopy of Inner Protoplanetary Disks and the Star-Disk Interface.
In Mannings, V., Boss, A. P., and Russell, S. S., editors, *Protostars and Planets IV*, page 457.

Natta, A., Testi, L., Alcalá, J. M., et al. (2014).
X-shooter spectroscopy of young stellar objects. V. Slow winds in T Tauri stars.
Astronomy & Astrophysics, 569:A5.

Osterbrock, D. E. and Ferland, G. J. (2006).
Astrophysics of gaseous nebulae and active galactic nuclei.
University Science Books.

Pantolmos, G., Zanni, C., and Bouvier, J. (2020).
Magnetic torques on T Tauri stars: Accreting versus non-accreting systems.
Astronomy & Astrophysics, 643:A129.

Pascucci, I., Cabrit, S., Edwards, S., et al. (2023).
The Role of Disk Winds in the Evolution and Dispersal of Protoplanetary Disks.
In Inutsuka, S., Aikawa, Y., Muto, T., Tomida, K., and Tamura, M., editors, *Protostars and Planets VII*, volume 534 of *Astronomical Society of the Pacific Conference Series*, page 567.

Pepe, F., Cristiani, S., Rebolo, R., et al. (2021).
ESPRESSO at VLT. On-sky performance and first results.
Astronomy & Astrophysics, 645:A96.

Petrov, P. P., Gahm, G. F., Gameiro, J. F., et al. (2001).
Non-axisymmetric accretion on the classical TTS RW Aur A.
Astronomy & Astrophysics, 369:993–1008.

Petrov, P. P., Gahm, G. F., Herczeg, G. J., et al. (2014a).
Doppler probe of accretion onto a T Tauri star.

Astronomy & Astrophysics, 568:L10.

Petrov, P. P., Gahm, G. F., Stempels, H. C., et al. (2011).
Accretion-powered chromospheres in classical T Tauri stars.
Astronomy & Astrophysics, 535:A6.

Petrov, P. P., Kurosawa, R., Romanova, M. M., et al. (2014b).
Facing the wind of the pre-FUor V1331 Cyg.
Monthly Notices of the Royal Astronomical Society, 442(4):3643–3652.

Pringle, J. E. (1977).
Soft X-ray emission from dwarf novae.
Monthly Notices of the Royal Astronomical Society, 178:195–202.

Pringle, J. E. (1981).
Accretion discs in astrophysics.
Annual Review of Astronomy & Astrophysics, 19:137–162.

Pringle, J. E. and King, A. (2007).
Astrophysical Flows.
Cambridge University Press.

Pudritz, R. E., Ouyed, R., Fendt, C., and Brandenburg, A. (2007).
Disk Winds, Jets, and Outflows: Theoretical and Computational Foundations.
In Reipurth, B., Jewitt, D., and Keil, K., editors, *Protostars and Planets V*, page 277.

Ray, T. (2012).
Losing spin: the angular momentum problem.
Astronomy and Geophysics, 53(5):5.19–5.22.

Ray, T., Dougados, C., Bacciotti, F., et al. (2007).
Toward Resolving the Outflow Engine: An Observational Perspective.
In Reipurth, B., Jewitt, D., and Keil, K., editors, *Protostars and Planets V*, page 231.

Rayleigh (1882).
Investigation of the character of the equilibrium of an incompressible heavy fluid of variable density.
Proceedings of the London Mathematical Society, s1-14(1):170–177.

Ricker, G. R., Winn, J. N., Vanderspek, R., et al. (2014).
Transiting Exoplanet Survey Satellite (TESS).
In Oschmann, Jacobus M., J., Clampin, M., Fazio, G. G., and MacEwen, H. A., editors, *Space Telescopes and Instrumentation 2014: Optical, Infrared, and Millimeter Wave*, volume 9143 of *SPIE Conf. Ser.*, page 914320.

Rigliaco, E., Natta, A., Testi, L., et al. (2012).
X-shooter spectroscopy of young stellar objects. I. Mass accretion rates of low-mass T Tauri stars in σ Orionis.
Astronomy & Astrophysics, 548:A56.

Rigliaco, E., Pascucci, I., Gorti, U., et al. (2013).
Understanding the Origin of the [O I] Low-velocity Component from T Tauri Stars.
Astrophysical Journal, 772(1):60.

Roman-Duval, J., Proffitt, C. R., Taylor, J. M., et al. (2020).
Ultraviolet legacy library of young stars as essential standards (ullyses): Data release i.
Res. Notes of the AAS, 4(11):205.

Romanova, M. M. and Kulkarni, A. K. (2009).
Discovery of drifting high-frequency quasi-periodic oscillations in global simulations of magnetic boundary layers.
Monthly Notices of the Royal Astronomical Society, 398(3):1105–1116.

Romanova, M. M., Kulkarni, A. K., and Lovelace, R. V. E. (2008).
Unstable Disk Accretion onto Magnetized Stars: First Global Three-dimensional Magnetohydrodynamic Simulations.
Astrophysical Journal Letters, 673(2):L171.

Romanova, M. M. and Owocki, S. P. (2015).
Accretion, Outflows, and Winds of Magnetized Stars.
Space Science Reviews, 191:339–389.

Romanova, M. M., Ustyugova, G. V., Koldoba, A. V., and Lovelace, R. V. E. (2002).
Magnetohydrodynamic Simulations of Disk-Magnetized Star Interactions in the Quiescent Regime: Funnel Flows and Angular Momentum Transport.
Astrophysical Journal, 578(1):420–438.

Romanova, M. M., Ustyugova, G. V., Koldoba, A. V., and Lovelace, R. V. E. (2009).

Launching of conical winds and axial jets from the disc-magnetosphere boundary: axisymmetric and 3D simulations.
Monthly Notices of the Royal Astronomical Society, 399:1802–1828.

Rucinski, S. M., Matthews, J. M., Kuschnig, R., et al. (2008).
Photometric variability of the T Tauri star TW Hya on time-scales of hours to years.
Monthly Notices of the Royal Astronomical Society, 391(4):1913–1924.

Sacco, G. G., Argiroffi, C., Orlando, S., et al. (2008).
X-ray emission from dense plasma in classical T Tauri stars: hydrodynamic modeling of the accretion shock.
Astronomy & Astrophysics, 491(2):L17–L20.

Scargle, J. D. (1982).
Studies in astronomical time series analysis. II. Statistical aspects of spectral analysis of unevenly spaced data.
Astrophysical Journal, 263:835–853.

Setiawan, J., Henning, T., Launhardt, R., et al. (2008).
A young massive planet in a star-disk system.
Nature, 451(7174):38–41.

Shakura, N. I. and Sunyaev, R. A. (1973).
Black holes in binary systems. Observational appearance.
Astronomy & Astrophysics, 24:337–355.

Sicilia-Aguilar, A., Campbell-White, J., Roccatagliata, V., et al. (2023).
Stable accretion in young stars: the cases of EX Lupi and TW Hya.
Monthly Notices of the Royal Astronomical Society, 526(4):4885–4907.

Sicilia-Aguilar, A., Fang, M., Roccatagliata, V., et al. (2015).
Accretion dynamics of EX Lupi in quiescence. The star, the spot, and the accretion column.
Astronomy & Astrophysics, 580:A82.

Simon, M. N., Pascucci, I., Edwards, S., et al. (2016).
Tracing Slow Winds from T Tauri Stars via Low-velocity Forbidden Line Emission.
Astrophysica Journal, 831(2):169.

Siwak, M., Ogloza, W., Rucinski, S. M., et al. (2016).
Stable and unstable accretion in the classical T Tauri stars IM Lup and RU Lup as observed by MOST.
Monthly Notices of the Royal Astronomical Society, 456(4):3972–3984.

Siwak, M., Rucinski, S. M., Matthews, J. M., et al. (2011).
Analysis of variability of TW Hya as observed by MOST and ASAS in 2009.
Monthly Notices of the Royal Astronomical Society, 410(4):2725–2729.

Siwak, M., Rucinski, S. M., Matthews, J. M., et al. (2014).
A stable quasi-periodic 4.18-d oscillation and mysterious occultations in the 2011 MOST light-curve of TW Hya.
Monthly Notices of the Royal Astronomical Society, 444(1):327–335.

Stempels, H. C., Gahm, G. F., and Petrov, P. P. (2007).
Periodic radial velocity variations in RU Lupi.
Astronomy & Astrophysics, 461(1):253–259.

Stock, C., McGinnis, P., Caratti o Garatti, A., et al. (2022).
Accretion variability in RU Lup.
Astronomy & Astrophysics, 668:A94.

Taylor, G. (1950).
The Instability of Liquid Surfaces when Accelerated in a Direction Perpendicular to their Planes. I.
Proceedings of the Royal Society of London. Series A, 201(1065):192–196.

Tokovinin, A., Fischer, D. A., Bonati, M., et al. (2013).
CHIRON—A Fiber Fed Spectrometer for Precise Radial Velocities.
Publications of the Astronomical Society of the Pacific, 125(933):1336.

Ustyugova, G. V., , Koldoba, A. V., Romanova, M. M., and Lovelace, R. V. E. (2006).
"Propeller" Regime of Disk Accretion to Rapidly Rotating Stars.
Astrophysical Journal, 646:304–318.

Valenti, J. A., Basri, G., and Johns, C. M. (1993).
T Tauri Stars in Blue.
Astronomical Journal, 106:2024.

Velikhov, E. P. (1959).
Stability of an Ideally Conducting Liquid Flowing between Cylinders Rotating in a Magnetic Field.
Soviet Journal of Experimental and Theoretical Physics, 9(5):995–998.

Vernet, J., Dekker, H., D'Odorico, S., et al. (2011).
X-shooter, the new wide band intermediate resolution spectrograph at the eso very large telescope.
Astronomy & Astrophysics, 536:A105.

Walker, M. F. (1972).
Studies of Extremely Young Clusters.VI. Spectroscopic Observations of the Ultraviolet-Excess Stars in the Orion Nebula Cluster and NGC 2264.
Astrophysical Journal, 175:89.

Weber, M. L., Ercolano, B., Picogna, G., et al. (2020).
The interpretation of protoplanetary disc wind diagnostic lines from X-ray photoevaporation and analytical MHD models.
Monthly Notices of the Royal Astronomical Society, 496(1):223–244.

Whelan, E. T., Pascucci, I., Gorti, U., et al. (2021).
Evidence for an MHD Disk Wind via Optical Forbidden Line Spectroastrometry.
Astrophysical Journal, 913(1):43.

Wilson, T. J. G., Matt, S., Harries, T. J., and Herczeg, G. J. (2022).
Hydrogen emission from accretion and outflow in T Tauri stars.
Monthly Notices of the Royal Astronomical Society, 514:2162–2180.

Zanni, C. and Ferreira, J. (2009).
MHD simulations of accretion onto a dipolar magnetosphere. I. Accretion curtains and the disk-locking paradigm.
Astronomy & Astrophysics, 508(3):1117–1133.

Acknowledgments

Funnily enough, I'm writing these acknowledgments exactly three years after I accepted the PhD position I am now about to complete. Looking back at it, it seems like another life. These past three years have been the most intense, complex, yet deeply rewarding of my life, with several emotional upside-downs but the single, vivid dream of studying stars that brought me here to the end of this journey. Like any meaningful adventure, I couldn't have done it without all the people who supported me along the way, and even if it's harder than writing a PhD thesis, I'll do my best to acknowledge them all.

To Beate, thank you for teaching me how to survive in this jungle called research. From the very beginning, you saw my potential and provided me with the resources and, most importantly, the freedom to pursue my work in the direction I wanted to. This is worth more than a thousand words of appreciation.

To all the people I have met during these three years, and there are many of you, you have been the best part of this experience abroad. The opportunity to learn about new cultures, so different from mine, has been enriching. Your presence has made this journey unforgettable, and I am grateful for the friendships and memories we have shared.

To my office mates, Enza and Wilhelmina, for making everyday working life a little easier. Enza, you have been like an elder sister to me, and I am grateful for this. Wilhelmina, you've added so much flavor to our office life, just like a perfectly spiced Indian dish. My biggest achievement is certainly having converted you to a lover of good Italian coffee—now you can't survive without a good espresso!

To my italian friends, I know that you some of you will need to translate this paragraph but that won't stop me from expressing how much your support has meant to me. Every time I came back, you were there waiting for me as if I had never left. I've been away from Italy for three years now, and yet I've managed to maintain strong connections with most of you, and even form new one with people who are now part of my everyday life. This tells a lot about the strength of the bonds we share.

To all my relatives, your love and support from far away have been a constant source of strength during my time abroad.

Finally, to Mum and Dad. It's difficult to find the right words to express my gratitude for you. Nothing in these three years would have been possible without your support. Knowing that I've made you proud means more to me than any PhD degree.

I thank each of you for being part of my life during these unforgettable years.

PUBLISHED PAPERS

A&A, 679, A14 (2023)
https://doi.org/10.1051/0004-6361/202347051

Astronomy & Astrophysics

PENELLOPE

V. The magnetospheric structure and the accretion variability of the classical T Tauri star HM Lup★

A. Armeni[1], B. Stelzer[1,2], R. A. B. Claes[3], C. F. Manara[3], A. Frasca[4], J. M. Alcalá[5], F. M. Walter[6], Á. Kóspál[7,8,9,10], J. Campbell-White[3], M. Gangi[11,12], K. Mauco[3], and L. Tychoniec[3]

[1] Institut für Astronomie und Astrophysik, Eberhard-Karls Universität Tübingen, Sand 1, 72076 Tübingen, Germany
e-mail: armeni@astro.uni-tuebingen.de
[2] INAF – Osservatorio Astronomico di Palermo, piazza del Parlamento 1, 90134 Palermo, Italy
[3] European Southern Observatory, Karl-Schwarzschild-Strasse 2, 85748 Garching bei München, Germany
[4] INAF – Osservatorio Astrofisico di Catania, via S. Sofia 78, 95123 Catania, Italy
[5] INAF – Osservatorio Astronomico di Capodimonte, via Moiariello 16, 80131 Napoli, Italy
[6] Department of Physics & Astronomy, Stony Brook University, Stony Brook, NY 11794-3800, New York, USA
[7] Konkoly Observatory, HUN-REN Research Centre for Astronomy and Earth Sciences, Konkoly-Thege Miklós út 15-17, 1121 Budapest, Hungary
[8] CSFK, MTA Centre of Excellence, Konkoly Thege Miklós út 15-17, 1121 Budapest, Hungary
[9] ELTE Eötvös Loránd University, Institute of Physics, Pázmány Péter sétány 1/A, 1117 Budapest, Hungary
[10] Max-Planck-Institut für Astronomie, Königstuhl 17, 69117 Heidelberg, Germany
[11] INAF – Osservatorio Astronomico di Roma, via Frascati 33, 00078 Monte Porzio Catone, Italy
[12] ASI, Italian Space Agency, via del Politecnico snc, 00133 Rome, Italy

Received 30 May 2023 / Accepted 15 September 2023

ABSTRACT

HM Lup is a young M-type star that accretes material from a circumstellar disk through a magnetosphere. Our aim is to study the inner disk structure of HM Lup and to characterize its variability. We used spectroscopic data from HST/STIS, X-shooter, and ESPRESSO taken in the framework of the ULLYSES and PENELLOPE programs, together with photometric data from TESS and AAVSO. The 2021 TESS light curve shows variability typical for young stellar objects of the "accretion burster" type. The spectra cover the temporal evolution of the main burst in the 2021 TESS light curve. We compared the strength and morphology of emission lines from different species and ionization stages. We determined the mass accretion rate from selected emission lines and from the UV continuum excess emission at different epochs, and we examined its relation to the photometric light curves. The emission lines in the optical spectrum of HM Lup delineate a temperature stratification along the accretion flow. While the wings of the H I and He I lines originate near the star, the lines of species such as Na I, Mg I, Ca I, Ca II, Fe I, and Fe II are formed in an outer and colder region. The shape and periodicity of the 2019 and 2021 TESS light curves, when qualitatively compared to predictions from magnetohydrodynamic models, suggest that HM Lup was in a regime of unstable ordered accretion during the 2021 TESS observation due to an increase in the accretion rate. Although HM Lup is not an extreme accretor, it shows enhanced emission in the metallic species during this high accretion state that is produced by a density enhancement in the outer part of the accretion flow.

Key words. accretion, accretion disks – stars: pre-main sequence – stars: variables: T Tauri, Herbig Ae/Be – stars: individual: HM Lup

1. Introduction

Classical T Tauri stars (CTTSs) are young (~1–10 Myr), low-mass (<2 $M_\odot$) objects surrounded by a circumstellar disk (Hartmann et al. 2016). Their strong magnetic fields truncate the disk at a few stellar radii (typically 5 $R_\star$, Hartmann et al. 1998). The current paradigm for the interaction between the disk and the star is the magnetospheric accretion (Bouvier et al. 2007), in which the material free-falls onto the star following the magnetic field lines. The rich emission line spectrum typical of CTTSs (Joy 1945; Herbig 1962) can be explained in the framework of this model (Hartmann et al. 1994; Muzerolle et al. 1998), as well as the continuum excess flux, which results from the accretion shock at the stellar surface (Calvet & Gullbring 1998).

Young stellar objects (YSOs) are known to be variable, both photometrically and spectroscopically (Joy 1945; Herbst et al. 1994; Hartmann et al. 2016; Fischer et al. 2023). Many different processes can contribute to this variability, such as variable accretion rate, rotational modulation due to stellar spots, circumstellar extinction, and flares (Cody et al. 2014, 2022). The accretion process is often accompanied by outflows (Hartmann et al. 2016; Bally 2016), either in the form of disk winds or jets (e.g., Romanova et al. 2009; Ferreira 2013, and references therein).

Since the spectro-photometric variability of YSOs shows up in a broad range of wavelengths, from the X-rays to the infrared (Appenzeller & Mundt 1989), it is essential to study these objects using a multiwavelength approach, by means of simultaneous

★ Based on observations collected at the European Southern Observatory under ESO programmes 089.C-0143(A), 106.20Z8.003, and 106.20Z8.004.

observations in different spectral regions. Many works have shown the capabilities of simultaneous spectro-photometry in determining stellar and accretion parameters, unveiling the inner disk structure of CTTSs and studying accretion variability on different timescales (e.g., Bouvier et al. 2007; Alencar et al. 2018; Zsidi et al. 2022a,b; Fiorellino et al. 2022). This requires coordinated monitoring campaigns of a range of instruments, which are notoriously difficult to achieve. The *Hubble* UV Legacy Library of Young Stars as Essential Standards, (ULLYSES, Roman-Duval et al. 2020; Espaillat et al. 2022) now offers such a possibility. The aim of this program is to obtain low and medium resolution spectra of YSOs covering the wavelength range from the far-UV (~150 nm) to the infrared (~1000 nm) with the *Hubble* Space Telescope (HST). Together with the accompanying optical program PENELLOPE (Manara et al. 2021) at ESO Very Large Telescope (VLT), it provides an unprecedented spectroscopic dataset to study the accretion variability of YSOs.

PENELLOPE typically provides three high resolution spectra either with the Echelle SPectrograph for Rocky Exoplanets and Stable Spectroscopic Observations (ESPRESSO, Pepe et al. 2021) or the Ultraviolet and Visual Echelle Spectrograph (UVES, Dekker et al. 2000) and one medium resolution X-shooter (Vernet et al. 2011) spectrum per target taken close in time to the ULLYSES observations. The high resolution spectra are needed to study variability in the emission line profiles, while the X-shooter spectrum is used to constrain the stellar and accretion parameters. As much as possible, the ULLYSES and PENELLOPE observations are scheduled during times where the targets are observed with the Transiting Exoplanet Survey Satellite (TESS, Ricker et al. 2014). TESS produces short-cadence, about one-month-long light curves for many YSOs with a spectral response that covers the red/infrared wavelength range (~0.6–1.1 μm). Since most of the excess flux due to accretion is emitted in the near-UV to optical spectral region, at wavelengths shorter than the TESS filter band (Calvet & Gullbring 1998), it is also important to obtain simultaneous multiband photometry (Robinson et al. 2022).

In this work we take advantage of the wealth of data provided by the aforementioned programs to study in detail a single target, chosen because of the simultaneous coverage with all the relevant programs. The target of this study is HM Lup (Sz 72), a CTTS with spectral type M2 and a mass of 0.37 $M_\odot$ (Alcalá et al. 2014; Manara et al. 2023) located in the Lupus cloud at a distance of 156 pc (Gaia Collaboration 2021). It hosts a disk with a dust mass of 4.09 $M_\oplus$ and a radius of 10.97 au (Manara et al. 2023), inclined by 53 ± 19 deg relative to the line of sight (Ansdell et al. 2016).

The goal of this paper is twofold. First, we aim to study the temperature stratification of the magnetosphere of HM Lup using a range of emission lines. Secondly, we aim to investigate the spectrophotometric variability of the system.

The paper is structured as follows. In Sect. 2 we describe the observations. We report the basic properties of the star in Sect. 3. We present the results based on the optical spectrum of the system in Sect. 4 and the results on the spectrophotometric variability in Sect. 5, while we discuss them in Sect. 6.

2. Observations

For our study, we selected HM Lup as one of the PENELLOPE targets having spectra taken simultaneously with a TESS observation, in this case in sector 38 (2021). HM Lup was also observed with TESS in Sector 12 (2019).

2.1. Simultaneous data

We downloaded the TESS light curves of sectors 12 and 38 from the MAST archive[1]. The full frame images (FFI) were reduced by the TESS Science Processing Operations Center (SPOC), producing a 10 minute cadence light curve. We define the beginning of TESS Sector 38 observations, $\mathrm{MJD}_0 \equiv 59\,333.363$, as the reference time for all the simultaneous spectroscopic and photometric data. Figure 1 shows the TESS light curve in which the pre-search data conditioning simple aperture photometry (PDCSAP) flux (F) was converted into TESS magnitudes (T) using the relation $T = -2.5 \cdot \log_{10} F + ZP$ where $ZP = 20.44$ is the TESS Zero Point magnitude (Fausnaugh et al. 2021; Vanderspek et al. 2018).

We downloaded $\mathrm{BVR_cI_c}$ photometry available for HM Lup from the American Association of Variable Star Observers (AAVSO) International Database[2]. Most of the data were secured from the beginning of TESS observations and span ~140 days. Data from different observers were sometimes obtained during the same day at small temporal distance ($\Delta t \sim$ 15 min). To have a better view of the variability, we binned the photometry to 0.15 day.

HM Lup was selected as an ULLYSES target and observed on 4 May 2021 with the Space Telescope Imaging Spectrograph (STIS) camera between 1650 and 10 200 Å with a resolving power of $R \sim 1500$. Contemporaneous to the HST data, medium-high resolution optical spectroscopy was obtained in the framework of PENELLOPE (Manara et al. 2021). The journal of the spectroscopic observations is reported in Table 1, while Fig. 1 shows the temporal position of the spectra relative to the 2021 photometric data. High resolution spectra were obtained with ESPRESSO in Pr. Id. 106.20Z8.003 (PI Manara). Since in the first observation the conditions did not fulfill the requirements, namely the seeing was >1.55″, the observation was repeated the day after. However, with its signal-to-noise ratio (S/N) of 12, the first spectrum can still be used. The ESPRESSO spectra cover a wavelength range between 3800 and 7880 Å with a resolution of 140 000. These spectra were flux-calibrated as explained in Appendix A. The X-shooter spectrum taken from Pr. Id. 106.20Z8.004 (PI Manara) is divided into three arms, UVB (3000–5600 Å, $R \sim 5400$), VIS (5600–10 200 Å, $R \sim 18\,400$), and NIR (10 200–24 800 Å, $R \sim 11\,600$). In order to achieve this spectral resolution, the observation was carried out with slit widths of 1″, 0.4″, 0.4″ in the UVB, VIS and NIR arms, respectively. The absolute flux calibration correcting for slit losses was achieved using a short exposure taken with a 5″ slit, as explained by Manara et al. (2021). Telluric correction was performed on the ESPRESSO and X-shooter spectra using the molecfit tool (Smette et al. 2015). All the optical spectra were reduced by the PENELLOPE team and made publicly available on Zenodo[3].

2.2. Nonsimultaneous data

In addition to the simultaneous spectro-photometric data, we have also included observations of HM Lup taken at other epochs. In particular, an X-shooter spectrum obtained on 18 April 2012, which was already presented by Alcalá et al. (2014, 2017) and Frasca et al. (2017) taken from Pr. Id. 089.C-0143(A) (PI Alcalá), and the TESS light curve from sector 12, obtained

[1] https://archive.stsci.edu/
[2] https://www.aavso.org/aavso-international-database-aid
[3] https://zenodo.org/communities/odysseus/

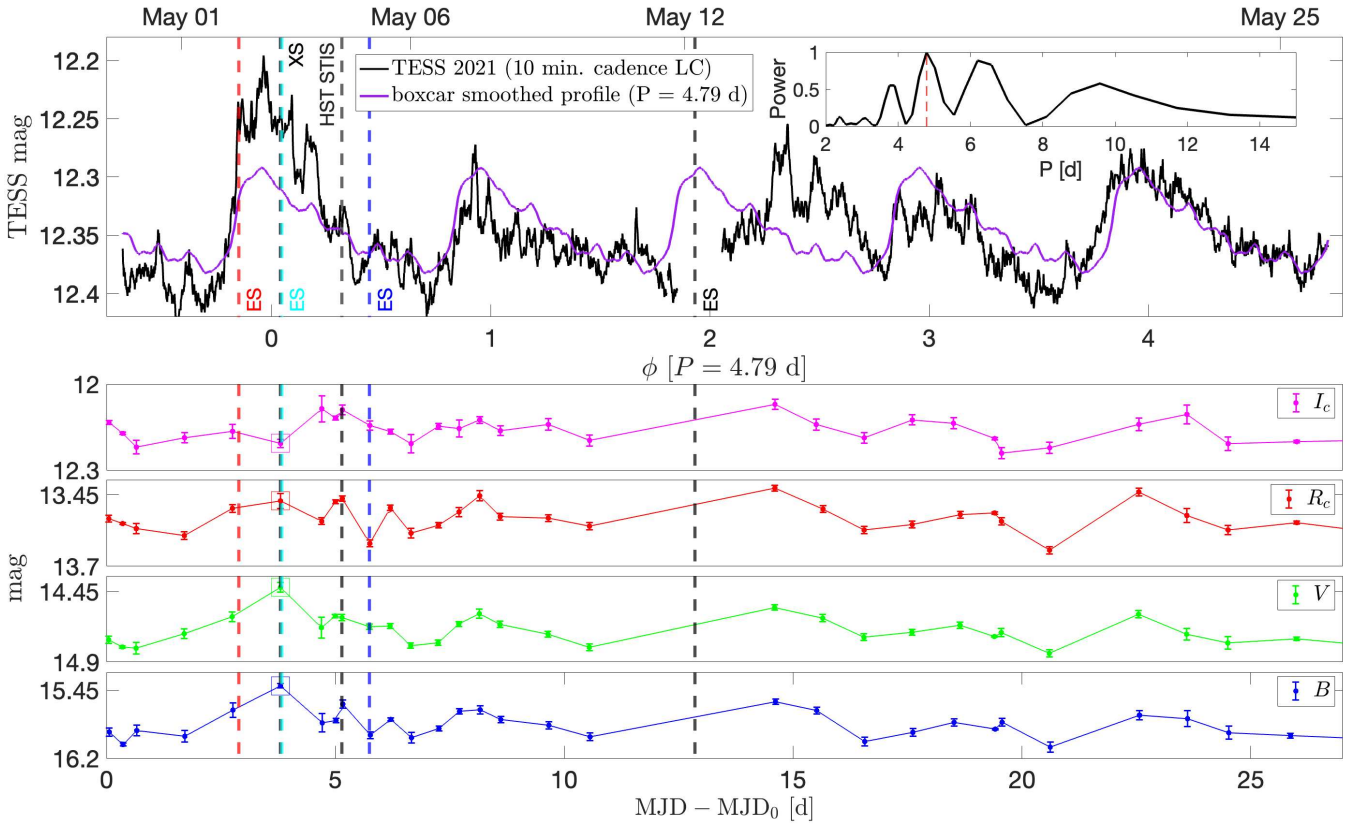

Fig. 1. Light curves and timing of simultaneous spectroscopy for HM Lup. The topmost panel shows the 2021 10 minute cadence TESS light curve (Sector 38). The inset displays the Lomb–Scargle Periodogram for the TESS light curve. Overlaid in purple is a boxcar smoothed version of the light curve produced by phase-folding the data with the period of the highest peak in the Lomb–Scargle periodogram, 4.79 day. The phase ϕ was computed with this period and $\phi = 0$ at the maximum of the TESS light curve, MJD 59 336.97. The vertical dashed lines mark the epochs of the simultaneous spectroscopic observations. Here ES = ESPRESSO and XS = X-shooter. The other panels show the part of the AAVSO BVR$_c$I$_c$ photometry that is simultaneous with TESS, with a linear interpolation as a guideline. The large open squares mark the synthetic photometry obtained from the X-shooter spectrum for the four filters. We defined MJD$_0$ = 59 333.363 as the beginning of TESS Sector 38 observation.

Table 1. Journal of the spectroscopic observations.

Instrument	MJD − MJD$_0$ (days)	t_{exp} (s)
X-shooter	−3298.17	300–250–100
ESPRESSO	2.89	1650
X-shooter	3.80	470–380–100
ESPRESSO	3.83	1650
HST/STIS	5.14	1230
ESPRESSO	5.75	1650
ESPRESSO	12.86	1650

Notes. The exposure time values for the X-shooter spectra are for the UVB, VIS and NIR arms respectively. MJD$_0$ = 59 333.363.

on 25 May 2019, UT 01:11:43 (MJD$_1$ ≡ 58 628.050) and shown in Fig. 2.

3. Stellar parameters

The properties of the system were determined by Alcalá et al. (2017) and Frasca et al. (2017) by fitting the 2012 X-shooter spectrum. While the first paper focused on the spectral type (SpT), the stellar luminosity $L_\star$ and the accretion properties, the second work used the ROTFIT routine (Frasca et al. 2015) to derive the atmospheric parameters of the accreting star, namely the effective temperature $T_{\rm eff}$, the gravity $\log g$, the projected rotational velocity $v \sin i$, and the systemic radial velocity RV. Manara et al. (2023) updated the values from Alcalá et al. (2017) using the *Gaia* DR3 distance and assuming the Herczeg & Hillenbrand (2014) relation between SpT and $T_{\rm eff}$ and non-magnetic evolutionary tracks by Feiden (2016). We applied the same procedure to the 2021 X-shooter and ESPRESSO spectra. Except for the RV, the parameters are in agreement with the previous result. The best fit RV value for the 2012 spectrum was 6.9 ± 2.4 km s^{-1} while we obtained RV = -2.7 ± 1.9 km s^{-1} from the 2021 X-shooter spectrum, suggesting a possible companion. We measured the RVs in the ESPRESSO spectra, obtaining -3.1 ± 0.7 km s^{-1}, -3.6 ± 0.7 km s^{-1}, -2.5 ± 0.3 km s^{-1}, and -2.7 ± 0.5 km s^{-1} for the epochs 1, 2, 3, and 4 respectively. Therefore, no RV variation (within 1σ) emerges from the spectra during the 2021 PENELLOPE campaign. We did not find other signs of binarity in the spectra, such as asymmetric absorption lines. In summary from the RV measurements, we cannot exclude that HM Lup is actually a long-period ($P \gtrsim 10$ d) single-lined spectroscopic binary.

Table 2 reports the stellar parameters of the system. Regarding $v \sin i$ and RV, we adopted the values obtained from an average of the best fit values for the ESPRESSO spectra, given their higher resolution. We computed the stellar radius $R_\star$ inverting the relation $L_\star = 4\pi R_\star^2 \sigma T_{\rm eff}^4$.

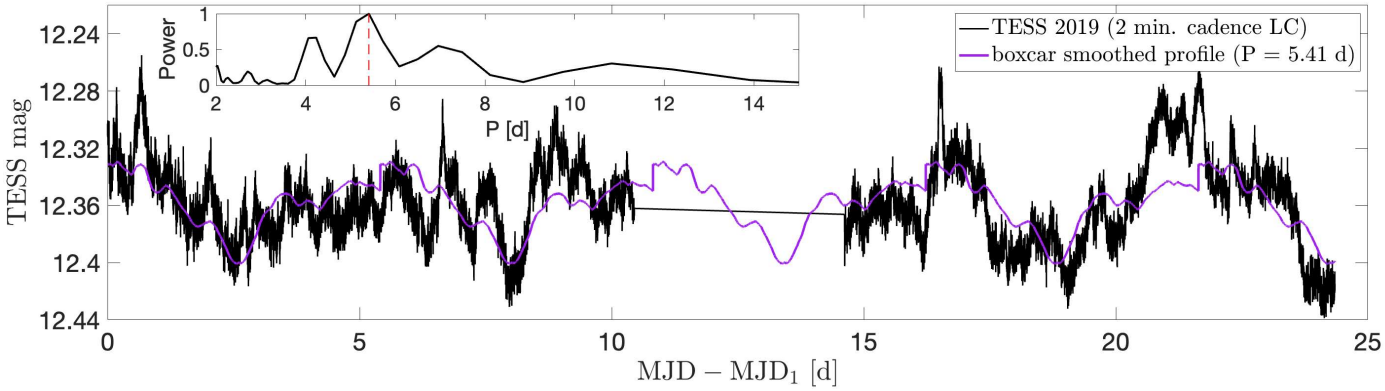

Fig. 2. TESS 2019 two-minute cadence light curve (Sector 12) of HM Lup. The inset shows the Lomb–Scargle periodogram. Overlaid in purple is a boxcar smoothed version of the light curve produced by phase-folding the data with the period of the highest peak in the Lomb–Scargle periodogram, 5.41 d. We defined MJD$_1$ ≡ 58 628.050 as the beginning of the TESS Sector 12 observation.

Table 2. Stellar parameters of HM Lup obtained by fitting the spectra as described in Sect. 3.

Parameter	Value	Reference
$T_{\rm eff}$ (†)	3550 ± 70 K	Frasca et al. (2017)
$\log g$ (†)	4.18 ± 0.28 dex	Frasca et al. (2017)
$L_\star$ (†)	0.27 ± 0.13 $L_\odot$	Manara et al. (2023)
$M_\star$ (†)	0.37 ± 0.12 $M_\odot$	Manara et al. (2023)
$R_\star$ (†)	1.39 ± 0.34 $R_\odot$	This work
$v \sin i$ (‡)	5.8 ± 0.4 km s^{-1}	This work
RV (‡)	−2.4 ± 0.6 km s^{-1}	This work
$i_{\rm d}$	53 ± 19 deg	Ansdell et al. (2016)

Notes. Parameters derived from the 2012 X-shooter spectrum (†) and the 2021 ESPRESSO spectra (‡).

In Fig. 3, we show HM Lup in the $\dot{M}_{\rm acc}$-$M_\star$ diagram together with the whole X-shooter Lupus sample. Both the 2012 measurement of the accretion rate and our anticipated new values (from Sect. 5.2) are included, showing that HM Lup is a strongly accreting CTTS.

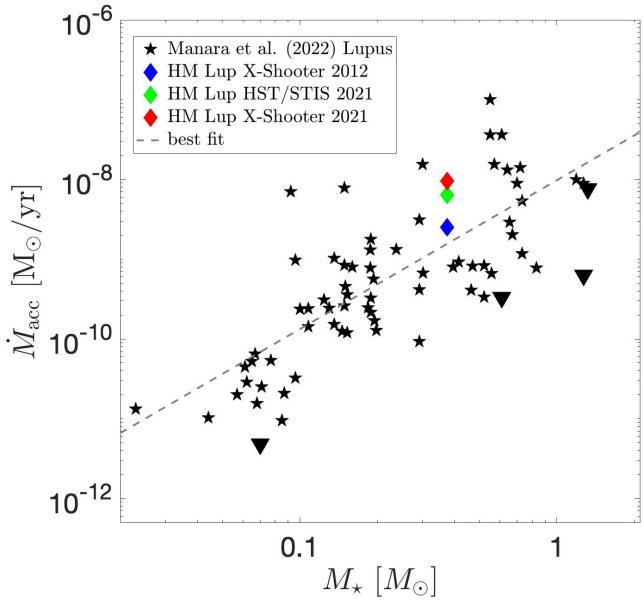

Fig. 3. $\dot{M}_{\rm acc}$-$M_\star$ diagram for X-shooter targets in Lupus, using the values from Manara et al. (2023). The black triangles indicate upper limits on the measured accretion rate. The blue, green and red diamonds mark the accretion rate of HM Lup in 2012 and 2021 (Sect. 5.2). The dashed gray line is a linear best fit to the data.

4. The optical spectrum of the system

The optical spectrum of HM Lup is rich in emission lines, the strongest being the Balmer series and the Ca II H & K lines. In addition, permitted emission lines from many other species can be identified, such as He I and singly and doubly ionized metallic elements, for example, Na I, Ca I, Ti I and Ti II, Fe I, and Fe II. We detected more than 150 emission lines from the iron peak elements. This feature is reminiscent of the outburst spectra of EXors (Sicilia-Aguilar et al. 2012, 2017) or the spectra of other strong accretors, such as DR Tau (Beristain et al. 1998). We found outflow signatures in the spectra, such as the [O I] 6300 line in emission and blueshifted absorption in the He I 10 830 line. However, these features will not be analyzed in this work. A selection of the observed permitted spectral lines is shown in Fig. 4 for the four ESPRESSO spectra.

The different excitation potentials of the observed transitions and the differences in the emission line profiles indicate the presence of a thermally stratified environment, with multiple regions that contribute to the observed spectrum. In this section, we focus on a single spectrum, the epoch 2 of ESPRESSO (cyan in Fig. 4), to illustrate the stratification of the accretion flow. We chose this spectrum because of its high S/N and the strength of the emission lines from low excitation transitions of neutral and singly ionized species. We discuss the line variability in Sect. 5.3. The atomic parameters for the analyzed emission lines were taken from the NIST Atomic Spectra Database[4].

4.1. Balmer series, He I, Ca II K

According to the morphological line profile classification by Reipurth et al. (1996), the Balmer series, except for Hα, and the Ca II K line have a Type IIB profile, that is, a double-peaked emission profile in which the secondary peak exceeds half the

[4] https://physics.nist.gov/PhysRefData/ASD/lines_form.html

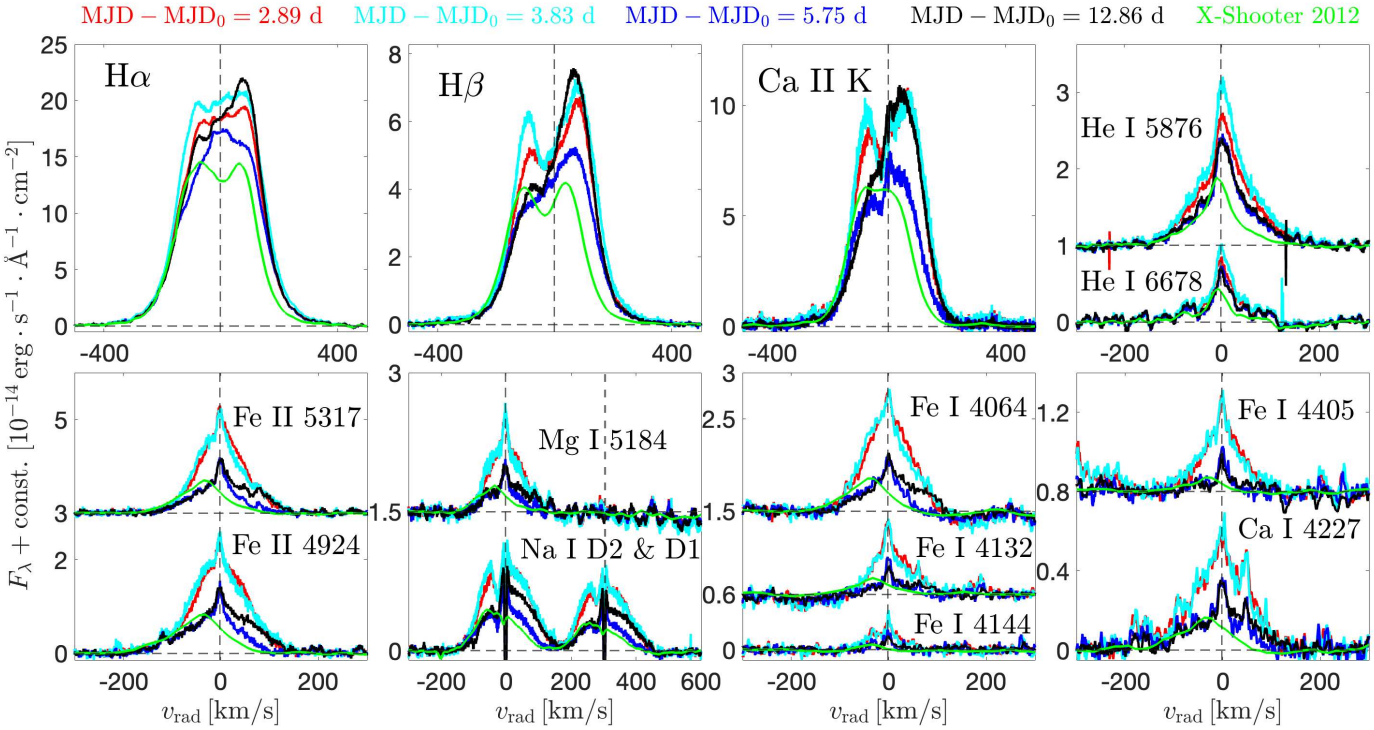

Fig. 4. Selection of continuum subtracted emission lines in the ESPRESSO spectra of HM Lup. The colors for the ESPRESSO spectra are the same as in Fig. 1. The lines from the 2012 X-shooter spectrum are shown in green for comparison. The vertical dashed lines mark the radial velocity of the system, while the horizontal dashed lines highlight the zero-flux level for each set of lines. The Fe I and Ca I lines were smoothed with a 7 points boxcar filter.

strength of the primary peak. The Hα line has instead a flat-topped emission profile. Balmer and Ca II K emission lines have symmetrical wings up to ±400 km s^{-1}. The He I lines have less broad wings, up to ∼±200 km s^{-1}, and consist of a narrow component (NC) and a broad component (BC). In the rest of the paper, we focus our analysis on the BC emission.

In the magnetospheric accretion scenario, the BC is expected to originate in the infalling material (Beristain et al. 1998, 2001; Hartmann et al. 2016). The free fall velocity onto a star of mass $M_\star$ starting from rest at the disk truncation radius $R_{\rm T}$ is

$$v_{\rm ff}(r) = (2GM_\star)^{1/2}\left(\frac{1}{r} - \frac{1}{R_{\rm T}}\right)^{1/2}. \quad (1)$$

Assuming $R_{\rm T} = 5\ R_\star$ (Gullbring et al. 1998) and the stellar parameters of HM Lup from Table 2, we obtain a free fall velocity of ∼175 km s^{-1} at $r = 2\ R_\star$, consistent with the observed line wings of the Ca II K and He I 5876 lines. The wings of the lower Balmer lines, especially Hα and Hβ, exceed these values, possibly due to Stark broadening (Muzerolle et al. 2001; Wilson et al. 2022). Conversely, the higher lines of the series are less affected by Stark broadening and their wings agree well with the wings of He I 5876, as shown in the left panel of Fig. 5 for the H9 line. This suggests a common origin for the BC of the H I and the He I lines. Given the high excitation potentials of the He I lines, which have upper states with energies $E_j \gtrsim 20$ eV, a source of ionizing radiation is required (Beristain et al. 2001). In the magnetospheric accretion flow, these conditions are met in the pre-shock region, that is heated by soft X-rays emitted by the accretion shock (Hartmann et al. 2016). Singly ionized calcium, with its ionization potential of 11.87 eV, is almost completely ionized in such conditions. Azevedo et al. (2006) studied

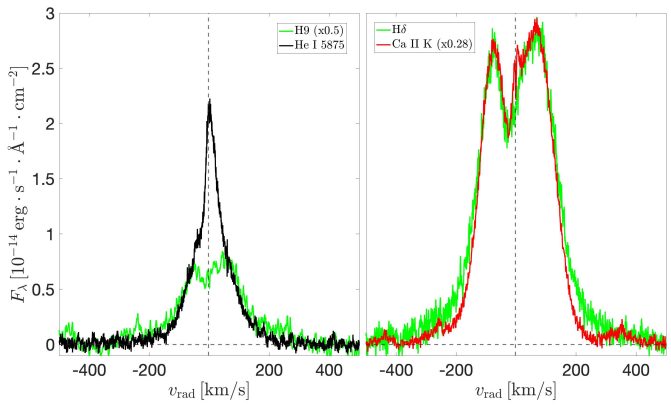

Fig. 5. Continuum subtracted profiles of selected magnetospheric lines in the epoch 2 ESPRESSO spectrum. In the left panel, H9 (3835 Å) and He I 5876. In the right panel, Hδ and Ca II K. The vertical dashed line marks the radial velocity of the system. The H9 line was smoothed with a boxcar filter and multiplied by 0.5 to match the He I 5876 wings. The Ca II K line was rescaled to Hδ in a similar way.

the formation of the Ca II infrared triplet lines and showed that the gas departs from LTE conditions. Close to the star, because of the higher dilution factor for the accretion shock radiation, calcium is mostly in the doubly ionized stage (Ca III). However, we observe strong Ca II emission at all ESPRESSO epochs (Fig. 4). This suggests that the Ca II lines are emitted from an outer part of the magnetospheric flow, where calcium is predominantly in the singly ionized stage. The right panel of Fig. 5 shows how the wings of the Ca II K line are less pronounced than the wings of, for example, Hδ, in agreement with this hypothesis.

Table 3. Atomic parameters and integrated fluxes of the selected set of metallic lines.

Ion	χ_I (eV)	λ (Å)	A_{ji} (s^{-1})	E_i (eV)	E_j (eV)	g_j	F_{int} (10^{-14} erg s^{-1} cm^{-2}) Epoch 2	Epoch 3
Na I	5.14	5889.95	6.16×10^7	0.00	2.10	4	5.8 ± 0.5	2.6 ± 0.6
Ca I	6.11	4226.73	2.18×10^8	0.00	2.93	3	3.1 ± 0.9	1.3 ± 1.2
Mg I	7.65	5183.60	5.61×10^7	2.89	5.11	3	4.5 ± 0.7	1.6 ± 0.8
Fe I	7.90	4143.87	1.33×10^7	1.56	4.55	9	1.0 ± 0.7	0.5 ± 1.0
Fe I	7.90	4063.59	6.65×10^7	1.56	4.61	7	7.2 ± 1.6	2.4 ± 2.2
Fe I	7.90	4132.06	1.18×10^7	1.61	4.61	7	2.8 ± 1.6	0.3 ± 0.6
Fe I	7.90	4404.75	2.75×10^7	1.56	4.37	9	1.8 ± 1.0	0.3 ± 1.3
Fe II	16.20	4923.93	4.30×10^6	2.89	5.41	4	12.5 ± 1.0	5.3 ± 1.2
Fe II	16.20	5316.61	3.90×10^5	3.15	5.48	10	9.6 ± 0.7	3.7 ± 0.9
Ca II	11.87	8542.09	9.90×10^6	1.70	3.15	4	7.67 ± 1.1	–
Mg II	15.04	4481.13	2.33×10^8	8.86	11.63	8	<0.1	–

Notes. The spectra were dereddened with $A_V = 1$ mag (Sect. 5.2) for the flux integration.

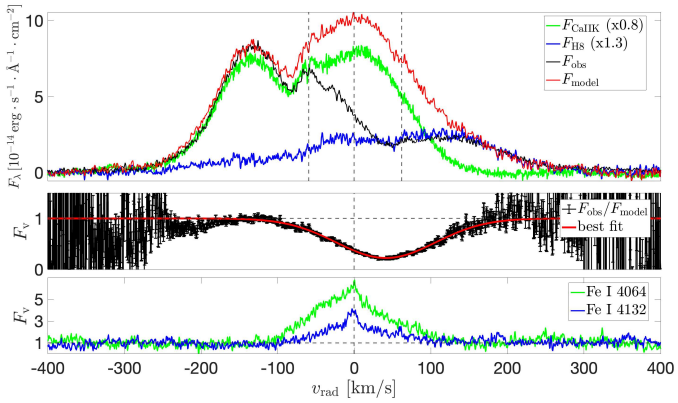

Fig. 6. Reconstruction of the Fe I absorption. All profiles are from the epoch 2 ESPRESSO spectrum. All lines are plotted relative to the rest wavelength of Fe I 3969. The top panel shows the continuum subtracted profile of the Ca II H + Hϵ blend (black) compared to the Ca II K (green) and H8 (blue) lines. The red line is the model for the unabsorbed blend (Eq. (2)). The vertical dashed lines indicate the velocity displacement of Ca II H, Fe I 3969 and Hϵ relative to the rest wavelength of Fe I 3969. The middle panel shows the Fe I 3969 absorption profile, reconstructed as explained in Sect. 4.2, and its best fit. The bottom panel shows the Fe I 4064 and 4132 emission lines.

4.2. Fe I fluorescence

The third plot in the second row of Fig. 4 compares the Fe I 4064, 4132, and 4144 lines. The first two are a doublet, having a common upper level. Although these three lines are from the same multiplet, the integrated flux in the Fe I 4132 line, the weaker line of the doublet, is more than twice the integrated flux of the Fe I 4144 line, as shown in Table 3. This behavior was first recognized by Herbig (1945), who proposed that the unusual strength of this doublet is due to a fluorescence mechanism. The Fe I line at 3969.26 Å, which shares the upper level with the doublet, is nearly coincident in wavelength with Ca II H (3968.47 Å) and Hϵ (3970.08 Å). Absorption in this line can produce an overpopulation of the y^3F^0 ($J = 3$) level, from which the fluorescent emission lines originate. The top panel of Fig. 6 shows that the Ca II H + Hϵ blend is strongly absorbed in the region of Fe I 3969.

We reconstructed the Fe I 3969 absorption profile by creating a model for the unabsorbed emission in the Ca II H + Hϵ blend. To this end, we used the Ca II K and H8 lines as template for Ca II H and Hϵ, respectively. We subtracted the continuum in these lines and shifted them in radial velocity to the position of Ca II H and Hϵ relative to the Fe I 3969 rest wavelength. The non-absorbed model profile was computed as a linear combination,

$$F_{model} = 0.8F_{CaIIK} + 1.3F_{H8}. \quad (2)$$

The coefficients were determined by matching the wings of the blended profile ($|v_{rad}| \gtrsim 150$ km s^{-1}), where absorption from Fe I is not expected, to the wings of the two template lines. The absorption profile was then obtained by dividing the observed Ca II H + Hϵ blend by its model. The result is shown in the middle panel of Fig. 6. We fit this profile with a Gaussian

$$F_v = 1 + C \exp\left[\frac{(v - v_0)^2}{2\sigma^2}\right]. \quad (3)$$

The best fit parameters are $C = -0.777 \pm 0.002$, $v_0 = 41.4 \pm 0.2$ km s^{-1}, $\sigma = 64.8 \pm 0.3$ km s^{-1}. The line width is in agreement with those observed in the fluorescent lines (bottom panel of Fig. 6).

The Fe I 3969 profile provides constraints on the structure of the circumstellar envelope (Willson 1975). Since the Ca II and H I lines are formed in the pre-shock region (Sect. 4.1), a foreground structure that is opaque in Fe I must be present to produce absorption. From the Gaussian best fit of the profile and assuming a purely extinguishing medium for which $F(v) = \exp(-\tau_v)$, we obtain a minimum optical depth at line center $\tau_0 \sim 1.5$. Therefore, this region is optically thick in Fe I. This is confirmed by the integrated flux ratio of the fluorescent lines, r_{FeI}, that is equal to 2.6 at epoch 2, much lower than the ratio of the A_{ji} values, 5.6. The line center is redshifted by ~40 km s^{-1}, indicating that the absorption is produced in infalling material.

Overall, the reconstructed Fe I 3969 absorption profile is similar to the core of the Balmer lines (e.g., Hβ in Fig. 4) in the epoch 1 and 2 ESPRESSO spectra. To compare the two features quantitatively, we fit the Hβ line in the epoch 2 ESPRESSO spectrum with a triple Gaussian model. We forced one Gaussian to fit the broad emission and the other two to reproduce the asymmetric depression. Figure 7 displays the results of the fit. Compared

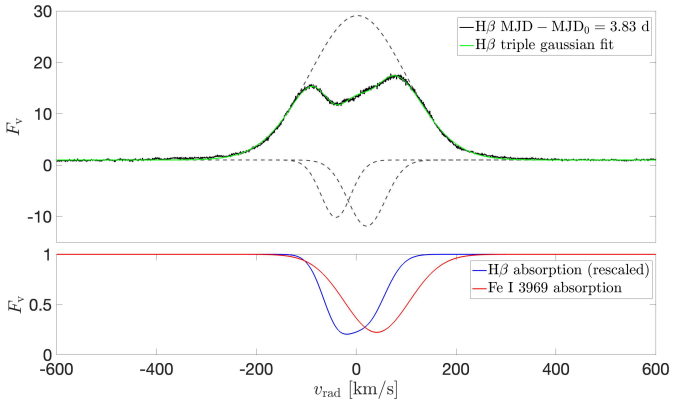

Fig. 7. Comparison between the Hβ and Fe I 3969 absorption components. Top panel: triple Gaussian fit of the continuum normalized Hβ line in the epoch 2 ESPRESSO spectrum. The dashed lines show the three Gaussian components. Bottom panel: COMPARISON between the continuum normalized absorption profiles in Hβ and Fe I 3969. The red line is the Gaussian best fit of the Fe I 3969 from Fig. 6. The blue line is the sum of the two Gaussian absorption components in Hβ, rescaled relative to the continuum to allow the comparison with the Fe I 3969 absorption profile.

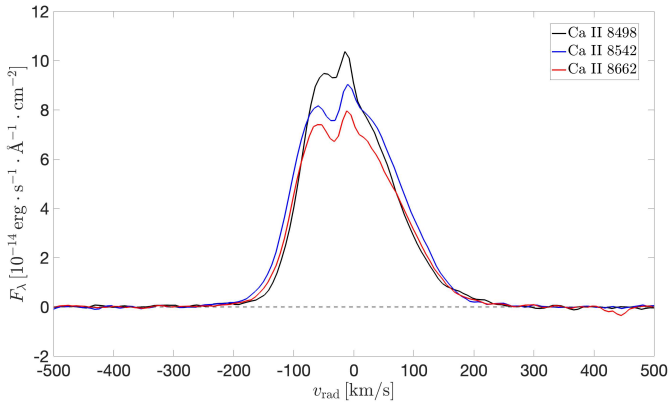

Fig. 8. Continuum subtracted profiles of the Ca II IRT lines in the X-shooter spectrum at MJD – MJD$_0$ = 3.80 days, almost simultaneous to the ESPRESSO epoch 2 spectrum.

to Fe I 3969, the absorption in Hβ has a blueshifted centroid and extends to lower positive velocities. The difference probably stems from the fact that Hβ is self-absorbed, while Fe I 3969 absorbs against Ca II H and Hϵ. This means that, in the case of the Balmer lines, absorption can take place only if emission at a given radial velocity is intercepted by hydrogen gas moving at the same v_{rad}[5] along the line of sight. On the other hand, the fluorescence phenomenon couples regions having radial velocity differences equal to the shift between the rest wavelengths of Ca II H and Hϵ relative to Fe I 3969, that is, $\sim$−59 km s^{-1} and $\sim$+62 km s^{-1} respectively. This indicates the presence of velocity gradients in the accretion flow, in agreement with the magnetospheric accretion scenario. An outer zone of the magnetosphere sees Ca II H emission that is redshifted, leading to the tuned absorption in Fe I 3969 (Gahm 2001). For the same reason, absorption in Fe I can take place due to H I emission that is seen as blueshifted by Fe I. This result also demonstrates that the Ca II emission at moderate blueshifted velocities ($-100\,\mathrm{km\,s^{-1}} \lesssim v_{rad} \lesssim 0\,\mathrm{km\,s^{-1}}$) is produced in the infalling gas.

4.3. Other metallic lines

Among the numerous metallic lines observed in the spectrum of HM Lup, we selected a set of emission lines that belong to different species and have different ionization potentials and excitation energies, so that they potentially probe different conditions in the accretion structure. Table 3 reports the atomic parameters of the selected transitions. The lines are shown in the second row of Fig. 4. All the lines display a NC+BC structure. The BC has a full width at half maximum (FWHM) of $\sim$115 km s^{-1} and an emission profile that is skewed to the red. The last two columns show the integrated flux for each line in the epoch 2 and 3 ESPRESSO spectra, chosen as representative of the line behavior during and just after the accretion burst. Before integrating, we dereddened the spectra using A_V = 1 mag (Sect. 5.2) and the Cardelli et al. (1989) extinction law with R_V = 3.1. At epoch 2, the emission is strongest in Fe II, followed by the Na I D lines. Fe I lines are weaker than Fe II lines, typically by a factor of $\sim$5–7, except for the Fe I 4064 and 4132 lines (Sect. 4.2). This is different than EX Lup, for which Sicilia-Aguilar et al. (2012) found a ratio of two for the Fe II vs. Fe I during the outburst.

Figure 8 shows the Ca II infrared triplet (IRT) lines from the 2021 X-shooter spectrum, that have profiles similar to those of the metallic lines. The components of the Ca II IRT have relative intensities that differ from the 1:9:5 relation that is expected from the ratios of their gf-values[6], indicating that these lines are formed in an optically thick environment. This sets a lower limit to the electron density of 10^{11} cm^{-3} (Hamann & Persson 1992).

Additional information on the optical depth of the medium can be obtained from the flux ratio of lines that share the upper level. We chose the Fe II 4549 and 4352 lines (E_j = 5.55 eV) for this exercise, since they are strong, not blended and near in wavelength. The integrated flux ratio for the epoch 2 ESPRESSO spectrum is $r_{FeII} \approx 1.16$. This value is lower than the ratio of their A_{ji} values, 2.04, confirming that the region where the metallic lines are formed is optically thick. This complicates the derivation of the properties of the medium in terms of line ratios, since the line emission depends on the escape probability (Sobolev 1960; Kogure & Leung 2007). The comparison between the line ratio and the ratio of the A_{ji} values for the selected Fe I and Fe II doublets indicate that this region is more optically thick in Fe I than in Fe II. Moreover, the observation of the Fe I fluorescence (Sect. 4.2) suggests that non-LTE (NLTE) effects can be important in the region where the metallic lines are formed. Therefore, the Fe II to Fe I ratio cannot be taken as an unambiguous diagnostic of the actual conditions of this region.

Some constraints on n_e and T can still be placed from line ratios under the assumption of LTE conditions (Appendix B). In the conditions for the coexistence of Mg I, Fe I and Fe II, neutral sodium and calcium are almost completely ionized. In such an environment, the Na I D and Ca I 4227 lines are therefore less optically thick than the Fe I lines. Hence, the Ca II to Ca I ratio is a better temperature indicator than the Fe II to Fe I ratio. The Ca I 4227 line can be compared to one of the IRT lines, for instance the Ca II 8542 line. Another temperature diagnostic for the emitting region is the Mg II to Mg I ratio. The non-detection of Mg II 4481, which has an upper state with E_j = 11.63 eV, provides an upper limit to the temperature. We computed this upper limit by estimating the noise level in the continuum subtracted spectrum at the nominal position of the Mg II line. The atomic parameters of the Mg II 4481 line and the Ca II 8542 line are

[5] The difference can be on the order of the local thermal velocity.

[6] The gf-values are proportional to $g_j \cdot A_{ji}$.

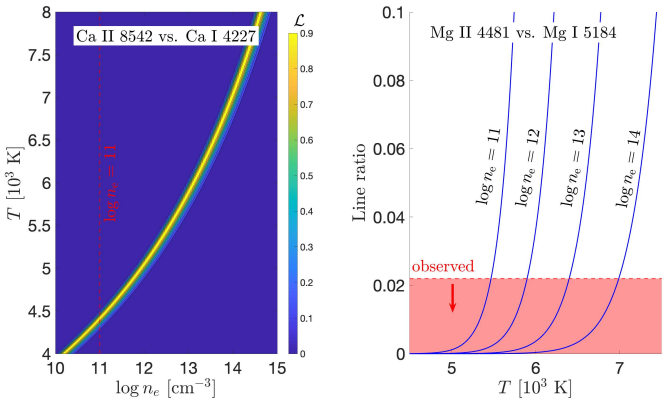

Fig. 9. Result of the Saha-Boltzmann analysis for Ca and Mg. Observed line ratios were computed from the epoch 2 ESPRESSO spectrum. Left panel: likelihood for the observed Ca II 8542 vs. Ca I 4227 ratio as a function of $\log n_e$ and T. Right panel: theoretical Mg II 4481 vs. Mg I 5184 ratios as a function of T for $\log n_e$ [cm^{-3}] = 11, 12, 13, 14. The red area marks the upper limit on the observed ratio.

reported in the last two rows of Table 3. Figure 9 shows the result of the LTE analysis described in Appendix B for Ca and Mg. For $11 \lesssim \log n_e \lesssim 14$, the Ca II to Ca I ratio is reproduced with temperatures between ∼4000 and 7000 K, in agreement with the density-dependent upper limit on T placed by the nondetection of Mg II 4481 (Fig. 9).

5. Spectrophotometric variability

5.1. Photometry

Figure 1 summarizes all available photometric data in 2021, while Fig. 2 shows the TESS Sector 12 light curve from May 2019. We lack AAVSO data in the highest flux peak of the 2021 TESS light curve, that is, in the range 3 days $\lesssim$ MJD − MJD$_0$ $\lesssim$ 5 d, which is coincident with the X-shooter spectrum. To complement the multiband light curve at that epoch, we computed synthetic BVR$_c$$I_c$ photometry from the X-shooter spectrum using the filter transmission curves downloaded from the SVO Filter Profile Service[7] (Rodrigo et al. 2012; Rodrigo & Solano 2020).

There are differences in the light curve morphology between the two TESS epochs. The 2019 TESS data show no clear periodicity pattern and a tendency for showing dips, while quasi-periodic spikes are observed in the 2021 TESS photometry. To quantify the different morphology, we computed the variability metrics introduced by Cody et al. (2014) for both light curves. The parameter Q describes the degree of periodicity and the parameter M the (a) symmetry around the median value of a given light curve. Q ranges between 0 (= highly periodic) and 1 (= aperiodic), while strongly negative (positive) values of M indicate the tendency of showing bursts (dips) in the light curve. We obtained $Q = 0.39$ and $M = -0.66$ for the 2021 TESS light curve and $Q = 0.57$ and $M = -0.18$ for the 2019 TESS light curve, suggesting a higher degree of periodicity and a more pronounced bursting behavior in 2021.

We performed a Lomb–Scargle (Lomb 1976; Scargle 1982) analysis on the TESS light curves. The Lomb–Scargle Periodograms (LSPs) for the TESS 2021 and 2019 light curves are shown in the insets of Figs. 1 and 2, respectively. We detected four peaks in both LSPs, all below a False Alarm Probability (FAP) of 10^{-5}. We chose the periods associated to the highest peak of each periodogram, 4.79 d and 5.41 d for the light curves from 2021 and 2019 respectively, as representative of the periodicity of the light curves. This is shown in Figs. 1 and 2 by visually comparing the light curves to an average profile produced by phase folding the data with those periods and smoothing the phase folded light curve with a boxcar filter with a width of 0.25 in phase, as described by Cody et al. (2014). We estimated the uncertainties on the periods as the standard deviation of a Gaussian function fitted to the peaks in the LSPs. The results are $P = 4.79 \pm 0.28$ days for the year 2021 and $P = 5.41 \pm 0.35$ days for 2019. Although the central value is different, the two periods agree within the uncertainties. The LSP of both TESS light curves present additional, weaker peaks with the same structure. For the case of the 2021 light curve they are at 3.76, 6.20 and 9.58 days. The 2019 light curve shows peaks at similar values. The latter is the first harmonic of the 4.79 days period. To understand whether the other two periods are significant, we produced an average profile analogous to the one shown in purple in Fig. 1. The comparison to the observed light curve showed poor match. This suggests that these peaks are aliases.

We studied the periodicity of the AAVSO light curves by means of continuous wavelet analysis, which is a useful tool to determine the frequency content of a signal as a function of time. We chose as wavelet template the Morse wavelet (Lilly & Olhede 2012) with a symmetry parameter $\gamma = 3$ and a time-bandwidth product $\mathcal{P} = 90$, that produces a time resolution of ∼30 days. Since the wavelet analysis works only on evenly spaced data, we linearly interpolated the AAVSO data to 0.25 d centers to remove the gaps in the light curves. Higher cadences did not change the results of the analysis. The continuous wavelet transform (CWT) of the B band photometry is shown in Fig. 10. The light curve and its CWT can be divided into three time segments with different power spectra, as shown in the lower panel of Fig. 10. In the first segment (B1), which is simultaneous to the 2021 TESS light curve, the detected period P_{B1} is compatible with the period of the TESS light curve, 4.79 days. In the other two segments the main periods detected are $P_{B2} = 6.24$ days and $P_{B3} = 8.84$ days. In the LSP of the whole light curve, in which the time dependence of the power spectrum is lost, these multiple contributions are averaged out. We considered only P_{B3} as statistically relevant, since it has FAP = 2.5% in the LSP.

The part of the AAVSO data that is simultaneous with TESS data follow the shape of the TESS light curve, as shown in Fig. 1. The relative magnitude variations vary across the bands, being 0.3 mag in R_c and I_c, 0.5 mag in V and 0.7 mag in B. The approximately enhanced variability amplitude in the blue part of the spectrum is compatible with changes in the accretion rate, since the excess flux is expected to peak at shorter wavelengths (Calvet & Gullbring 1998).

5.2. Accretion rate variability

A comparison between the two X-shooter spectra and the STIS spectrum in the 3200–10 000 Å range is shown in Fig. 11. Marked differences in the Balmer continuum and the Balmer jump are evident between the three spectra. In the 2021 X-shooter spectrum the Balmer continuum was ∼3 times higher than in 2012. The ratio is reduced to a factor ∼1.5 in the Paschen continuum. The flux in the STIS spectrum lies approximately between these two.

[7] http://svo2.cab.inta-csic.es/theory/fps/

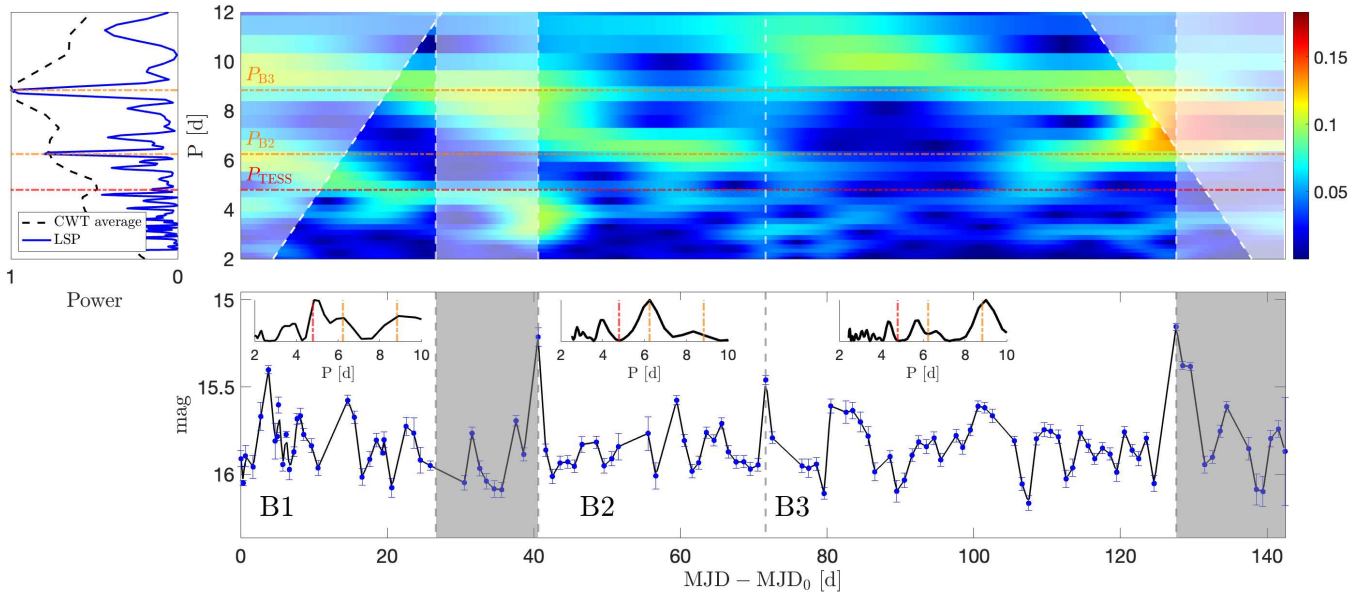

Fig. 10. Continuous wavelet analysis of the AAVSO *B* band photometry. The top panel shows the CWT. The inset on the left displays the LSP of the whole dataset, together with a temporal average of the CWT. The orange horizontal dot-dashed lines mark the periods obtained from the LSP analysis, i.e., P_{B2} = 6.24 days and P_{B3} = 8.84 day, while the red one indicates the 2021 TESS period, P_{TESS} = 4.79 days. The bottom panel displays the AAVSO *B* band light curve and its linear interpolation. The insets show the LSP for three different time segments. We excluded the shaded areas from the calculation of the LSPs to highlight the different timescales detected.

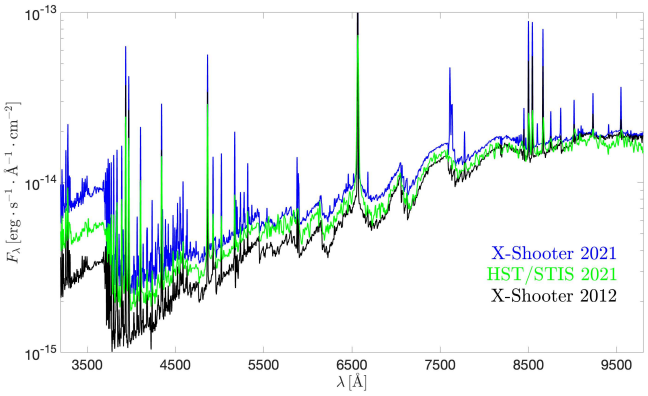

Fig. 11. VLT/X-shooter and HST/STIS spectra of HM Lup in the STIS wavelength range. The spectra were smoothed to the HST resolution with a Gaussian filter for clarity.

We derived the accretion parameters by fitting each spectrum with a combination of a photospheric (nonaccreting) template and a model for continuum emission from a slab of hydrogen representing the accretion shock. This method yields simultaneously with the UV accretion luminosity ($L_{acc,UV}$), the spectral type, and extinction (A_V) of the star. For more details on the procedure we refer to Manara et al. (2013). For the 2012 spectrum we used published values obtained with the same method. That spectrum was first analyzed by Alcalá et al. (2014), but in this work we use the updated values from Manara et al. (2023). The resulting values of A_V, $L_{acc,UV}$, and $\dot{M}_{acc}$ are listed in Table 4. Typical uncertainties on these parameters are 0.1 mag, 0.25, and 0.45 dex respectively (Manara et al. 2013, 2021; Alcalá et al. 2014). The best fit of the 2021 X-shooter spectrum returned a SpT M2, in agreement with the fit obtained by Alcalá et al. (2014) for the 2012 spectrum, and A_V = 1 mag. The STIS spectrum was fitted in the X-shooter wavelength range. Its low resolution ($R \sim 1500$) prevents constraining the SpT. Therefore, we fixed it to M2 in the fitting routine and obtained A_V = 1.5 mag and $\dot{M}_{acc} = 1.53 \times 10^{-8}\ M_\odot\ yr^{-1}$. Since this spectrum is only ∼1.3 d separated in time from the second X-shooter observation, variations in A_V on the order of ΔA_V = 0.5 mag seem unlikely, given that variations in the TESS bandpass are only about 0.2 mag, as shown in Fig. 1. Hence, we fixed A_V = 1 mag in the STIS best fit, obtaining the accretion rate reported in Table 4.

We obtained an independent measure of the accretion rate from the line luminosities, L_{line}, using their empirical relation with $L_{acc,UV}$, calibrated by Alcalá et al. (2017). For the X-shooter spectra, we integrated the available Balmer and Paschen lines, Brγ, Ca II K and infrared triplet (IRT) and He I 5876 and 6678 lines. Since the ESPRESSO spectra cover a narrower wavelength range, we integrated only the Balmer, He I, and Ca II K lines. For the STIS spectrum, we excluded the He I lines because of their low S/N. Before integrating, we dereddened the spectra using the A_V value obtained from the slab model fit of the X-shooter spectrum. Figure 12 shows the comparison between the accretion luminosity derived from the lines, $L_{acc,lines}$, and $L_{acc,UV}$ for the 2021 X-shooter spectrum. Most of the lines are in agreement with the accretion luminosity obtained from the slab model, but the Ca II lines overpredict the accretion luminosity. For this reason, we excluded these lines from the calculation of $L_{acc,lines}$. We further discuss this issue in Sect. 6.1. A global value for $L_{acc,lines}$ was then derived from a weighted average of the values obtained for the individual lines. This mean value was used to compute the accretion rate from the formula $\dot{M}_{acc} = 1.25 L_{acc} R_\star / (G M_\star)$ (Hartmann et al. 1998). The results are reported in Table 4.

Additional information on the variations in the accretion rate of CTTSs can be derived by measuring the veiling, that is, the excess emission due to the accretion process that makes photospheric absorption lines appear less deep (Hartigan et al. 1989). This parameter is defined as the ratio of the excess flux relative to the photospheric flux, $r_\lambda = F_{acc}(\lambda)/F_{phot}(\lambda)$. We computed r_λ

Table 4. Main accretion parameters derived from the spectra.

Instrument	MJD − MJD$_0$ (days)	A_V (mag)	$\log(L_{acc}/L_\odot)$		$\dot{M}_{acc}$ (10^{-9} $M_\odot$ yr^{-1})		r_{6000}
			Slab Model	Lines	Slab Model	Lines	
X-shooter	−3298.17	0.75	−1.77 ± 0.25	−1.50 ± 0.07	2.5	4.8	≤0.2 (‡)
ESPRESSO	2.89	1 (†)	–	−1.16 ± 0.08	–	10.5	2.24 ± 0.76
X-shooter	3.80	1	−1.20 ± 0.25	−1.08 ± 0.07	9.5	12.7	1.60 ± 0.2 (‡)
ESPRESSO	3.83	1 (†)	–	−1.09 ± 0.07	–	12.4	1.41 ± 0.74
HST/STIS	5.14	1 (†)	−1.37 ± 0.25	−1.23 ± 0.08	6.4	9.0	–
ESPRESSO	5.75	1 (†)	–	−1.27 ± 0.08	–	8.2	0.92 ± 0.44
ESPRESSO	12.86	1 (†)	–	−1.21 ± 0.08	–	9.4	0.6 ± 0.3

Notes. (†)Extinction assumed from X-shooter 2021 fit; (‡)veiling at 6200 Å.

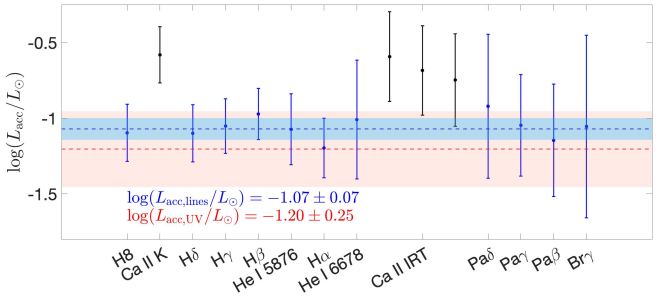

Fig. 12. Comparison between the accretion luminosity derived from emission lines and that derived from the UV excess in the 2021 X-shooter spectrum. $L_{acc,UV}$ and its uncertainty are displayed with the red dashed line and the red shaded area. The blue dashed line and the blue shaded area are the value of $L_{acc,lines}$ and its uncertainty, obtained from a weighted average of the line values. The lines marked in black were excluded from the calculation of the average.

at 6000 Å for the available spectra using the ROTFIT routine, as described by Frasca et al. (2015) and Manara et al. (2021). The result is shown in the last column of Table 4.

The comparison between L_{acc} in 2012 and 2021 indicates that HM Lup was observed in a more active state in 2021, with an accretion rate ∼3–4 times higher. The computed values of $\dot{M}_{acc}$ and r_{6000} support the hypothesis that the photometric behavior of the system in the main burst of the 2021 TESS light curve was caused by an increase in the accretion rate by a factor of ∼1.5.

5.3. Line variability

The variability of the Hα, Hβ, Ca II K, and He I 5876 and 6678 lines between the four ESPRESSO spectra is shown in the first row of Fig. 4. The shape of the He I lines is invariant, but the line flux changes. It is highest in the second epoch and lowest in the third and fourth, in agreement with the photometric behavior during the accretion burst. The Hβ and Ca II K lines evolve from a double peaked structure in the first two epochs to a profile with a single red-shifted peak in the third and fourth. Hα always remains flat-topped, suggesting that the double peaks are caused by an optical depth effect. If the temperature and density of the magnetosphere increase, as is likely to happen during the accretion burst, Hβ and the higher lines of the series can develop a self-absorption component (Muzerolle et al. 2001). The same happens for Ca II K which, being a resonance line, is more prone to absorption. On the other hand the Hα line, given its higher opacity, can be strongly optically thick and thermalized in these physical conditions, resulting in the disappearance of the self-absorption component (Hartmann et al. 2016).

The flux emitted in the metallic lines follows the photometric behavior of the system. It is strongest in the first two epochs, while it returns to its quiescent level after the accretion burst, as suggested by the comparison of line fluxes between the third ESPRESSO epoch and 2012 X-shooter spectra in Fig. 4. In the third and fourth epoch, the BC is absent in Fe I and reduced in flux by a factor of ∼2–3 in Fe II, Mg I, and Na I. The fact that the emission is stronger in both the Fe I and Fe II lines during the high accretion state suggests that the outburst spectrum is mainly the result of a density enhancement, that is, an overall increase in the number of emitters, rather than a temperature increase. Table 3 shows how the Fe II to Fe I ratio at epoch 2 is lower than at epoch 3. This is compatible with an increase in the electron density during the outburst that favors the LTE population of Fe I relative to Fe II (Appendix B).

To quantify the line variability we fit the Fe II 4924 line in each ESPRESSO epoch with a triple Gaussian model (Appendix C) as shown in Fig. 13. We chose this transition as template for the line variability because it has the highest S/N among the metallic lines. The best fit parameters are reported in Table 5. The line variations can be explained in terms of a broad emission component plus a variable redshifted absorption that reproduces the observed red skewness. The line is symmetric at epoch 1. Then, a redshifted absorption at ∼+40 km s^{-1} appears at epoch 2, it becomes more pronounced, broader and at higher positive velocities at epoch 3, and eventually disappears at epoch 4. The evolution of the redshifted absorption is indicative of optical depth changes in the infalling material, which is likely associated to the rotation of a non-axisymmetric accretion structure, similar to what observed in EX Lup (Sicilia-Aguilar et al. 2012) or CVSO109 (Campbell-White et al. 2021).

5.4. Epoch 4 ESPRESSO spectrum

Although the veiling is constant within the uncertainties between the epoch 3 and 4 ESPRESSO spectra, the accretion rate predicted from the lines is higher in epoch 4 than in epoch 3. This happens because the redshifted emission peak increases relative to the continuum in the higher lines of the Balmer series, as shown in Fig. 4. On the other hand, the He I BC does not change between the two epochs. This further supports the hypothesis that the lines are formed in a stratified environment, both in temperature and in density. The Balmer emission peaks are not linked to the region that produces the veiling, namely,

Table 5. Best fit parameters for the Fe II 4924 line profiles in the four ESPRESSO spectra.

MJD − MJD$_0$ (days)	C_2	v_2 (km s^{-1})	σ_2 (km s^{-1})	C_3	v_3 (km s^{-1})	σ_3 (km s^{-1})
2.89	4.12 ± 0.05	−2.6 ± 0.7	54.5 ± 0.4	0.36 ± 0.07	45 ± 3	20 ± 4
3.83	4.28 ± 0.04	−0.2 ± 0.5	57.9 ± 0.2	−0.65 ± 0.05	38 ± 1	28 ± 2
5.75	2.5 ± 0.2	11 ± 5	76 ± 2	−1.3 ± 0.2	77 ± 2	49 ± 3
12.86	2.19 ± 0.02	9 ± 1	82 ± 1	−0.46 ± 0.04	126 ± 2	35 ± 2

Notes. Since we are interested in fitting the BC only, we do not report the parameters for the NC, i.e., C_1, v_1, σ_1.

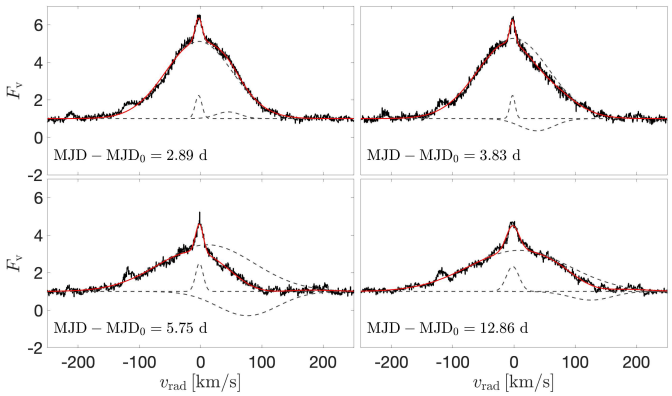

Fig. 13. Triple Gaussian fit of the Fe II 4924 line profiles in the four ESPRESSO spectra. See Appendix C for the fit function.

the continuum emission, unlike the wings of the Balmer and He I lines.

Although we lack photometric information for the ESPRESSO epoch 4 spectrum, the phase-folded TESS light curve suggests that during this epoch the system is roughly in the same configuration as in the first two epochs. The phases are indeed $\phi_4 = 1.97$, $\phi_1 = -0.11$ and $\phi_2 = 0.08$. However, the line profiles are remarkably different. The metallic lines are weaker and the double peaked profile is absent in the Balmer lines (Fig. 4). According to the metallic lines and the veiling HM Lup has returned to a lower state of accretion in the epoch 4 ESPRESSO spectrum. The behavior of the metallic lines between the epoch 3 and 4 spectra (Fig. 13 and Sect. 5.3) suggests that the enhanced redshifted emission in the Balmer series at epoch 4 is caused by an increase in the emissivity in the outer region of the accretion flow, where these lines are produced. An alternative explanation could be a decrease in the opacity of this region, that has caused redshifted absorption at epoch 3.

6. Discussion

6.1. Temperature stratification of the accretion flow

The many emission lines in the optical spectrum of HM Lup allowed us to probe the temperature stratification of the accretion flow. Figure 14 shows a schematic representation of the structure that emerges from the line analysis. The He I and H I emission wings are produced in the pre-shock region, that we call the inner magnetosphere in Fig. 14, in high temperature conditions ($T \approx 10\,000$ K). The metallic lines originate in a more external region (near the disk) in which there is coexistence of Na, Mg, Ca, Ca$^+$, Fe, and Fe$^+$. This region, that we call the outer magnetosphere, has $T \approx 6000$ K. The strength of the Ca II lines relative to the H I lines, as well as the observation of the Fe I absorption against Ca II, suggests that the Ca II emission extends further inward, likely between the outer and inner magnetosphere.

According to shock models, the pre-shock region is responsible for the Balmer continuum emission (Calvet & Gullbring 1998; Gullbring et al. 2000). Therefore, the He I lines and the H I line wings are related to the UV excess. Since the Ca II lines are not produced in the pre-shock region, the fact that they overpredict the accretion luminosity might indicate a stronger emissivity from the outer part of the accretion flow in this system, relative to the stars in the Alcalá et al. (2017) sample.

6.2. Origin of the spectrophotometric variability

The analysis of the photometric data indicates that the magnetospheric interaction between the disk and the star is unsteady and highly dynamic in HM Lup. Three-dimensional magnetohydrodynamic (MHD) simulations showed that CTTSs may accrete in either a stable or an unstable regime (Romanova et al. 2003, 2004; Kulkarni & Romanova 2008; Pantolmos et al. 2020). In the stable regime, accretion proceeds in two funnel streams and forms two polar hot spots on the stellar surface. In the unstable regime, the matter accretes in equatorial tongues and forms multiple hot spots on the surface of the star. The light curves are expected to be periodic with the stellar rotation period ($P_\star$) in the stable regime and stochastic in the unstable regime. The transition between these two regimes depends on the ratio between the magnetospheric truncation radius $R_{\rm T}$ and the corotation radius $R_{\rm co}$ (Blinova et al. 2016). Accretion is unstable if $R_{\rm T}/R_{\rm co} \lesssim 0.71$ and stable otherwise. Blinova et al. (2016) showed that when $R_{\rm T}/R_{\rm co}$ decreases below ∼0.59, unstable accretion becomes ordered. In the ordered regime, the matter accretes in one or two ordered tongues that rotate with the inner disk period.

The comparison between the morphology of the two TESS light curves suggests that the accretion changed from a chaotic regime in 2019 to a more organized regime in 2021, which could be either the stable or the unstable ordered regime. The 2021 TESS light curve was in a quasi-periodic bursting state with $P = 4.79 \pm 0.28$ days. In the stable accretion scenario, this period would correspond to $P_\star$. The period detected in the third segment of the long term B band AAVSO light curve, $P_{\rm B3} = 8.84$ days, is roughly twice the 2021 TESS period and can be interpreted as its first harmonic, that is easier to detect in the AAVSO light curve given the lower (∼1 d) cadence. However, using the 4.79 days period as $P_\star$ and the $v \sin i$ and $R_\star$ values of Table 2 we obtain an inclination $i_\star = 23 \pm 6$ deg for the stellar rotation axis, that is, a star that is almost face-on. This is not in agreement with the observed quasi-periodic behavior

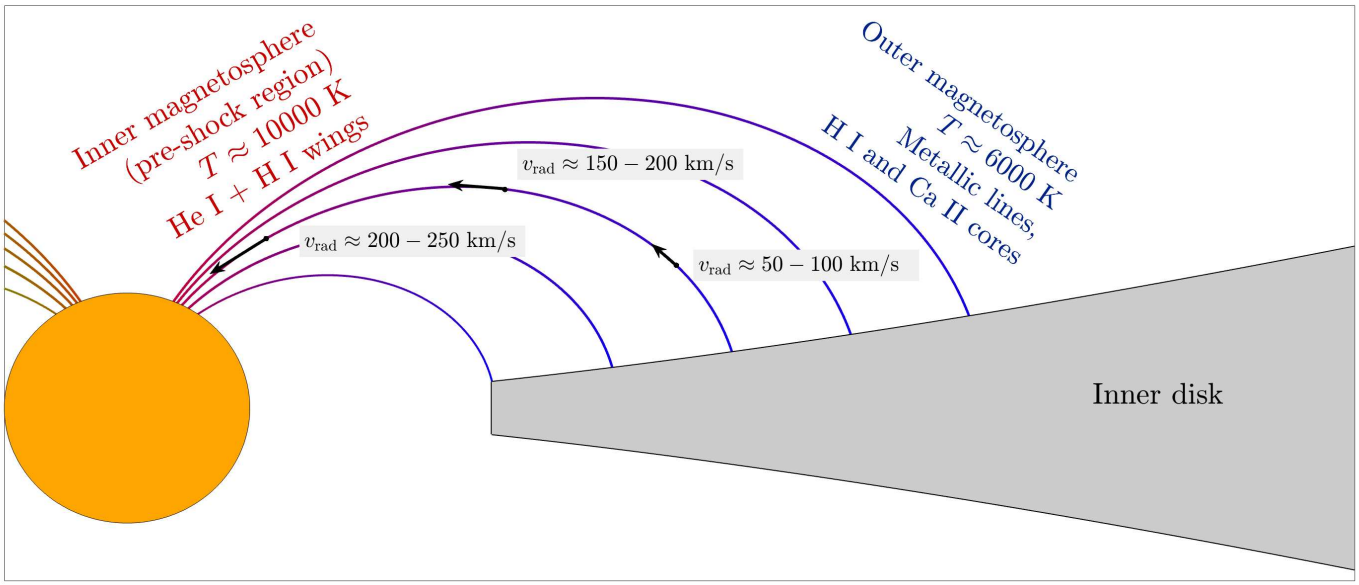

Fig. 14. Temperature structure of the accretion flow that emerges from the line analysis.

of the light curve, that is likely the result of rotational modulation and therefore suggests a higher value for $i_\star$, as shown for instance by the 1D hydrodynamic simulations of Robinson et al. (2021).

We propose that the quasi-periodic bursting behavior in the 2021 TESS light curve was the result of an increase in the accretion rate that compressed the magnetosphere and drove the system into a regime of unstable ordered accretion. In this scenario, the 4.79 d period detected in the LSP is not the stellar rotation period but it approximately corresponds to the timescale at which matter rotates at the truncation radius. At the boundary between the chaotic and ordered regime, the ratio of the stellar rotation period to the Keplerian rotation period at $R_{\rm T}$ is equal to $(R_{\rm T}/R_{\rm co})^{-3/2} = (0.45)^{-1} = 2.22$ (ω_s^{-1} in Blinova et al. 2016). Therefore, $P_\star$ should be in the 8–10 days range, compatible with $P_{\rm B3}$. Assuming this value as $P_\star$ we obtain $i_\star = 47 \pm 15$ deg, compatible with the observed quasi-periodic modulation. This value is also in agreement with the inclination of the outer disk axis (Table 2) measured by Ansdell et al. (2016). The cycle-to-cycle variability of the bursts in the 2021 TESS light curve further supports this interpretation. According to the simulations by Blinova et al. (2016), the two tongues may carry different amounts of matter and one of them may sometimes disappear.

The simultaneous spectroscopic data made it possible to characterize the photometric variability of the system during the main burst in the 2021 TESS observation in terms of variations in the accretion rate. However, part of the line variability may be due to the rotational modulation of the accretion flow, as suggested by our analysis of the Fe II 4924 line variability and shown in simulations (e.g., Kurosawa et al. 2008; Kurosawa & Romanova 2013). Although the quasi-periodic behavior of the 2021 TESS light curve supports this scenario, our limited spectroscopic coverage does not allow to test the variability of the emission lines as a function of the rotational phase. We found that during the high accretion state the Balmer lines, except for Hα, develop an absorption component and the emission of low-ionization species increases. This is similar to what has been observed in VW Cha by Zsidi et al. (2022b). The dominant effect during the outburst is an increase in the density of the accretion flow. This produces a spectroscopic signature of the colder region near the disk, that is, the enhanced emission in the metallic species.

7. Conclusions

We presented a comprehensive spectrophotometric study of the CTTS HM Lup. We examined the 2021 TESS light curve and the simultaneous spectroscopy obtained in the framework of the ULLYSES and PENELLOPE programs. The photometric data from 2021 were also compared with the 2019 TESS light curve and the long-term AAVSO monitoring.

The analysis shows that HM Lup is a star in which the accretion process is unsteady and rapidly variable. Using different emission lines, we reconstructed the temperature structure of the magnetosphere. The He I lines and the wings of the Balmer lines are formed in the pre-shock region and are related to the UV excess continuum. The emission lines from metallic species (Na I, Ca I, Ca II, Mg I, Fe I, and Fe II) are instead formed in lower temperature conditions, as already shown by Muzerolle et al. (2001) for the Na I D lines. It must be stressed that the line forming region is more complex than our schematic picture. Density and temperature vary continuously along the accretion flow, and NLTE conditions are expected for the gas (Azevedo et al. 2006). A detailed model should take into account the radiative transfer of light through a structure in which the local velocity and optical depth are functions of the distance from the star. The rich emission line spectrum of HM Lup makes this system ideal to test the temperature gradient in non-isothermal magnetospheric models.

The photometric behavior of HM Lup can be explained as the result of variations in the accretion rate in a system in which the magnetospheric radius is smaller than the corotation radius. At the epoch sampled by the 2019 TESS light curve HM Lup was in an unstable and chaotic regime of accretion. During the TESS 2021 observation, the system entered into a regime of ordered accretion due to an increase in the accretion rate. The detected 4.79 d period can be mistaken with the stellar period but it is likely associated to the Keplerian rotation of the matter at the truncation radius. We observed period variations in the long term AAVSO monitoring, in agreement with the simulations by

Blinova et al. (2016). In particular, in the third segment of the *B* band observations, the system has a periodicity of 8.84 d, which could be the actual rotation period of the star. The spectrum of the system during the burst shows the following three main characteristics: (1) emission in the He I lines increases without changes in the shape of the profile, (2) the Balmer lines develop an absorption component, (3) emission in the metallic species increases.

HM Lup gives the possibility to monitor a system with an outburst spectrum that is similar to, but less extreme than, that of EXors. Additional observational material, such as an observing campaign capable of covering a timescale of ∼10 days with high resolution spectra at nightly cadence and simultaneous photometry, is needed to better understand the nature of the complex variability of this Classical T Tauri Star.

Acknowledgements. This work has been supported by Deutsche Forschungsgemeinschaft (DFG) in the framework of the YTTHACA Project (469334657) under the project codes STE 1068/9-1 and MA 8447/1-1. A.F.R., and J.M.A. acknowledge financial support from the project PRIN-INAF 2019 "Spectroscopically Tracing the Disk Dispersal Evolution" (STRADE) and the Large Grant INAF 2022 "YSOs Outflows, Disks and Accretion: towards a global framework for the evolution of planet forming systems" (YODA). C.F.M., J.C.W., and K.M. are funded by the European Union (ERC, WANDA, 101039452). Views and opinions expressed are however those of the author(s) only and do not necessarily reflect those of the European Union or the European Research Council Executive Agency. Neither the European Union nor the granting authority can be held responsible for them. This work benefited from discussions with the ODYSSEUS team (https://sites.bu.edu/odysseus/) (HST AR-16129). The authors acknowledge Eleonora Fiorellino, Suzan Edwards, and René Oudmaijer for suggestions on this work. A.A. acknowledges Steve Shore for valuable discussions on this system. Funding for the TESS mission is provided by NASA's Science Mission directorate. The authors acknowledge with thanks the variable star observations from the AAVSO International Database contributed by observers worldwide and used in this research, and Elizabeth Waagen for coordinating the AAVSO Alerts. The authors acknowledge the use of the electronic bibliography maintained by the NASA/ADS (https://ui.adsabs.harvard.edu) system.

References

Alcalá, J. M., Natta, A., Manara, C. F., et al. 2014, A&A, 561, A2
Alcalá, J. M., Manara, C. F., Natta, A., et al. 2017, A&A, 600, A20
Alencar, S. H. P., Bouvier, J., Donati, J. F., et al. 2018, A&A, 620, A195
Ansdell, M., Williams, J. P., van der Marel, N., et al. 2016, ApJ, 828, 46
Appenzeller, I., & Mundt, R. 1989, A&ARv, 1, 291
Azevedo, R., Calvet, N., Hartmann, L., et al. 2006, A&A, 456, 225
Bally, J. 2016, ARA&A, 54, 491
Beristain, G., Edwards, S., & Kwan, J. 1998, ApJ, 499, 828
Beristain, G., Edwards, S., & Kwan, J. 2001, ApJ, 551, 1037
Blinova, A. A., Romanova, M. M., & Lovelace, R. V. E. 2016, MNRAS, 459, 2354
Bouvier, J., Alencar, S. H. P., Boutelier, T., et al. 2007, A&A, 463, 1017
Bouvier, J., Alencar, S. H. P., Harries, T. J., Johns-Krull, C. M., & Romanova, M. M. 2007, in Protostars and Planets V, eds. B. Reipurth, D. Jewitt, & K. Keil, 479
Calvet, N., & Gullbring, E. 1998, ApJ, 509, 802
Campbell-White, J., Sicilia-Aguilar, A., Manara, C. F., et al. 2021, MNRAS, 507, 3331
Cardelli, J. A., Clayton, G. C., & Mathis, J. S. 1989, ApJ, 345, 245
Cody, A. M., Stauffer, J., Baglin, A., et al. 2014, AJ, 147, 82
Cody, A. M., Hillenbrand, L. A., & Rebull, L. M. 2022, AJ, 163, 212
Dekker, H., D'Odorico, S., Kaufer, A., Delabre, B., & Kotzlowski, H. 2000, SPIE Conf. Ser., 4008, 534
Espaillat, C. C., Herczeg, G. J., Thanathibodee, T., et al. 2022, AJ, 163, 114
Fausnaugh, M. M., Vallely, P. J., Kochanek, C. S., et al. 2021, ApJ, 908, 51
Feiden, G. A. 2016, A&A, 593, A99
Ferreira, J. 2013, in EAS Pub. Ser., 62, eds. P. Hennebelle, & C. Charbonnel, 169
Fiorellino, E., Zsidi, G., Kóspál, Á., et al. 2022, ApJ, 938, 93
Fischer, W. J., Hillenbrand, L. A., Herczeg, G. J., et al. 2023, ASP Conf. Ser., 534, 355
Frasca, A., Biazzo, K., Lanzafame, A. C., et al. 2015, A&A, 575, A4
Frasca, A., Biazzo, K., Alcalá, J. M., et al. 2017, A&A, 602, A33
Gahm, G. 2001, in ASP Conf. Ser., 242, Eta Carinae and Other Mysterious Stars: The Hidden Opportunities of Emission Spectroscopy, eds. T. R. Gull, S. Johannson, & K. Davidson, 263
Gaia Collaboration (Brown, A. G. A., et al.) 2021, A&A, 649, A1
Gullbring, E., Hartmann, L., Briceño, C., & Calvet, N. 1998, ApJ, 492, 323
Gullbring, E., Calvet, N., Muzerolle, J., & Hartmann, L. 2000, ApJ, 544, 927
Hamann, F., & Persson, S. E. 1992, ApJS, 82, 247
Hartigan, P., Hartmann, L., Kenyon, S., Hewett, R., & Stauffer, J. 1989, ApJS, 70, 899
Hartmann, L., Hewett, R., & Calvet, N. 1994, ApJ, 426, 669
Hartmann, L., Calvet, N., Gullbring, E., & D'Alessio, P. 1998, ApJ, 495, 385
Hartmann, L., Herczeg, G., & Calvet, N. 2016, ARA&A, 54, 135
Herbig, G. H. 1945, PASP, 57, 166
Herbig, G. H. 1962, A&A, 1, 47
Herbst, W., Herbst, D. K., Grossman, E. J., & Weinstein, D. 1994, AJ, 108, 1906
Herczeg, G. J., & Hillenbrand, L. A. 2014, ApJ, 786, 97
Hubeny, I., & Mihalas, D. 2014, Theory of Stellar Atmospheres (Princeton University Press)
Joy, A. H. 1945, ApJ, 102, 168
Kogure, T., & Leung, K. 2007, The Astrophysics of Emission-Line Stars, 342 (New York, NY: Springer)
Kulkarni, A. K., & Romanova, M. M. 2008, MNRAS, 386, 673
Kurosawa, R., & Romanova, M. M. 2013, MNRAS, 431, 2673
Kurosawa, R., Romanova, M. M., & Harries, T. J. 2008, MNRAS, 385, 1931
Lilly, J. M., & Olhede, S. C. 2012, IEEE Trans. Signal Process., 60, 6036
Lomb, N. R. 1976, Ap&SS, 39, 447
Manara, C. F., Beccari, G., Da Rio, N., et al. 2013, A&A, 558, A114
Manara, C. F., Frasca, A., Venuti, L., et al. 2021, A&A, 650, A196
Manara, C. F., Ansdell, M., Rosotti, G. P., et al. 2023, ASP Conf. Ser., 534, 539
Muzerolle, J., Hartmann, L., & Calvet, N. 1998, AJ, 116, 455
Muzerolle, J., Calvet, N., & Hartmann, L. 2001, ApJ, 550, 944
Pantolmos, G., Zanni, C., & Bouvier, J. 2020, A&A, 643, A129
Pepe, F., Cristiani, S., Rebolo, R., et al. 2021, A&A, 645, A96
Reipurth, B., Pedrosa, A., & Lago, M. T. V. T. 1996, A&AS, 120, 229
Ricker, G. R., Winn, J. N., Vanderspek, R., et al. 2014, SPIE Conf. Ser., 9143, 914320
Robinson, C. E., Espaillat, C. C., & Owen, J. E. 2021, ApJ, 908, 16
Robinson, C. E., Espaillat, C. C., & Rodriguez, J. E. 2022, ApJ, 935, 54
Rodrigo, C., & Solano, E. 2020, in XIV.0 Scientific Meeting of the Spanish Astronomical Society, 182
Rodrigo, C., Solano, E., & Bayo, A. 2012, SVO Filter Profile Service Version 1.0, IVOA Working Draft 15 October 2012
Roman-Duval, J., Proffitt, C. R., Taylor, J. M., et al. 2020, RNAAS, 4, 205
Romanova, M. M., Ustyugova, G. V., Koldoba, A. V., Wick, J. V., & Lovelace, R. V. E. 2003, ApJ, 595, 1009
Romanova, M. M., Ustyugova, G. V., Koldoba, A. V., & Lovelace, R. V. E. 2004, ApJ, 610, 920
Romanova, M. M., Ustyugova, G. V., Koldoba, A. V., & Lovelace, R. V. E. 2009, MNRAS, 399, 1802
Scargle, J. D. 1982, ApJ, 263, 835
Sicilia-Aguilar, A., Kóspál, Á., Setiawan, J., et al. 2012, A&A, 544, A93
Sicilia-Aguilar, A., Oprandi, A., Froebrich, D., et al. 2017, A&A, 607, A127
Smette, A., Sana, H., Noll, S., et al. 2015, A&A, 576, A77
Sobolev, V. V. 1960, Moving Envelopes of Stars (Harvard University Press)
Vanderspek, R., Doty, J. P., Fausnaugh, M., et al. 2018, TESS Instrument Handbook
Vernet, J., Dekker, H., D'Odorico, S., et al. 2011, A&A, 536, A105
Willson, L. A. 1975, ApJ, 197, 365
Wilson, T. J. G., Matt, S., Harries, T. J., & Herczeg, G. J. 2022, MNRAS, 514, 2162
Zsidi, G., Fiorellino, E., Kóspál, Á., et al. 2022a, ApJ, 941, 177
Zsidi, G., Manara, C. F., Kóspál, Á., et al. 2022b, A&A, 660, A108

Table A.1: Scaling factors for the flux calibration of the ESPRESSO spectra.

Spectrum	MJD − MJD_0 [d]	r	χ^2_{min}
ESPRESSO 1	2.89	0.59 ± 0.02	64
ESPRESSO 2	3.83	0.56 ± 0.01	2
ESPRESSO 3	5.75	0.56 ± 0.02	25
ESPRESSO 4	12.86	1.26 ± 0.01	13

Appendix A: Flux calibration of the ESPRESSO spectra

We flux-calibrated the four ESPRESSO spectra by re-scaling them to match the available BVR_cI_c photometry. Since no photometric data were obtained simultaneously with the spectra, we linearly interpolated the AAVSO light curves to obtain the magnitude values at the ESPRESSO epochs. We treated the flux calibration as a least squares minimization problem, namely, we found the best scaling factor r that matched the BVR_cI_c photometry by minimizing the chi-square function

$$\chi^2(r) = \sum_{i=B,V,R_c,I_c} \left[\frac{m_i - M_i(r)}{dm_i}\right]^2 \tag{A.1}$$

where m_i and dm_i are the observed magnitudes and uncertainties and $M_i(r)$ are the r-dependent "model" magnitudes, obtained by multiplying the original ESPRESSO spectra by r and integrating over the passbands i using the respective filter transmission curve. The uncertainty on the scaling factor was estimated as the standard deviation of $\exp(-\chi^2)$. Since the ESPRESSO spectra do not reach 9100 Å, the upper limit of the I_c filter, we appended a rescaled version of the X-shooter spectrum to the ESPRESSO ones long-ward of 7580 Å. The mean ratio of the two spectra between 7200 and 7500 Å was used as scaling factor for X-shooter. We repeated the fit without including the I_c magnitudes, and the scaling parameter did not change within the uncertainties. The obtained scaling factors are reported in Table A.1. To check the reliability of this procedure, we compared the ESPRESSO spectrum at MJD − MJD_0 = 3.83 d to the X-shooter spectrum, which was observed only ∼1 h before. We computed the ratio of the two spectra, finding a mean flux ratio of 0.57, in agreement with the scaling factor we obtained from the best fit procedure.

Appendix B: Saha and Boltzmann equations

In LTE, the population of the atomic levels of an ion is given by the Saha and Boltzmann equations (e.g., Hubeny & Mihalas 2014). The Saha equation provides the ratio of the populations of two successive ionization stages for a given atomic species

$$\frac{N_{j+1}}{N_j} = \frac{1}{n_e}\left(\frac{2\pi m_e k_B T}{h^2}\right)^{3/2} \frac{2U_{j+1}(T)}{U_j(T)}\, e^{-\chi_j/k_B T} \tag{B.1}$$

where T is the temperature, N_j and U_j are the number of atoms and the partition function of the j^{th} ionization stage, n_e is the electron density, m_e is the electron mass, h is the Planck constant, k_B is the Boltzmann constant and χ_j is the ionization potential of the lower ionization stage. The Boltzmann equation governs instead the population of the atomic levels in a given ion

$$\frac{n_j}{N_{ion}} = \frac{g_j}{U_{ion}(T)}\, e^{-E_j/k_B T} \tag{B.2}$$

where n_j is the population of the level with energy E_j and multiplicity g_j relative to the population of the ion N_{ion}.

To compute the partition functions of the ions we obtained the energy levels and the ionization potentials from the NIST Atomic Spectra Database[8]. If we assume that emission lines are optically thin, we can determine the properties of the emitting region by means of line ratios. The line strength can be defined as

$$j_{line} = \frac{A_{ji}}{\lambda_{line}}\, n_j(n_e, T) \tag{B.3}$$

where A_{ji} and λ_{line} are the Einstein coefficient and the wavelength of the transition and n_j is the population of the upper level of the line, that depends on N_{ion} through the Boltzmann equation. The Saha equation gives N_{ion} as a percentage relative to the element population N_{elem}. The line ratio between two lines from the same species is therefore a function of n_e and T.

In Sect. 4.3, we use this formalism to compute predicted LTE line flux ratios for a grid of n_e and T values, with $10 \leq \log n_e \leq 14$ and 4000 K ≤ T ≤ 8000 K. The observed line ratios were statistically compared to the predicted LTE ratios by maximizing the likelihood function

$$\mathcal{L}(n_e, T) = \exp\left[-\left(\frac{r_o - r_m(n_e, T)}{dr_o}\right)^2\right] \tag{B.4}$$

where r_o and dr_o are the observed ratio and its uncertainty and r_m is the expected LTE ratio.

Appendix C: Triple Gaussian model

In Sects.4.2 and 5.3 we used a triple Gaussian model to fit the continuum-normalized emission lines in the spectrum of HM Lup. The fit model is

$$F_v = 1 + \sum_{i=1}^{3} C_i\, \exp\left[\frac{(v - v_i)^2}{2\sigma_i^2}\right]. \tag{C.1}$$

For each Gaussian C_i is the amplitude, v_i is the velocity center and σ_i is the standard deviation.

[8] https://physics.nist.gov/PhysRefData/ASD/levels_form.html

A&A, 690, A225 (2024)
https://doi.org/10.1051/0004-6361/202451065

Astronomy & Astrophysics

Evidence for magnetic boundary layer accretion in RU Lup

A spectrophotometric analysis★

A. Armeni[1,★★], B. Stelzer[1], A. Frasca[2], C. F. Manara[3], F. M. Walter[4], J. M. Alcalá[5], P. C. Schneider[6], A. Sicilia-Aguilar[7], J. Campbell-White[3], E. Fiorellino[5], J. F. Gameiro[8,9], and M. Gangi[10,11]

[1] Institut für Astronomie und Astrophysik, Eberhard Karls Universität Tübingen, Sand 1, 72076 Tübingen, Germany
[2] INAF – Osservatorio Astrofisico di Catania, via S. Sofia 78, 95123 Catania, Italy
[3] European Southern Observatory, Karl-Schwarzschild-Strasse 2, 85748 Garching bei München, Germany
[4] Department of Physics & Astronomy, Stony Brook University, Stony Brook, NY 11794-3800, USA
[5] INAF – Osservatorio Astronomico di Capodimonte, via Moiariello 16, 80131 Napoli, Italy
[6] Hamburger Sternwarte, Gojenbergsweg 112, 21029 Hamburg, Germany
[7] SUPA, School of Science and Engineering, University of Dundee, Nethergate, DD1 4HN, Dundee, UK
[8] Instituto de Astrofísica e Ciências do Espaço, Universidade do Porto, CAUP, Rua das Estrelas, 4150-762 Porto, Portugal
[9] Departamento de Física e Astronomia, Faculdade de Ciências, Universidade do Porto, Rua do Campo Alegre 687, 4169-007 Porto, Portugal
[10] INAF – Osservatorio Astronomico di Roma, via Frascati 33, 00078 Monte Porzio Catone, Italy
[11] ASI, Italian Space Agency, via del Politecnico snc, 00133 Rome, Italy

Received 11 June 2024 / Accepted 9 August 2024

ABSTRACT

Context. It is well established that classical T Tauri stars accrete material from a circumstellar disk through magnetic fields. However, the physics regulating the processes in the inner (0.1 AU) disk is still not well understood.
Aims. Our aim is to characterize the accretion process of the classical T Tauri Star RU Lup.
Methods. Optical high-resolution spectroscopic observations with CHIRON and ESPRESSO were obtained simultaneously with photometric data from AAVSO and TESS.
Results. We detected a periodic modulation in the narrow component of the He I 5876 line with a period that is compatible with the stellar rotation period, indicating the presence of a compact region on the stellar surface that we identified as the footprint of the accretion shock. We show that this region is responsible for the veiling spectrum, which is made up of a continuum component plus narrow line emission that fills in the photospheric lines. An analysis of the high-cadence TESS light curve reveals quasi-periodic oscillations on timescales shorter than the stellar rotation period, suggesting that the accretion disk in RU Lup extends inward of the corotation radius, with a truncation radius at ∼2 $R_\star$. This is compatible with predictions from three-dimensional magnetohydrodynamic models of accretion through a magnetic boundary layer (MBL). In this scenario, the photometric variability of RU Lup is produced by a nonstationary hot spot on the stellar surface that rotates with the Keplerian period at the truncation radius. We also qualitatively discuss how more complex hot spot shapes may generate the same variability pattern. The analysis of the broad components of selected emission lines reveals the existence of a non-axisymmetric, temperature-stratified flow around the star, in which the gas leaves the accretion disk at the truncation radius and accretes onto the star channeled by the magnetic field lines. The unusually rich metallic emission line spectrum of RU Lup might be characteristic of the MBL regime of accretion.
Conclusions. Our extensive multiwavelength database of RU Lup reveals many similarities to predictions from the scenario of accretion through a magnetic boundary layer. Alternative explanations would require the existence of a hot spot with a complex shape, perhaps made of two brighter knots, or a warped structure in the inner disk.

Key words. accretion, accretion disks – stars: individual: RU Lup – stars: pre-main sequence – stars: variables: T Tauri, Herbig Ae/Be

1. Introduction

Classical T Tauri stars (CTTSs) are young (∼1–10 Myr), low-mass (<2 $M_\odot$) objects that accrete material from a circumstellar disk (Hartmann et al. 2016). Their strong magnetic fields truncate the disk at a few stellar radii (typically 5 $R_\star$, Hartmann et al. 2016). The current paradigm for the interaction between the disk and the star is magnetospheric accretion (Bouvier et al. 2007b), in which the material free-falls onto the star following the magnetic field lines.

The rich emission line spectrum is one of the defining characteristics of these systems (Joy 1945; Herbig 1962). The optical spectrum of CTTSs displays strong and broad (with a full width at zero intensity ≳200 km s^{-1}) permitted emission lines, such as the Balmer, He I, and Ca II H & K lines. Sometimes other metallic species such as Na I, Mg I, Ca I, Ca II, Fe I, and Fe II are observed in emission, especially during epochs of an increased accretion rate (e.g., Sicilia-Aguilar et al. 2012; Armeni et al. 2023). Permitted lines are thought to be formed in different

★ Based on observations collected at the European Southern Observatory under ESO programs 106.20Z8.003 and 106.20Z8.007.
★★ Corresponding author; armeni@astro.uni-tuebingen.de

structures around the star. The observed supersonic velocities, roughly consistent with free-fall velocities, suggest that the broad component (BC) of permitted emission lines is formed in the magnetospheric accretion flow (Hartmann et al. 2016). Many studies have shown that the Balmer and other emission line profiles and variability are compatible with this scenario (e.g., Muzerolle et al. 1998; Alencar et al. 2012; Bouvier et al. 2007a) and that their luminosity is related to the accretion rate of the system (Alcalá et al. 2017). The helium and metallic lines are also useful tracers of the dynamics of the accretion flow (Beristain et al. 1998, 2001). These lines typically show a narrow component (NC) superposed on the BC. The NC is formed in the footprint of the magnetic field on the stellar surface – that is, the post-shock region – and it is rotationally modulated with the stellar rotation period (Sicilia-Aguilar et al. 2015; Campbell-White et al. 2021). The different behavior between the BC of the He I and metallic lines and their different excitation conditions suggest the presence of temperature and density gradients in the accretion flow (Armeni et al. 2023). In particular, the He I lines require high-energy conditions that can be achieved in the pre-shock region, which is irradiated by the X-rays from the shock (Hartmann et al. 2016). Under such conditions, species such as Na, Ca, and Fe are expected to be highly ionized. For this reason, the low-ionized metallic lines are thought to originate closer to the disk (Sicilia-Aguilar et al. 2012, 2023; Armeni et al. 2023), where the dilution factor of the radiation from the shock is lower (Azevedo et al. 2006).

Another observational feature in the optical spectrum of CTTSs is the presence of a continuum excess flux relative to the photospheric spectrum, which results from the accretion shock at the stellar surface (Calvet & Gullbring 1998). This excess makes the photospheric absorption lines appear less deep in normalized spectra, an effect known as veiling (Hartigan et al. 1989). The veiling fraction (VF) is defined as the ratio of the excess flux, $F_{\rm acc}$, due to accretion relative to the photospheric flux, $F_{\rm phot}$; that is, $\mathrm{VF}_\lambda = \mathrm{F_{acc}}(\lambda)/\mathrm{F_{phot}}(\lambda)$. Gahm et al. (2008) showed that for extremely veiled ($\mathrm{VF} \gtrsim 2$) CTTSs another component contributes to the veiling: line filling emission in the absorption lines, which dilutes the photospheric spectrum without any changes in the continuum emission from shocked regions.

Three-dimensional (3D) magnetohydrodynamic (MHD) simulations showed that the interaction between the star and the disk is complex (Romanova & Owocki 2015). It has been shown that CTTSs may accrete in either a stable or an unstable regime (Romanova et al. 2003, 2004; Kulkarni & Romanova 2008; Pantolmos et al. 2020). In the stable regime, the disk matter is channeled in funnel streams by the magnetic fields, forming polar hot spots on the stellar surface. In the Rayleigh-Taylor (RT) unstable regime, the matter penetrates through the magnetosphere in tongues. This leads to the formation of several chaotic hot spots close to the stellar equator. The light curves are expected to be periodic with the stellar rotation period ($P_\star$) in the stable regime and stochastic in the unstable regime.

According to the simulations, the transition between the stable and unstable regimes depends on the ratio between the magnetospheric truncation radius, $R_{\rm T}$, and the corotation radius, $R_{\rm co}$. The corotation radius is the radius at which the Keplerian angular velocity of the disk matches the angular velocity of the star. The truncation radius is defined as the radius where the magnetic field pressure is equal to the ram pressure in the disk. By fitting the results of a series of 3D MHD simulations, Kulkarni & Romanova (2013) showed that

$$\frac{R_{\rm T}}{R_\star} = 1.06 \left(\frac{B_\star^4 R_\star^5}{\dot{M}_{\rm acc}^2 G M_\star} \right)^{1/10}, \quad (1)$$

where $R_\star$ is the stellar radius, $B_\star$ is the strength of the stellar dipolar magnetic field at the stellar surface, $\dot{M}_{\rm acc}$ is the mass accretion rate from the disk, G is the gravitational constant, and $M_\star$ is the stellar mass. All parameters are in cgs units. Accretion is unstable if $R_{\rm T}/R_{\rm co} \lesssim 0.71$ and stable otherwise (Blinova et al. 2016).

Romanova & Kulkarni (2009) showed that in systems with small magnetospheres, unstable accretion proceeds through a magnetic boundary layer (MBL). In this regime, two ordered streams are formed. These tongues of matter and the resulting hot spots rotate with the Keplerian period, $P_{\rm T}$, at the truncation radius. This leads to the observation of quasi-periodic oscillations (QPOs) at $P_{\rm T}$ in the light curves. In their simulations, the authors observed a correlation between the size of the magnetosphere and the period of the QPOs. When the magnetosphere is smaller, the detected period decreases. Blinova et al. (2016) further investigated the conditions for the development of this regime, showing that it occurs for systems with $R_{\rm T} \lesssim 4.2\ R_\star$ when $R_{\rm T}/R_{\rm co} \lesssim 0.59$.

This work focuses on RU Lup (Sz 83), a young K7 star (Alcalá et al. 2017) located in the Lupus cloud at a distance of 158.9 ± 0.7 pc (Gaia Collaboration 2021). RU Lup is a monitoring target within the *Hubble UV Legacy Library of Young Stars as Essential Standards*, (ULLYSES, Roman-Duval et al. 2020; Espaillat et al. 2022) survey for CTTSs. Manara et al. (2023) reported a value of $\dot{M}_{\rm acc} = 10^{-7}\ M_\odot\ \mathrm{yr}^{-1}$ for RU Lup, making it the strongest accretor in Lupus. This star is also very active, with an accretion rate that can vary up to a factor of 2 on a timescale of weeks (Stock et al. 2022). Wendeborn et al. (2024a) show that the accretion rate reached median values of $1.7 \times 10^{-7}\ M_\odot\ \mathrm{yr}^{-1}$ in 2021, and it dropped considerably one year later, with a median of $6 \times 10^{-8}\ M_\odot\ \mathrm{yr}^{-1}$. Stempels et al. (2007) derived $P_\star = 3.71$ d by analyzing the radial velocity of the photospheric absorption lines. Many works have focused on the photometric variability of RU Lup, but failed to recover any stable periodicity (Percy et al. 2010; Siwak et al. 2016; Wendeborn et al. 2024b).

Herczeg et al. (2005) estimated $A_{\rm v} \sim 0.07$ mag for RU Lup. This value is compatible with its pole-on orientation, obtained from both spectroscopy (Stempels et al. 2007) and interferometry (GRAVITY Collaboration 2021). This allows us to study the accretion process and its variability without the contribution of variable extinction due to circumstellar dust in our line of sight. The optical spectrum of RU Lup comprises a plethora of emission lines from metallic species.

These characteristics make RU Lup suitable for studying the magnetospheric accretion process in a likely RT-unstable regime (given its high $\dot{M}_{\rm acc}$, Stock et al. 2022) by comparing photometric observations with 3D MHD simulations. The spectroscopic data allows instead to study the star-disk interaction and the physics regulating the processes in the inner, gaseous disk.

This paper is organized as follows. In Sect. 2, we present the observations. We update the stellar parameters of RU Lup in Sect. 3. We present the analysis of the NCs and the veiling spectrum in Sect. 4, the analysis of the BC of the metallic lines in Sect. 5, and the analysis of the TESS light curve in Sect. 6. We discuss the results in Sect. 7 and outline our conclusions in Sect. 8.

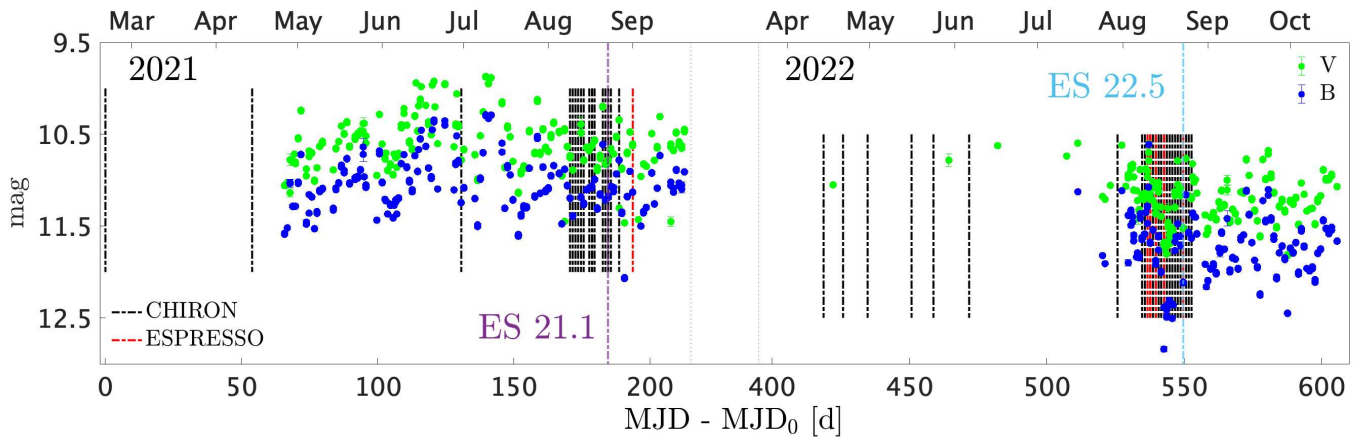

Fig. 1. AAVSO *B* (blue) and *V* (green) photometry contemporaneous to the spectroscopic observations in 2021 and 2022. The vertical dashed lines mark the epochs of the CHIRON (black) and ESPRESSO (red) observations. The ES 21.1 and ES 22.5 spectra shown in Fig. 2 are marked in violet and light blue. Here, $MJD_0 \equiv 59264.336$.

2. Observations

In this section, we describe the data that we used to study RU Lup.

2.1. Spectroscopy

The spectroscopic data were obtained with two different instruments. Medium-resolution optical (4080–8900 Å) spectra were obtained with CHIRON (Tokovinin et al. 2013), an echelle spectrograph mounted on a 1.5 m telescope that is part of the Small and Moderate Aperture Research Telescope System (SMARTS) at Cerro Tololo Inter-American Observatory. A total of 58 spectra were taken in three different epochs: 19 spectra in 2021, 27 spectra in 2022, and 12 spectra in 2023. Except for three observations taken at a resolving power of $R = 78\,000$ in 2021, the rest of the CHIRON observations have $R = 27\,800$. The spectra were reduced and flux-calibrated in the manner described by Walter (2018)[1].

High-resolution ($R = 140\,000$) optical (3800–7880 Å) spectra were obtained with the Echelle SPectrograph for Rocky Exoplanets and Stable Spectroscopic Observations (ESPRESSO, Pepe et al. 2021) in the framework of the PENELLOPE program (Manara et al. 2021). Two spectra were obtained in 2021 in Pr. ID 106.20Z8.003 and five in 2022 in Pr. ID 106.20Z8.007 (PI Manara). The ESPRESSO spectra were reduced by the PENELLOPE team, as is described in Manara et al. (2021). Telluric correction was performed using the molecfit tool (Smette et al. 2015).

For clarity, throughout this article each spectrum is labeled as "ID yy.j" where ID is either CH or ES for a CHIRON or ESPRESSO observation, respectively, *yy* are the last two digits of the year, and *j* is the j^{th} observation from that spectrograph in that year. For example, the third ESPRESSO observation from 2022 is called ES 22.3. The log of the spectroscopic observations is reported in Table A.1.

2.2. Photometry

RU Lup was observed with the Transiting Exoplanet Survey Satellite (TESS, Ricker et al. 2014). TESS produces short-cadence, about one-month-long light curves with a spectral response that covers the red/infrared wavelength range (~0.6–1.1 μm). The observation is a 200 seconds cadence light curve from Sector 65 (2023). We downloaded the light curve, extracted and reduced by the TESS Science Processing Operations Center (SPOC), from the MAST archive[2]. The TESS Sector 65 light curve is contemporaneous to nine CHIRON observations from 2023.

To supplement the spectroscopic observations with multi-band photometry, we downloaded data from the American Association of Variable Star Observers (AAVSO) International Database[3]. This data set is composed of BVR_cI_c photometry taken in 2021 and 2022. For spectroscopic data that were taken close in time to a set of photometric observations, we used the B, V, R_c photometry to flux-calibrate the spectra, following the procedure outlined by Armeni et al. (2023). We set an upper limit of 0.25 days (6 hours) on the temporal distance between the spectrum and the photometry, based on the photometric variability of the system inferred from TESS (Sect. 6). Figure 1 shows the AAVSO B and V photometry, together with the spectroscopic observations from 2021 and 2022.

In summary, we have three different epochs of spectroscopic observations: 2021, 2022, and 2023. The first two are supplemented by the AAVSO photometry, while the last one by the TESS Sector 65 light curve.

3. Stellar parameters with ESPRESSO

The photospheric parameters of RU Lup were previously estimated by Frasca et al. (2017) by fitting a medium-resolution ($R \sim 17\,400$) X-Shooter (Vernet et al. 2011) spectrum with the ROTFIT routine (Frasca et al. 2015). Here, we take advantage of the higher resolution of the ESPRESSO spectra to improve these measurements.

Fitting a spectrum of a highly accreting CTTS such as RU Lup is not an easy task. In some epochs, the spectrum is dominated by broad emission lines that make it difficult to identify the continuum. In addition, the photospheric lines are weaker because of veiling. An example of such an extreme veiling state is the ES 21.1 observation, shown in Fig. 2 in violet. The region between 5770 and 5805 Å shows the effect of line-filling

[1] https://www.astro.sunysb.edu/fwalter/SMARTS/CHIRON/ch_reduce.pdf

[2] https://archive.stsci.edu/

[3] https://www.aavso.org/aavso-international-database-aid

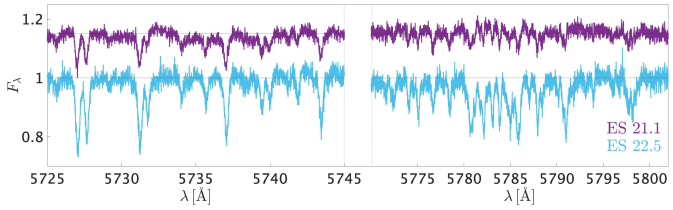

Fig. 2. ES 21.1 and ES 22.5 spectra in two regions where the photospheric absorption lines are observed. The region between 5770 and 5805 Å shows the effect of line-filling emission.

Table 1. Stellar parameters of RU Lup.

Parameter	Value	Ref.
d	158.9 ± 0.7 pc	[1]
SpT	K7	[2]
$T_{\rm eff}$	4250 ± 60 K	[3]
$v \sin i$	8.6 ± 1.4 km s^{-1}	[3]
RV	0.55 ± 0.06 km s^{-1}	[3]
VF_{5500}	1.57 ± 0.31	[3]
$L_\star$	1.46 ± 0.67 $L_\odot$	[4]
$M_\star$	0.55 ± 0.13 $M_\odot$	[4]
$R_\star$	2.27 ± 0.52 $R_\odot$	[3]
$P_\star$	3.71 ± 0.01 d	[5]
$i_\star$	16 ± 5°	[3]
$i_{\rm d}$	16^{+6}_{-8}°	[6]
$R_{\rm co}$	∼3.64 $R_\star$	[3]
$A_{\rm v}$	∼0.07 mag	[7]

Notes. [1] Gaia Collaboration (2021); [2] Alcalá et al. (2017); [3] this work (Sect. 3); [4] Manara et al. (2023); [5] Stempels et al. (2007); [6] GRAVITY Collaboration (2021); [7] Herczeg et al. (2005).

emission of the photospheric lines. The multi-epoch monitoring of RU Lup with ESPRESSO allowed us to observe the system in a state of lower veiling with a signal-to-noise ratio (S/N) of ∼40. This observation (ES 22.5) is shown in Fig. 2 in light blue. We focused on this spectrum to determine the stellar parameters.

We applied ROTFIT to different portions of the spectrum, masking emission lines where necessary. We used as templates a library of *High Accuracy Radial velocity Planet Searcher* (HARPS, Mayor et al. 2003) spectra of real stars retrieved from the ESO Archive (see Manara et al. 2021). This library is mostly composed of main-sequence stars, with the exception of the early-K spectral type for which subgiant stars are also included. We avoided including weak-lined T Tauri stars because for most of them the projected rotational velocities are too high for the fitting purposes. Moreover, some of their lines are contaminated by strong chromospheric emission. Since the templates are more evolved than our targets, the values of $\log g$ determined with these templates can be overestimated. For this reason we do not report here the $\log g$ measured for RU Lup. The stellar parameters obtained from the ROTFIT analysis of the ESPRESSO spectra are reported in Table 1, together with the other properties of RU Lup adopted from the literature. Thanks to the high resolution of ESPRESSO, we improved the measurement of the projected stellar rotational velocity ($v \sin i$), reducing the uncertainty by a factor of ∼3.5 relative to the uncertainty given by Frasca et al. (2017).

Using the stellar luminosity ($L_\star$) obtained by Manara et al. (2023), we computed the stellar radius by inverting the Stefan-Boltzmann law $L_\star = 4\pi R_\star^2 \sigma T_{\rm eff}^4$. The estimate of the stellar mass ($M_\star$) from Manara et al. (2023), together with $P_\star$ (Stempels et al. 2007) results in $R_{\rm co} = 8.26 \pm 0.65\ R_\odot = 3.64 \pm 0.88\ R_\star$.

4. Hot spot revealed by narrow component variability

The magnetospheric accretion scenario predicts the presence of hot spots on the stellar surface. The hot spots produce an excess continuum flux (Calvet & Gullbring 1998), that can be observed photometrically (e.g., Espaillat et al. 2021), and NCs in emission lines of species such as He I, He II, Fe I, Fe II, Ca II, etc. (Dodin & Lamzin 2012) that can be traced spectroscopically (McGinnis et al. 2020). Since they are formed close to the stellar surface, the NCs are expected to be rotationally modulated with $P_\star$. The radial velocity of the NC describes a sinusoidal curve as the star rotates

$$v_{\rm rad}(\phi) = v_0 + v \sin i \cdot \cos\theta_{\rm S} \cdot \sin\left[2\pi(\phi - \phi_{\rm S})\right] \quad (2)$$

(e.g., Sicilia-Aguilar et al. 2015; McGinnis et al. 2020). Here, v_0 is an offset velocity that includes the stellar systemic velocity and any other velocities due to additional motions of the emitting material (such as infall), ϕ and $\phi_{\rm S}$ are phase angles ($0 \le \phi, \phi_{\rm S} < 1$), and $\theta_{\rm S}$ is the latitude of the spot; that is, the angle between the position of the spot and the stellar equator. The amplitude $A = v \sin i \cdot \cos\theta_{\rm S}$ of the modulation is, thus, a fraction of $v \sin i$ and the closer the spot is to the pole, the smaller the modulation.

The study of the NC variability in EX Lup and TW Hya (Campbell-White et al. 2021; Sicilia-Aguilar et al. 2023) showed how lines from different species exhibit different amplitudes and phases, and hence trace material at different positions on the stellar surface. These studies also revealed that these line-emitting regions are surprisingly stable over several years, even when the accretion rate increases (e.g., during the bursts of EX Lup, Sicilia-Aguilar et al. 2023). In our case, the study of the NCs is limited by the spectral resolution of the observations. The NC of the metallic lines is typically narrower than, for instance, the NC of the He I lines, making it difficult to detect in the lower resolution CHIRON spectra. Moreover, strong line blends (e.g., between the He I 5016 and Fe II 5018 lines) and contamination by photospheric absorption lines (e.g., in the He II 4686 line) complicate the fit of the NC. For these reasons, we focused on the He I 5876 line, the NC of which can always be discerned in our spectra.

4.1. Modulation of the He I 5876 narrow component

The usual approach is to fit the line profile with two Gaussian functions, one for the BC and one for the NC (e.g., Campbell-White et al. 2021). However, the He I 5876 line profiles of RU Lup are more complex and we had to modify the fit function (see Appendix B). We used three Gaussian functions, two accounting for the BC and one for the NC. In addition, we allowed the Gaussian for the NC to be asymmetric, with two different widths (parameterized by the standard deviation, σ), one for the red wing ($\sigma_{\rm r}$) and the other for the blue wing ($\sigma_{\rm b}$). Figure 3 displays the best fit of the He I 5876 line for the ES 21.1 spectrum with two different models, one using three symmetric Gaussian functions (3S) and one using the asymmetric Gaussian for the NC (2S+1A). The 2S+1A best fit demonstrates that the NC red wing is more extended than the blue wing, with

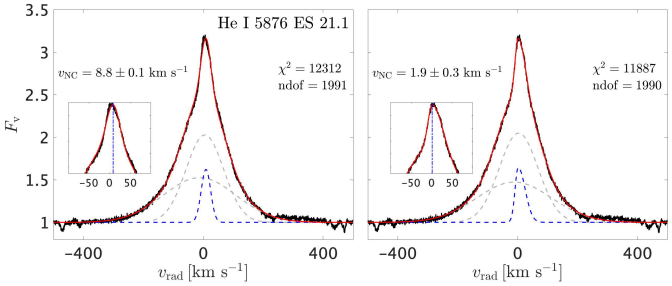

Fig. 3. Best fit of the He I 5876 line in ES 21.1 with two different models. Both models use three Gaussian functions. In the left panel, the Gaussian for the NC is symmetric, while in the right panel it has two different σ. See Appendix B for details on the model. The single components are marked with dashed lines, with the blue one indicating the Gaussian for the NC. The insets are a zoom on the NC.

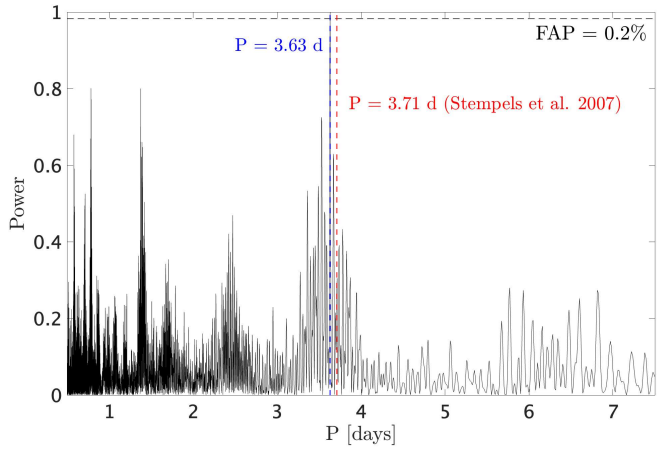

Fig. 4. Lomb Scargle Periodogram of the radial velocity of the He I 5876 NC.

$\sigma_r = 32.9 \pm 0.5$ km s^{-1} and $\sigma_b = 14.9 \pm 0.4$ km s^{-1}. This is in agreement with formation in an infalling region. The comparison between the chi-square (χ^2) of the two models indicates that the 2S+1A model better reproduces the line profile.

We fit our observations with the 2S+1A model and obtained the radial velocity of the NC (v_{NC}), defined as in Eq. (B.1), as a function of time. Then, we computed the Lomb-Scargle Periodogram (LSP, Lomb 1976; Scargle 1982) of these radial velocity measurements. The result is shown in Fig. 4. We detected a signal with a false alarm probabilty (FAP) of 0.2% at a period of 3.63 days, that differs by ∼2 h from the stellar rotation period presented by Stempels et al. (2007). The discrepancy with the Stempels et al. (2007) period can be attributed to the intrinsic variability of the region that is traced by the NC.

Figure 5 shows the radial velocity curve, phase-folded using the detected period and $MJD_0 \equiv 59264.336$ as reference date for $\phi = 0$. Although there is a ∼1 km s^{-1} variability between different epochs and some outliers (e.g, at $\phi \approx 0.6$) the modulation is overall sinusoidal. The best fit of the radial velocity curve with a sinusoidal function (Eq. (2)) gives information about the position of the emitting region on the stellar surface (Sicilia-Aguilar et al. 2015). We obtained $v_0 = 1.46 \pm 0.09$ km s^{-1}, $A = 2.53 \pm 0.13$ km s^{-1}, and $\phi_S = 0.75 \pm 0.01$. Using $v \sin i = 8.6 \pm 1.4$ km s^{-1} (Sect. 3), we derived $\theta_S = 73 \pm 3$ °. The magnetic obliquity $\Theta = 90° - \theta_S$, that is, the angle between the stellar rotation axis and the position of the NC-emitting region (McGinnis et al. 2020), is ∼20°, indicating that the magnetic field axis is misaligned with respect to the stellar rotation axis. The footprint of the magnetic field is close to the stellar pole, similar to what is observed for EX Lup and TW Hya (Sicilia-Aguilar et al. 2023).

4.2. Narrow component of the helium and metallic lines

Although the resolution and the S/N of the CHIRON spectra did not allow us to study the modulation of the NC of the metallic lines, these components can be discerned in the ESPRESSO spectra with high S/N. We selected six emission lines that show a NC in ES 22.5, namely the He I 5876, He II 4686, Mg I 5184, Si II 6347, Fe I 5447, and Fe II 5317 lines. The profile of some of these lines is severely contaminated by the underlying photospheric absorption. Therefore, we used our best fit non-accreting template to remove the stellar contribution. For each line, we adjusted the veiling to match the depth of the photospheric lines. This procedure worked for all but the Fe II 5317 line, for which the photospheric HARPS template has a gap. However, the line is strong enough that its profile can be fit even without removing the photospheric spectrum.

We fit the photospheric subtracted spectra with the multiple Gaussian model introduced in Sect. 4.1, with the aim of deriving the parameters of the NC. For all lines, an asymmetric Gaussian was used to fit the NC. The results are illustrated in Fig. 6. The red asymmetry already observed in the He I 5876 NC appears to be a common feature of the NCs of the metallic lines, with the higher-excitation lines (i.e., Si II and Fe II) being more asymmetric. Conversely, the He II line appears to be symmetric. The NCs of the helium lines are substantially broader than those of the metallic lines, suggesting that these two sets of NCs are formed in different regions of the hot spot structure. This is in agreement with the energy requirements for the formation of the helium lines. Since the upper level of the He II 4686 line has $E_j = 51.01$ eV, this line must be formed in a region that is irradiated by the X-rays from the accretion shock. Under such conditions, magnesium and iron are expected to be ionized at least once.

4.3. Anti-phase radial velocity variations

We calculated the photospheric velocity relative to the ES 22.5 spectrum, v_{phot}, by cross-correlating the latter with the other ESPRESSO spectra in the region between 5725 and 5745 Å. Figure 7 shows how v_{phot} is in anti-phase with v_{NC}. This effect was already observed for RW Aur (Petrov et al. 2001), DR Tau (Petrov et al. 2011), and EX Lup (Sicilia-Aguilar et al. 2015), and can be explained with the rotation of a hot spot that emits in narrow emission lines and distorts the photospheric absorption lines. This feature is offset relative to the stellar rotation axis, producing a rotational modulation of the centroids of both emission and absorption lines, which are in anti-phase (e.g., Petrov et al. 2011; Rei et al. 2018). Therefore, the anti-phase radial velocity variations of the He I 5876 NC and the photospheric lines confirms the hypothesis that the NCs are produced in a hot spot on the stellar surface in RU Lup.

4.4. Veiling spectrum: Continuum and line emission

We focused on the high-resolution ESPRESSO spectra to study the veiling spectrum. Figure 2 shows how the photospheric lines are not only veiled by an excess continuum, but also by narrow line-filling emission likely coming from the hot spot (Sect. 4.3).

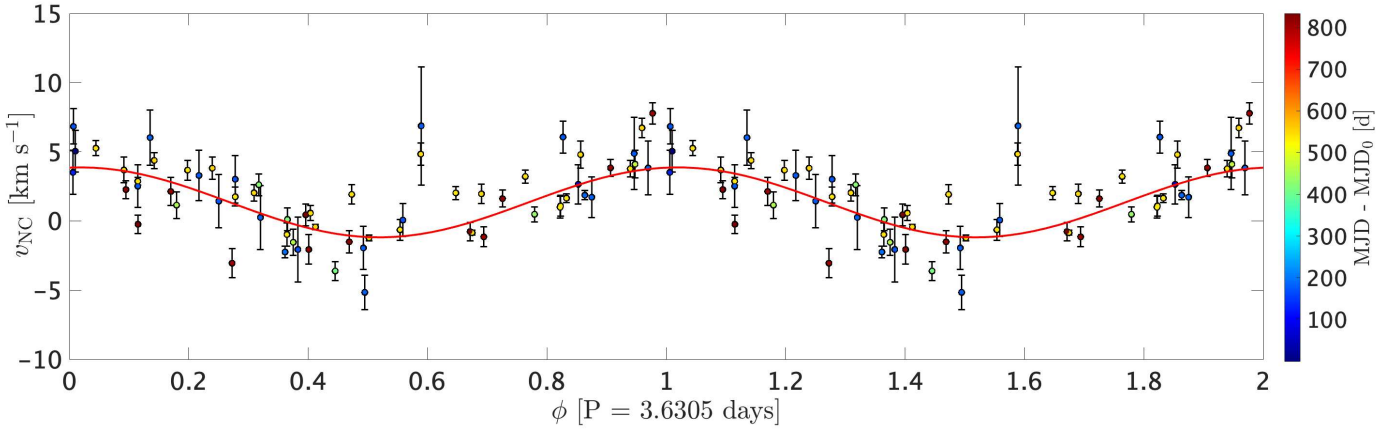

Fig. 5. Phase-folded radial velocity curve of the He I 5876 NC. The red line is the best fit with a sinusoidal function.

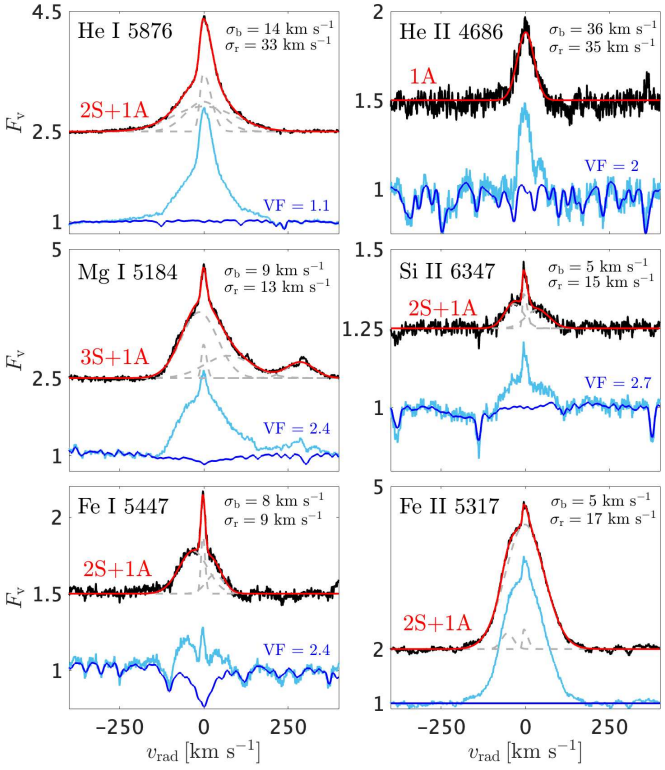

Fig. 6. Selection of emission lines that have a NC. The light blue spectrum is ES 22.5. The dark blue spectra are the template that best fits the stellar spectrum (Sect. 3), veiled to match the depth of the photospheric lines. The photospheric subtracted spectra are shown in black, with Gaussian best fits superposed in red. The red label specifies the multiple Gaussian model used (Appendix B).

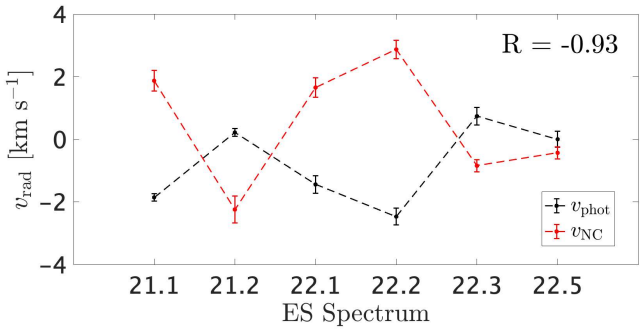

Fig. 7. Anti-phase radial velocity variations of the He I 5876 NC (red) and the photospheric lines (black) in the ESPRESSO spectra. R is the Pearson correlation coefficient between v_{phot} and v_{NC}.

Since the ESPRESSO spectra are absolutely flux-calibrated, it is possible to disentangle the continuum and the line emission contribution to the veiling. To do this, we subtracted ES 22.5 from the other ESPRESSO observations, after correcting for shifts in radial velocity by cross-correlating the spectra. This procedure is a flux-calibrated version of the one employed by Herczeg et al. (2023) to measure the veiling in TW Hya. The result is illustrated in Fig. 8 for the region around 5800 Å.

Under the assumption that the ES 22.5 observation represents the photospheric spectrum plus a featureless continuum with a VF of $VF_T = 1.57$ (Sect. 3), the subtraction removes the photospheric spectrum and reveals the veiling spectrum, which consists of two components: continuum and line emission. The continuum veiling fraction relative to ES 22.5 (VF_C) can be directly calculated as the ratio between the average fluxes of the subtracted spectrum and the ES 22.5 spectrum in the region between 5800 and 5803 Å, where the spectra are free of absorption lines. This means that in the subtracted spectra, that region represents the excess continuum relative to ES 22.5.

In Appendix C, we calculated the relative veiling, VF_{rel}, between any given spectrum and the template ES 22.5 by finding the value that best fits the normalized spectrum assuming that the photospheric lines are weakened only by an excess continuum. This value is much higher than the value of VF_c that we find above for the same wavelength region. As an example, we calculated $VF_{rel} = 2.91 \pm 0.11$ and $VF_C = 0.52 \pm 0.03$ for the ES 21.1 observation. The values of VF_C and VF_{rel} are different because of the effect of line-filling emission, which reduces the depth of the photospheric lines in normalized spectra in the same way as a diluting continuum (see, e.g., Fig. C.1). This result highlights the importance of the contribution of the line-filling emission to the veiling in highly veiled CTTSs, as already discussed by Gahm et al. (2008), Petrov et al. (2011), and Rei et al. (2018).

5. Spectroscopic variability of the metallic lines

The two spectra in Fig. 2 represent two different states of veiling of RU Lup. We estimated the veiling of the ES 21.1 observation, as is explained in Appendix C, obtaining VF = 5.6 ± 0.9.

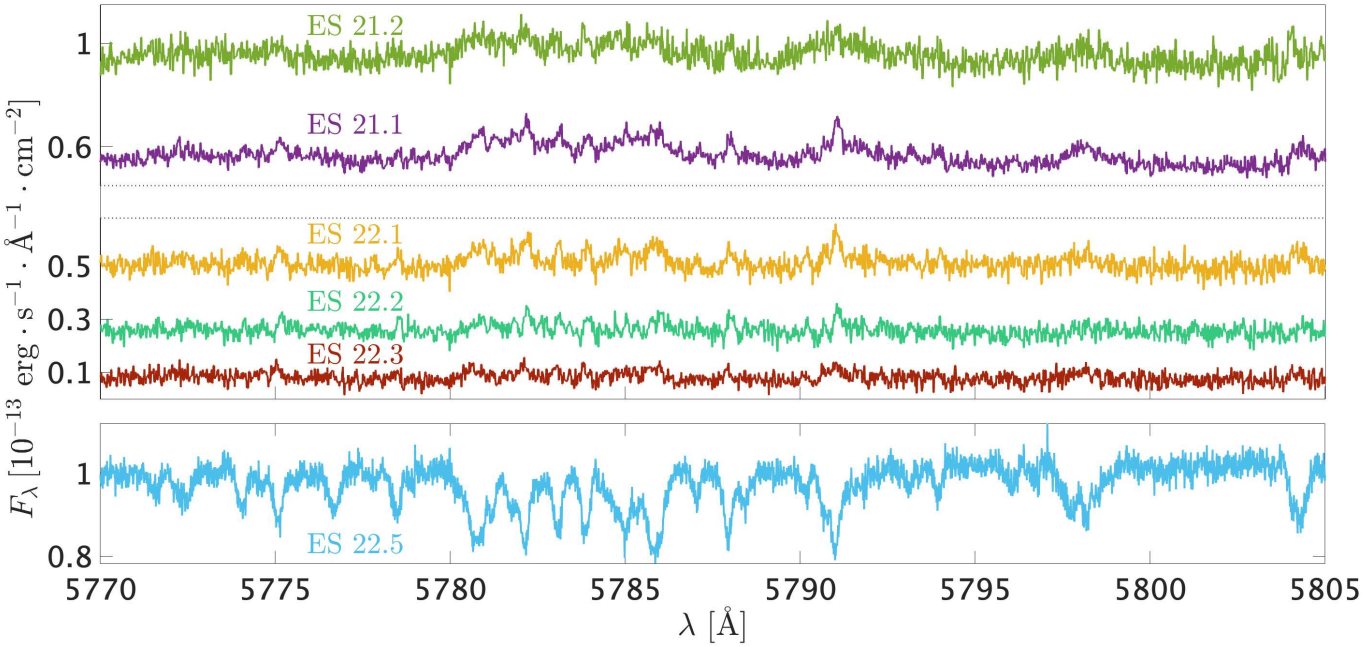

Fig. 8. Flux-subtraction of the ES 22.5 spectrum from the other ESPRESSO spectra. The top panel shows the five subtracted spectra median filtered to three points. ES 22.5 is shown in the bottom panel for reference.

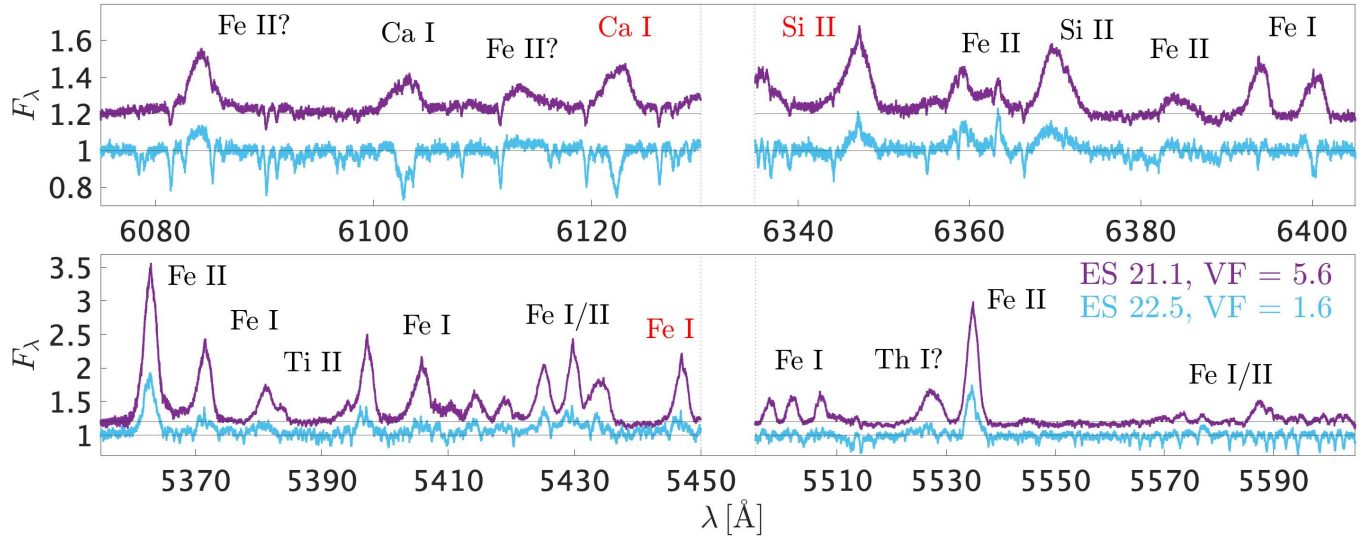

Fig. 9. Comparison between the ES 21.1 and ES 22.5 spectra in regions dominated by metallic emission lines. Species producing line emission are marked. The Fe I 5447, Si II 6347, and Ca I 6122 lines used in Sect. 6.1 are marked in red.

For the ES 22.5 spectrum, we derived VF = 1.6 ± 0.3 (Sect. 3). Figure 9 shows the differences in the emission line spectrum between these two observations. Emission lines from Fe II (e.g, Fe II 5363 and 5535) are present in both spectra, but they are stronger relative to the continuum in ES 21.1. The emission line spectrum is richer in ES 21.1, with a large number of transitions, mostly from neutral species such as Fe I and Ti I, appearing in emission. These metallic lines have a BC with a full width at half maximum (FWHM) of ∼150 km s^{-1}. In Fig. 9 we marked in red the Fe I 5447, Si II 6347, and Ca I 6122 lines, which are not blended with other lines and are clear examples of how the line strength increases relative to the continuum in the spectrum with higher veiling. The Ca I doublet ($\lambda\lambda$ 6103, 6122) has the most striking variability between the two observations, being strongly in absorption in ES 22.5 but completely filled in with emission in ES 21.1. The comparison between the ES 21.1 and 22.5 spectra indicates that the strength of these lines can be used as proxy of states of the accretion state.

Several studies (e.g., Petrov et al. 2001; Sicilia-Aguilar et al. 2012, 2023) showed that the BC of the metallic lines is formed in the circumstellar environment of the star. However, these lines must be formed in a different region with respect to, for instance, the He I lines. Iron and calcium are expected to be ionized in the high temperature conditions required for the formation of the He I lines (Armeni et al. 2023).

To understand the difference between the region of formation of these species, we selected four emission lines to analyze their BC. These lines are the He I 6678, Fe I 5447, Fe II 5317, and Si II 6347 lines. The λ5447 and λ5317 lines are among the few iron lines that are isolated and not blended with other emission

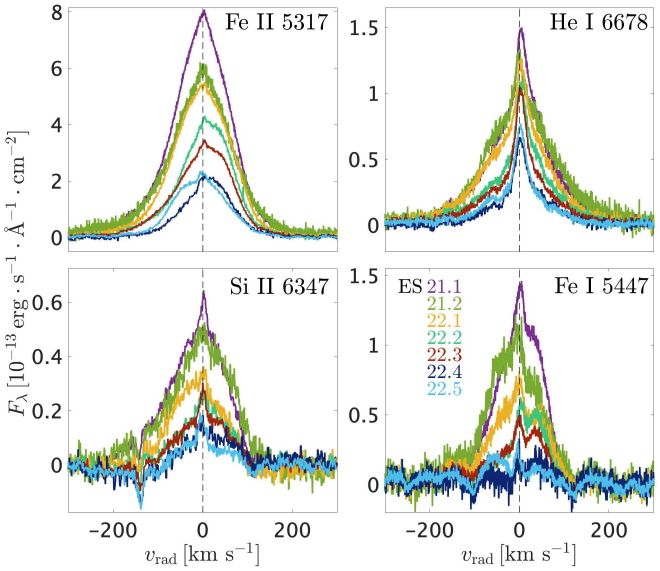

Fig. 10. Continuum subtracted profiles of the Fe II 5317, He I 6678, Si II 6347, and Fe I 5447 lines in the ESPRESSO spectra.

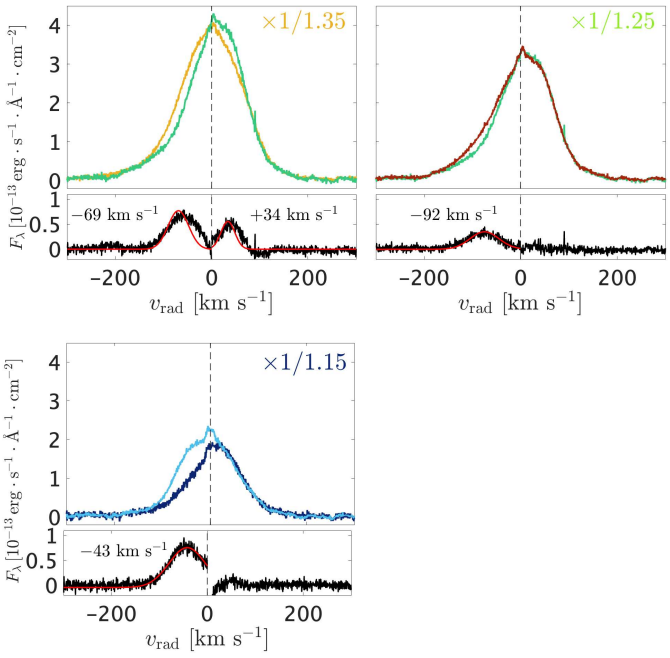

Fig. 11. Subtraction between consecutive Fe II 5317 ESPRESSO spectra. The color code is the same as in Fig. 10. The profiles were rescaled by a constant (upper right corner). The bottom panels show the subtracted profiles, with Gaussian fits superposed.

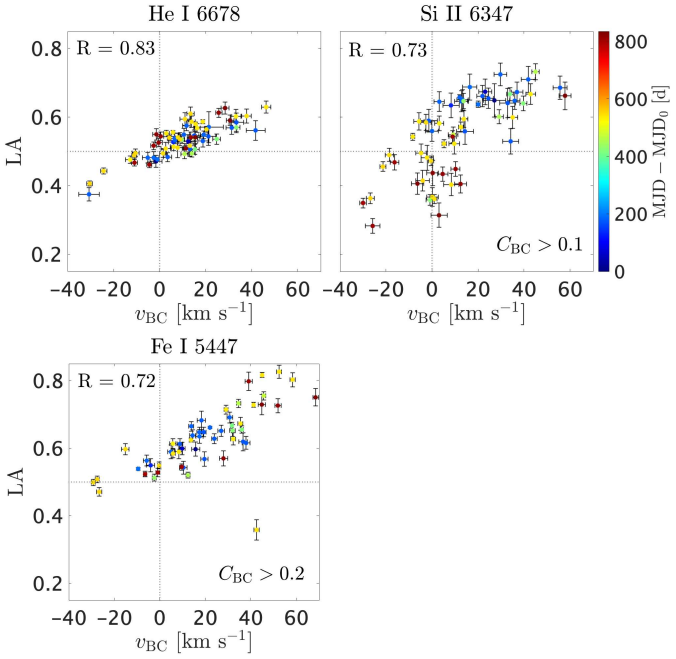

Fig. 12. Relation between $v_{\rm BC}$ and LA for the He I 6678, Si II 6347, and Fe I 5447 lines. R is the Pearson correlation coefficient.

lines. We chose the λ6678 line instead of the λ5876 line for He I because it is less optically thick, hence a better tracer of the gas dynamics. The Si II 6347 line was selected because its profile is not contaminated by photospheric absorption, given the high energy of its lower level ($E_{\rm i}$ = 8.12 eV). The lines are plotted in absolute flux in Fig. 10.

The comparison between the Fe II 5317 line profiles in the ESPRESSO spectra shows the existence of a component with a variable radial velocity. This is illustrated in Fig. 11, where three sets of two consecutive ESPRESSO observations are subtracted from each other in the Fe II 5317 line. Before subtracting, we rescaled the line profiles so that the wings matched. The subtraction reveals that the component has velocity centroids ranging between ∼−90 and ∼+35 km s^{-1} and it is responsible for the variations in the shape of the line.

The variability of the asymmetry of the BC suggests the presence of a non-axisymmetric structure rotating around the star. To further explore this scenario, we fit the other three selected lines with Gaussian functions. For all three lines, we used an asymmetric Gaussian to fit the BC. The NC of the He I 6678 line can be always discerned in our observations. Therefore, we fit the He I line profiles with a 1S+1A model. Conversely, the NC of the Fe I and Si II lines is sometimes absent or it cannot be discerned in observations with lower S/N. For this reason, we masked the profiles of these lines between –15 and +15 km s^{-1} and fit the remaining line profile with a 1A model. The fit parameters for the BCs are the strength of the component relative to the continuum ($C_{\rm BC}$), its velocity ($v_{\rm BC}$), and the widths of the blue and red wings ($\sigma_{\rm b}$ and $\sigma_{\rm r}$). From the widths, we derived the FWHM and the line asymmetry to the blue (LA) as FWHM = $\sqrt{2\ln 2}\cdot(\sigma_{\rm b}+\sigma_{\rm r})$ and LA = $\sigma_{\rm b}/(\sigma_{\rm b}+\sigma_{\rm r})$. When the line was weak relative to the continuum, the fit did not converge. For this reason, we excluded fits with $C_{\rm BC} < 0.2$ for Fe I 5447 and $C_{\rm BC} < 0.1$ for Si II 6347. The results of the best fits are displayed in Fig. 12 in the form of the relation between $v_{\rm BC}$ and LA for each emission line. There is a high (Pearson R > 0.70) positive correlation between these two parameters for each line, that is, the higher LA, the more the line center is redshifted. The He I 6678 BC is less influenced by line shifts, it is most of the times asymmetric to the blue (LA > 0.5) and redshifted. Also the Fe I 5547 BC is redshifted in 42 out of 53 observations, and it is sometimes highly blue-skewed (with LA $\gtrsim$ 0.7). The Si II 6347 BC is the only one with significant asymmetry to the red (LA < 0.5). All the lines have $v_{\rm BC}$ between −30 and +60 km s^{-1}.

A selection of four observations that highlight the variability of the line asymmetry is shown in Fig. 13. In CH 21.10 and CH 22.7 the Si II BC is blue-skewed, while in CH 22.27 and

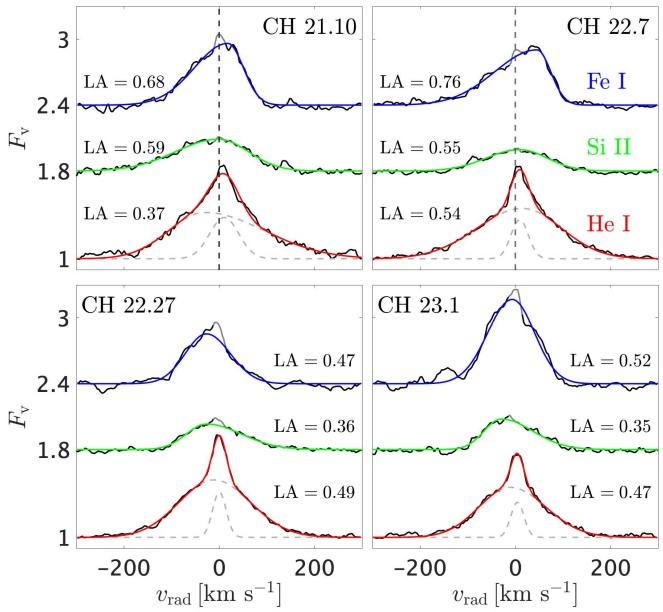

Fig. 13. Selected observations showing the variability of the asymmetry of the He I 6678, Si II 6347, and Fe I 5447 lines. Here, LA is the line asymmetry to the blue.

CH 23.1 it is red-skewed. The change from red to blue asymmetry is in agreement with what is observed in the Fe II 5317 line and further supports the hypothesis of a non-axysimmetric flow rotating around the star. Different transitions have different line asymmetries in the same observation, suggesting that although these emission lines are produced in the accretion flow, they trace different regions of it. This is confirmed by the different FWHM of the lines, which is on average ∼250, 190, and 173 km s^{-1}, for the He I, Si II, and Fe I lines, respectively. These values are compatible with a formation in a stratified flow, as observed for HM Lup (Armeni et al. 2023). The He I 6678 line has the most extreme excitation conditions among the three lines, since its upper level has E = 23.07 eV. Therefore, it must be formed closer to the star, where the gas is likely irradiated by the X-ray radiation from the shock and has higher velocity, than the Si II and Fe I lines.

6. TESS light curve

The TESS Sector 65 light curve of RU Lup is displayed in Fig. 14. We converted the TESS pre-search data conditioning simple aperture photometry (PDCSAP) flux (F) into TESS magnitudes T using the relation $T = -2.5 \log_{10} F + \mathrm{ZP}$, where ZP = 20.44 is the TESS Zero Point magnitude (Vanderspek et al. 2018). The time t is computed relative to the MJD of the beginning of the observation ($\mathrm{MJD_{beg}}$ = 60068.25).

If the hot spot has a photometric signature, we expect its maximum contribution at phase ϕ_S (Sect. 4), marked with dashed blue lines in Fig. 14. This phase is a quarter of period after the maximum blueshift and a quarter of period before the maximum redshift of the hot spot, hence it is the position where the spot area projected along the line of sight is maximum. For most cycles this phase does not coincide with a maximum in the TESS light curve. This suggests that either the hot spot does not contribute significantly to the photometry or the period detected from the analysis of the NC is not the actual rotation period of the spot. We further discuss this issue in Sect. 7.

The light curve displays two epochs of quasi-periodic bursts superposed on a base level of ∼10.2 mag. In the first epoch the system reaches 9.5 mag as maximum brightness. In the second epoch this value is reduced to 9.8 mag. The transition between these two regimes is at $t \approx 9.15$ days. A visual inspection of the light curve suggests that the typical timescale of the variability is smaller than $P_\star$. This can be seen, for example, between $\phi = 1.7$ and $\phi = 2.7$, where we observe three maxima instead of one.

We used the continuous wavelet analysis to determine the frequency content of the light curve as a function of time. In the analysis of the QPOs, we used the quality factor as a measure of the coherence of the oscillations. It is defined as $Q = P_0/\Delta P$, where P_0 is the detected period and ΔP is the FWHM of the peak. The continuous wavelet transform (CWT) of the light curve (Fig. 15) reveals how these two segments have a different frequency content. To refine the estimate of the timescales, we computed a separate Lomb-Scargle Periodogram (LSP) for each segment of the light curve. For both segments, we detected a double-peaked structure in the LSP. There is power around $P_\star$ but the peak is broad, that is, the oscillations are not coherent. For $t \lesssim 9.15$ days, we obtained $P = 1.31 \pm 0.06$ days with $Q \approx 9.1$ and $P = 2.15 \pm 0.14$ days with $Q \approx 6.5$. For $t \gtrsim 9.15$ days, we found instead $P = 1.66 \pm 0.07$ days with $Q \approx 10.1$ and $P = 2.08 \pm 0.10$ days with $Q \approx 8.7$. The 1σ uncertainties were obtained from the quality factor by converting the FWHM to the standard deviation of a Gaussian (FWHM = $2\sqrt{2 \ln 2}\sigma$). A similar multiple-peak structure of the LSP is observed in 3D MHD simulations (e.g., Kulkarni & Romanova 2009) and indicates that the oscillations are not purely sinusoidal (Romanova & Kulkarni 2009).

For both time segments, the shorter period has the higher quality factor, and we propose that this period is the actual timescale of the oscillations. We show this by superposing a sinusoidal oscillation with that period on the relative portion of the light curve. The sine function is parameterized as $\mathrm{mag}(t) = C + A \sin[2\pi(t - t_0)/P]$. We adjusted the free parameters of the sine function (i.e., C, A, and t_0) in order to visually reproduce the behavior of the QPOs. To do this, we further split the second segment in two parts, with separation at $t \approx 15.75$ days. This is the time where the light curve returns to the base level, after which the oscillations seem to be delayed by ∼0.5 days. Figure 15 shows the results of this procedure. Most of the maxima in the sinusoids match a peak in the TESS light curve. The cycle-to-cycle variability indicates that the environment traced by TESS changes on dynamical (1–2 days) timescales. We conclude that $P_1 = 1.31$ days and $P_2 = 1.66$ days are the typical timescales of the variability, while the higher period peaks in the LSPs are due to the non-sinusoidal nature of the oscillations. In the RT-unstable accretion scenario, these periods are interpreted as the Keplerian periods at the truncation radius R_T.

6.1. Contemporaneous CHIRON spectroscopy

The maximum magnitude level reached in the two segments of the TESS Sector 65 light curve differs by ∼0.3 mag, that is, a factor ∼30% in flux. The system attains the higher flux in the first segment, where the detected period is lower. 3D MHD simulations of accretion through a MBL showed how an increase in $\dot{M}_{acc}$ leads to a decrease in the detected period (Romanova & Kulkarni 2009). If the flux increase is caused by an increase in $\dot{M}_{acc}$, the change of the QPO period within the TESS Sector 65 light curve is an observational signature of R_T moving toward the

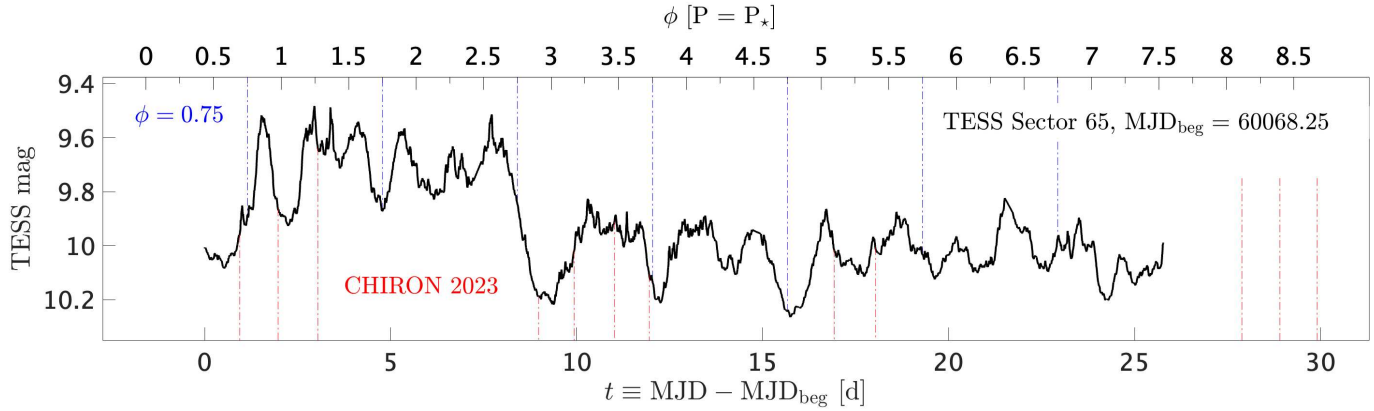

Fig. 14. TESS light curve of RU Lup from Sector 65 (2023). The light curve is plotted as a function of the time t from the beginning of the observation (MJD$_{beg}$ ≡ 60068.25). The top axis show the phase ϕ computed with P = 3.63 days (i.e., the spot period, Sect. 4.1). The reference date for ϕ = 0 is MJD$_0$ ≡ 59264.336. The blue lines mark the phase ϕ_S (from Sect. 4.1), where the maximum contribution from the hot spot is expected. The red lines mark the epochs of the CHIRON spectroscopic observations.

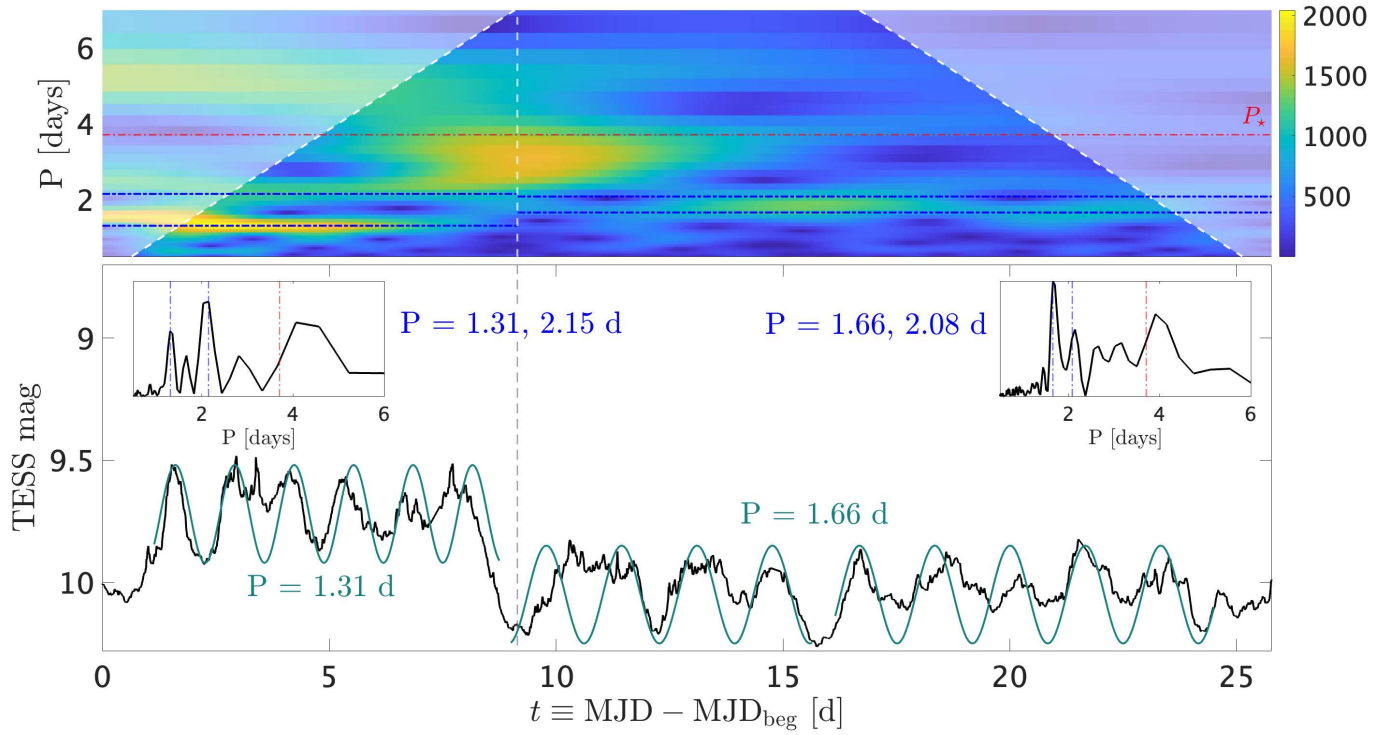

Fig. 15. Continuous wavelet analysis of the TESS Sector 65 light curve. The top panel shows the CWT. The bottom panel displays the light curve. The insets show the LSP for the two portions of the light curve. The blue and red lines mark the detected period and $P_\star$, respectively. Sinusoidal oscillations are superposed to the TESS observation in green, with the period of the oscillations in each portion reported with the same color.

star. The spectroscopic data from CHIRON confirm this hypothesis. Table A.1 shows that among the CHIRON observations from 2023 the first three spectra, which are taken in the epoch of highest flux, have the highest veiling. Figure 16 shows the Fe I 5447, Si II 6347, and Ca I 6122 lines in the 9 CHIRON observations that are simultaneous to the TESS Sector 65 light curve. The first three spectra are the ones with the higher EW of these lines, indicating that the system is in a state of higher accretion rate in the first portion of the light curve (see the discussion in Sect. 5). Assuming a constant $B_\star$ during the TESS observing run, the ratio P_1/P_2 can be converted to a ratio between accretion rates. Since $P_T \propto R_T^{3/2}$ and $R_T \propto (B_\star^2/\dot{M}_{acc})^{2/10}$ (Eq. (1)), we find $\dot{M}_{acc,1}/\dot{M}_{acc,2} = (P_1/P_2)^{-10/3} \approx 2.2$.

6.2. Oscillations from a nonstationary hot spot

All timescales observed in the TESS light curve are shorter than the stellar rotation period. There are two regions that can produce variability at such timescales: a non-axisymmetric portion of the disk that extends inward of R_{co} and rotates around the star (Sicilia-Aguilar et al. 2023), or a nonstationary hot spot on the surface of the star (Romanova & Kulkarni 2009).

A simple, planar portion of the disk which revolves around the star such as the one proposed by Sicilia-Aguilar et al. (2023) cannot account for the quasi-periodic variability observed in RU Lup. The reason is that the angle between the surface of the disk and the line of sight is constant, since the disk lies on a plane. If the structure is located in the disk, it must have a

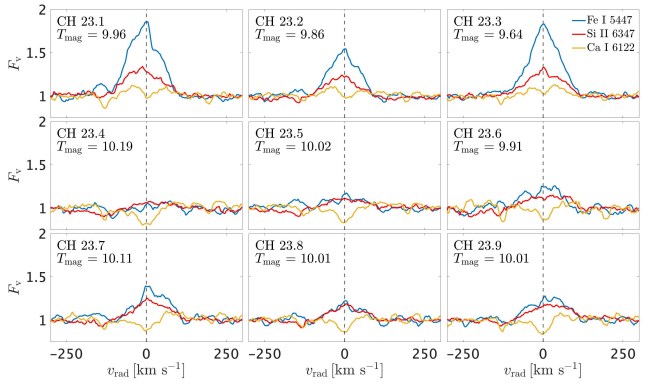

Fig. 16. Normalized profiles of the Fe I 5447, Si II 6347, and Ca I 6122 lines in the 9 CHIRON spectra that are contemporaneous to the TESS Sector 65 light curve. T_{mag} is the TESS magnitude at these epochs.

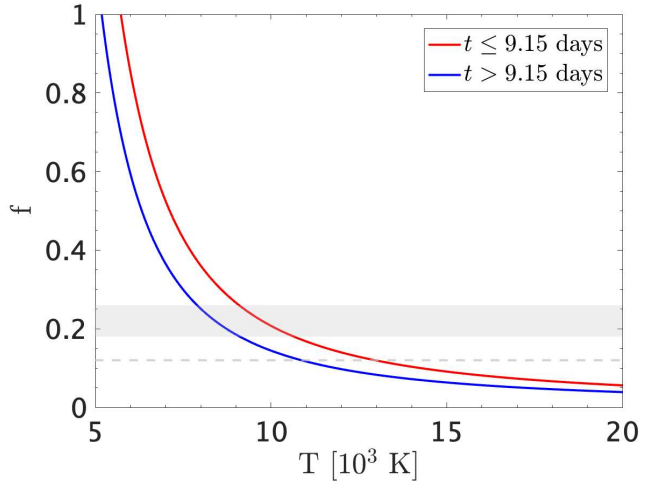

Fig. 17. Relation between the filling factor (f) and the temperature (T) (Appendix D), for a spot that reproduces the modulations observed in the TESS Sector 65 light curve. The gray area marks $0.18 \leq f \leq 0.26$ (Wendeborn et al. 2024a), while the dashed line marks $f = 0.12$ (Dodin & Lamzin 2012).

more complicated configuration, such that its projected surface changes as it revolves around the star.

On the other hand, a moving hot spot on the surface of the star can reproduce the observed variability, since its projected area varies with the azimuthal position as the spot rotates. The amplitude and zero point of the oscillations observed with TESS can be reproduced with an analytical model, assuming a spot with temperature T and filling factor f, located at a latitude θ_S on the stellar surface (Appendix D). We analyzed the two portions of the light curve with different maximum fluxes separately. We obtained $\theta_{S1} = 61°$ and $\theta_{S2} = 65°$ for the latitude of the spot in the two segments (Eq. (D.7)). Figure 17 shows the degenerate relation between the filling factor and the temperature of the spot that best fits the modulations in the light curve (Eq. (D.8)). The analytical model indicates that the spot is either more extended or hotter, or both, during the epoch of increased accretion ($t \leq 9.15$ days in Fig. 17).

7. Discussion

There are two main results of this work. First, the narrow component of the He I 5876 line is modulated with a period of 3.63 days, close to $P_\star = 3.71$ days derived by Stempels et al. (2007) from the radial velocity changes in the absorption lines of RU Lup. The fact that v_{NC} is in anti-phase with v_{phot} indicates that the photospheric lines are distorted by narrow emission components produced in a hot spot (Sect. 4.3) and not by a cold spot as suggested by Stempels et al. (2007).

Second, the timescales detected in the TESS light curve of RU Lup are shorter than $P_\star$, and they can be interpreted as evidence of accretion from inward of R_{co}. The photometric variability can be produced by either a complex warped structure in the disk or spot(s) on the stellar surface. In addition, we observed a change in the period throughout the TESS light curve that appears to be related to variations in $\dot{M}_{acc}$. In the rest of the section, we discuss scenarios that might explain the discrepancy between the timescales detected in spectroscopy and photometry. We conclude the discussion with the analysis of the accretion flow inferred from the emission lines.

7.1. TESS light curve and regime of accretion

The study of the frequency spectrum of the TESS light curve allows us to obtain an indirect measure of the position of the truncation radius R_T. Interpreting $P_1 = 1.31$ days and $P_2 = 1.66$ days (Sect. 6) as the Keplerian rotation at the truncation radius R_T, we convert these measures to positions of R_T using $R_T/R_{co} = (P_T/P_\star)^{2/3}$. We obtain $R_T = 0.5\ R_{co}$ for the first epoch and $R_T = 0.59\ R_{co}$ for the second epoch. The derived R_T/R_{co} ratios indicate that RU Lup accretes in a RT-unstable regime (Blinova et al. 2016; Pantolmos et al. 2020), in agreement with the result by Stock et al. (2022). Together with the estimate of R_{co} (Table 1), we find that R_T is approximately 2 $R_\star$ (~1.82 $R_\star$ and ~2.15 $R_\star$ for the first and second epoch, respectively).

The position of the truncation radius can be estimated independently, knowing $\dot{M}_{acc}$ and $B_\star$ (Eq. (1)). We obtained an estimate of $\dot{M}_{acc}$ for the CH 23.4 spectrum[4] using the He I 5876 line as follows. We calculated the line luminosity from the integrated flux of the line using the *Gaia* DR3 distance (Table 1) and converted it to an accretion luminosity (L_{acc}) using the relation calibrated by Alcalá et al. (2017). Then, assuming that the free-fall starts at R_{co} (i.e., $R_T = R_{co}$), we derived $\dot{M}_{acc}$ by inverting the relation

$$L_{acc} = \frac{GM_\star \dot{M}_{acc}}{R_\star}\left(1 - \frac{R_\star}{R_T}\right) \quad (3)$$

(Hartmann et al. 2016). We obtained $\dot{M}_{acc} = 1.48 \times 10^{-7}\ M_\odot\ yr^{-1}$. Using the upper limit of ~0.5 kG derived by Johnstone & Penston (1986) for the dipolar magnetic field of RU Lup, we find an upper limit of 2.1 $R_\star$ for R_T, in good agreement with the values inferred photometrically[5].

Blinova et al. (2016) showed that the unstable regime can be divided in two sub-regimes; namely, the chaotic regime and the ordered (or MBL, Romanova & Kulkarni 2009) regime. The difference between the two regimes is in the stability of the QPOs. In the chaotic regime, short-lived hot spots, which last for only a few rotations around the star, produce short-duration QPOs (Kulkarni & Romanova 2009). In the MBL regime, the QPOs are more stable (Romanova & Kulkarni 2009). The clear QPOs observed throughout the TESS Sector 65 light curve are

[4] We used this spectrum because it is the only one that is absolutely flux-calibrated among the CHIRON spectra from 2023.
[5] This derivation has the subtlety that the spectroscopic estimate of $\dot{M}_{acc}$ depends in turn on R_T.

more compatible with the latter regime of accretion. The values of R_T/R_{co} that we derived above are in agreement with the results of 3D MHD simulations of accretion in the MBL regime ($R_T/R_{co} \lesssim 0.59$, Blinova et al. 2016). In this scenario, accretion proceeds in two ordered tongues controlled by the RT instability, which produce hot spots on the surface of the star.

7.2. Properties of the hot spot inferred from spectroscopy

The radial velocity amplitude of the He I 5876 NC modulation is smaller than $v \sin i$, indicating that the NC-emitting region is located on the stellar surface, at high latitude. The NC emission in high energy lines (e.g., He I and He II) identify this region as the post-shock region.

The red asymmetry observed in the NC of the He I line, with emission up to ∼+100 km s^{-1} (i.e., $\sim 3\sigma_r$ for He I, Fig. 6) is compatible with formation in the post-shock region, where the gas decelerates to 1/4 of the pre-shock velocity (Hartmann et al. 2016). The blue wing of the line might be indicative of the broadening mechanism, with either thermal or turbulent motions that broaden the emission line. Using $\sigma = (2k_B T/Am_p)^{1/2}$, where k_B is the Boltzmann constant, m_p is the proton mass, and $A = 4$ is the atomic number of helium, we get an upper limit of ∼50 000 K for the temperature of the post-shock region from $\sigma_b = 14$ km s^{-1} (Fig. 6). The post-shock region cools in X-rays (Lamzin 1999; Sacco et al. 2008) and high energy ultraviolet lines (Ardila et al. 2013). Therefore, we do not expect it to directly contribute in the TESS bandpass. In that wavelength range, most of the contribution comes from the heated photosphere below the shock (Calvet & Gullbring 1998). This region is heated from above by 3/4 of the shock energy, reaching temperatures up to ∼8000 K (Hartmann et al. 2016).

Dodin & Lamzin (2012) showed that the heated photosphere not only emits in the continuum, but is also responsible for the emission in the NC of the metallic species. The NCs are formed in a layer with a temperature inversion (i.e., a chromospheric-like structure) above the continuum-emitting region. Our analysis of the NCs possibly highlights the vertical stratification of this layer. The more energetic lines (Fe II and Si II) are indeed more asymmetric to the red than the less energetic ones (Fe I and Mg I), suggesting that the former could originate in the upper part of this structure (at higher T) and still have a residual infall velocity, as sketched in Fig. 18.

In Sect. 4.4, we showed how the veiling spectrum of RU Lup at 5800 Å is composed of a continuum plus line emission that fills in the photospheric absorption lines. The anticorrelation between v_{NC} of the He I 5876 line and v_{phot} (Sect. 4.3) imply that the veiling spectrum is formed in a confined region on the stellar surface, in other words, a spot. This spot, which we identify as the heated photosphere below the post-shock region, must also contribute to the emission in the TESS bandpass, which extends from 5800 to 11 200 Å.

7.3. Properties of the hot spot inferred from photometry

By using the analytical model of Appendix D, we were able to infer the properties of the photometric spot, assuming that it is nonstationary on the surface of the star. The degeneracy between the filling factor and the temperature of the spot can be removed by considering values of f from the literature. Using a typical value of $f \approx 0.05$ for CTTSs (Calvet & Gullbring 1998; Calvet et al. 2004), we get a temperature of ∼20 000 K for the spot. However, specific works on RU Lup showed how the filling factor of the spot is higher than the usual values for CTTSs.

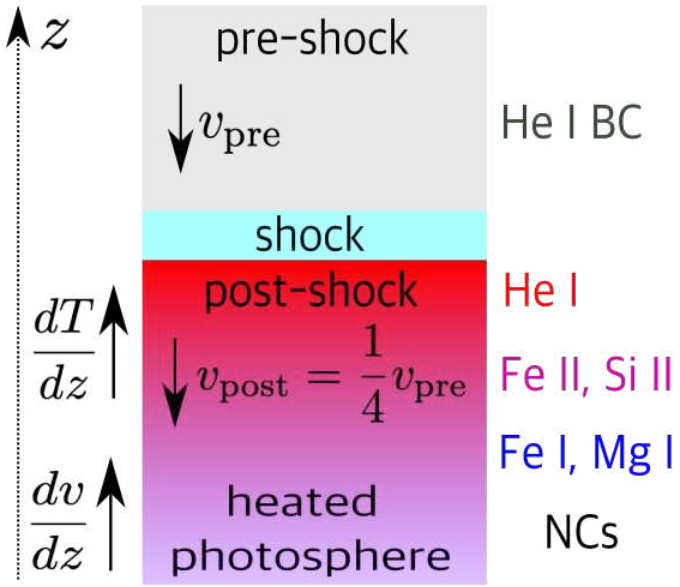

Fig. 18. Sketch of the possible vertical stratification of the hot spot inferred from the analysis of the NCs. v_{pre} and v_{post} are the pre-shock and post-shock velocities.

In Fig. 17 we report the values obtained by Wendeborn et al. (2024a) from a best fit of the 2021 ultraviolet spectra of RU Lup with a shock model ($0.18 \leq f \leq 0.26$) and the value derived by Dodin & Lamzin (2012) by fitting the veiling spectrum of RU Lup ($f = 0.12$). In these cases, we obtain a colder spot with $T \sim 8000 - 12\,000$ K, more compatible with the typical values for CTTSs (Hartmann et al. 2016).

Assuming a spherical cap geometry for the spot (Appendix E), and a filling factor between 0.1 and 0.2 as mentioned in the previous literature of RU Lup, the half-opening angle of the spot is between 37° and 57°. If the hot spot is as extended as that, then the spot model from Appendix D is too simplistic and the derived θ_S must be regarded as an average latitude of the continuum-emitting region.

7.4. Comparison between spectroscopy, photometry, and magnetohydrodynamic simulations of the spot

The spectroscopic results on the hot spot seem to disagree with what is derived from the analysis of the TESS light curve and with the results of 3D MHD simulations of a system accreting in the MBL regime, due to the latitude/extension of the spots and the detected timescales. We propose that the spectroscopic and photometric spot are part of the same structure, which we identify as the region in which the accreting gas impacts the stellar surface. The He I NC – that is, the tracer of the spectroscopic spot – originates in the post-shock region. The continuum emission in the TESS bandpass, associated with the photometric spot, is formed instead in the heated photosphere below the shock. This region emits also in the NC of the metallic species and it is responsible for the line-filling component of the veiling (Dodin & Lamzin 2012).

Considering the typical extension of the spot in RU Lup ($f \approx 0.1$–0.2), we might expect a discrepancy between the latitude derived from spectroscopy and photometry. The region traced by the He I NC (i.e., the post-shock region) must be somewhat less extended than the heated photosphere traced by TESS. Otherwise, considering the low inclination of the system and

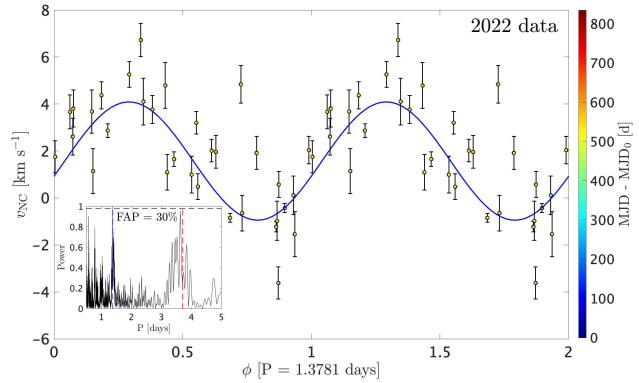

Fig. 19. Radial velocity curve of the He I 5876 NC for the 2022 observations only. The inset shows the LSP, with the detected P and $P_\star$ marked with dashed blue and red lines, respectively.

the intrinsic variability of this region as a consequence of the accretion process, it would be impossible to detect a rotational modulation (Sicilia-Aguilar et al. 2023).

A possible explanation of the inconsistency in the detected periods lies in the variability of the mass accretion rate. The 3.63 day period was derived in Sect. 4.1 using data from epochs that have different $\dot{M}_{\rm acc}$. In Sect. 6 we discussed how variations in the accretion rate lead to variations in the detected period. Stock et al. (2022) showed that the accretion rate of RU Lup varies by a factor of ∼2 on a timescale of weeks. Since $P_{\rm T} \propto \dot{M}_{\rm acc}^{-3/10}$ (Eq. (1)), this means that the period of a nonstationary hot spot would vary by a factor of $2^{3/10} \approx 1.23$ on such timescales. If the He I 5876 NC traces a nonstationary hot spot on the stellar surface produced by tongues originating at $R_{\rm T}$, it is plausible that its radial velocity is modulated with both $P_\star$ and the inner disk period ($P_{\rm T}$). In this situation, if one were to look for periodicity combining observations that represent different accretion states, the power at $P_\star$ would be enhanced in the periodogram because of the stability of this period among different epochs.

These complications are illustrated in Fig. 19, where we recomputed the LSP of the He I 5876 NC using only the data from 2022. The periodogram has maximum power at P = 1.38 days, but the FAP of this signal is >30%; that is, it is not statistically significant. The second highest peak is close to $P_\star$. The period with maximum power is similar to the periods derived from TESS. This suggests that the apparent lack of continuum emission from the spot (Sect. 6) could be actually caused by an incorrect phase-folding of the radial velocity of the He I 5876 NC. If the period of the hot spot is not correct, then the phase ϕ_S where we expect its maximum contribution is different from what we derived, and might be in agreement with maxima in the TESS light curve.

Therefore, we conclude that in the MBL picture the disagreement between the period detected from spectroscopy ($P_\star$) and the period inferred from photometry ($<P_\star$) might be attributed to an observational problem, namely, the difficulty of tracing a hot spot that rotates with the inner disk period, with the latter being sensitive to variations in $\dot{M}_{\rm acc}$.

7.5. Alternative explanations: sub-structure of the spot and inner disk warp

Although accretion in the MBL regime can explain the photometric behavior of RU Lup, the detected periods are close to $P_\star/2$. Hence, the photometric behavior could also be explained with a modulation at a period close to $P_\star$ but with a brightness distribution on the visible hemisphere more closely resembling two hot spots; that is, a single, extended hot spot that has a non-homogeneous surface brightness, such that we see two brighter features. The brightness distribution of this region could vary on dynamical timescales and the detected periods could be aliases produced by the complex structure of this region. Similarly, the change in the quasi-period between the two epochs of the TESS light curve could be due to an intrinsic variability in the shape and brightness of this extended spot. Since the velocity modulation of emission lines mainly traces the average brightness distribution, a large non-homogeneous spot would lead to a modulation at $\sim P_\star$ in the radial velocity of the NCs, as we observe for the He I 5876 line.

Periods close to $P_\star$ would be compatible with a scenario in which RU Lup is in a stable accretion regime. However, 3D MHD simulations of accretion in the stable regime showed how the spots are formed close to the magnetic pole and are antipodal (e.g., Romanova et al. 2003, 2004) so that it is unlikely to see two distinct, antipodal spots given the low inclination ($i_\star = 16 \pm 6\,^\circ$) of the stellar rotation axis in RU Lup. Rather, the brightness modulation would require sub-structure of a single spot. MHD simulations of accretion in the stable regime predict the hot spots to be bow-shaped around the magnetic axis (Romanova et al. 2004) with a temperature gradient from the center to the edges (Kulkarni & Romanova 2013); that is, a structure that is different from the requirements of period aliasing. Hence, the structure of the hot spot must be somewhat different from what is predicted by 3D MHD simulations if accretion in RU Lup proceeds in the stable regime. Moreover, independent of the true variability, the TESS light curve shows that the dominant periodicity changes, with the shorter period pertaining to epochs with higher (optical) luminosity, in agreement with MHD models of accretion in the unstable regime (Kulkarni & Romanova 2009). Therefore, we think that the MBL scenario fits the observations better than the hypothesis of accretion in a stable regime.

A third explanation is motivated by the high values of the filling factor that we derived for RU Lup. Such a high (0.1–0.2) filling factor could be achieved if the part of the continuum-emitting region lies in the disk. In Sect. 6.2 we discussed how a structure located in the disk must have a complex geometry in order to produce a quasi-periodic modulation. A warp in the inner disk inward of $R_{\rm co}$ might satisfy this condition, and would naturally explain the observed timescales. In this scenario, the continuum emitting region would be spatially separated from the region emitting in the NCs, because the latter is unequivocally associated with shocked gas on the stellar surface. Such a structure could be characteristic of systems accreting through a compact magnetosphere, and it might be a non-axisymmetric version of the classical boundary layer. To our knowledge, no models of quasi periodic oscillations from a warped structure in the disk have been studied.

7.6. Inner disk dynamics

7.6.1. Structure of the flow

The width of the metallic lines points toward an origin in the circumstellar matter. Their velocity centroids ($v_{\rm BC}$) are between −30 and +60 km s^{-1} (Fig. 12), compatible with the projected velocities of flows within the inner disk. For a Keplerian disk seen at an inclination i, the radial velocity is

$$v_{\rm rad}(r, \phi_{\rm D}) = \sqrt{\frac{GM_\star}{r}} \sin i \sin \phi_{\rm D} \quad (4)$$

where r is the distance from the star and ϕ_D is the azimuth relative to the observer (e.g., Horne & Marsh 1986). For $i = 16°$ (Table 1), we get a maximum v_{rad} of ∼50, 45, 40, and 30 km s^{-1} for $r = 0.4, 0.5, 0.6$, and 1 R_{co}. Hence, the observed v_{BC} values are compatible with the position of the truncation radius derived from TESS data, suggesting that the lines are formed in a disk-like structure that revolves around the star.

To reproduce the variability of the line asymmetry, this structure must be non-axisymmetric, and it might look like a portion of a Keplerian disk, as proposed by Sicilia-Aguilar et al. (2023) to model the BC variability of the Ca II lines in EX Lup. However, the lines are much broader than the maximum v_{rad} that can be observed from a Keplerian disk, that is, $(GM_\star/R_\star)^{1/2} \sin i \approx 60$ km s^{-1} for RU Lup. Therefore, they are either broadened by turbulent motions in the Keplerian portion of the disk, as proposed by Sicilia-Aguilar et al. (2023), or formed in a flow with higher velocities.

In the case of RU Lup, the analysis of the Fe II 5317 line (Fig. 11) reveals how a turbulent portion of a Keplerian disk cannot completely account for the line velocities. The discrete emission components detected with the subtraction of consecutive spectra have centroids – bulk velocities $>(GM_\star/R_\star)^{1/2} \sin i$ – indicating that part of the line emission is produced by macroscopic flows in non-Keplerian motion.

Radial velocities of the order of 100–150 km s^{-1} are compatible with free fall along dipolar magnetic field lines. The free fall velocity starting from rest at R_T is

$$v_{ff}(r) = \sqrt{GM_\star \left(\frac{1}{r} - \frac{1}{R_T}\right)}. \quad (5)$$

For $R_T = 2\ R_\star$ (Sect. 6) we get $v_{ff}(R_\star) \approx 205$ km s^{-1}. The observed velocity is significantly lower for a pole-on system, because the velocity vector of the gas moving along the magnetic field lines is almost transverse to the line of sight. The observed radial velocity is reduced by a factor

$$\frac{(3/2)\sin 2\theta \cos\phi \sin i + (2 - 3\cos^2\theta)\cos i}{\sqrt{4 - 3\cos^2\theta}} \quad (6)$$

(Calvet & Hartmann 1992; Wilson et al. 2022). Here, θ is the latitude, ϕ is the azimuth relative to the observer, and the gas is assumed to be moving along a dipolar streamline with equation $r = R_T \cos^2\theta$. The maximum redshifted and blueshifted radial velocities that can be observed are obtained for $\phi = 0$ and π and are +110 and −60 km s^{-1}, respectively, assuming $R_T = 2\ R_\star$. The fact that the maximum negative v_{rad} is lower than maximum positive v_{rad} is a projection effect. This red-blue asymmetry is similar to the variation in v_{BC} for RU Lup throughout our observations. This argues in favor of line formation in a magnetospheric accretion column and against formation in a structure that is confined to a plane, such as a Keplerian disk or equatorial accretion tongues. In that case, the redshifted and blueshifted line shifts would be the same.

7.6.2. Temperature stratification

The different line widths, which correlate with the excitation energy of the analyzed emission lines (Sect. 5), indicate the existence of a stratification in the accretion flow of RU Lup. The He I lines must be formed close to the shock in high temperature conditions, and their higher FWHM relative to the Fe I and Si II lines indicate a formation in a flow with higher velocities.

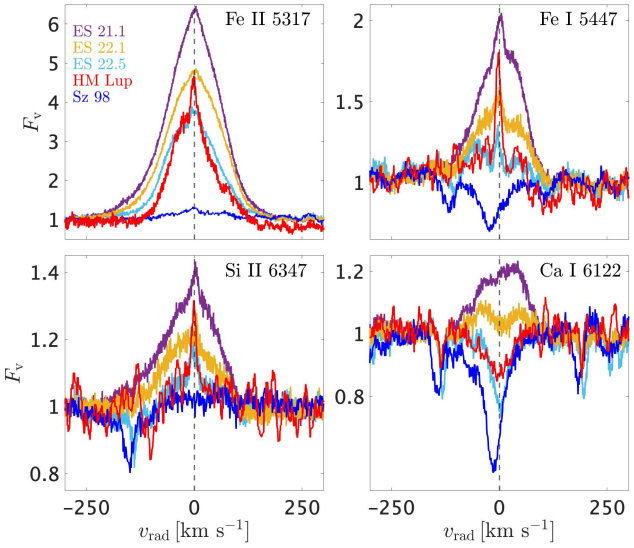

Fig. 20. A selection of metallic lines in the spectra of RU Lup, HM Lup, and Sz 98.

Conversely, neutral species like Fe I and Ca I are formed closer to the disk, where the material starts to accrete onto the star in accretion tongues. This region must be non-axisymmetric in order to explain the line variability, and it might be similar to the azimuthally-limited Keplerian disk proposed by Sicilia-Aguilar et al. (2023). The singly ionized species such as Fe II and Si II have velocities that are not consistent with Keplerian flows, and require higher temperature conditions than what can be achieved in an irradiated disk. The extreme line asymmetry to the red that is sometimes observed in the Si II 6347 line (see Fig. 13) suggests that these species are partly formed in the flow along the magnetic field lines. The different line asymmetry observed for emission lines from the same observation support the stratification hypothesis, since lines tracing different regions of the accretion flow might be asymmetric at different times.

In conclusion, the variability of the He I and metallic lines can be explained with the lines being formed in a temperature stratified structure which is a combination of a non-axisymmetric Keplerian disk and an inflow along magnetic field lines. This structure is sensitive to variations in the accretion rate.

7.7. Formation of the metallic lines

Analogous to the case of the H I, He I, and Ca II lines (Alcalá et al. 2017), one would expect the strength of the metallic lines to be dependent on $\dot{M}_{acc}$. Figure 20 compares RU Lup with two other CTTSs; namely HM Lup, which shows prominent metallic emission, and Sz 98, which has the same stellar parameters of RU Lup (Manara et al. 2023). We show the second ESPRESSO observation analyzed by Armeni et al. (2023) for HM Lup, and an Ultraviolet and Visual Echelle Spectrograph (UVES, Dekker et al. 2000) spectrum taken on 10/05/2022 as part of the PENELLOPE survey for Sz 98. The accretion rates for HM Lup and Sz 98, taken from the literature, are $0.95 \times 10^{-8}\ M_\odot$ yr^{-1} (Armeni et al. 2023) and $3.6 \times 10^{-8}\ M_\odot$ yr^{-1} (Manara et al. 2023), respectively.

The comparison between the spectrum of HM Lup and the ES 22.5 spectrum of RU Lup shows that despite $\dot{M}_{acc}$ being one order of magnitude lower for HM Lup, the emission line profiles are very similar. The only strong emission line is Fe II 5317. The Fe I 5447 and Si II 6347 lines are weak, while the Ca I 6122 is

in absorption in both spectra. Although Sz 98 has $\dot{M}_{\rm acc}$ between HM Lup and RU Lup, Fig. 20 shows how the metallic lines are very weak in its spectrum. The only detectable emission is in Fe II 5317, with the line being slightly above the continuum. This suggests that the strength of these transitions relative to the continuum is not directly related to $\dot{M}_{\rm acc}$. We propose that the actual parameter that controls the strength of the metallic lines is the ratio $R_{\rm T}/R_{\rm co}$. The smaller this ratio is, the stronger the emission lines are. Different species appear at different $R_{\rm T}/R_{\rm co}$ ratios, with the Fe II lines being the first ones that show up, followed by the Fe I and Si II lines, and, finally, from the Ca I $\lambda\lambda$ 6103, 6122 doublet. This transition is visually illustrated by the ES 22.5, ES 22.2 and ES 21.1 spectra in Fig 20.

If related to $R_{\rm T}/R_{\rm co}$, emission in metallic species is a direct indication of accretion in the RT-unstable regime. This can be explained by a simple energetic argument. When $R_{\rm T} < R_{\rm co}$, the material at $R_{\rm T}$ rotates faster than the star. Since the magnetic field lines co-rotate with the star, the gas must dissipate energy and angular momentum in order to accrete. This dissipation could give rise to the local heating required to collisionally excite the metallic lines (Beristain et al. 1998).

8. Conclusions

We have presented a spectrophotometric study of the CTTS RU Lup. Figure 21 shows a schematic picture of the circumstellar environment of RU Lup that we inferred from our observations. The main results are the following.

- We have improved the measurement of the stellar parameters, summarized in Table 1.
- We detected a modulation at a period of 3.63 days, close to $P_\star$ = 3.71 days (Stempels et al. 2007), in the NC of the He I 5876 line, indicating the presence of a compact region on the stellar surface that we identify as the post-shock region that originates at the footprint of the magnetic field.
- The heated photosphere below the accretion shock (i.e., a hot spot) is also responsible for the veiling of the photospheric lines in the spectrum.
- This veiling spectrum is composed of a continuum component plus line emission that fills in the stellar absorption lines. The use of flux-calibrated, high-resolution spectra allowed us to disentangle these two contributions.
- We detected timescales shorter than $P_\star$ in the TESS light curve of RU Lup. These timescales are related to the Keplerian period at the truncation radius, $R_{\rm T}$.
- From these timescales, we inferred the size of the magnetosphere of RU Lup to be ~2 $R_\star$.
- The behavior of the TESS Sector 65 light curve of RU Lup is consistent with simulations of accretion through a MBL (Romanova & Kulkarni 2009), in which the QPOs are produced by a non-stationary hot spot on the stellar surface.
- The hot spot is not as equatorial as predicted by the MHD simulations of accretion in the MBL regime, and it appears to be more extended than in typical CTTSs, with a filling factor of ~0.1–0.2.
- Alternatively, more complex explanations would require either a spot with a complex shape, perhaps made of two brighter knots which vary on dynamical timescales, or a warped structure in the inner disk.
- The BCs are formed in a non-axisymmetric, temperature stratified flow around the star in which the gas leaves the accretion disk at $R_{\rm T}$ and accretes onto the star in tongues of matter channeled by the magnetic field.

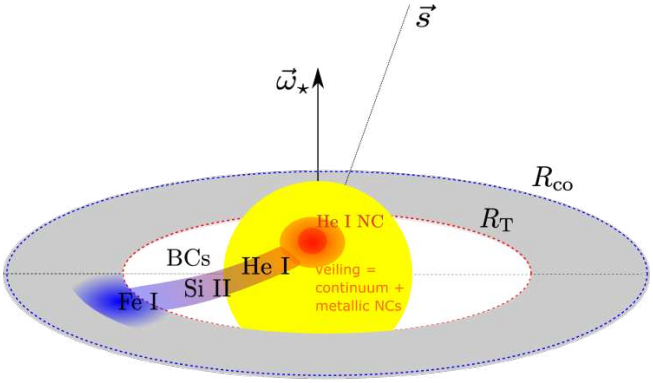

Fig. 21. Schematic picture of the circumstellar environment of RU Lup. $\omega_\star$ and $\hat{s}$ are the stellar rotation axis and the line of sight to the observer, respectively.

- The strength of the metallic emission lines might be an indicator of accretion in the RT-unstable regime, being related to the ratio between $R_{\rm T}$ and $R_{\rm co}$.

The spectrophotometric analysis presented in this work revealed the complexity of the accretion process in RU Lup, and showed how the physics regulating the accretion flow in this system might be somewhat different from the current theoretical paradigms of accreting CTTSs. Future studies should aim at covering high-cadence photometric data (TESS) with high-resolution spectroscopic observations, in order to try to infer the structure of the spot. An update of the measurement of the stellar magnetic field through spectro-polarimetry would be needed to more precisely derive the position of the truncation radius and confirm or reject the hypothesis of accretion through a compact magnetosphere.

Acknowledgements. The authors thank the anonymous referee for their review of this manuscript. This work has been supported by Deutsche Forschungsgemeinschaft (DFG) in the framework of the YTTHACA Project (469334657) under the project codes STE 1068/9-1 and MA 8447/1-1. PCS acknowledges support from DLR 50 OR 2205. AF, EF, and JMA acknowledge financial support from the project PRIN-INAF 2019 "Spectroscopically Tracing the Disk Dispersal Evolution" (STRADE) and the Large Grant INAF 2022 "YSOs Outflows, Disks and Accretion: towards a global framework for the evolution of planet forming systems" (YODA). CFM and JCW are funded by the European Union (ERC, WANDA, 101039452). Views and opinions expressed are however those of the author(s) only and do not necessarily reflect those of the European Union or the European Research Council Executive Agency. Neither the European Union nor the granting authority can be held responsible for them. JFG was supported by Fundação para a Ciência e Tecnologia (FCT) through the research grants UIDB/04434/2020 and UIDP/04434/2020. This work benefited from discussions with the ODYSSEUS team[6] (HST AR-16129). Observing time with Chiron was awarded through NOIRLab programs 2022a-492217, 2022B-994458, and 2023A-579477 (PI FMW). Chiron is operated by the SMARTS Consortium. Funding for the TESS mission is provided by NASA's Science Mission directorate. The authors acknowledge Thomas Sperling, Michael Siwak, Ignacio Mendigutía, Konstantin Grankin, Rebeca Garcia López, and Jerome Bouvier for comments and suggestions on this work. The authors acknowledge with thanks the variable star observations from the *AAVSO International Database* contributed by observers worldwide and used in this research, and Elizabeth Waagen for coordinating the AAVSO Alerts. The authors acknowledge the use of the electronic bibliography maintained by the NASA/ADS[7] system.

References

Alcalá, J. M., Manara, C. F., Natta, A., et al. 2017, A&A, 600, A20
Alencar, S. H. P., Bouvier, J., Walter, F. M., et al. 2012, A&A, 541, A116
Ardila, D. R., Herczeg, G. J., Gregory, S. G., et al. 2013, ApJS, 207, 1
Armeni, A., Stelzer, B., Claes, R. A. B., et al. 2023, A&A, 679, A14

[6] https://sites.bu.edu/odysseus/
[7] https://ui.adsabs.harvard.edu

Azevedo, R., Calvet, N., Hartmann, L., et al. 2006, A&A, 456, 225
Beristain, G., Edwards, S., & Kwan, J. 1998, ApJ, 499, 828
Beristain, G., Edwards, S., & Kwan, J. 2001, ApJ, 551, 1037
Blinova, A. A., Romanova, M. M., & Lovelace, R. V. E. 2016, MNRAS, 459, 2354
Bouvier, J., Alencar, S. H. P., Boutelier, T., et al. 2007a, A&A, 463, 1017
Bouvier, J., Alencar, S. H. P., Harries, T. J., Johns-Krull, C. M., & Romanova, M. M. 2007b, in Protostars and Planets V, eds. B. Reipurth, D. Jewitt, & K. Keil, 479
Calvet, N., & Gullbring, E. 1998, ApJ, 509, 802
Calvet, N., & Hartmann, L. 1992, ApJ, 386, 239
Calvet, N., Muzerolle, J., Briceño, C., et al. 2004, AJ, 128, 1294
Campbell-White, J., Sicilia-Aguilar, A., Manara, C. F., et al. 2021, MNRAS, 507, 3331
Dekker, H., D'Odorico, S., Kaufer, A., Delabre, B., & Kotzlowski, H. 2000, SPIE Conf. Ser., 4008, 534
Dodin, A. V., & Lamzin, S. A. 2012, Astron. Lett., 38, 649
Espaillat, C. C., Robinson, C. E., Romanova, M. M., et al. 2021, Nature, 597, 41
Espaillat, C. C., Herczeg, G. J., Thanathibodee, T., et al. 2022, AJ, 163, 114
Frasca, A., Biazzo, K., Lanzafame, A. C., et al. 2015, A&A, 575, A4
Frasca, A., Biazzo, K., Alcalá, J. M., et al. 2017, A&A, 602, A33
Gahm, G. F., Walter, F. M., Stempels, H. C., Petrov, P. P., & Herczeg, G. J. 2008, A&A, 482, L35
Gaia Collaboration (Brown, A. G. A., et al.) 2021, A&A, 649, A1
GRAVITY Collaboration (Perraut, K., et al.) 2021, A&A, 655, A73
Hartigan, P., Hartmann, L., Kenyon, S., Hewett, R., & Stauffer, J. 1989, ApJS, 70, 899
Hartmann, L., Herczeg, G., & Calvet, N. 2016, ARA&A, 54, 135
Herbig, G. H. 1962, A&A, 1, 47
Herczeg, G. J., Walter, F. M., Linsky, J. L., et al. 2005, AJ, 129, 2777
Herczeg, G. J., Chen, Y., Donati, J.-F., et al. 2023, ApJ, 956, 102
Horne, K., & Marsh, T. R. 1986, MNRAS, 218, 761
Johnstone, R. M., & Penston, M. V. 1986, MNRAS, 219, 927
Joy, A. H. 1945, ApJ, 102, 168
Kulkarni, A. K., & Romanova, M. M. 2008, MNRAS, 386, 673
Kulkarni, A. K., & Romanova, M. M. 2009, MNRAS, 398, 701
Kulkarni, A. K., & Romanova, M. M. 2013, MNRAS, 433, 3048
Lamzin, S. A. 1999, Astron. Lett., 25, 430
Lomb, N. R. 1976, Ap&SS, 39, 447
Manara, C. F., Frasca, A., Venuti, L., et al. 2021, A&A, 650, A196
Manara, C. F., Ansdell, M., Rosotti, G. P., et al. 2023, in Protostars and Planets VII, 534, eds. S. Inutsuka, Y. Aikawa, T. Muto, K. Tomida, & M. Tamura, 539
Mayor, M., Pepe, F., Queloz, D., et al. 2003, The Messenger, 114, 20
McGinnis, P., Bouvier, J., & Gallet, F. 2020, MNRAS, 497, 2142
Muzerolle, J., Hartmann, L., & Calvet, N. 1998, AJ, 116, 455
Pantolmos, G., Zanni, C., & Bouvier, J. 2020, A&A, 643, A129
Pepe, F., Cristiani, S., Rebolo, R., et al. 2021, A&A, 645, A96
Percy, J. R., Esteves, S., Glasheen, J., et al. 2010, JAAVSO, 38, 151
Petrov, P. P., Gahm, G. F., Gameiro, J. F., et al. 2001, A&A, 369, 993
Petrov, P. P., Gahm, G. F., Stempels, H. C., Walter, F. M., & Artemenko, S. A. 2011, A&A, 535, A6
Rei, A. C. S., Petrov, P. P., & Gameiro, J. F. 2018, A&A, 610, A40
Ricker, G. R., Winn, J. N., Vanderspek, R., et al. 2014, SPIE Conf. Ser., 9143, 914320
Rodrigo, C., & Solano, E. 2020, in XIV.0 Scientific Meeting of the Spanish Astronomical Society, 182
Roman-Duval, J., Proffitt, C. R., Taylor, J. M., et al. 2020, RNAAS, 4, 205
Romanova, M. M., & Kulkarni, A. K. 2009, MNRAS, 398, 1105
Romanova, M. M., & Owocki, S. P. 2015, Space Sci. Rev., 191, 339
Romanova, M. M., Ustyugova, G. V., Koldoba, A. V., Wick, J. V., & Lovelace, R. V. E. 2003, ApJ, 595, 1009
Romanova, M. M., Ustyugova, G. V., Koldoba, A. V., & Lovelace, R. V. E. 2004, ApJ, 610, 920
Sacco, G. G., Argiroffi, C., Orlando, S., et al. 2008, A&A, 491, L17
Scargle, J. D. 1982, ApJ, 263, 835
Sicilia-Aguilar, A., Kóspál, Á., Setiawan, J., et al. 2012, A&A, 544, A93
Sicilia-Aguilar, A., Fang, M., Roccatagliata, V., et al. 2015, A&A, 580, A82
Sicilia-Aguilar, A., Campbell-White, J., Roccatagliata, V., et al. 2023, MNRAS, 526, 4885
Siwak, M., Ogloza, W., Rucinski, S. M., et al. 2016, MNRAS, 456, 3972
Smette, A., Sana, H., Noll, S., et al. 2015, A&A, 576, A77
Stempels, H. C., Gahm, G. F., & Petrov, P. P. 2007, A&A, 461, 253
Stock, C., McGinnis, P., Caratti o Garatti, A., Natta, A., & Ray, T. P. 2022, A&A, 668, A94
Tokovinin, A., Fischer, D. A., Bonati, M., et al. 2013, PASP, 125, 1336
Vanderspek, R., Doty, J. P., Fausnaugh, M., et al. 2018, TESS Instrument Handbook
Vernet, J., Dekker, H., D'Odorico, S., et al. 2011, A&A, 536, A105
Wendeborn, J., Espaillat, C. C., Lopez, S., et al. 2024a arXiv e-prints [arXiv:2405.21038]
Wendeborn, J., Espaillat, C. C., Thanathibodee, T., et al. 2024b arXiv e-prints [arXiv:2405.21071]
Wilson, T. J. G., Matt, S., Harries, T. J., & Herczeg, G. J. 2022, MNRAS, 514, 2162

Appendix A: Log of spectroscopic observations

Table A.1 reports the log of the spectroscopic observations.

Appendix B: Gaussian fits

We used a multiple Gaussian model to fit the continuum-normalized emission lines in the spectrum of RU Lup. This model is a sum of symmetric (S) and asymmetric (A) Gaussian functions. The asymmetric Gaussian function $\mathcal{G}_A$ is defined as

$$\mathcal{G}_A(v) = C \exp\left[-\frac{(v-v_0)^2}{2\sigma^2}\right], \text{ with } \sigma = \begin{cases}\sigma_b & \text{if } v < v_0\\ \sigma_r & \text{if } v \geq v_0\end{cases} \quad \text{(B.1)}$$

where C is the amplitude relative to the continuum, v_0 is the line center and σ, σ_b, and σ_r are standard deviations. The symmetric Gaussian function $\mathcal{G}_S$ has $\sigma_b = \sigma_r$. The model is called nS+mA in the main text, where n and m are the number of symmetric and asymmetric Gaussian functions, respectively. It is expressed as

$$F(v) = 1 + \sum_{i=1}^{n} \mathcal{G}_{Si}(v) + \sum_{i=1}^{m} \mathcal{G}_{Ai}(v). \quad \text{(B.2)}$$

Appendix C: Calculation of continuum veiling

We estimated the veiling in our spectra using the ES 22.5 observation as template, which is the spectrum with the highest S/N among the ones with lower veiling in our sample. This method simplifies the calculation of the veiling, because the template does not have to be rotationally broadened. In addition, there are epochs in which the line-filling emission is so strong that the fit with ROTFIT did not converge allowing $v \sin i$ to vary (e.g., ES 21.1).

The veiling of the spectra relative to the ES 22.5 template (VF_{rel}) is defined as $VF_{rel} = [F_{obs}(\lambda) - F_T(\lambda)]/F_{T,c}$, where $F_{obs}(\lambda)$ and $F_T(\lambda)$ are the observed and template spectra and $F_{T,c}$ is the continuum of the template. VF_{rel} can be converted to the absolute veiling; that is the veiling with respect to that of a hypothetical spectrum of RU Lup if it did not exhibit any accretion. The absolute veiling is $VF_{abs} = [F_{obs}(\lambda) - F_0(\lambda)]/F_{0,c}$ where $F_0(\lambda)$ and $F_{0,c}$ is the wavelength-dependent flux of the non-accreting version of RU Lup and its continuum, respectively. VF_{abs} can be determined because the absolute veiling VF_T of the template could be computed independently with ROTFIT (Sect. 3). Since VF_T is defined as $VF_T = [F_T(\lambda) - F_0(\lambda)]/F_{0,c}$, and this relation also holds for the continua — that is, $VF_T = [F_{T,c} - F_{0,c}]/F_{0,c}$ — it can be shown that the equation for the conversion is

$$1 + VF_{abs} = (1 + VF_{rel}) \cdot (1 + VF_T). \quad \text{(C.1)}$$

We computed the veiling in the two spectral regions shown in Fig. 2. We define the veiling in these two regions as VF_{5735} and VF_{5800}. For both regions, we used $VF_T = 1.57 \pm 0.31$ for the ES 22.5 spectrum. The procedure to estimate VF_{rel} consisted of the following steps:

1. normalization of the spectra with a linear fit of selected portions of the spectrum where the continuum is seen;
2. down-grading of the template to the resolution of the observed spectrum;
3. cross-correlation between the template and the observation to match the position of the absorption lines;
4. exclusion of regions affected by line emission;
5. computation of the χ^2-function, defined as

$$\chi^2(VF_{rel}) = \sum_{\lambda_i} \left(F_{obs}(\lambda_i) - \frac{F_T(\lambda_i) + VF_{rel}}{1 + VF_{rel}}\right)^2 \quad \text{(C.2)}$$

as a function of VF_{rel}.

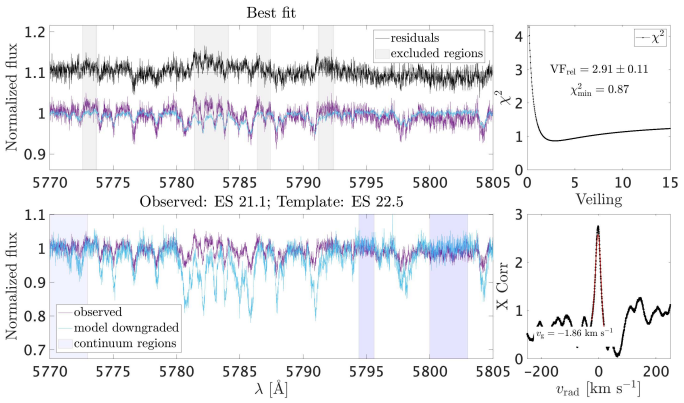

Fig. C.1: Veiling calculation for the ES 21.1 spectrum. The bottom left panel shows the ES 21.1 and ES 22.5 spectra, normalized used the shaded regions. The top left panel shows the veiled ES 22.5 spectrum that best fits the ES 21.1 spectrum. The right panels display the cross correlation function (bottom) and the χ^2 as a function of VF (top).

The best fitting VF_{rel} was found minimizing the χ^2, and the uncertainty as the standard deviation of $\exp(-\chi^2)$. Then, we converted VF_{rel} to VF_{abs} using Eq. C.1.

Figure C.1 shows the procedure to compute VF_{5800} for the ES 21.1 spectrum, pointing out the effect of line emission in the estimation of the VF. Due to the resolution, the S/N, and the effect of line emission, sometimes the fits did not converge. Therefore, we selected the observations for which VF_{5735} and VF_{5800} differed by more than 1σ, we visually inspected the results of the procedure for both regions, and we excluded the cases that we considered unclear. When both VF_{5735} and VF_{5800} agreed with each other, we derived a single measure of VF_{abs} by computing a weighted average (with weights $w_i = 1/dVF_i^2$) of the two values. The results are reported in Table A.1.

Appendix D: Spot model

We derived an analytical model to reproduce the variability of the TESS light curve. We assumed a spot with a constant temperature T, filling factor f, located at a latitude θ_S and azimuth ϕ on the surface of the star. The spot radiates as a black-body: its energy per unit time, area, solid angle, and wavelength interval is given by

$$B_\lambda(T) = \frac{2hc^5}{\lambda^5} \frac{1}{\exp(hc/k_B T) - 1}, \quad \text{(D.1)}$$

where h is the Plank constant, c is the speed of light, k_B is the Boltzmann constant, and λ is the wavelength. The projected surface of the spot varies as

$$S(\phi) = S_0(\hat{n} \cdot \hat{s}), \quad \text{(D.2)}$$

Table A.1: Log of the spectroscopic observations.

ID	MJD (days)	S/N	VF	V_{mag} (mag)	ID	MJD (days)	S/N	VF	V_{mag} (mag)
CH 21.1	0.04	65	$5.4 \pm 0.9^{(\ddagger)}$	-	CH 22.12	537.64	50	2.9 ± 0.4	10.79
CH 21.2	53.92	66	12 ± 2	-	ES 22.2	537.73	44	$3.2 \pm 0.4^{(\dagger)}$	11.14
CH 21.3	130.72	58	-	10.78	CH 22.13	538.63	44	3.5 ± 0.5	11.22
CH 21.4	170.66	29	-	10.73	CH 22.14	539.66	45	$2.8 \pm 0.6^{(\ddagger)}$	11.29
CH 21.5	171.64	51	4.1 ± 0.5	10.89	ES 22.3	539.76	42	2.9 ± 0.4	11.29
CH 21.6	172.66	70	$9 \pm 1^{(\dagger)}$	-	CH 22.15	540.72	65	4.0 ± 0.5	11.07
CH 21.7	173.64	63	$11 \pm 2^{(\dagger)}$	-	CH 22.16	541.66	44	2.4 ± 0.4	11.39
CH 21.8	174.68	65	6.5 ± 0.7	10.39	CH 22.17	542.66	48	1.4 ± 0.3	11.74
CH 21.9	175.65	52	5.3 ± 0.6	10.78	ES 22.4	542.76	24	1.8 ± 0.2	11.74
CH 21.10	177.70	44	-	10.68	CH 22.18	543.71	42	1.8 ± 0.4	11.81
CH 21.11	178.68	52	$8 \pm 1^{(\dagger)}$	10.63	CH 22.19	544.73	50	1.9 ± 0.4	11.59
CH 21.12	178.80	62	-	10.63	CH 22.20	545.70	40	1.9 ± 0.4	11.63
CH 21.13	179.68	57	10 ± 1	10.56	CH 22.21	546.71	50	3.9 ± 0.5	11.17
CH 21.14	179.69	33	-	10.56	CH 22.22	547.68	64	6.3 ± 0.7	11.05
CH 21.15	182.69	40	$7 \pm 1^{(\ddagger)}$	10.21	CH 22.23	548.72	64	3.5 ± 0.5	11.17
CH 21.16	183.66	47	5.2 ± 0.6	10.83	CH 22.24	549.67	40	1.8 ± 0.4	11.53
ES 21.1	184.66	57	$5.6 \pm 0.9^{(\dagger)}$	10.79	ES 22.5	549.70	38	1.6 ± 0.3	11.53
CH 21.17	184.70	62	7.1 ± 0.8	10.79	CH 22.25	550.71	71	6.5 ± 0.7	10.76
CH 21.18	185.64	55	$10 \pm 1^{(\ddagger)}$	10.67	CH 22.26	551.69	61	3.8 ± 0.5	11.17
CH 21.19	188.67	58	-	10.35	CH 22.27	552.70	65	3.4 ± 0.5	11.19
ES 21.2	193.73	43	$8 \pm 1^{(\dagger)}$	10.63	CH 23.1	804.86	38	4.3 ± 0.5	-
CH 22.1	411.86	59	5.1 ± 0.6	-	CH 23.2	805.88	57	3.9 ± 0.5	-
CH 22.2	418.83	52	4.6 ± 0.5	-	CH 23.3	806.96	56	$4.6 \pm 0.8^{(\ddagger)}$	-
CH 22.3	425.92	30	3.4 ± 0.4	-	CH 23.4	812.89	41	1.8 ± 0.3	11.54
CH 22.4	434.86	51	4.5 ± 0.5	-	CH 23.5	813.84	56	2.8 ± 0.4	-
CH 22.5	450.83	64	4.7 ± 0.6	-	CH 23.6	814.93	28	-	-
CH 22.6	458.80	49	4.7 ± 0.6	-	CH 23.7	815.86	48	$2.4 \pm 0.5^{(\dagger)}$	-
CH 22.7	471.77	62	6.6 ± 0.7	-	CH 23.8	820.83	53	2.8 ± 0.4	-
CH 22.8	525.77	56	5.5 ± 0.6	-	CH 23.9	821.94	44	2.5 ± 0.4	-
CH 22.9	534.69	48	3.6 ± 0.5	11.16	CH 23.10	831.80	49	$2.5 \pm 0.6^{(\ddagger)}$	-
CH 22.10	535.69	68	3.5 ± 0.7	11.15	CH 23.11	832.82	46	$2.3 \pm 0.6^{(\ddagger)}$	-
CH 22.11	536.67	67	$7.4 \pm 0.8^{(\dagger)}$	10.96	CH 23.12	833.82	47	2.9 ± 0.4	-
ES 22.1	536.70	47	6.7 ± 0.7	10.96					

Notes. The MJDs were computed relative to $MJD_0 \equiv 59264.336$. The S/N was computed at 5830 Å. $^{(\dagger)}$-$^{(\ddagger)}$: VF computed only with VF_{5735} or VF_{5800}, respectively (Appendix C). The typical uncertainty on V_{mag} is 0.01. The resolving power R is 140000 for the ESPRESSO spectra and 27800 for all the CHIRON spectra except for CH 21.4, 21.14, and 21.15 which have $R = 78000$.

where $S_0 = 4\pi R_\star^2 f$ is the surface of the spot, $\hat{n} = (\cos\theta_S \cos\phi, \cos\theta_S \sin\phi, \sin\theta_S)$ is the normal to the surface, and $\hat{s} = (\sin i, 0, \cos i)$ is the line of sight toward an observer located at an angle i from the rotation axis. Therefore, the flux observed with TESS is

$$F(T, f, \theta_S, \phi) = F_\star + \left[\frac{R_\star^2}{d^2} f \int B_\lambda(T) R(\lambda) d\lambda\right] \cdot (\cos\theta_S \sin i \cos\phi + \sin\theta_S \cos i) \quad \text{(D.3)}$$

where d is the distance to the system, $R(\lambda)$ is the response function of the TESS filter, and

$$F_\star = \frac{R_\star^2}{2d^2} \int B_\lambda(T_{\rm eff}) R(\lambda) d\lambda = 2.7 \times 10^{-14} \text{ erg s}^{-1} \text{ cm}^{-2} \quad \text{(D.4)}$$

is the integrated flux of the star in the TESS bandpass[8]. We downloaded the TESS response function from the SVO Filter Profile Service[9] (Rodrigo & Solano 2020). The modulation can be written as

$$F(T, f, \theta_S, \phi) = F_\star + A \cos\phi + C. \quad \text{(D.5)}$$

with

$$A = \left[\frac{R_\star^2}{d^2} f \int B_\lambda(T) R(\lambda) d\lambda\right] \cos\theta_S \sin i \quad \text{(D.6)}$$

and

$$C = A \frac{\tan\theta_S}{\tan i}. \quad \text{(D.7)}$$

The latitude of the spot can be directly obtained from the inversion of Eq. D.7, while from the amplitude A of the

[8] The factor 1/2 comes from the fact that we see only one hemisphere.
[9] http://svo2.cab.inta-csic.es/theory/fps/

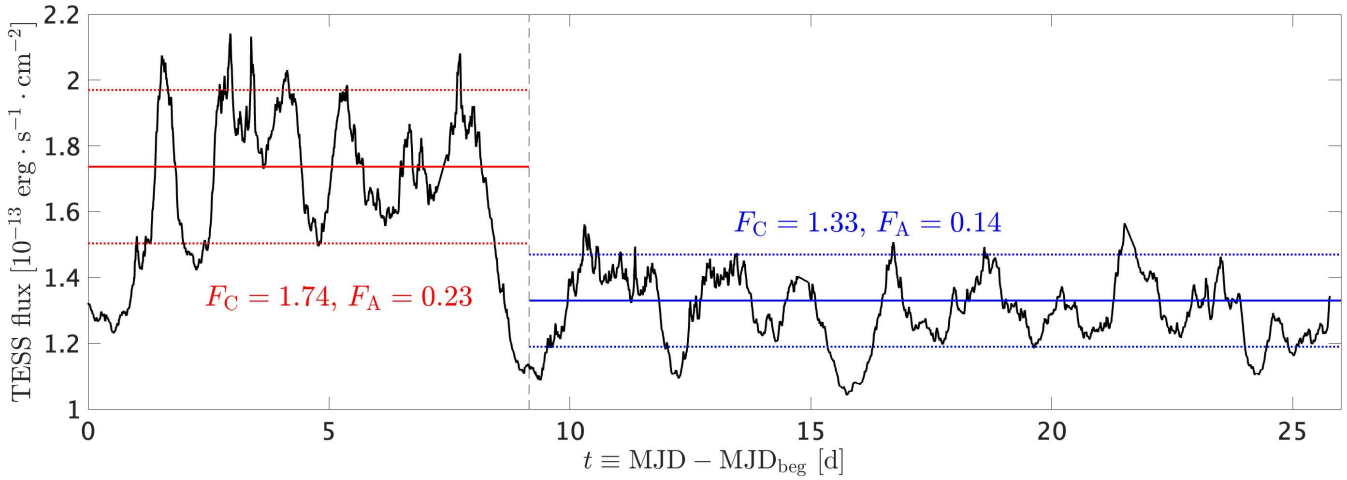

Fig. D.1: TESS Sector 65 light curve converted in absolute flux in the TESS bandpass. The solid lines mark the zero point of the oscillations, while the dotted lines mark the maximum and the minimum of the oscillations. The vertical dashed lines indicate the transition between the two portions. $F_{\rm C}$ and $F_{\rm A}$ are the zero point and the amplitude fluxes, respectively, in units of 10^{-13} erg s^{-1} cm^{-2}.

oscillations we get a relation between f and T

$$f = A\frac{d^2}{R_\star^2}\left[\int B_\lambda(T)R(\lambda)d\lambda\right]^{-1}(\cos\theta_{\rm S}\sin i)^{-1}. \tag{D.8}$$

We converted the TESS magnitude T to flux F using the formula $F = {\rm ZP}_\lambda\ 10^{-{\rm T}/2.5}$, where ${\rm ZP}_\lambda = 1.33 \times 10^{-9}$ erg s^{-1} cm^{-2} is the zero point flux of TESS, that we took from the SVO Filter Profile Service. Then, we visually estimated the amplitude $F_{\rm A}$ and the zero point $F_{\rm C}$ of the oscillations for the two portions of the light curve, defined as in Sect. 6. The values are reported in Fig. D.1. The latitude of the spot and the relation between f and T can be derived from Eqs. D.7 and D.8 with $C = F_{\rm C} - F_\star$ and $A = F_{\rm A}$. We derived $\theta_{\rm S1} = 61°$ and $\theta_{\rm S2} = 65°$ for the latitude of the spot in the two segments. The relation between f and T (Eq. D.8) is shown in Fig. 17.

Appendix E: Filling factor of a spherical cap

A spherical cap is a portion of a sphere cut by a plane. In spherical coordinates, it is defined as

$$\{(\theta,\phi) \quad | \quad \frac{\pi}{2} - \Delta\theta_{\rm S} \le \theta \le \frac{\pi}{2}, \quad 0 \le \phi \le 2\pi\} \tag{E.1}$$

where θ and ϕ are the latitude and the azimuth, and $\Delta\theta_{\rm S}$ is the half-aperture angle of the cap (spot). The filling factor of the cap can be computed by integrating

$$f = \frac{1}{4\pi R_\star^2}\int_{\pi/2-\Delta\theta_{\rm S}}^{\pi/2}\int_0^{2\pi} R_\star^2\cos\theta d\theta d\phi = \frac{1}{2}(1-\cos\Delta\theta_{\rm S}). \tag{E.2}$$

Inverting this relation, we obtain

$$\Delta\theta_{\rm S} = \arccos(1-2f). \tag{E.3}$$

Astronomy & Astrophysics manuscript no. output
March 17, 2025

Spinning-down RU Lup. Constraints on the physics of the outflow from high-resolution spectroscopy⋆

A. Armeni[1], B. Stelzer[1], A. Frasca[2], C. F. Manara[3], J. Campbell-White[3], J. F. Gameiro[4,5], and M. Gangi[6,7]

[1] Institut für Astronomie und Astrophysik, Eberhard Karls Universität Tübingen, Sand 1, 72076 Tübingen, Germany
e-mail: armeni@astro.uni-tuebingen.de
[2] INAF – Osservatorio Astrofisico di Catania, via S. Sofia 78, 95123 Catania, Italy
[3] European Southern Observatory, Karl-Schwarzschild-Strasse 2, 85748 Garching bei München, Germany
[4] Instituto de Astrofísica e Ciências do Espaço, Universidade do Porto, CAUP, Rua das Estrelas, P-4150-762 Porto, Portugal
[5] Departamento de Física e Astronomia, Faculdade de Ciências, Universidade do Porto, Rua do Campo Alegre 687, P-4169-007 Porto, Portugal
[6] INAF – Osservatorio Astronomico di Roma, via Frascati 33, 00078 Monte Porzio Catone, Italy
[7] ASI, Italian Space Agency, via del Politecnico snc, 00133 Rome, Italy

15/05/2024

ABSTRACT

Context. Magnetic winds are a key mechanism for angular momentum removal in young stars.
Aims. We aim at studying the physics of the outflow in the Classical T Tauri Star (CTTS) RU Lup, constraining its structure and the spin-down mechanism.
Methods. The unprecedented high resolution of the *Echelle SPectrograph for Rocky Exoplanets and Stable Spectroscopic Observations* (ESPRESSO) enabled a detailed study of the connection between the forbidden lines (FELs) and the blueshifted absorption in the lines of the Na I and Ca II doublets, which we resolved in three components.
Results. For the FELs, we identified three components. Two of them, the high velocity component (HVC) and the low velocity narrow component (LVC-NC) were previously discussed and ascribed to a collimated jet and a magnetohydrodynamic (MHD) wind from the outer disk, respectively. We detected a third component, the low velocity broad component (LVC-BC), in the [O I] 5577 line. The observed velocities in the LVC-BC are compatible with the Keplerian velocity at the disk truncation radius, $R_{\rm T}$, suggesting that it traces an MHD disk wind originating from close to $R_{\rm T}$. We detected a set of three discrete absorption components (DACs) in the blue wings of the Na I D and Ca II H & K doublets, which we labelled as low, medium, and high velocity absorptions (LVA, MVA, and HVA). A qualitative comparison with MHD simulations of outflows in CTTSs suggests that these DACs trace the "onion-like" structure of the RU Lup outflow. By fitting the line profiles of the LVA and MVA, we separated the vertical and toroidal velocity component. Using these velocities together with geometrical constraints on the structure of the outflow, we inferred that the LVA is formed in the same MHD disk wind traced by the LVC-BC while the MVA traces the peripheral part of the jet. We estimated the amount of angular momentum per unit mass carried by each region, which is 6 AU km s^{-1} and 11 AU km s^{-1} for the disk wind and the peripheral part of the jet, respectively. The HVA is associated to the high velocity emission in the FELs and originates in the low-density, large-scale structure of the jet. With an estimate on the accretion torque, we showed that the disk wind and the periphery of the jet are not capable of spinning-down the star. Therefore, we suggested that most of the angular momentum is removed by the portion of the jet close to the axis, for which we derived an upper limit on the Alfvèn radius of $\sim 17.7\ R_\star$.
Conclusions. Our findings highlight the existence of an onion-like structure of the outflow close to the launching region and indicate that different components of the outflow remove the excess angular momentum at different efficiencies.

Key words. Accretion, accretion disks – Stars: pre-main sequence – Stars: variables: T Tauri, Herbig Ae/Be – Stars: individual: RU Lup

1. Introduction

Classical T Tauri Stars (CTTSs) are low-mass ($\lesssim 2\ M_\odot$) stars in the early ($\sim 1-10$ Myr) stages of their formation. They accrete matter from a circumstellar disk through a magnetosphere (Bouvier et al. 2007; Hartmann et al. 2016). The evolution of these young stellar objects (YSOs) and the formation of their planetary systems are fundamentally shaped by the interplay between accretion and mass loss.

The removal of angular momentum from the accretion disk is essential for disk material to move inward and ultimately accrete onto the star. Turbulence driven by the magnetorotational instability (MRI, Balbus & Hawley 1991) has been found to be largely ineffective in transporting angular momentum outward in protostellar disks, primarily due to the expected low ionization fraction (e.g., Hartmann 2008). As a result, magnetohydrodynamic (MHD) disk winds have emerged as the leading mechanism for extracting angular

⋆ Based on observations collected at the European Southern Observatory under ESO programmes 106.20Z8.003 and 106.20Z8.007.

momentum from the accretion disk (Lesur 2021; Pascucci et al. 2023).

Another key problem in star formation is how the star counteracts the natural spin-up caused by accretion. The strong (~ 1 kG) magnetic field of CTTSs can truncate the disk at a few stellar radii, and the accreting matter transfers angular momentum to the star (e.g., Matt & Pudritz 2005a,b). The typical angular momentum per unit time transferred from the disk to the star is sufficient to spin it up to break-up velocity in much less than ~ 1 Myr (Hartmann & Stauffer 1989). However, CTTSs typically rotate at velocities an order of magnitude lower (Bouvier et al. 2014). This discrepancy requires a spin-down mechanism, that is, a process that carries away excess angular momentum and regulates the stellar rotation rate.

Observationally, forbidden emission lines (FELs) are well-known tracers of the outflowing gas in YSOs (e.g., Edwards et al. 1987; Ray et al. 2007; Ercolano & Pascucci 2017; Banzatti et al. 2019). These lines typically show two distinct velocity components: a high velocity component (HVC) with blueshifted emission that can reach hundreds of km s^{-1}, and a low velocity component (LVC) with blueshifted velocities less than ~ 50 km s^{-1} (Hartigan et al. 1995). The HVC is thought to originate in a jet that is collimated by magnetic fields (Kwan & Tademaru 1988) and typically extends to hundreds AU (Hirth et al. 1997). The LVC originates in a more compact region than the HVC and it is resolved into broad (BC) and narrow (NC) kinematic components (Rigliaco et al. 2013; Simon et al. 2016; Fang et al. 2018). The large widths of the LVC–BCs point to an MHD disk wind origin at launching radii $\lesssim 0.5$ AU (e.g., Campbell-White et al. 2023). The LVC–NC is likely formed at larger disk radii either in a photoevaporative thermal wind (Weber et al. 2020) or in an MHD wind from the outer disk.

This work focuses on RU Lup (Sz 83), a young K7 star (Alcalá et al. 2017) located in the Lupus 2 cloud at a distance of 158.9 ± 0.7 pc (Gaia Collaboration et al. 2021). In Armeni et al. (2024) (hereafter, Paper I), we analyzed the accretion dynamics of RU Lup, constraining its accretion rate and the location of the disk truncation radius. However, to fully understand the angular momentum evolution of RU Lup, it is crucial to also characterize its outflows.

The FEL profiles of RU Lup exhibit a complex structure (Natta et al. 2014), and high-resolution spectroscopy enables a more detailed examination of these profiles compared to lower-resolution observations (e.g., Nisini et al. 2018). Recent studies have provided significant insights into the outflow mechanisms of RU Lup. Whelan et al. (2021) performed a spectro-astrometric analysis of the forbidden emission lines (FELs) in the spectrum of RU Lup with the *Ultraviolet and Visual Echelle Spectrograph* (UVES, Dekker et al. 2000). Their findings revealed that the LVC-NC of the FELs traces wide-angled MHD disk wind originating from the circumstellar disk of RU Lup. Building on these results, Birney et al. (2024) imaged the outflow of RU Lup with the *Multi Unit Spectroscopic Explorer* (MUSE, Bacon et al. 2010), providing information on the spatial width and collimation of the components. They showed that the MHD disk wind traced by the LVC-NC has a full opening angle (θ) of $\sim 37^{\circ}$, while the jet is more collimated, with $\theta \sim 25^{\circ}$.

The ability of integrated field spectroscopy to spatially resolve the emission regions makes it particularly useful for tracing the large-scale structure of YSO outflows. However, to study the physics of the wind close to the star, we need to resort to spectroscopy. For this reason, in this work we analyze the high-resolution spectra presented in Paper I with a focus on the physics of the RU Lup outflow close to the launching region. Our aim is to find a mechanism that is capable of maintaining the star in spin equilibrium.

This paper is organized as follows. In Sect. 2, we introduce the observations. We present the analysis of the high resolution spectra in Sect. 3, where we analyze the FELs, and Sect. 4, where we study the absorption from the wind. We discuss the results of our analysis and the implications for the structure of the outflow in Sect. 5, followed by a summary of our conclusions in Sect. 6.

2. Observations

High resolution ($R = 140000$) optical ($3800 - 7880$ Å) spectra were obtained with the *Echelle SPectrograph for Rocky Exoplanets and Stable Spectroscopic Observations* (ESPRESSO, Pepe et al. 2021) in the framework of the PENELLOPE program (Manara et al. 2021). Two spectra were obtained in 2021 in Pr. Id. 106.20Z8.003 and five in 2022 in Pr. Id. 106.20Z8.007 (PI Manara). The ESPRESSO spectra were reduced by the PENELLOPE team as described by Manara et al. (2021). Telluric correction was performed using the molecfit tool (Smette et al. 2015). ESPRESSO is a fiber-fed spectrograph, and the aperture on the sky of the fiber was $1''$ during the observations. At the distance of RU Lup, this limits the size of the observing region to ~ 160 AU.

As in Paper I, throughout this article each spectrum is labelled as "ID yy.j" where ID is an identification for the spectrograph, yy are the last two digits of the year and j, when needed, is the jth observation from that spectrograph in that year. For example, the 3rd ESPRESSO observation from 2022 is called ES 22.3. Table A.1 reports the log of the spectroscopic observations.

3. Forbidden emission lines

Figure 1 shows three prominent FELs in the ES 22.5 spectrum of RU Lup, the [O I] 5577, [O I] 6300, and [S II] 6731 lines. We removed the photospheric spectrum in the FELs as explained in Appendix C. Given their different critical electron densities, n_c, these lines potentially probe distinct regions of the outflow. The values are $n_c = 10^8$ cm^{-3}, $n_c = 1.8 \times 10^6$ cm^{-3}, and $n_c = 1.6 \times 10^4$ cm^{-3}, respectively.

Although the profiles are too complicated to fit with a combination of Gaussians, we can distinguish three different components in the FELs. The first one is the HVC that is observed in the [O I] 6300 and [S II] 6731 lines. It traces a jet that extends out to ~ 100 AU from the star (Whelan et al. 2021). The second component is the LVC-NC, observed in the same transitions as the HVC. This component is formed in the MHD wind launched from the outer disk (Whelan et al. 2021). Both the HVC and the LVC-NC have been imaged with MUSE (Birney et al. 2024).

The third component is the LVC-BC which, unlike the other two line components, extends also to redshifted velocities. The LVC-BC is most evident in the [O I] 5577 line. It is also observed in the [O I] 6300 line, but not in the [S II] 6731

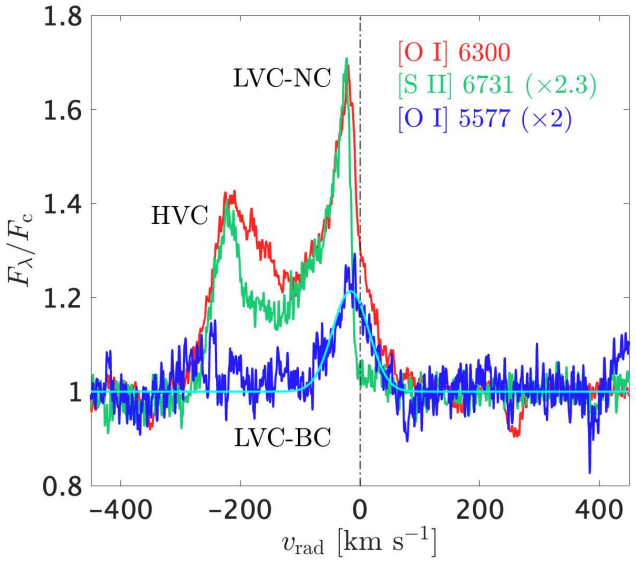

Fig. 1: Photospheric subtracted profiles of the [O I] 5577, [O I] 6300, and [S II] 6731 lines in the ES 22.5 spectrum of RU Lup. The cyan line is the best fit to the [O I] 5577 line with a Gaussian model.

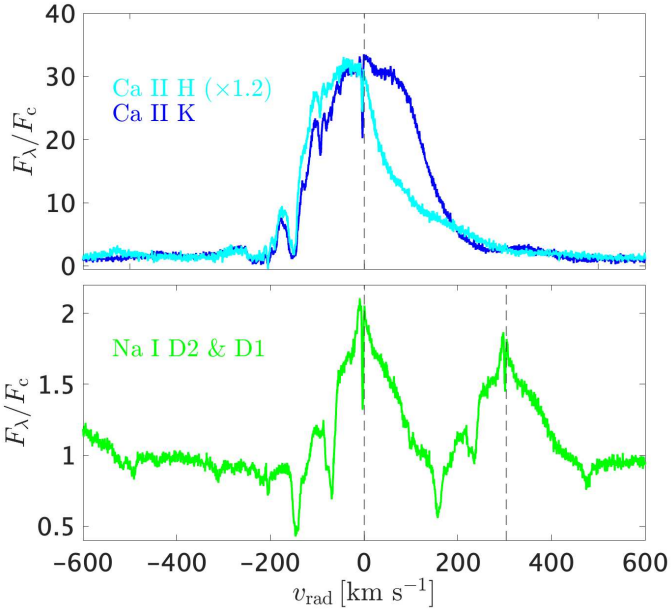

Fig. 2: Ca II H & K and Na I D2 & D1 doublets in the ES 22.5 spectrum of RU Lup. The Ca II H & K lines are plotted in velocity relative to their rest wavelengths, while the Na I doublet is plotted in velocity relative to the rest wavelength of the D2 line. The red wing of the Ca II H line is suppressed because of the "Herbig" fluorescence phenomenon which we have discussed in Armeni et al. (2023) for HM Lup.

line, which has a profile with a sharp drop from the peak of the LVC-NC to $v_{rad} \approx 0$ km s^{-1}. Since the [O I] lines have higher n_c values, we conclude that their LVC-BC traces material denser than the jet and the outer disk wind. The [O I] 5577 LVC-BC can be fit with a Gaussian. The result is shown in Fig. 1. The relevant best fit parameters are the centroid velocity, $v_0 = -15.7 \pm 1.5$ km s^{-1}, and the width of the Gaussian, $\sigma = 30.5 \pm 1.5$ km s^{-1}. The blueshifted centroid is compatible with formation in a wind. Emission in the [O I] 5577 line extends up to $v_{rad} \approx \pm 75$ km s^{-1}. Velocities of this order of magnitude are compatible with formation in a region that is in Keplerian rotation. The radial velocity in a pure Keplerian flow is

$$v_{rad}(r, \phi) = \sqrt{\frac{GM_\star}{r}} \sin i_\star \sin \phi, \quad (1)$$

where r is the distance from the rotation axis, ϕ is the azimuth relative to the observer and $i_\star$ is the inclination of the stellar rotation axis, which we assume to be aligned to the disk axis. Using the parameters of RU Lup from Table B.1, at $R_T = 2\ R_\star$ the maximum radial velocity is ~ 40 km s^{-1}, which is about a factor of two smaller than the observed redshifted velocities. However, departures from a pure Keplerian flow are expected in the vicinity of the truncation radius, because the velocity field is altered by the presence of the magnetic field. The flow is likely not confined to a plane and may acquire a poloidal component if the magnetic field lines have an open configuration. In addition, part of the line broadening could be thermal. For these reasons, we believe that the line width is consistent with a rotating flow anchored to the inner disk.

Despite the absence of emission at positive velocities, the [S II] 6731 has a blueshifted component with velocities between -125 km s^{-1} and -50 km s^{-1} which is similar to the blue wing of the LVC-BC. but it extends to higher blueshifted velocities than the ones observed in the [O I] 5577 line.

4. Discrete absorption components in resonance lines

RU Lup shows prominent emission in metallic species (Paper I). In this work we focus on two strong resonance lines, the Na I D2 and the Ca II K lines. Both lines are one of the two components of a doublet, namely the Na I D doublet (D1 at $\lambda = 5895.92$ Å, D2 at $\lambda = 5889.95$ Å) and the Ca II H & K doublet (H at $\lambda = 3968.47$ Å, K at $\lambda = 3933.66$ Å). These lines have been already analyzed with UVES by (Gahm et al. 2013), who noticed a series of absorption components in their blue wings. However, the unprecedented resolution of ESPRESSO allows a detailed study of the line profiles. The line profiles are shown in Fig. 2 on the example of the ES 22.5 spectrum.

Figure 3 zooms in to the blue wing of the Ca II K and Na I D2 lines in the ES 22.5 spectrum. The broad ($\sim 350 - 400$ km s^{-1}) emission is locally attenuated in a set of discrete absorption components (DACs). We distinguish three main DACs in ES 22.5, namely a high velocity absorption component (HVA) that extends between -260 km s^{-1} and -180 km s^{-1}, a medium velocity absorption component (MVA) that extends between -170 km s^{-1} and -130 km s^{-1}, and a low velocity absorption component (LVA) that extends between -90 km s^{-1} and -60 km s^{-1}. These absorption components are not photospheric, because they are much broader than $v \sin i$, which is 8.6 ± 1.4 km s^{-1} for RU Lup (Paper I). They likely originate in the outflowing gas. The narrow absorption at ~ 0 km s^{-1} is from the interstellar medium.

The optical depth is different from DAC to DAC, and between the Ca II K and Na I D2 lines. The HVA component

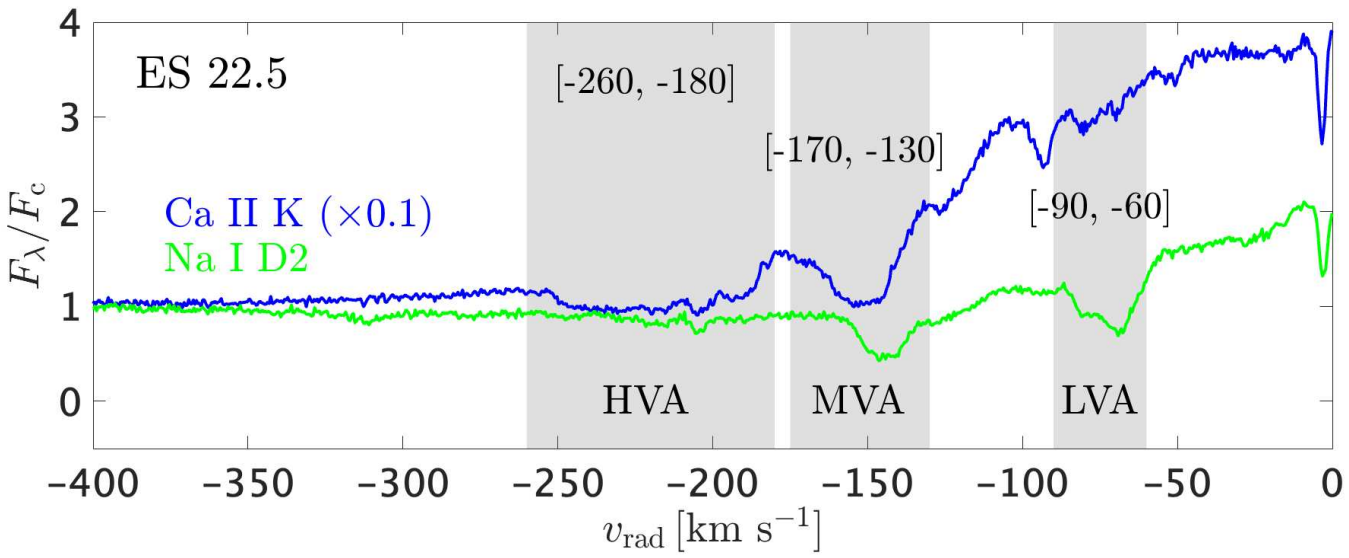

Fig. 3: Discrete absorption components observed for the Na I D2 (green) and Ca II K (blue) lines in the ES 22.5 spectrum of RU Lup. The shaded areas mark the velocity ranges where absorption is observed.

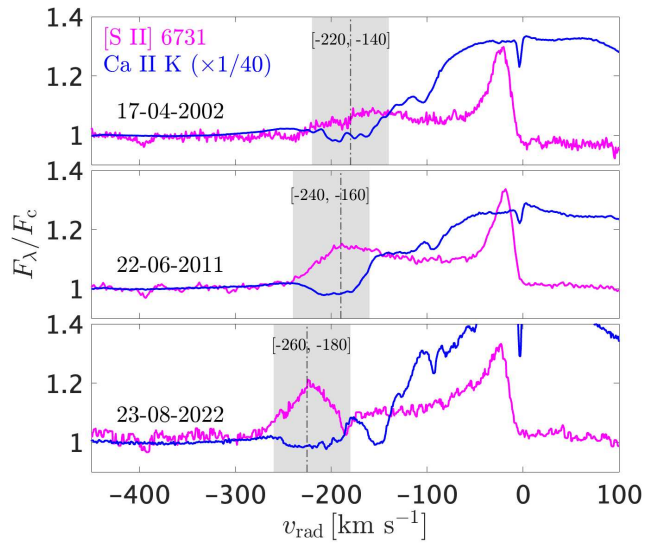

Fig. 4: Comparison between the Ca II K (blue) and [Si II] 6731 (magenta) lines for a selection of spectra of RU Lup. From the top panel to the bottom panel, the spectra are from UVES, ESPaDOnS, and ESPRESSO. The Ca II K lines were scaled by 1/40. The shaded areas trace the evolution of the two components, while the vertical lines mark the maximum $v_{\rm rad}$ of the HVC.

is well defined only in Ca II K. The MVA is present in both transitions, although with a different velocity structure. It is more extended in Ca II K, and the profile minimum is more blue-shifted in Ca II K than in Na I D2. The LVA is observed only in Na I D2. These differences indicate that the DACs originate in distinct regions of the outflow. While neutral sodium likely probes a colder region of the wind, absorption in Ca II requires ionized material.

4.1. Comparison with forbidden emission lines

The HVA observed in the Ca II K line has the same velocity range as the HVC of the FELs (see Fig. 4), indicating that these two features are connected. In Fig. 4 we supplemented the ES 22.5 observation (bottom panel) with two archival spectra. One is from ESPaDOnS (middle panel) and it is part of the spectra analyzed by Stock et al. (2022). The other one is from UVES (top panel) and it is part of the observations discussed in Stempels et al. (2007) and Gahm et al. (2008). The blueshifted extension of the [S II] 6731 line profile evolves in the same way as the Ca II K HVA. In particular, the two components drift towards higher blueshifted velocities and the HVC gets stronger relative to the continuum with time.

4.2. Variability

We used the ESPRESSO spectra to study the variability of the DACs. Figure 5 shows the blue wings of the Ca II K and Na I D2 lines for all existing ESPRESSO observations of RU Lup.

The very high resolution of ESPRESSO makes it possible to resolve the velocity sub-components of each DAC. These sub-components change from spectrum to spectrum, even within the observing season. This indicates that substructures of the flow within the regions that produce the DACs vary on dynamical timescales.

In the HVA, the variability of the sub-components of the profile is more pronounced in 2021 than in 2022. In the 2021 spectra, the HVA of the Ca II K line is broad, while it is more compact in 2022, and the velocity sub-components appear to be more stable. For the Na I D2 line, absorption in the high-velocity range is variable in 2021, but stable in 2022. From ES 21.1 to ES 21.2, which are ~ 9 days apart, a component at ~ -200 km s^{-1} is replaced by another component that falls between the definition ranges of the HVA and the MVA.

The strength of the MVA around the absorption minimum (~ -130 km s^{-1}) changes in 2021. From ES 21.1 to

ES 21.2, the MVA strengthens in Na I D2 but weakens in Ca II K. From 2021 to 2022, in both lines the entire MVA component shifts by ~ 20 km s^{-1} in velocity. It is not clear whether this variability reflects the outward motion of the same region or if the two components represent distinct transient features. In 2022, the MVA remains more stable in both the Ca II K and Na I D2 lines.

The LVA is prominent in the ESPRESSO spectra from 2022, but its presence in 2021 remains unclear. Only a weak, narrow absorption feature is observed at ~ -80 km s^{-1}, but there is no way to determine whether it is connected to the LVA seen in 2022.

The spectral variability of the DACs provides insight into their regions of formation. The HVA has significant variability only between the two observing epochs, that is, on a timescale of ~ 1 yr. In contrast, the MVA and LVA components change even within the same epoch, and their variability is more pronounced in 2021, an epoch characterized by a higher accretion rate and strong accretion variability (Paper I and Wendeborn et al. 2024). This suggests that the LVA and the MVA originate from closer to the star than the HVA, and that their variability is likely related to the dynamic interaction between the star and the disk.

5. Discussion

The DACs and their connection with the FELs provide important insights into the structure of the outflow of RU Lup. Here we outline the implications of our observations on the physics of the MHD-driven wind of RU Lup and, by extension, of CTTSs in general. We conclude the discussion linking the properties of the wind with our findings on the accretion flow of RU Lup (Paper I). Table B.1 lists the parameters of RU Lup needed for the discussion.

MHD simulations (Romanova et al. 2009; Kurosawa & Romanova 2012) have demonstrated that CTTSs outflows generally exhibit an "onion-like" structure, characterized by a well-collimated, fast, low-density jet enclosed within a more open, slower, and denser conical wind. Therefore, the poloidal velocity in the outflow, $v_{\rm p}$, increases with the distance from the star (like in any wind) and decreases with the distance from the rotation axis. In addition, the conical wind has also a toroidal velocity component, v_ϕ, that is higher closer to the launching region. The nested structure of CTTSs outflows has been confirmed by observations (e.g., Bacciotti et al. 2002; Pyo et al. 2006; Krist et al. 2008; Bacciotti et al. 2025).

Figure 6 shows a sketch of the outflow expected for RU Lup with contours of constant $v_{\rm p}$. This illustration visually explains how the DACs are formed. Emission from either the magnetosphere (in Na I) or the wind itself (in Ca II, Sect. 5.1) is absorbed by gas in the line of sight at different velocities.

5.1. Origin of the broad Ca II emission

In Paper I we showed that the rich emission spectrum of RU Lup is formed in the accretion flow that leaves the disk at $R_{\rm T}$. The Na I D lines have excitation conditions and line profiles similar to those of the neutral metallic lines which we studied in Paper I, for example the Fe I 5447 line (see Fig. 7). Hence, they must be formed in a similar way, as we have already discussed in Armeni et al. (2023).

On the other hand, Fig. 3 shows that the Ca II H & K lines are much broader than the Na I D lines, with detectable emission up to ~ -400 km s^{-1}. According to MHD simulations, such velocities can be reached in a CTTS jet (e.g., Romanova et al. 2009).

Coffey et al. (2007) observed the jet of the CTTS DG Tau with the *Hubble Space Telescope Imaging Spectrograph* (HST/STIS) in the near-ultraviolet (NUV) by placing the slit at a distance of $0.3''$ from the star, corresponding to a de-projected distance along the jet of 68 AU. They demonstrated that the blue wing emission of the Mg II h & k doublet in DG Tau forms within the jet. Comparing their observation with an HST spectrum of DG Tau with a $2''$ coverage centered on the star (Ardila et al. 2002) in which the Mg II k line showed a deep blueshifted absorption, Coffey et al. (2007) concluded that the jet is both absorbing and emitting in Mg II (Fig. 9 of their paper). The Mg II h & k doublet is analogous to the Ca II H & K doublet (hence the same denomination); both calcium and magnesium are alkaline-earth metals and have similar atomic structures. This similarity suggests that the wings of the Ca II H & K doublet lines also originate in the jet, and that the absorption components observed in the Ca II K line are a manifestation of the jet *absorbing against itself*.

5.2. LVC-BC: conical wind from the inner disk

The HVC and LVC-NC components of the FELs have a known origin (Whelan et al. 2021, and Sect. 3). Here we focus on the newly identified LVC-BC, which is most evident in the [O I] 5577 line.

We propose that the LVC-BC is formed in an MHD disk wind that is launched from the inner disk, close to the truncation radius, $R_{\rm T} \approx 2\ R_\star = 0.02$ AU (Table B.1). This conclusion is supported by: (1) the absence of a spectroastrometric signal in the [O I] 5577 line, which places an upper limit of 9 AU on the extent of the emission region (Whelan et al. 2021); (2) the absence of the LVC-BC in the [S II] 6371 line, indicating that the region that emits the LVC-BC is denser than the jet; (3) the blueshifted centroid of the [O I] 5577 line, in accordance with the face-on orientation of the system; (4) the facts that the profile is symmetric around the line center and extends to positive velocities of the order of the Keplerian velocity at $R_{\rm T}$, which are indications of a rotating flow.

The properties of the LVC-BC fit the description of the conical wind observed in MHD simulations (Romanova et al. 2009). The conical wind is the outermost shell of the outflow structure, and it is a hollow cone which originates in the disk between $R_{\rm T}$ and $R_{\rm co}$. This wind surrounds the jet and is both denser and slower than the jet itself. The typical values of $v_{\rm p}$ are of the order of ~ 50 km s^{-1}, while at the base of the wind v_ϕ is the Keplerian velocity in the disk.

5.3. LVA component: absorption in the conical wind

The LVA has significantly lower velocities (~ 70 km s^{-1}) compared to the other two DACs. Such low velocities are typical of the outermost shell of the outflow, that is, in the denser conical wind. Figure 22 of Romanova et al. (2009) shows that the terminal poloidal velocity for the conical wind of a CTTS is ~ 55 km s^{-1}, which is close to the

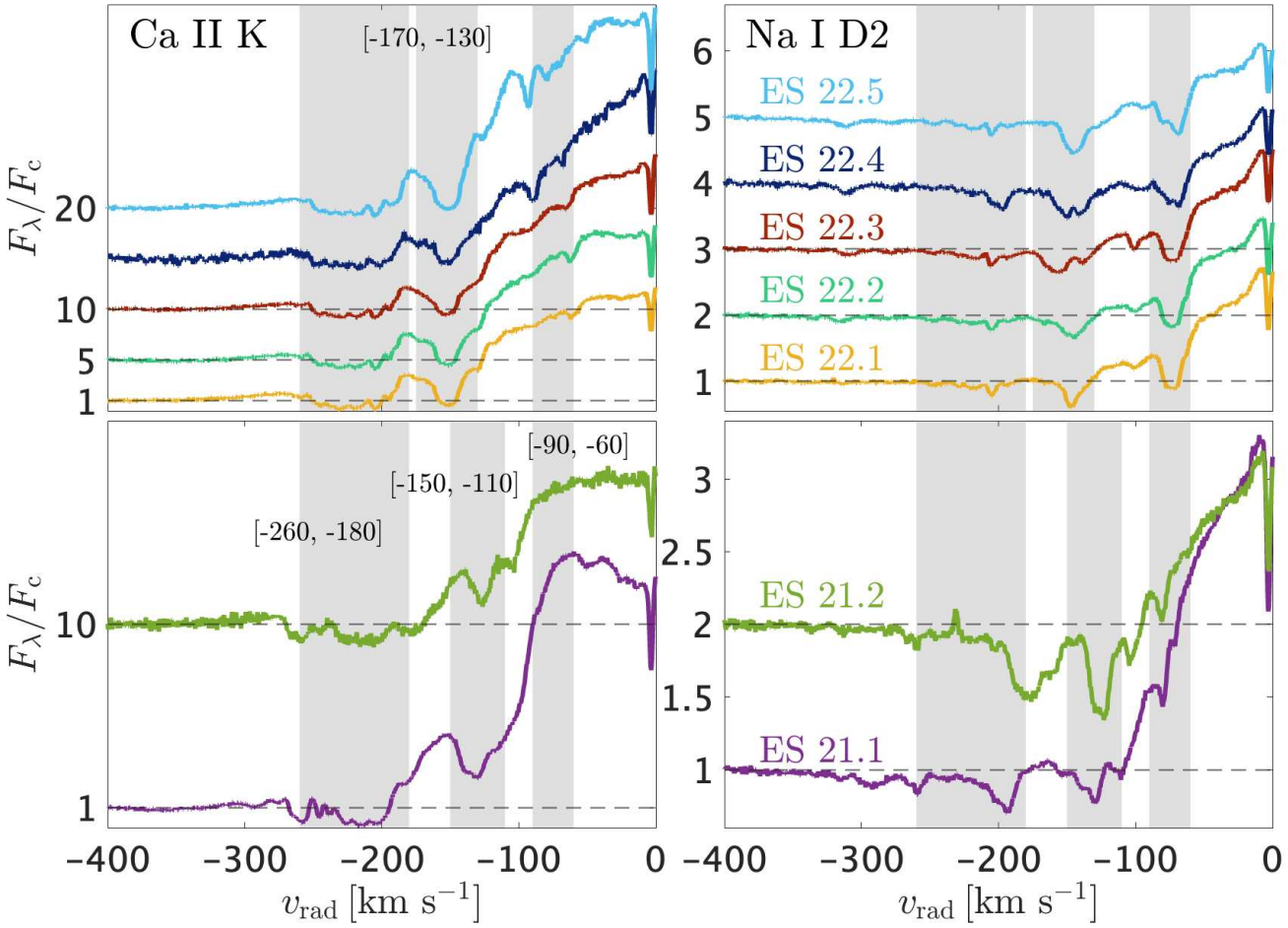

Fig. 5: Variability of the Ca II K and Na I D2 lines in the high resolution ESPRESSO spectra (Table A.1). The shaded areas mark the velocity ranges where absorption is observed. These ranges are the same as in Fig. 3 for the spectra from 2022, while the velocity range of the MVA is different in 2021.

velocities that we observe in the LVA. Therefore, we propose that the LVA component originates in the conical wind that is also traced by the LVC-BC.

We estimated the hydrogen column density, N_H, required for producing the LVA component by computing the equivalent width (EW) of the Na I D2 line and assuming solar abundance ratios, as described in Appendix D. This quantity is related to the hydrogen density, n_H, by $N_H = n_H l$, where l is the path length along the line of sight. The absence of the LVC-BC in the [S II] 6731 line provides a lower limit on the electron density, $n_e > 1.6 \times 10^4$ cm^{-3}. Given that $n_H \geq n_e$, this constraint yields an upper limit on l of ~ 2 AU. However, the observed emission in both the [O I] 5577 and [O I] 6300 lines suggests that n_e more likely falls within the range between 10^6 cm^{-3} and 10^8 cm^{-3}. In addition, since hydrogen is predominantly neutral, the ionization fraction, $x = n_e/n_H$, is expected to be $\ll 1$. Consequently, the actual path length l is likely significantly smaller than the conservative upper limit derived from the [S II] 6731 line, implying that the LVA component originates from a spatially compact region along the line of sight. This raises the question of how such a region can produce the observed broad absorption profile, which has a typical width of ~ 30 km s^{-1} in the LVA component (Fig. 3). At the temperatures where sodium is neutral, the thermal broadening is only ~ 1 km s^{-1} and it cannot account for the observed line width. Romanova et al. (2009) showed that in the region where the gas has reached the terminal v_p, the conical wind still retains a substantial v_ϕ. Thus, we suggest that the observed line width reflects the existence of a toroidal velocity component in the absorbing region.

To clarify this, consider a cylindrical coordinate system (r, ϕ, z), where r represents the distance from the rotation axis in the x-y plane, ϕ is the azimuthal angle measured relative to the x-axis, and z corresponds to the rotation axis (Fig. 8). Although the region is not extended along the line of sight (i.e., both in r and z), it can still have significant extension in the azimuthal direction. In cylindrical coordinates the velocity vector is $\boldsymbol{v} = v_r\hat{\boldsymbol{r}} + v_\phi\hat{\boldsymbol{\phi}} + v_z\hat{\boldsymbol{z}}$. The unit vectors are given by $\hat{\boldsymbol{r}} = (\cos\phi, \sin\phi, 0)$, $\hat{\boldsymbol{\phi}} = (-\sin\phi, \cos\phi, 0)$, and $\hat{\boldsymbol{z}} = (0, 0, 1)$ in Cartesian coordinates. The radial velocity is $v_{rad} = -\boldsymbol{v}\cdot\hat{\boldsymbol{s}}$, where $\hat{\boldsymbol{s}} = (\sin i_\star, 0, \cos i_\star)$ represents the observer's line of sight. The dot product yields

$$v_{rad} = -v_r \cos\phi \sin i_\star + v_\phi \sin\phi \sin i_\star - v_z \cos i_\star. \quad (2)$$

Assuming that the poloidal flow is predominantly parallel to the z-axis, we can neglect v_r with respect to v_z. Then, the shape of the line profile depends on the angles

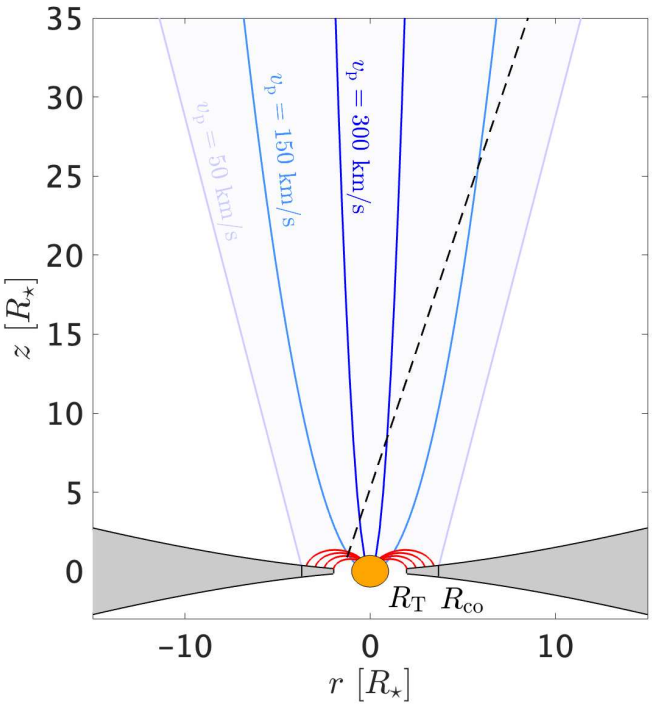

Fig. 6: Illustration of the "onion-like" structure predicted by MHD simulations for the outflow of a CTTS, using the parameters of RU Lup. The outflow is represented as a truncated cone with a full opening angle of 25° (Birney et al. 2024) that departs from the corotation radius R_{co}. The parabolas approximate surfaces of constant poloidal velocity, v_p. Typical values of v_p from Romanova et al. (2009) are reported. The dashed line is the line of sight to the magnetosphere for $i_\star = 16°$ (Table B.1).

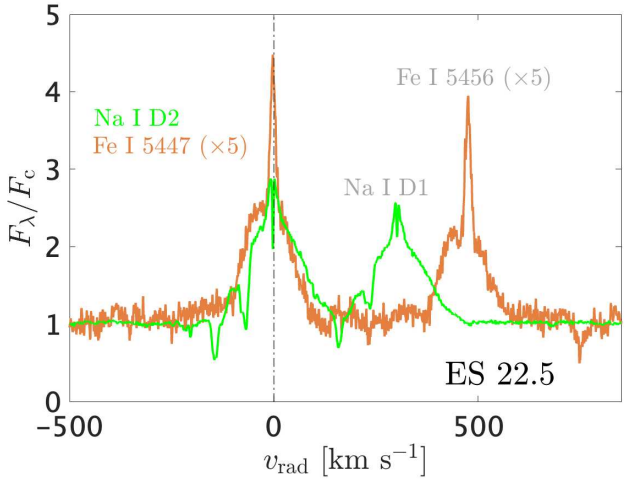

Fig. 7: Comparison between the Na I D, Fe I 5447, and Fe I 5456 lines in the ES 22.5 spectrum of RU Lup. The spectrum is photospheric-subtracted.

ϕ_1 and ϕ_2 which limit the sampled region in azimuth. We produced synthetic absorption profiles for a variety of ϕ_1 and ϕ_2 as explained in Appendix E. We show the morphology of the profiles in Fig. E.1. The profiles have two main characteristics. First, they are double-dipped and the velocities of the dips are $v_1 = -v_z \cos i_\star + v_\phi \sin\phi_1 \sin i_\star$ and $v_2 = -v_z \cos i_\star + v_\phi \sin\phi_2 \sin i_\star$. Second, when the profiles are symmetric, the center is at $v_0 = -v_z \cos i_\star$.

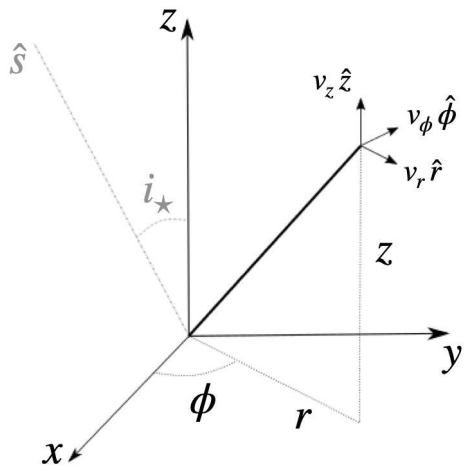

Fig. 8: Sketch of the decomposition of the velocity vector in cylindrical coordinates.

This model helps us understanding the origin of the DACs variability. It tells us that the line profile depends on the radiative coupling between the emitting and the absorbing regions. For the Na I D2 line, structural variations in the accretion flow (i.e., where the emission likely comes from) induce changes in the absorption profile. In addition, since the absorption originates in a portion of a rotating outflow, rotational motion introduces additional variability.

The Na I D2 LVA of the ES 22.5 spectrum appears to have a double-dipped structure (Fig. 3). This is the only spectrum in which it is possible to determine the shape of the LVA normalized profile (Appendix D and Fig. D.1). Consequently, we focused on this LVA component and attempted to fit the normalized profile using the absorption model of Appendix E. The other LVAs do not show a similar double-dipped structure, making it impossible to constrain ϕ_1 and ϕ_2. This absence of distinct dips could be the result of a small azimuthal extension, or a significant local broadening (parameterized by σ) which smooths out the dips. However, the widths of the LVAs in the other spectra are consistent with that of the LVA in ES 22.5, suggesting comparable toroidal velocities.

We considered only the interval between -90 km s^{-1} and -15 km s^{-1} in the profile of Fig. D.1. The model has 7 parameters: v_z and v_ϕ, the angles ϕ_1 and ϕ_2, and the scaling parameters σ, τ_0 and CF (see Appendix E for their definition). Since there is a degeneracy between τ_0 and CF (Fig. E.1), we fixed CF $= 1$, that is, we assumed complete coverage of the emitting region. The result of the fit is shown in Fig. 9. The best fit has $\chi^2 = 216$ for 144 degrees of freedom. The parameters are $v_z = 77.03 \pm 0.62$ km s^{-1}, $v_\phi = 29.2 \pm 1.2$ km s^{-1}, $\phi_1 = -100 \pm 21$ °, $\phi_2 = 163 \pm 43$ °, $\tau_0 = 0.126 \pm 0.001$, and $\sigma = 4.39 \pm 0.03$ km s^{-1}. The best-fit azimuthal limits suggest that the region is significantly extended in azimuth, with $\Delta\phi = \phi_2 - \phi_1 \approx 3\pi/4$.

By separating the vertical and toroidal velocity components, we can apply the conservation of energy and angular momentum along a magnetic field line to determine the wind's launching point (Anderson et al. 2003). To achieve

this, we must first estimate the radial distance r where the absorption occurs. We adopt the geometry depicted in Fig. 6, which describes an outflow with a full opening angle of $\theta = 25^{\circ}$ (Birney et al. 2024) that originates from $R_{\rm co}$ (Romanova et al. 2009). Additionally, we assume that the absorption takes place at the limb of the conical outflow. We then estimate r by solving the system

$$z = \frac{r + r_1}{\tan i_\star}; \quad z = \frac{r - R_{\rm co}}{\tan \theta/2}. \tag{3}$$

Here $r_1 = [0, R_{\rm T}]$ is the radial range of the region from which the magnetospheric emission originates. The system corresponds to the intersection of the line of sight to the magnetosphere and the boundary of the conical wind that is closer to us (Fig. 6). The result is

$$r = -\frac{r_1 \tan\theta/2 + R_{\rm co} \tan i_\star}{\tan\theta/2 - \tan i_\star}. \tag{4}$$

For r_1 between 0 and $R_{\rm T}$, and the values of $R_{\rm T}$ and $R_{\rm co}$ from Table B.1, we find $r = 19.5 \pm 3.4\ R_\star$. To find the launching radius in the disk, $r_{\rm d}$, we solve the equation

$$r v_\phi \Omega_{\rm d} - \frac{3}{2}(GM_\star)^{2/3}\,\Omega_{\rm d}^{2/3} - \frac{v_z^2 + v_\phi^2}{2} = 0, \tag{5}$$

where $\Omega_{\rm d}$ is the Keplerian velocity of the disk at $r_{\rm d}$, that is, $\Omega_{\rm d} = (GM_\star/r_{\rm d}^3)^{1/2}$ (Anderson et al. 2003, and Appendix F). This is a cubic equation in $\Omega_{\rm d}^{1/3}$. The result is $\Omega_{\rm d} = 3.5 \times 10^{-5}$ s^{-1}, and $r_{\rm d} = 0.026$ AU $= 2.47$ R$_\star$. This values confirm that the LVA is produced in a wind that is launched from the very inner disk, close to the truncation radius.

The known value of $v_\phi = 29.2$ km s^{-1} at a distance r where the magnetic field is negligible allows to derive the angular momentum per unit mass carried by the conical wind, $l = r v_\phi = 6 \pm 1$ AU km s^{-1}. The Alfvén radius, $R_{\rm A}$, of the conical wind can be found using angular momentum conservation, $\Omega_{\rm d} R_{\rm A}^2 = r v_\phi$ (e.g., Mestel 1984; Anderson et al. 2003). We find $R_{\rm A} = 7.3 \pm 0.3\ R_\star$, where the uncertainty is dominated by the error on r.

5.4. MVA component: absorption in the jet close to the star

Whelan et al. (2021) derived the radial velocity gradient along the jet axis for the gas traced by the HVC of the [O I] 6300 and [S II] 6731 lines based on UVES spectra of RU Lup. A visual linear fit of their $v_{\rm rad}$ vs. Δz relation (Fig. 8 of their paper) gives $dv/dz \approx 3.5$ km s^{-1} AU^{-1} for the [O I] 6300 HVC and $dv/dz \approx 1$ km s^{-1} AU^{-1} for the [S II] 6731 HVC. Their HVC is defined between -225 km s^{-1} and -90 km s^{-1}, that comprises our MVA. Gas travelling at $v \sim 150 - 170$ km s^{-1} (i.e., the velocity of the MVA in the ESPRESSO spectra) covers a distance of approximately $31 - 36$ AU over the time interval between the 2021 and 2022 observing epochs. If the MVA is produced in the low density part of the jet traced by the FELs, then we expect a drift in velocity of $\sim 110 - 120$ km s^{-1} and $\sim 30 - 40$ km s^{-1} using dv/dz from the [O I] 6300 and [S II] 6731 HVCs, respectively. However, the MVA shifts only by $\Delta v \sim 20$ km s^{-1}. Additionally, the shape of this DAC varies significantly in the Ca II K line from ES 21.1 to ES 21.2, corresponding to a time span of ~ 9 days. These facts indicate that the MVA is not associated with the low-density gas traced by the FELS, but is likely formed closer to the star.

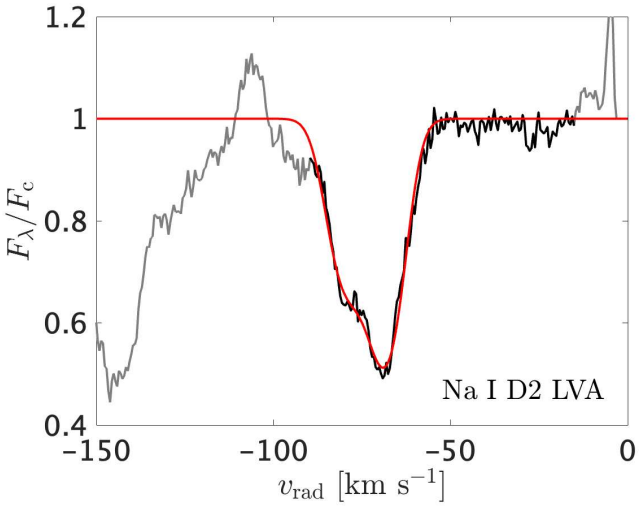

Fig. 9: Best fit (red line) of the normalized absorption profile of the LVA component in the Na I D2 line from the ES 22.5 spectrum (black line). The profile is the same as that of Fig. D.1. The regions excluded from the fit are plotted in gray.

Although the MVA and the LVA have similar EWs in Na I, the MVA is strongly optically thick in Ca II. This tells us that the absorbing gas is likely ionized, but its exact ionization level remains uncertain. The saturation of the Ca II MVA prevents us from determining its column density, as the conversion from EW to $N_{\rm H}$ is not possible outside the optically thin regime.

The MVA profiles in the 2022 ESPRESSO spectra are similar to those of the LVA. The MVA is ~ 40 km s^{-1} broad and sometimes shows a double-dipped structure, for example in the Na I D2 line of ES 22.4. This suggests that it is broadened by a similar mechanism, that is, a radial velocity gradient induced by the toroidal component (see Sect. 5.3). Therefore we fit the MVA component in the ES 22.4 spectrum, where this profile type is most prominent, to disentangle v_z and v_ϕ. In this case, we used the Na I D1 line instead of the D2. This because the MVA of the D1 line is between the Na I D2 redshifted wing and the Na I D1 blueshifted wing, making it simple to find a local continuum. Figure 10 shows the result of the fit. The best fit has $\chi^2 = 376$ for 194 degrees of freedom. The parameters are $v_z = 151.49 \pm 0.44$ km s^{-1}, $v_\phi = 34.8 \pm 1.8$ km s^{-1}, $\phi_1 = -165 \pm 33$ °, $\phi_2 = 113 \pm 15$ °, $\tau_0 = 0.106 \pm 0.002$, and $\sigma = 4.45 \pm 0.04$ km s^{-1}. The gas responsible for the MVA has higher toroidal velocity than the LVA gas, indicating a different origin. According to MHD simulations (Romanova et al. 2009), the gas has higher v_ϕ closer to the rotation axis. Thus, we propose that the MVA component is produced in the jet.

Under this assumption, we can derive the radial distance at which this absorption is formed by using a conservation equation similar to that of Anderson et al. (2003). The equation is

$$\Omega_\star r v_\phi - \frac{GM_\star}{R_\star} - \frac{1}{2}(v_{\rm z}^2 + v_\phi^2) = 0 \tag{6}$$

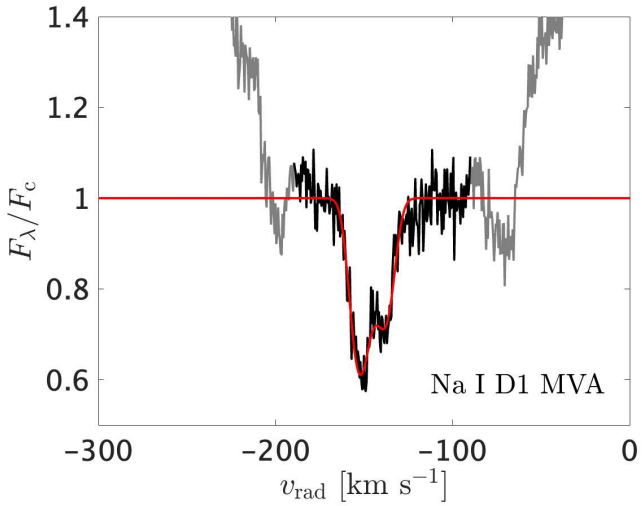

Fig. 10: Best fit (red line) of the normalized absorption profile of the MVA component in the Na I D1 line from the ES 22.4 spectrum (black line). The regions excluded from the fit are plotted in gray.

(Appendix F). Using the known value of the stellar angular velocity, $\Omega_\star = 1.95 \times 10^{-6}$ s^{-1}, the derived velocities v_z and v_ϕ, and the stellar parameters $M_\star$ and $R_\star$, the equation yields $r = 0.57$ AU $= 54.1$ R$_\star$. Assuming that the MVA originates inside the cone of Fig. 6, we obtain a lower limit on the distance from the disk plane, $z > (r - R_{co})/\tan\theta/2 = 2.40$ AU $= 227$ R$_\star$.

The gas traced by the MVA transports an angular momentum per unit mass $l = rv_\phi = 19.83$ AU km s^{-1}. From $\Omega_\star R_A^2 = l$, we find $R_A = 7.8\ R_\star$ for the portion of the jet traced by the MVA.

5.5. HVA component: jet knot at large scale

The similar velocity structure between the Ca II HVA and the HVC of the FELs (see Fig. 4) indicates a common origin. This has been already observed for the CTTS V1331 Cyg by Petrov et al. (2014), who called the DACs "shell profiles".

For RU Lup, Whelan et al. (2021) showed that the HVC component of the [S II] 6371 line is formed in a "knot" of the outflow at ~ 55 AU along the outflow position angle (PA). The knot is likely formed due to a shock within the jet, in which ionized atoms recombine in the post-shock region (e.g., Hartigan et al. 1995). The observed velocity sub-structure in the Ca II HVA is compatible with a formation in a shocked region, where the flow is likely turbulent and parcels of gas might have a local velocity component relative to the bulk velocity of the knot. The presence of the knot at distances of tens of AU from the star further supports the hypothesis that the Ca II emission originates in the wind, because the high velocity portion of the wind intersects the line of sight to the magnetosphere at distances smaller than $\sim 35\ R_\star \approx 0.35$ AU, as illustrated in Fig. 6. This is significantly smaller than the distance at which the knot is observed, implying that the wind both emits and absorbs in Ca II.

Unlike the LVA and the MVA, which trace the outflow close to the launching region, the HVA is associated with the large scale structure of the jet, that has low density and is also observed in the FELs. For the HVA, the line width is likely not representative of the toroidal velocity in the flow. The lack of an HVA in Na I indicates that sodium is fully ionized. Similarly, hydrogen is expected to be ionized, implying $n_H \approx n_e$. Given the lower density of the outflow, the column required to produce such an optically thick absorption component must be significantly greater than in the regions responsible for the other two DACs. Consequently, the observed velocity range could result from the gradient in v_z along the line of sight, or from turbulent broadening within the shocked region.

5.6. Alfvèn radius of the high velocity jet

A main result of Paper I was the determination of the location of the disk truncation radius, R_T, of RU Lup from the analysis of the light curve obtained with the *Transiting Exoplanet Survey Satellite* (TESS, Ricker et al. 2014). We derived $R_T \approx 2\ R_\star$ and showed that R_T varies with the accretion rate, $\dot{M}_{acc}$. We estimated $\dot{M}_{acc} = 1.47 \times 10^{-7}\ M_\odot$ yr^{-1} during the TESS Sector 65 observation. Together with $M_\star$ (Table B.1), these measures allow us to compute the accretion torque,

$$\tau_{acc} = \dot{M}_{acc}\sqrt{GM_\star R_T} \quad (7)$$

(e.g., Matt & Pudritz 2005b; Pantolmos et al. 2020). We obtain $\tau_{acc} = 9.46 \times 10^{43}$ g cm^2 s^{-2} or, in convenient units, $\tau_{acc} = 3.2 \times 10^{-7}\ M_\odot$ yr^{-1} AU km s^{-1}.

This torque spins up the star on a characteristic timescale $t_{acc} = I_\star \Omega_\star / \tau_{acc}$, where $I_\star = (2/5) M_\star R_\star^2$ is the stellar moment of inertia and $\Omega_\star = 2\pi/P_\star$ is the stellar angular velocity. Using $P_\star = 3.71$ days (Table B.1), we derive $t_{acc} \approx 3.57 \times 10^4$ yr for RU Lup. Since the star has an age of $\sim 2 - 3$ Myr (Herczeg et al. 2005), it should already rotate at break-up velocity. Thus, most of the accretion torque must be balanced by a braking torque, τ_{wind}, that is due to the angular momentum lost through a wind.

In the theory of magnetic stellar winds (e.g., Mestel 1984; Matt & Pudritz 2005a), the spin-down torque is parameterized as

$$\tau_{wind} = -k\dot{M}_{wind}\Omega_0 R_A^2. \quad (8)$$

where $\dot{M}_{wind}$ is the rate of mass loss, Ω_0 is the angular velocity at the base of the flow, and R_A is the Alfvén radius. Beyond R_A the outflow becomes matter-dominated, that is, the magnetic field no longer controls the dynamics of the flow. The parameter k depends on the wind geometry and is of order unity. For a spherically symmetric wind, $k = 2/3$ (Matt & Pudritz 2005a).

Birney et al. (2024) derived a rate of mass loss $\dot{M}_{wind} = 4.7 \times 10^{-9}\ M_\odot$ yr^{-1} for the jet traced by the HVC of the FELs of RU Lup. Since this jet must originate at the stellar surface, we assume $\Omega_0 = \Omega_\star$ in Eq. 8. Using the value of R_A obtained from the analysis of the MVA ($7.8\ R_\star$) and $k = 2/3$, we estimate the angular momentum loss rate in the jet, $\tau_{wind} = 6.2 \times 10^{-8}\ M_\odot$ yr^{-1} AU km s^{-1}. This is a factor of 5 lower than τ_{acc}, implying that the portion of the jet traced by the MVA is ineffective in spinning down the star.

The MHD simulations of Romanova et al. (2009) showed that different portions of the jet carry varying amounts of

mass and angular momentum. Specifically, while the outer parts of the outflow transport most of the mass, the inner regions near the axis are responsible for carrying the majority of the angular momentum. Based on this, we propose that the HVC of the FELs traces the jet component that removes most of the excess angular momentum and prevents stellar spin-up.

Since we cannot independently determine the mass-loss rate for each component of the outflow, we adopt the value of $\dot{M}_{\rm wind}$ derived by Birney et al. (2024) to place an upper limit on the Alfvén radius of the high-velocity jet component. Assuming that this component carries away the excess angular momentum required for spin equilibrium ($\tau_{\rm acc} + \tau_{\rm wind} = 0$), and taking $k = 2/3$ in Eq. 8, we estimate $R_{\rm A} \lesssim 17.7\ R_\star$. This corresponds to an angular momentum loss per unit mass equal to $\Omega_\star R_{\rm A}^2 = 102$ AU km s^{-1}. Notably, the ratio $R_{\rm A}/R_\star$ is comparable to the solar value, $R_{\rm A}/R_\odot = 12 - 16$ (Li 1999).

5.7. Spinning down RU Lup: spin-down efficiency of the stratified outflow

The high resolving power and signal-to-noise ratio of the ESPRESSO spectra allowed us to study the physics of the outflow of RU Lup close to the star. We found evidence of an onion-like structure in which the jet, launched from the stellar surface, is contained in an MHD disk wind launched from close to the disk truncation radius and it is likely denser than the jet itself. Moreover, we showed that the peripheral parts of the jet have lower velocities compared to the region closer to the rotation axis. Table 1 summarizes the properties of the region in the outflow of RU Lup from the spectroscopic tracers analyzed in this work.

Our analysis allows for some conclusions on the spin-down mechanism. We showed that different regions of the outflow remove angular momentum with varying efficiencies. In particular, the conical wind and the peripheral part of the jet are not able to extract enough angular momentum to spin down the star. Therefore, we suggested that the "backbone" of the jet—the region close to the rotation axis—is responsible for removing the most angular momentum. This scenario is in agreement with the MHD simulations by Romanova et al. (2009).

6. Conclusions

In this work we used the high resolution ESPRESSO spectra of RU Lup, obtained as part of the PENELLOPE program (Manara et al. 2021), to study the structure of the outflow of this strongly accreting CTTS. The observations trace the outflow close to the launching region and constrain the spin-down mechanism. Specifically, we combined the information that can be extracted from the forbidden emission lines with the study of absorption components in the permitted resonance lines of the Na I D1 & D2 and Ca II H & K doublets. Figure 11 sketches the inferred structure of the outflow.

The main results are outlined below.

- The outflow of RU Lup has an "onion-like" structure, where a stellar jet is enclosed within a slower, denser MHD-driven disk wind.
- The LVC-BC of the [O I] 5577 and [O I] 6300 lines traces an MHD wind launched from the inner disk, which we identify with the conical wind predicted from MHD simulations (Romanova et al. 2009).
- The LVA component originates in the conical wind, where it absorbs magnetospheric emission in Na I.
- The MVA component traces the peripheral region of the jet and its variability is linked to the accretion process.
- The HVA component is connected to the HVC of the FELs, both of which originate in the low-density outer region of the jet at distances $\gtrsim 50$ AU.
- Different components of the outflow extract angular momentum with varying efficiencies. If the star is in spin equilibrium, the majority of the angular momentum must be carried away by the inner jet close to the rotation axis, while the jet's periphery and the inner disk wind contribute less efficiently to the angular momentum loss.

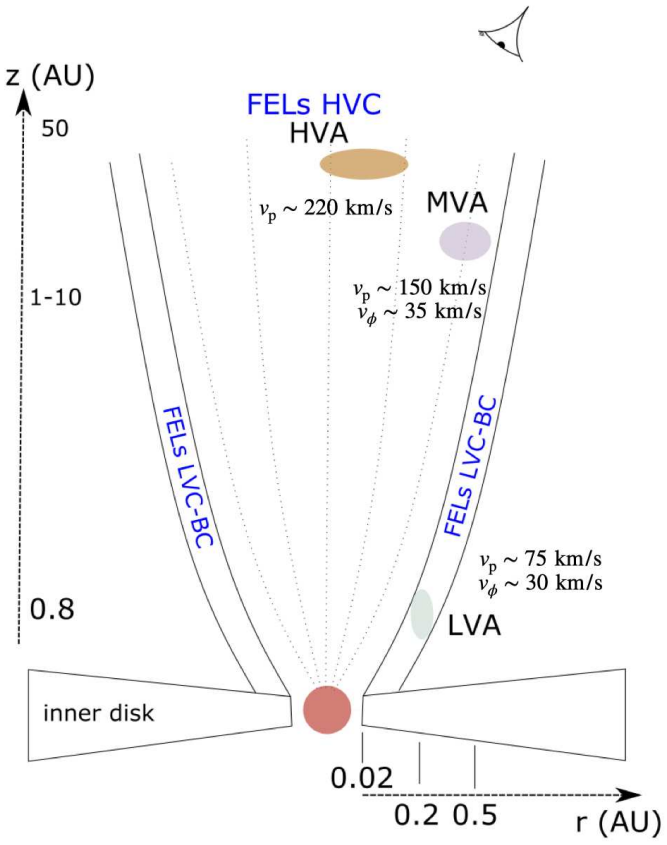

Fig. 11: Sketch of the outflow structure of RU Lup inferred from our analysis. The figure is not to scale.

Future studies should aim at extending this analysis to other systems. While the low inclination of RU Lup provides a direct view of the outflow, systems observed at higher inclinations are expected to exhibit a higher radial velocity gradient due to the toroidal motion. Additionally, time-resolved spectroscopic observations across different timescales would enable a detailed investigation of the variability of the different components of the outflow and their connection to the accretion process.

Acknowledgements. This work has been supported by Deutsche Forschungsgemeinschaft (DFG) in the framework of the YTTHACA Project (469334657) under the project codes STE 1068/9-1 and MA

Table 1: Properties of the outflow derived from the analysis of the FELs and the DACs of RU Lup.

Tracer	Region	v_z [km s^{-1}]	v_ϕ [km s^{-1}]	l [AU km s^{-1}]	Ω_0 [10^{-5} s^{-1}]	R_A [$R_\star$]
LVA & LVC-BC	conical wind	77	29	6	3.5	7.3
MVA	jet periphery	151	35	20	1.96	7.8
HVA & HVC	jet backbone	~ 220	?	102	1.96	17.7

Notes. Here, l is the angular momentum per unit mass, Ω_0 is the angular velocity at the footpoint of the wind, and R_A is the Alfvèn radius.

8447/1-1. AF acknowledges financial support from the project PRIN-INAF 2019 "Spectroscopically Tracing the Disk Dispersal Evolution" (STRADE) and the Large Grant INAF 2022 "YSOs Outflows, Disks and Accretion: towards a global framework for the evolution of planet forming systems" (YODA). CFM and JCW are funded by the European Union (ERC, WANDA, 101039452). Views and opinions expressed are however those of the author(s) only and do not necessarily reflect those of the European Union or the European Research Council Executive Agency. Neither the European Union nor the granting authority can be held responsible for them. JFG was supported by Fundação para a Ciência e Tecnologia (FCT) through the research grants UIDB/04434/2020 and UIDP/04434/2020. The authors acknowledge the use of the electronic bibliography maintained by the NASA/ADS[1] system.

References

Alcalá, J. M., Manara, C. F., Natta, A., et al. 2017, A&A, 600, A20
Anderson, J. M., Li, Z.-Y., Krasnopolsky, R., & Blandford, R. D. 2003, ApJ, 590, L107
Ardila, D. R., Basri, G., Walter, F. M., Valenti, J. A., & Johns-Krull, C. M. 2002, ApJ, 567, 1013
Armeni, A., Stelzer, B., Claes, R. A. B., et al. 2023, A&A, 679, A14
Armeni, A., Stelzer, B., Frasca, A., et al. 2024, A&A, 690, A225
Asplund, M., Grevesse, N., Sauval, A. J., & Scott, P. 2009, ARA&A, 47, 481
Bacciotti, F., Nony, T., Podio, L., et al. 2025, arXiv e-prints, arXiv:2501.03920
Bacciotti, F., Ray, T. P., Mundt, R., Eislöffel, J., & Solf, J. 2002, ApJ, 576, 222
Bacon, R., Accardo, M., Adjali, L., et al. 2010, in Society of Photo-Optical Instrumentation Engineers (SPIE) Conference Series, Vol. 7735, Ground-based and Airborne Instrumentation for Astronomy III, ed. I. S. McLean, S. K. Ramsay, & H. Takami, 773508
Balbus, S. A. & Hawley, J. F. 1991, ApJ, 376, 214
Banzatti, A., Pascucci, I., Edwards, S., et al. 2019, ApJ, 870, 76
Birney, M., Whelan, E. T., Dougados, C., et al. 2024, A&A, 692, L5
Bouvier, J., Alencar, S. H. P., Harries, T. J., Johns-Krull, C. M., & Romanova, M. M. 2007, in Protostars and Planets V, ed. B. Reipurth, D. Jewitt, & K. Keil, 479
Bouvier, J., Matt, S. P., Mohanty, S., et al. 2014, in Protostars and Planets VI, ed. H. Beuther, R. S. Klessen, C. P. Dullemond, & T. Henning, 433
Campbell-White, J., Manara, C. F., Benisty, M., et al. 2023, ApJ, 956, 25
Coffey, D., Bacciotti, F., Ray, T. P., Eislöffel, J., & Woitas, J. 2007, ApJ, 663, 350
Dekker, H., D'Odorico, S., Kaufer, A., Delabre, B., & Kotzlowski, H. 2000, in Society of Photo-Optical Instrumentation Engineers (SPIE) Conference Series, Vol. 4008, Optical and IR Telescope Instrumentation and Detectors, ed. M. Iye & A. F. Moorwood, 534–545
Edwards, S., Cabrit, S., Strom, S. E., et al. 1987, ApJ, 321, 473
Ercolano, B. & Pascucci, I. 2017, Royal Society Open Science, 4, 170114
Fang, M., Pascucci, I., Edwards, S., et al. 2018, ApJ, 868, 28
Frasca, A., Biazzo, K., Lanzafame, A. C., et al. 2015, A&A, 575, A4
Gahm, G. F., Stempels, H. C., Walter, F. M., Petrov, P. P., & Herczeg, G. J. 2013, A&A, 560, A57
Gahm, G. F., Walter, F. M., Stempels, H. C., Petrov, P. P., & Herczeg, G. J. 2008, A&A, 482, L35
Gaia Collaboration, Brown, A. G. A., Vallenari, A., et al. 2021, A&A, 649, A1
Hartigan, P., Edwards, S., & Ghandour, L. 1995, ApJ, 452, 736
Hartmann, L. 2008, Accretion Processes in Star Formation, 2nd edn., Cambridge Astrophysics (Cambridge University Press)
Hartmann, L., Herczeg, G., & Calvet, N. 2016, ARA&A, 54, 135
Hartmann, L. & Stauffer, J. R. 1989, AJ, 97, 873
Herczeg, G. J., Walter, F. M., Linsky, J. L., et al. 2005, AJ, 129, 2777
Hirth, G. A., Mundt, R., & Solf, J. 1997, A&AS, 126, 437
Krist, J. E., Stapelfeldt, K. R., Hester, J. J., et al. 2008, AJ, 136, 1980
Kurosawa, R. & Romanova, M. M. 2012, MNRAS, 426, 2901
Kwan, J. & Tademaru, E. 1988, ApJ, 332, L41
Lesur, G. R. J. 2021, A&A, 650, A35
Li, J. 1999, MNRAS, 302, 203
Manara, C. F., Ansdell, M., Rosotti, G. P., et al. 2023, in Protostars and Planets VII, ed. S. Inutsuka, Y. Aikawa, T. Muto, K. Tomida, & M. Tamura, Vol. 534, 539
Manara, C. F., Frasca, A., Venuti, L., et al. 2021, A&A, 650, A196
Matt, S. & Pudritz, R. E. 2005a, ApJ, 632, L135
Matt, S. & Pudritz, R. E. 2005b, MNRAS, 356, 167
Mayor, M., Pepe, F., Queloz, D., et al. 2003, The Messenger, 114, 20
Mestel, L. 1984, in Cool Stars, Stellar Systems, and the Sun, ed. S. L. Baliunas & L. Hartmann, Vol. 193, 49
Natta, A., Testi, L., Alcalá, J. M., et al. 2014, A&A, 569, A5
Nisini, B., Antoniucci, S., Alcalá, J. M., et al. 2018, A&A, 609, A87
Pantolmos, G., Zanni, C., & Bouvier, J. 2020, A&A, 643, A129
Pascucci, I., Cabrit, S., Edwards, S., et al. 2023, in Astronomical Society of the Pacific Conference Series, Vol. 534, Protostars and Planets VII, ed. S. Inutsuka, Y. Aikawa, T. Muto, K. Tomida, & M. Tamura, 567
Pepe, F., Cristiani, S., Rebolo, R., et al. 2021, A&A, 645, A96
Petrov, P. P., Kurosawa, R., Romanova, M. M., et al. 2014, MNRAS, 442, 3643
Pyo, T.-S., Hayashi, M., Kobayashi, N., Tokunaga, A, T., et al. 2006, Adaptive Optics Spectroscopy of the [Fe II] Outflows from HL Tauri and RW Aurigae
Ray, T., Dougados, C., Bacciotti, F., Eislöffel, J., & Chrysostomou, A. 2007, in Protostars and Planets V, ed. B. Reipurth, D. Jewitt, & K. Keil, 231
Ricker, G. R., Winn, J. N., Vanderspek, R., et al. 2014, in SPIE Conf. Ser., Vol. 9143, Space Telescopes and Instrumentation 2014: Optical, Infrared, and Millimeter Wave, ed. J. Oschmann, Jacobus M., M. Clampin, G. G. Fazio, & H. A. MacEwen, 914320
Rigliaco, E., Pascucci, I., Gorti, U., Edwards, S., & Hollenbach, D. 2013, ApJ, 772, 60
Romanova, M. M., Ustyugova, G. V., Koldoba, A. V., & Lovelace, R. V. E. 2009, MNRAS, 399, 1802
Simon, M. N., Pascucci, I., Edwards, S., et al. 2016, ApJ, 831, 169
Smette, A., Sana, H., Noll, S., et al. 2015, A&A, 576, A77
Spitzer, L. 1998, Physical Processes in the Interstellar Medium
Stempels, H. C., Gahm, G. F., & Petrov, P. P. 2007, A&A, 461, 253
Stock, C., McGinnis, P., Caratti o Garatti, A., Natta, A., & Ray, T. P. 2022, A&A, 668, A94
Weber, M. L., Ercolano, B., Picogna, G., Hartmann, L., & Rodenkirch, P. J. 2020, MNRAS, 496, 223
Wendeborn, J., Espaillat, C. C., Lopez, S., et al. 2024, ApJ, 970, 118
Whelan, E. T., Pascucci, I., Gorti, U., et al. 2021, ApJ, 913, 43

[1] `https://ui.adsabs.harvard.edu`

Table A.1: Log of the spectroscopic observations.

ID	MJD (−52300 days)	S/N	$t_{\rm exp}$ (s)
ES 21.1	7149.00	55	600
ES 21.2	7158.06	32	400
ES 22.1	7501.04	47	600
ES 22.2	7502.06	46	600
ES 22.3	7504.10	50	600
ES 22.4	7507.10	20	600
ES 22.5	7514.04	46	600

Notes. The spectra are labelled as in Paper I. The resolving power of the ESPRESSO spectra is $R = 140000$.

Table B.1: Stellar and accretion parameters of RU Lup.

Parameter	Value	Ref.
d	158.9 ± 0.7 pc	[1]
SpT	K7	[2]
$T_{\rm eff}$	4250 ± 60 K	[3]
$v \sin i$	8.6 ± 1.4 km s^{-1}	[3]
$i_\star$	16 ± 5 °	[3]
$R_\star$	2.27 ± 0.52 $R_\odot$	[3]
$M_\star$	0.55 ± 0.13 $M_\odot$	[4]
$L_\star$	1.46 ± 0.67 $L_\odot$	[4]
$P_\star$	3.71 ± 0.01 d	[5]
$R_{\rm co}$	~ 3.64 $R_\star$	[3]
$R_{\rm T}$	~ 2 $R_\star$	[3]

Notes. References: [1] Gaia Collaboration et al. (2021); [2] Alcalá et al. (2017); [3] Paper I; [4] Manara et al. (2023); [5] Stempels et al. (2007).

Appendix A: Log of spectroscopic observations

Table A.1 reports the spectroscopic observations used in this work.

Appendix B: Stellar and accretion parameters

For the convenience of the reader, we report in Table B.1 the stellar parameters of RU Lup which are needed for the analysis of the outflow, together with the position of the corotation radius ($R_{\rm co}$) and the truncation radius ($R_{\rm T}$).

Appendix C: Photospheric subtraction in the forbidden emission lines

The line profiles of the forbidden emission lines (FELs) of RU Lup are severely blended with the absorption lines from the photosphere of the star. To study the kinematics of the outflow, it is important to remove the stellar contribution from the profiles of the FELs. To this end, we used the template spectrum that we have identified in Paper I as best fitting the photospheric spectrum of RU Lup. The properties of the template were obtained using the ROTFIT code (Frasca et al. 2015), which uses a library of *High Accuracy Radial velocity Planet Searcher* (HARPS, Mayor et al. 2003) spectra from the ESO Archive to fit the photospheric spectrum. The details of the procedure to obtain the template are reported in Paper I. We note that future developments of the STAR-MELT package will include an automated method for removing photospheric contributions from high-resolution spectra, and we plan to make a comprehensive grid of reduced templates publicly available (Campbell-White et al., in preparation).

For each emission line, we adjusted the veiling fraction (VF) in its vicinity to match the depth of the photospheric lines. The procedure and the result of the photospheric subtraction are shown in Fig. C.1. Due to the effect of line filling emission in the photospheric lines, which we analyzed in Paper I, the photospheric subtraction has some imperfections. The absorption lines that sit on top of the [O I] 6300 and [S II] 6731 lines have been correctly removed, but the wings of the [O I] 5577 line are still slightly contaminated, especially the red one.

Appendix D: Column density of the low velocity absorption component

The LVA is detected only in the Na I lines. This suggests that most of the gas in the absorbing region is cold, hence neutral and in the ground state. Since Na I D2 is a resonance line, we can estimate the column density, N, of the absorbing material without any assumption on the temperature.

The easiest way to do this is computing the equivalent width (EW) of the line. In the optically thin limit, the EW is linearly related to the column density of sodium atoms. To this end, we need a model for the un-absorbed emission profile. We used the red wing of the Na I D2 line as a model for the blue wing emission, by folding the D2 line profile around the line center as shown in the top panel of Fig. D.1.

The normalized profile $F_\lambda/F_{\rm c}$ (bottom panel) is derived by dividing the blue wing by the folded red wing. The optical depth, assuming complete covering of the emitting region, is $\tau_\lambda = -\ln(F_\lambda/F_{\rm c})$. At line minimum we obtain $\tau_\lambda = 0.71$, confirming that the gas is not optically thick. We derived EW by integrating the normalized profile in the $v_{\rm rad}$ range of the LVA, that is, -90 km s^{-1} $\leq$ v$_{\rm rad}$ $\leq$ -60 km s^{-1}. The result is EW = 0.19 Å. We applied this procedure only to the ES 22.5 spectrum. For the other spectra, the red wing did not accurately reproduce the unabsorbed LVA profile.

We converted the EW to N by inverting the formula

$$\frac{\rm EW}{\lambda_0} = (8.85 \times 10^{-21})\, N \lambda_0 f, \tag{D.1}$$

where λ_0 and f are the rest wavelength in Å and the oscillator strength of the transition, respectively, and N is in cm^{-2} (e.g., Spitzer 1998). For the D2 line we used $\lambda_0 = 5889.95$ Å and $f = 0.641$ from the NIST Atomic Spectra Database[2].

The result is a column density of atoms in the ground state of the Na I ion, N_0, of 9.95×10^{11} cm^{-2}. Assuming that all sodium is neutral and in the ground state, then N_0 represents the total column density of sodium. Using the solar abundances from Asplund et al. (2009), we obtain the column density of hydrogen, $N_{\rm H} = 5.49 \times 10^{17}$ cm^{-2}.

Appendix E: Absorption line profiles in a wind with a toroidal velocity component

We calculated radial velocity profiles for absorption in a region of a wind that is narrow along the line of sight but

[2] https://physics.nist.gov/PhysRefData/ASD/lines_form.html

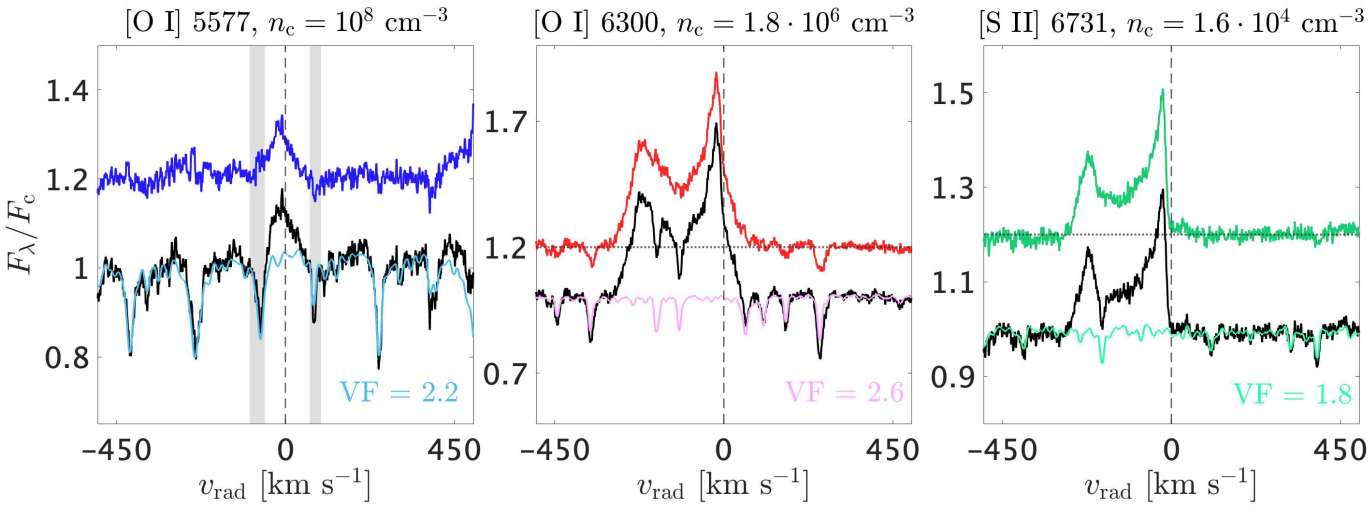

Fig. C.1: Photospheric subtraction procedure for the [O I] 5577, [O I] 6300, and [S II] 6731 lines in the ES 22.5 spectrum of RU Lup. The black lines are the observed spectra. The colored lines superposed on the observed spectra are from the K7 template for the photospheric spectrum of RU Lup, veiled to match the depth of the photospheric lines. Above these spectra are the photospheric-subtracted spectra, shifted vertically by 0.2 for clarity. In the left panel the shaded areas mark the region where the photospheric spectrum is not completely removed.

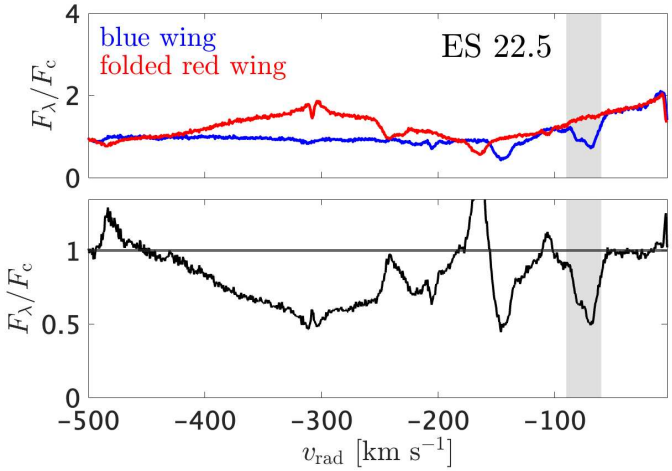

Fig. D.1: Extraction of the LVA component of the Na I D2 line in the ES 22.5 spectrum. The top panel shows the red wing line folded onto the blue wing. The bottom panel shows the ratio between the blue wing and the red wing, from which we computed the optical depth and EW. The shaded area marks the velocity extension of the LVA, as defined in Fig. 3.

extended in azimuth. To this end, we generated an array of azimuth angles (ϕ) between ϕ_1 and ϕ_2, and calculated the local optical depth as

$$d\tau_v(\phi) = \tau_0 \frac{1}{\sqrt{2\pi}\sigma} \exp\left[-\frac{(v - v_{\rm rad}(\phi))^2}{2\sigma^2}\right]. \quad \text{(E.1)}$$

where $v_{\rm rad}(\phi)$ and σ represent the center and standard deviation of the Gaussian function, and τ_0 is a scaling parameter. Using the radial velocity law of Eq. 2, we summed all contributions in ϕ to produce the total optical depth τ_v as a function of velocity. Then, we computed the resulting normalized line profile as

$$F_v = 1 - {\rm CF}[1 - \exp(-\tau_v)], \quad \text{(E.2)}$$

where CF is the covering factor, that is, the fraction of the emission region that is covered.

The shape of the line profile depends on the velocities v_z and v_ϕ, the angles ϕ_1 and ϕ_2, and the scaling parameters σ, τ_0, and CF. Figure E.1 displays examples of absorption profiles produced with this model for typical velocities observed in the LVA, that is, $v_z = 70$ km s^{-1} and $v_\phi = 50$ km s^{-1}. We assumed that the local broadening is thermal, that is, $\sigma = (2k_BT/Am_p)^{1/2}$, where $k_{\rm B}$ is the Boltzmann constant, T is the temperature, $m_{\rm p}$ is the proton mass, and A is the atomic number. In Fig. E.1, we fixed $T = 1000$ K and $A = 11$ (sodium), which yielded $\sigma = 1.22$ km s^{-1}.

Appendix F: Conservation equation for a stellar wind

Equation 5 has been obtained by Anderson et al. (2003) for a disk wind assuming the conservation of angular velocity (Ω), energy (E), and angular momentum (L) along a magnetic field line. Given these three quantities, we can construct a fourth conserved quantity that does not depend on the magnetic field components, $J = E - \Omega L$. Its expression in cylindrical coordinates is

$$J = \frac{1}{2}(v_{\rm p}^2 + v_\phi^2) - \frac{GM_\star}{\sqrt{r^2 + z^2}} - \Omega r v_\phi. \quad \text{(F.1)}$$

In the case of a wind originating from a Keplerian disk, at the launching radius r_0 we have $v_{\rm p} \approx 0$, $\Omega_0^2 = GM_\star/r_0^3$, and $v_\phi = \Omega_0 r_0$, so that $J = -(3/2)(GM_\star)^{2/3}\Omega_0^{2/3}$. The conservation of J between r_0 and a distance r where the gravitational potential is negligible gives Eq. 5.

In the case of a jet originating from the stellar surface, we have $\Omega_0 = \Omega_\star$. The difference with the previous case is that $GM_\star/R_\star^3$ is equal to the square of the Keplerian angular velocity at the stellar surface $\Omega_{\rm K}^2(R_\star)$, and not to $\Omega_\star^2$. Therefore, the value of the constant is

$$J \approx -\left[\Omega_{\rm K}^2(R_\star) + \frac{1}{2}\Omega_\star^2\right] R_\star^2 \quad \text{(F.2)}$$

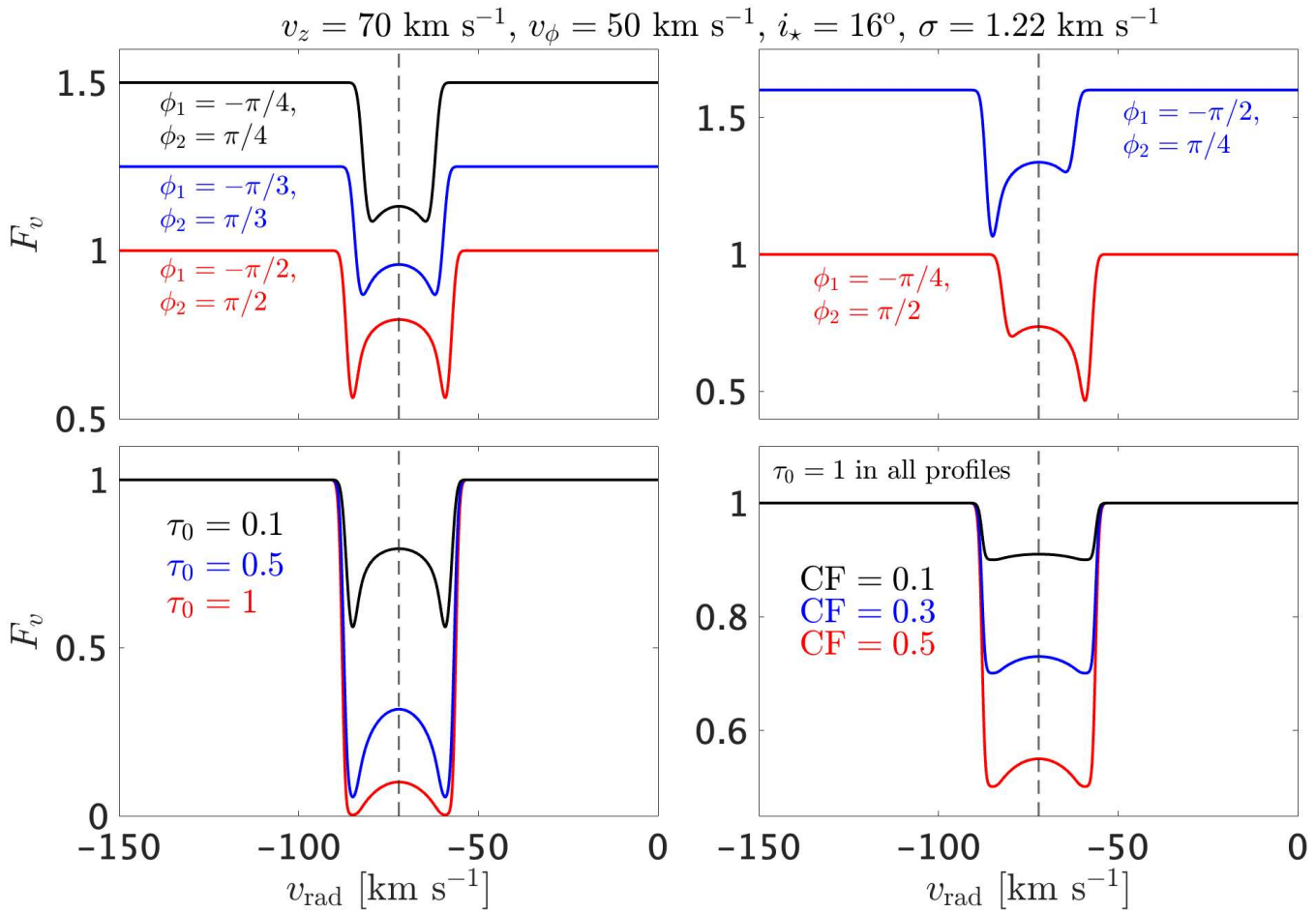

Fig. E.1: Gallery of absorption profiles for a vertically-narrow region of a wind which is extended in azimuth. In all plots, $v_z = 70$ km s^{-1}, $v_\phi = 50$ km s^{-1}, $i_\star = 16^\circ$, and $\sigma = 1.22$ km s^{-1}. If not reported, the parameters are $\phi_1 = -\pi/2$, $\phi_2 = \pi/2$, $\tau_0 = 0.1$, and CF $= 1$. The vertical dashed lines is are $-v_z \cos i_\star$.

Since $\Omega_\star \ll \Omega_{\rm K}(R_\star)$ in CTTSs, the second term can be neglected and the conservation equation becomes

$$\Omega_\star r v_\phi - \frac{GM_\star}{R_\star} - \frac{1}{2}(v_{\rm p}^2 + v_\phi^2) = 0. \qquad \text{(F.3)}$$